Entropy noise

Experimental and numerical investigation in turbomachinery

A thesis submitted to the

Board of the Faculty of the Engineering Science

in partial fulfilment of the requirements for the degree of

Doctor of Philosophy

Eduard Ron

Lady Margaret Hall

University of Oxford

Trinity Term 2015

To those I love

Acknowledgment

I first would like to thank my supervisor Prof Kam Chana, technical and commercial director of the Oxford Turbine Research Facility, for being supportive for three long years it took to complete this work. Experimental and numerical investigation of such a new and unique engineering issue as entropy noise would not be possible without his help, initiative and supervision.

I would also like to pay tribute to the experts from Rolls-Royce and ISVR, University of Southampton, who altogether with me and my supervisor formed the entropy noise investigation team. Keith Holland, a noise expert, was extremely helpful in the Green function technique procedure. Experts from Rolls-Royce are given thanks for their massive contribution to the overall progress of this work.

The design and manufacture of nozzles was carried out by David O'Dell, the Oxford Turbine Research Facility was operated by David Cardwell and Sunny Chana. A group of workshop technicians was involved in the instrumentation procedure for the experimental part of this work. They all deserve a grateful mark.

Abstract

Entropy noise is a type of combustion noise produced by the acceleration of entropy inhomogeneities in a fluid, and is typically produced in aeroengines when flow at the outlet from a combustor is accelerated in high pressure turbines. The entropy inhomogeneities arise from unsteady burning of the combustor flame and cooling introduced through the endwalls. To date there have only been limited attempts to experimentally study entropy noise generation. Some analytical and numerical contributions were made to its effect in a subsonic nozzle and turbine stage configuration.

The ever increasing noise emissions regulations produced a growing interest in optimising combustion noise and entropy noise in particular because the combustor exit temperature profile generates entropy noise due to its large temporal and spatial temperature variations. Therefore it became imperative to investigate and potentially quantify the sound pressure level of entropy noise emitted by a simple nozzle geometry with its subsequent application to a full turbine configuration. The present study utilised numerical and experimental methods to extend the understanding of entropy noise and its generation to a simple nozzle configuration and half a turbine stage.

Numerical simulation largely employed Large Eddy Simulation as a turbulence model to achieve a better accuracy and resolve energy transformation from kinetic energy contained between the shear layers of a temperature profile into acoustic perturbations. The accurate modelling of temporal and spatial temperature variations of a non-uniform temperature profile was performed, thus allowing the possibility to evaluate sound pressure levels of entropy noise generated in the Oxford Turbine Research Facility.

Experimental investigation was concentrated on two simple nozzle geometries with different acceleration rates in the nozzle guide vane region. The non-uniform and uniform temperature profiles were generated in a combustor simulator and noise measurements were performed at the outer wall of the duct extension. The noise evaluation showed that the presence of a temperature difference between the ‘hot spot’ and its environment produced an additional acoustic response of approximately 10dB in the crucial lower frequencies. Moreover, when the second nozzle was operated the sound pressure level of the uniform temperature profile was the same for two nozzle configurations, while that of the non-uniform temperature profile gave a noise difference in the frequency range from 10 to 3000Hz. This demonstrates that different acceleration rates produce different acoustic responses only when operated with non-uniform temperature profile. Following the acoustic analogy developed by James Lighthill it can be concluded that entropy noise was successfully measured.

The method developed for the numerical modelling of temperature variations of the non-uniform temperature profile was validated using the acquired experimental data. A good agreement was achieved between the predicted and measured results. This allowed an evaluation of sound pressure levels produced by typical rich-burn and lean-burn combustors. The numerical results confirmed that the lean-burn combustor is likely to produce a noise level larger than that of rich-burn by approximately 5-10dB in the lower frequencies for an equivalent mean temperature. A numerical parametric study of lean-burn combustor temperature profiles was performed and some recommendations on noise optimisation were explored.

Nomenclature

Roman

a	speed of sound at the turbine stage configuration $\left[\frac{m}{s}\right]$
B	bandwidth [*Hz*]
c_0	speed of sound $\left[\frac{m}{s}\right]$
C_μ	empirical RANS turbulence model constant
c_p	specific heat at constant pressure $\left[\frac{J}{kg \cdot K}\right]$
C_s	Smagorinsky coefficient
f	frequency [*Hz*]; fluid quantity
G	Green function; filter function
G_n	Green function measured experimentally
k	turbulent kinetic energy [J]
k_c	cut-off wave number $\left[\frac{1}{m}\right]$
l	length scale [m]
L_n	nozzle length [m]
L_p	sound pressure level [dB]
M	Mach number
N	number of time steps in numerical simulation
n	number of time steps; number of experiments
p	instantaneous pressure [*Pa*]
p_0	mean pressure [*Pa*]
p_n	measured static pressure due to real source [*Pa*]
p_{sn}	measured static pressure due to injection source [*Pa*]
$\hat{p}$	Fast Fourier Transform of static pressure [*Pa*]
R	acquired resistance [Ω]
R_0	initial resistance [Ω]
s	entropy $\left[\frac{J}{kg \cdot K}\right]$

s_0	mean entropy $\left[\frac{J}{kg \cdot K}\right]$
S_{ij}	strain rate tensor [*Pa*]
$\bar{S_s}$	dimensionless entropy variation in the entropy mode
t	time; measurement time [*s*]
t_s	time step [*s*]
T_{ij}	Lighthill's stress tensor [*Pa*]
T	instantaneous temperature [*K*]
T_0	mean temperature [*K*]
q	dimensionless strength of source
q_e	dimensionless strength of equivalent source
q_s	dimensionless strength of injection source
U	mean velocity component $\left[\frac{m}{s}\right]$
u	fluctuation velocity component; axial flow velocity $\left[\frac{m}{s}\right]$
$\bar{u}$	filtered velocity field $\left[\frac{m}{s}\right]$; dimensionless velocity
u^+	dimensionless velocity
u_0	initial voltage [*V*]
u_w	skin friction velocity $\left[\frac{m}{s}\right]$
w	wave frequency [*Hz*]
v	entropy mode velocity, radial flow velocity $\left[\frac{m}{s}\right]$; dimensionless velocity fluctuation
v_{pi}	velocity fluctuation in the acoustic mode $\left[\frac{Pa \cdot s}{m}\right]$
v_t	sub-grid scale viscosity [*Pa*]
x	location of the listener; axial distance [*m*]
y	source point location [*m*]
y^+	dimensionless measure of wall distance
Y	wavelength along the cascade [*m*]

Greek

α	coefficient of temperature sensitivity
γ	specific heat capacity

Δ	length scale [m]
Δu	voltage change [V]
ΔT_s	unsteady temperature variation [K]
δ	Dirac delta function
δ_{ij}	Kronecker delta
δx	axial spacing [m]
ϵ	dissipation rate of turbulent energy
η	indirect to direct combustion noise ratio; length scale [m]
κ	coefficient of thermal conductivity $\left[\frac{W}{m \cdot K}\right]$; wavenumber $\left[\frac{1}{m}\right]$
ξ	dimensionless space variable
π_{ij}	momentum flux of the real flow [Pa]
π_{ij}^0	momentum flux of the uniform acoustic medium [Pa]
ρ	instantaneous density; density $\left[\frac{kg}{m^3}\right]$
ρ_0	mean density $\left[\frac{kg}{m^3}\right]$
σ	standard deviation [dB]; dimensionless entropy fluctuation
σ_{ij}	viscous stress tensor [Pa]
τ	dimensionless time variable; time of density fluctuations generation by a point source [s]
τ_{ij}	sub-grid scale stress tensor [Pa]
τ_t	Reynolds stress tensor [Pa]
τ_w	shear stress [Pa]
φ	dimensionless pressure fluctuations
Ω	reduced frequency

Subscripts

0	combustor outlet
0’	combustor inlet
1	nozzle outlet
444	444K conditions
ent	entropy mode conditions
i	axial component

j	radial component
k	circumferential component
hs	'hot spot' conditions
ref	reference conditions
t	total condition

Superscripts

$'$	fluctuating quantity; sub-filtered portion
$+$	downstream propagating acoustic wave
$-$	upstream propagating acoustic wave
ent	entropy component
s	downstream propagating entropy wave

Abbreviation

1D	One-dimensional
2D	Two-dimensional
3D	Three-dimensional
CAD	Computer aided design
CFD	Computational fluid dynamics
EOTDF	Enhanced overall temperature distortion factor
FFT	Fast Fourier Transform
HP	High pressure
LE	Leading edge
LES	Large Eddy Simulation
NGV	Nozzle guide vane
OTRF	Oxford Turbine Research Facility
RANS	Reynolds-averaged Navier-Stokes
RQL	Rich-burn, quick-quench, lean-burn
TE	Trailing edge
URANS	Unsteady Reynolds-averaged Navier-Stokes

Contents

List of Figures

Chapter 1

Introduction

1.1 Overview of Aircraft Noise

Aircraft noise is of particular concern to the major aircraft companies and design engineers. Since the 1970s this topic has undergone constant development and currently is the subject of ever increasing scientific interest and financial investment. This is mainly because noise emanated from an aircraft causes physiological issues and general annoyance in and around airports. Long term effects of noise are structural and physiological impairment and decrease in efficiency of the observer. This explains the implementation of many noise emissions regulations currently in use. According to the International Civil Aviation Organization (ICAO Circular 313, 2007) the passenger-kilometre parameter is forecasting to experience an average annular increase of 4.6 per cent until 2025, this means a constant rise in overall noise emission and subsequently in its negative impacts.

Aircraft noise may be classified based on engine components producing it. Figure 1.1 illustrates the four largest noise sources in aircraft engines: fan, combustion, compressor and turbine, jet exhaust. Increase in high-bypass ratio of the turbofan engine enabled to significantly reduce the jet noise by minimising jet velocity for the same thrust, whereas the fan noise was decreased by designing new blade and vane geometries. Acoustic liners converting acoustic energy into heat were introduced further reducing fan noise at the aircraft departure. Thus, combustion noise is becoming a major noise source for aircrafts,

gas turbines and other propulsion devices. Figure 1.2 illustrates the contribution of combustion noise to the overall aircraft noise. With a decrease in the jet velocity, jet noise falls dramatically, whereas engine noise reduces more slowly.

Combustion is an isobaric stage of the working cycle of a jet engine where fuel is burnt and converted into thermal energy affiliated with an air velocity increase. Combustion chambers are situated after the compressor and before the turbine in the Brayton cycle. There are three types of combustion chambers commonly used in aeroengines: the multiple chamber, annular and cannular combustion chamber. All these types are composed of two zones: the first where the fuel is injected and burnt, and the second, where cooling air is introduced.

Hoch and Hawkins (Hoch, 1973) investigated the influence of the combustor design on the noise generated. When the combustor is separated into two chambers discharging into an annulus before entering the turbine stage (cannular design) the low-frequency noise is higher than one generated by a combustor without separate chambers (annular design). Simultaneously the high-frequency noise at blade-passing frequency was decreased. The most common combustor design nowadays is the annular chamber, which offers considerable reduction in engine length.

The annular combustor consists only of one flame tube. It has the fuel injectors and the igniters located circumferentially. The main advantage of this kind of combustor is that it can be 75% shorter than the cannular combustor in order to produce the same amount of power. Furthermore, it increases the efficiency and aids the control of combustor emissions, since it has a smaller wall area than other combustor designs which therefore

allows more air to be used in the combustion process as opposed to wall cooling. On the other hand, the drawback of this design is its structural complexity (Rolls-Royce, 2005).

Combustion noise originates in the combustor chamber and then propagates downstream through the turbine. It arises due to the presence of turbulence and heat release. There are two types of combustors: rich-burn and lean-burn. The rich-burn combustor is currently operating in the majority of civil aircrafts and is about to be superseded by a new generation lean-burn combustor. The latter is more economical and produces less NOx emissions due to the lower temperature peak value, the temperature of the 'hot spots' for lean-burn combustors is significantly lower than for rich-burn combustors. However, the lean-burn combustor appears to have larger temperature instabilities thus increasing the general noise level being generated. This is because lean premixed combustors burn more unsteadily.

1.2 Direct and Indirect Combustion Noise

Depending on its origin two types of combustion noise were classified by Strahle (Strahle, 1978): direct and indirect combustion noise. Direct combustion noise is a monopole acoustic source arising from unsteady burning of the combustor flame and representing itself as a volumetric expansion and contraction of the flow due to a change in the rate of heat release by the flame. These heat release fluctuations can be induced by a varying flame area or a change in the flame speed or density of the unburnt gas (Thomas & Williams, 1966).

Indirect combustion noise is another type of acoustic perturbations in the combustors, complex in its nature, and only recently started being considered as a potential contributor

to the overall aircraft noise. The dawn of modern aeroacoustics began in 1953 with the pioneering in-depth insight into generation of aerodynamic sound derived by James Lighthill (Lighthill, 1953). Lighthill's acoustic analogy deals with sound produced by turbulent stresses present in the real flow (Crighton, 1975). This 'excess noise' was deemed significant and classified into that associated with vorticity inhomogeneities, called vortex sound (Howe, 1975), entropy inhomogeneities (Morfey, 1973), entropy noise, and thermo-viscous dissipation (Crighton, 1975), regarded as a type of turbine noise.

Indirect combustion noise generation in the combustor is based on the superposition and interaction of three physical modes of wave perturbations: vorticity, entropy and acoustic modes. Their non-linear interactions were described by Chu and Kovasznay (Chu & Kovasznay, 1958). The product of entropy-acoustic second-order interaction was presented as thermal scattering of incident sound waves by entropy fluctuations. The other second-order terms leading to generation of acoustic response are acoustic-acoustic and vorticity-acoustic interactions. They were recognized as possible sources of subsonic rotor noise by FFowcs Williams and Hawkings (Williams & Hawkings, 1969). In order for entropy inhomogeneities to turn into an acoustic source, the acceleration of the mean flow driving and interacting with these inhomogeneities must take place. These entropy inhomogeneities are a product of the difference between the 'hot spot' originated due to flame burning and 'cold spot' produced by the endwall cooling. The intensity of entropy noise is proved to be proportional to temperature difference and mean flow velocity gradients. In the combustor the temperature difference between the 'hot spot' and its environment can reach up to 1000K, thus making entropy noise a potentially significant source of acoustic perturbations.

1.3 Aims of the Thesis

The purpose of this thesis is to prove experimentally the existence of indirect combustion noise generated during acceleration of the flow and being determined by entropy inhomogeneities arising from unsteady burning of the flame. This type of noise in aircraft is commonly called ‘entropy noise’. The experimental investigation was carried out for different non-uniform temperature profiles, thus allowing not only an estimate of entropy noise influence on overall noise propagating out of the nozzle, but also quantification of its dependence on temperature difference between the ‘hot spot’, the central area of the combustor exit temperature profile with higher temperature and larger temporal temperature variations, and its environment. Moreover, two nozzles were tested with different Mach number distributions within the nozzle guide vane region only, thus allowing validation of a successful entropy noise measurement. Two nozzles provided a good understanding of the acceleration rate role on the entropy noise generation and therefore, this investigation can potentially be useful for modelling of quieter stator blades in the first turbine stage.

In addition, the numerical evaluation of entropy noise is becoming more realistic, due to extensive use of reliable turbulence models, such as Large Eddy Simulation. Modelling of temperature profile with temperature variations in the radial and circumferential direction matching those measured experimentally will allow to perform comparison with the experimental data. The modelling of a quieter lean-burn combustor exit temperature profile thus becomes a possibility, and reduction of entropy noise by optimising temperature profile characteristics was performed.

The work presented in this thesis can be described as an experimental foundation of any entropy noise investigation. The experimental investigation was carried out with spatial and temporal temperature variations correctly representing those observed in the real combustor. The nozzles were characterised by an acceleration rates typical for a stator blades. Thus, the first evaluation of sound pressure level emanated from half a turbine stage was performed. The numerical part of the thesis paid a large contribution not only to the present work but expounded a new approach to well model temperature variations using Large Eddy Simulation. The developed numerical technique represents a novel method of sound pressure level evaluation generated by a temperature profile in a fluid and was used in lean-burn combustor temperature profile optimization.

1.4 Structure of the Thesis

Following the Introduction, the thesis is structured as:

Chapter 2 reviews the literature published on entropy noise generation providing a strong theoretical background.

Chapter 3 gives the background of the experimental investigation describing the Oxford Turbine Research Facility, the generation of the non-uniform temperature profile, data acquisition signal technique, and modelling of the nozzles investigated in the facility.

Chapter 4 presents the experimental data acquired for the first nozzle configuration. The comparison with numerical predictions performed using LES technique.

Chapter 5 provides experimental data for the second designed nozzle and turbine stage configuration. The comparison of sound pressure levels for two nozzles was carried out.

Chapter 6 investigates the generation of entropy noise in a nozzle configuration using numerical simulation alone.

Chapter 7 estimates entropy noise produced in half a turbine stage configuration. The quantification of entropy noise and its dependence on the Mach number of the flow is presented.

Chapter 8 evaluates entropy noise in lean-burn combustors. The modelling of nine temperature profiles representative of those produced by lean-burn combustors are considered and entropy noise generation optimisation was accomplished.

Chapter 9 draws conclusions and offers recommendations for future work.

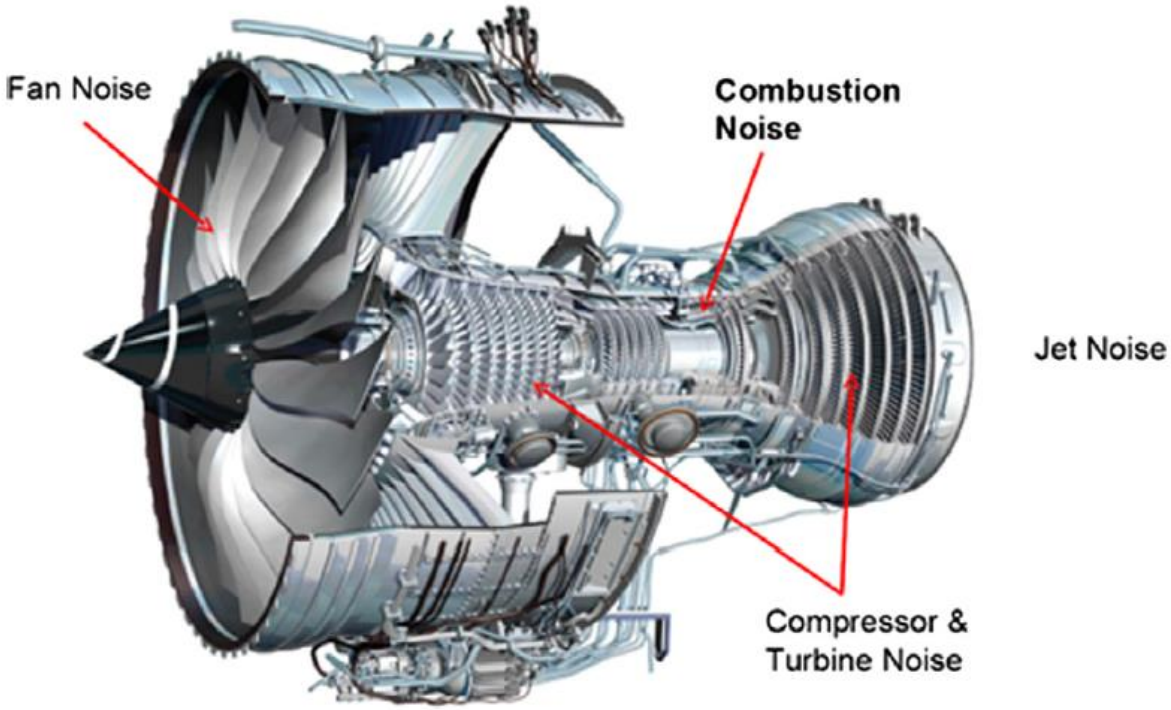

Figure 1.1: Four types of aircraft noise (Rolls-Royce Trent 1000, copyright Rolls-Royce)

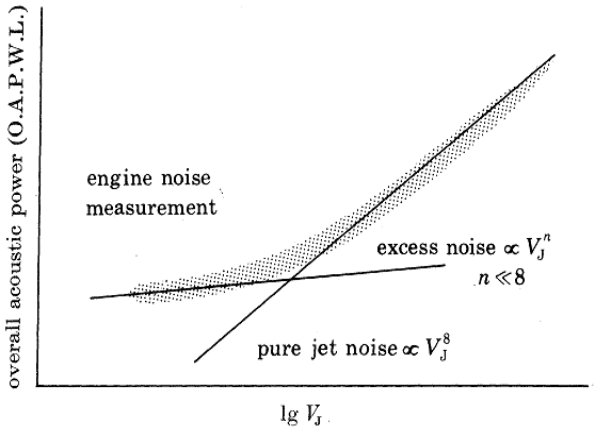

Figure 1.2: Schematic representation of variation of rear arc noise from a jet engine with jet velocity

Chapter 2

Literature Review

2.1 Lighthill's Acoustic Analogy

In 1952 James Lighthill (Lighthill, 1952) compared density fluctuations in the real fluid with those appropriate to a uniform acoustic medium at rest to form an exact, inhomogeneous wave equation whose source terms are important only within the turbulent region. Lighthill was initially interested in solving the problem of the sound produced by a turbulent nozzle flow. However, his original theory actually applies to the simpler situation, in which the sound is imagined to be generated by a finite region of rotational flow in an unbounded fluid. This avoids complications caused by the presence of the nozzle (Howe, 2003).

Lighthill looked at the incited flow fluctuations within a very large volume of fluid which is initially at rest at infinity, where the mean pressure, density, and sound speed are respectively p_0, ρ_0, c_0 (Lighthill, 1954). The Navier-Stokes and continuity equations for this flow were compared with a uniform acoustic medium at rest. The difference between the two sets of equations can be regarded as an effect of a fluctuating external force acting on the uniform field and, thus propagating turbulence generated sound in accordance with standard physical laws of linear acoustics.

The problem of calculating the turbulent generated sound is therefore equivalent to solving the following equation:

$$\left(\frac{1}{c_0^2}\frac{\partial^2}{\partial t^2} - \nabla^2\right)[c_0^2(\rho - \rho_0)] = \frac{\partial^2 T_{ij}}{\partial x_i \partial x_j}. \quad (2.1)$$

The left hand side of the equation (2.1) describes the sound generated by density fluctuations as a result of turbulence, the latter is determined by T_{ij} – Lighthill stress tensor given by the difference between momentum flux of stresses in the real flow π_{ij} and stresses in the uniform acoustic medium at rest π_{ij}^0.

$$T_{ij} = \pi_{ij} - \pi_{ij}^0 = \rho v_i v_j + \big((p - p_0) - c_0^2(\rho - \rho_0)\big)\delta_{ij} - \sigma_{ij}. \quad (2.2)$$

Equations (2.1) and (2.2) express the idea that the excess stresses of the real flow serve as an external stresses in the uniform acoustic medium, whose fluctuations produce an acoustic response. This makes it possible to estimate the level of sound generated by the turbulent fluid. In the uniform acoustic medium the momentum flux of stresses is that experienced due to a hydrostatic pressure field, where pressure variations are proportional to density variations through the speed of sound (Landau & Lifshitz, 1987).

The terms of T_{ij} in equation (2.2) not only account for the generation of sound, but also govern acoustic self-modulation caused by acoustic non-linearity, the convection of sound waves by the turbulence velocity, refraction caused by sound speed variations, and attenuation due to thermal and viscous actions (Goldstein, 1960).

The first term on the right hand side, Reynolds stress, describes the generation of noise produced by turbulence, called vortex sound. It is quadrupole acoustic source, numerically evaluated to be less influential than dipole noise generated by the second term (Dowling, 2015). Unsteady motion of the flow is also characterised by vorticity, which might be regarded as a distribution of intense turbulent velocity fluctuations. These fluctuations are

responsible for converting a fraction of jet rotational kinetic energy into longitudinal waves that constitute aerodynamic sound.

In the region outside the flow (or at least at sufficiently large distances from this flow) the linear acoustic approximation should apply, and hence the velocity v_i should be small (Goldstein, 1979). Moreover, we expect the effects of viscosity and heat conduction to be no different in this region than in any other sound field. That means that they only cause a slow damping due to the conversion of acoustic energy into heat due to viscosity and heat conduction and have a significant effect over very large distances. Thus, it should be possible to neglect the viscous stress tensor σ_{ij} (Kempton, 1976).

The second term of Lighhill's tensor describes the generation of noise determined by a difference in the momentum flux of stresses of the exact pressure field $(p - p_0)$ and that governed by the acoustic linear approximation $c_0^2(\rho - \rho_0)$. Fluctuating pressure creates a momentum flux which the Kronecker delta δ_{ij} marks as being isotropic, equal in all directions. The departure of the real momentum flux of stresses from uniformity can be regarded as an effect of a fluctuating external force acting on the fluid medium. Tanahashi carried out an evaluation of the acoustic source terms using Direct Numerical Simulation (Tanahashi, 2002). Contribution of the entropy term in the far-field was shown to be dominant especially in a reacting turbulent mixing layer. Using the second law of thermodynamics it is observed that pressure is a function of density and entropy variations. The pressure stresses in the uniform acoustic medium at rest are a function of density fluctuations only.

Thus, the second term of Lighthill's tensor T_{ij}^{ent}, responsible for generation of noise due to entropy inhomogeneities can be rewritten through fluctuations of specific entropy as (Lighthill, 1953):

$$T_{ij}^{ent} = [(p - p_0) - c_0^2(\rho - \rho_0)]\delta_{ij} = \frac{p_0}{c_p}(s - s_0)\delta_{ij} \quad (2.3)$$

It is worth noting that the sound generated by the entropy component of Lighthill's stress tensor is not determined by variations of temperature but rather specific entropy (Cumpsty & Marble, 1977). This noise is called entropy noise, since its generation is governed by entropy fluctuations.

In combustors spatial variations in entropy are directly linked to the complex temperature profile arising from the temperature difference between the 'hot spot' originating from unsteady burning of the flame and the 'cold spot' appearing due to introduction of the system cooling and combustor bypass air (Thomas & Williams, 1966; Howe, 2010).

The generation of entropy noise is governed by variations in temperature and static pressure in the direction of the flow motion. The temperature variations arise in the combustor due to the complex nature of the temperature profile and for a modern aero-engine a difference between the 'hot spot' and the cooler region can be as high as $\frac{T-T_0}{T} = 0.5$. The acceleration of flow, a change in static pressure, is necessary to convert stresses between the shear layers into an acoustic response. These stresses are a result of temperature inhomogeneities and during flow acceleration they fluctuate since, as equation (2.3) shows, they are proportional to the local static pressure values. These stresses are driven by the fluid motion and stationary in a frame of reference connected to the flow. When the static pressure experiences a change, the stresses fluctuate and

generate the acoustic response of entropy noise. That is similar to a fluctuating force applied to a membrane, causing vibration of this membrane and generation of noise. This is the mechanics of how kinetic energy of the fluid associated with entropy variations within a temperature profile is converted into an acoustic response propagating at the speed of sound.

2.2 Entropy Noise as an Acoustic Source

Lighthill's acoustic analogy is an inhomogeneous wave equation of linear acoustics. Solutions of such equations may be found by employing an auxiliary function, known as Green's function:

$$\left(\frac{1}{c_0^2}\frac{\partial^2}{\partial t^2} - \nabla^2\right) G(x, y, t-\tau) = \delta(x-y)\delta(t-\tau). \quad (2.4)$$

Green's function $G(x, y, t-\tau)$ is a solution of the wave equation describing the propagation of density fluctuations generated by an impulsive point source $\delta(x-y)\delta(t-\tau)$ located at the point $x = y$ at the time $t = \tau$. Symbolic function δ is known as Dirac delta function. (Lighthill, 1980)

Green's function might be interpreted as a displacement of the fluid due to an applied force of density δ concentrated at the source point. The density of this force is obtained as the limiting value of a total force of one unit applied over a finite region contacting the acoustic source as the region shrinks to zero; the shrinking processes are effected in such a manner as to ensure that the total force is always one unit (Roach, 1982). The two point Green's function allows to evaluate the displacement of the fluid at the listener's point x, appearing because of force fluctuations applied at the source point y. The temporal portion of Dirac

delta function makes Green's function causal allowing to take into account the time in which the acoustic wave travels between the source and the receptor.

The formal solution of Lighthill's equation with an outgoing wave behaviour can be given by:

$$c_0^2(\rho - \rho_0)(x,t) = \int_{-\infty}^{\infty} \frac{T_{ij}\left(y, t-\frac{|x-y|}{c_0}\right)}{|x-y|}\, d^3y \quad (2.5)$$

This is an alternative, integral representation of Lighthill's equation. It provides a useful prediction of aerodynamic sound generation only when T_{ij} is known. This is because the terms in Lighthill's stress tensor account not only for generation of sound but also govern acoustic self-modulation caused by acoustic nonlinearity (Goldstein, 1960), the convection of sound waves by the turbulent velocity, refraction caused by sound speed variations (Morfey, 1973), and attenuation due to thermal and viscous actions. The influence of acoustic nonlinearity and thermo-viscous dissipation is usually sufficiently weak to be neglected within the sound region, although they may affect propagation to a distant observer (Howe, 2003). Convection and refraction of sound within and near the source flow can be important, for example in the presence of a mean shear layer (in cases when Reynolds stress will include terms $\rho U_i u_j$ like where U_i and u_j respectively denote the mean and fluctuation components of instantaneous velocity) (Howe, 1998), or when there are large variations in the mean thermodynamic properties of the medium within the source region; such effects are described by the presence of unsteady linear terms of Lighthill's stress tensor (Ffowcs Williams, 1974).

Thus, to predict the radiated sound from Lighthill's equation (2.5) it is usually necessary to assume that all of these acoustic effects depending on fluid compressibility in the source

flow are negligible. That makes it possible to derive a good approximation for Lighthill's stress tensor by assuming the source flow is effectively incompressible. This is often possible when the characteristic Mach number is small, and when the wavelength of the sound is much larger than the size of the source region (Howe, 2003).

If no entropy variations are observed and the mean density and sound speed are uniform throughout the fluid, approximation can be made for Lighthill's tensor stress as:

$T_{ij} \approx \rho_0 v_i v_j$, (2.6)

on the condition that $M^2 \ll 1$ (Batchelor, 1967).

Applying the compact Green's function technique for an impulsive sound source, the solution of Lighthill's acoustic analogy at the receptor's point with only the entropy component retained might be written as:

$$p_{ent}(\bar{x}, t) = \int \frac{1}{4\pi} \frac{\partial^2}{\partial t^2} \left[\frac{p - p_0}{c_0^2} - (\rho - \rho_0) \right] \frac{d^3 \bar{y}}{|\bar{x} - \bar{y}|}, \quad (2.7)$$

where square brackets represent the evaluation of the excess density at the retarded time. Howe (Howe, 2010; Auregan et all, 2002) improved this by assuming that the motion of particles is isentropic, but that the mean density of the fluid varies within the source region. Disrespecting the term due to the difference of adiabatic compressibilities, which is very small in the ideal gas, an entropy noise solution can be presented as (Howe, 1998):

$$p_{ent}(\bar{x}, t) = \frac{\rho_o x_j}{4\pi c_0 |x|^2} \frac{\partial}{\partial t} \int \left[\left(\frac{1}{\rho_0} - \frac{1}{\rho} \right) \frac{\partial p}{\partial y_j} \right] d^3 \bar{y}, \quad (2.8)$$

showing that the strength of the entropy noise source is proportional to the difference between the acceleration of the fluid of source density and that which the fluid of mean

density would experience (Howe, 2015). That also means that generation of entropy noise is inextricably linked to acceleration of the flow. The term $\left(\frac{1}{\rho_0}-\frac{1}{\rho}\right)$ proves that the scattered entropy wave is dipole (Crighton, 1992).

To determine the order of magnitude of entropy noise the length scale l of the energy-containing eddies of the turbulence sources should be introduced. The value of the length scale depends on the mechanism responsible for turbulence production, such as the width of a jet mixing layer. The turbulence eddies are each acoustically compact. This means that when the integral in (2.8) is confined to a single eddy, the retarded time variations across that eddy can be neglected.

For an ideal gas in the jet, the magnitude of entropy noise with an eddy of scale l might be presented as proportional to the temperature difference between the 'hot spot' and its environment:

$$p_{ent}\sim\frac{l}{|\mathbf{x}|}\frac{\Delta T}{T}\rho_o c_0^2 M. \quad (2.9)$$

This difference may reach 0.4-0.5 in modern rich-burn combustors. The 'hot spot' arises from the flame burning unsteadily and producing temporal and spatial temperature variations, whereas the 'cold spot' near the wall is a result of cooling being introduced.

2.3 Generation of Entropy Noise

Any disturbance in the combustor governed by linear acoustic equations can be regarded as a superposition of three modal wave fields: acoustic, entropy and vorticity modes. Each of these modes satisfies its own dispersion relation between frequency and wave number significantly simpler than that of a general disturbance (Pierce, 1989). Except at

boundaries, these disturbances are linear and independent and might be considered separately (Dowling & Stow, 2003).

To split the observed fluctuations as the sum of compressible and incompressible parts, Kovasznay (Kovasznay, 1953) applied a small-parameter expansion to decompose compressible fluctuations into physical modes.

As proven by Chu and Kovasznay (Chu & Kovasznay, 1958) entropy noise is a product of energy convection of entropy disturbances within the 'hot spots' in the entropy mode.

The dispersion relation for thermal diffusion and conduction within the entropy mode in the absence of heat release may be written as an elliptic partial differential equation of heat transfer:

$$\nabla^2 s'_{ent} = \frac{\rho c_p}{\kappa} \frac{\partial s'_{ent}}{\partial t}. \qquad (2.10)$$

While rearrangement of the conservation of mass equation, the Navier-Stokes equation and the entropy conservation equation lead to the polarization equations for this mode (Cumpsty, 1979; Marble & Cumpsty, 1977; Pierce, 1989; Kovasznay, 1953; Gatski, 2013):

$$\rho'_{ent} = -\frac{\rho s'_{ent}}{c_p} \qquad T'_{ent} = \frac{T s'_{ent}}{c_p} \qquad \nabla \times v_{ent} = 0$$

$$p'_{ent} = 0 \qquad v_{ent} = \frac{\kappa}{\rho c_p} \frac{\nabla s'_{ent}}{c_p}. \qquad (2.11)$$

From (2.11) it follows that the entropy mode is incompressible, since it does not generate a pressure wave; it is dilatational, since the curl is zero and stationary, therefore it is driven by the flow velocity. Velocity v_{ent} appears as a result of viscosity effects (Garnier, 2009) and is small but not negligible, since the dispersion equation allows the possibility that

$|\nabla s'_{ent}|$ will be larger than $\left(\frac{w}{c}\right) s'_{ent}$ (Pierce, 1989), which is often the case for the lower frequencies of entropy noise (Duran, 2013).

For the ideal gas $v_{ent} = \frac{\kappa}{\rho c_p} \frac{\nabla T'_{ent}}{T}$, therefore in the entropy mode a weak dilatational (no rotations) velocity field, governed by the conservation of mass equation, compresses the colder region of the fluid medium in the direction of the hotter region (Chu & Kovasznay, 1958). At the 'hot spot' the dispersion relation dictates that temperature fluctuations must decrease with time (Pierce, 1989), being driven by the mean flow in the combustor, the nozzle or the turbine stage temperature fluctuations must decrease along the axial distance in an exponential manner. The fact that there is no pressure wave in the entropy mode means that the decrease in temperature is accompanied with a linear increase in density fluctuations. The fluid flows towards the 'hot spot' to balance the generation of density fluctuations.

A linear interaction of the entropy and acoustic mode was investigated by Chu and Kovasznay (Chu & Kovasznay, 1958) and Cumpsty (Cumpsty, 1979). It is shown to produce all three basic modes of interactions: acoustic, entropy and vorticity modes. In the entropy mode the fluctuations of entropy are the major noise source in contrast to the vorticity mode where they are absent and the acoustic mode in which entropy fluctuations are relatively small compared to those of static pressure.

The acoustic source appearing in the vorticity mode is baroclinic because it is generated by the excess of density causing a difference between the pressure and density gradients. It can be written as (Garnier, 2009):

$$-c_0^2 \frac{\partial}{\partial x_i}\left(\frac{s'}{c_p}\right) \times \frac{\partial}{\partial x_i}\left(\frac{P'}{\gamma P}\right). \quad (2.12)$$

That means that flow with temperature spots experiences a force in the radial direction resulting from entropy/acoustic mode interactions. This interaction causes a shift of the centre of mass of the fluid, and the force fails to pass through it producing a torque and an angular velocity, thus generating an additional solenoidal turbulent fluctuation.

The resulting source in the acoustic mode may be presented as:

$$-\frac{\partial^2}{\partial t \partial x_i}\left(\bar{S}_s \cdot \bar{v}_{pi}\right) = \frac{\partial}{\partial x_i}\left(\frac{s'}{c_p}\right)\gamma \frac{\partial P}{\partial x_i}. \quad (2.13)$$

Which is the entropy component of the Lighthill's stress tensor achieved by inserting equation (2.3) into (2.1). Equation (2.12) suggests that density fluctuations in the entropy mode ρ'_{ent} are converted into an acoustic source without any kind of dissipation. This process may be regarded as a scattering of the acoustic wave by entropy spots. The necessary of flow acceleration to generate entropy noise is resulting from this aspect. The heat convection within the entropy mode is governed by equation (2.10). Thus, entropy inhomogeneities being driven by the mean flow propagate with the speed of the flow and at the moment of entropy-acoustic interactions, when there are transforming themselves into an acoustic source, entropy noise is generated and propagate with the speed of sound (Crighton, 1972).

Similar results of entropy/acoustic mode interaction but for a theoretical nozzle were presented by Marble and Candel (Marble & Candel, 1977; Candel, 1972). They examined linearized Euler equations for a 1D nozzle and assuming compactness of the nozzle, the

fact that the wavelength is much larger than the axial dimension of the nozzle, they used harmonic analysis to derive the following equations:

$$\gamma\left(\frac{\partial}{\partial t}+\ u\frac{\partial}{\partial x}\right)\left(\frac{u'}{u}\right)+\frac{c_0^2}{u}\frac{\partial}{\partial x}\left(\frac{p'}{\gamma p}\right)=\left(\left(\frac{s'}{c_p}\right)-2\gamma\left(\frac{u'}{u}\right)+(\gamma-1)\left(\frac{p'}{\gamma p}\right)\right)\frac{du}{dx} \quad (2.14)$$

$$\left(\frac{\partial}{\partial t}+\ u\frac{\partial}{\partial x}\right)\left(\frac{s'}{c_p}\right)=0. \quad (2.15)$$

Non-homogeneous equation (2.14) unequivocally requires acceleration of the flow for generation of entropy noise to take place (Williams & Howe, 1975; Howe, 2010). Equation (2.15) adds to the previous explanation of a stationary manner of the entropy mode and proves that entropy fluctuations are propagated at the speed of the flow.

2.4 Analytical Parametric Study of Indirect to Direct Combustion Noise Ratio

The analytical solution of the linearized Euler equations through the invariants method can be used to perform a parametric study of indirect and direct combustion noise generation at the outlet of a nozzle, which is critical for a proper estimate of the entropy noise generation in real turbine stages (Duran, 2013).

The unsteady burning of the flame produces direct and indirect combustion noise. Direct noise is generated by acoustic waves due to volumetric contraction-expansion of the flow. In combustor that is caused by temporal variations in flame temperature. Indirect combustion noise is produced by accelerating entropy waves through the turbine stage. The entropy waves are being a result of temperature inhomogeneities in the flow. Thus, a ratio of indirect to direct combustion noise is an important parameter in the understanding of entropy noise generation.

Leyko (Leyko, 2009) performed an analytical comparison of indirect and direct combustion noise based on a generic combustor simulator with a one-dimensional flame proceeded by a compact convergent-divergent nozzle. The simplified model of combustor-nozzle is presented in Figure 2.1. The flame is simplified on the assumption that it only generates fluctuations in heat release. Thus, mass flow upstream and downstream of the flame are assumed to be equal.

The transfer functions between the upstream and downstream waves of the nozzle were obtained by Marble and Candel (Marble & Candel, 1977) using the compact nozzle assumption stating that the wavelengths of the acoustic and entropy perturbations are large compared to the axial dimension of the nozzle. This is consistent with entropy noise being observed only at the low frequency range. Using this assumption, matching of mass flow rate, total temperature and entropy upstream and downstream of the nozzle can be written as: (Leyko, 2012):

$$\left(\frac{\dot{m}'}{\dot{m}}\right)_0 = \left(\frac{\dot{m}'}{\dot{m}}\right)_1 \quad \left(\frac{T_t'}{T_t}\right)_0 = \left(\frac{T_t'}{T_t}\right)_1 \quad \left(\frac{s'}{c_p}\right)_0 = \left(\frac{s'}{c_p}\right)_1 . \text{(2.12-2.14)}$$

Using dimensionless pressure, velocity and entropy fluctuations

$$\varphi = \frac{p'}{\gamma p} \qquad v = \frac{u'}{u} \qquad \sigma = \frac{s'}{c_p}, \text{(2.15-2.17)}$$

downstream propagating acoustic wave, upstream propagating entropy wave and downstream propagating entropy wave can be presented as functions of these primitive non-dimensionless variables:

$$w^+ = \varphi + Mv \quad w^- = \varphi - Mv \quad w^s = \sigma. \text{(2.18-2.20)}$$

To solve the compact cold flame Leyko used the compact equations imposed at the inlet and outlet of the flame with the fluctuating heat release accounting for flame burning appearing in both energy and entropy equations:

$$(\varphi + v - \sigma)_{0'} = (\varphi + v - \sigma)_0 \quad (2.21)$$

$$[(\gamma - 1)M^2 v + (\gamma - 1)\varphi + \sigma]_{0'} + q' = [(\gamma - 1)M^2 v + (\gamma - 1)\varphi + \sigma]_0 \quad (2.22)$$

$$(\sigma)_{0'} + q' = (\sigma)_0 \quad (2.23)$$

The ratio of indirect to direct combustion noise η is defined as the ratio of the acoustic response generated at the outlet of the nozzle by entropy waves to the acoustic response at the outlet generated by acoustic waves produced by the fluctuating heat release (Duran, 2013):

$$\eta = \frac{w_1^+}{w_0^s} \cdot \frac{w_0^s}{w_0^+} \cdot \left[\frac{w_1^+}{w_0^+}\right]^{-1} . \quad (2.24)$$

The first term on the right hand side of equation (2.24), the entropy transfer function of the nozzle, defines the acoustic response of the nozzle due to entropy waves propagating downstream from the combustion chamber; the second term is the wave ratio describing the relationship between the entropy and acoustic waves generated by unsteady heat release of the flame with no incoming wave being imposed upstream of the cold flame; the third term, the acoustic transfer function, similarly to the first, determines the acoustic response downstream by acoustic waves upstream of the nozzle.

Using this compact solution, evaluation of the ratio of indirect to direct combustion noise becomes possible for varying inlet and outlet Mach numbers. The invariants method was used by Duran (Duran, 2013) to obtain the indirect to direct combustion noise ratio as a function of the reduced frequency of the unsteady heat release.

To do so, the linearized Euler equations are rewritten in dimensionless form, using dimensionless space and time variables, $\xi = x/L_n$ and $\tau = tf$, where L_n is the nozzle length and f is a characteristic frequency of the perturbation. The mean flow velocity is reduced using the sound speed at the inlet of the nozzle c_0, giving the dimensionless form $\bar{u} = u/c_0$. The equations are rewritten using the reduced frequency (or Helmholtz number) $\Omega = fL_n/c_0$ to compare the nozzle length with a characteristic acoustic wavelength. Six reduced frequencies were chosen for investigation from 0 to 2.5 with the 0.5 step. In this form the linearized Euler equations take the following form (Duran, 2013):

$$\left[\Omega\frac{\partial}{\partial\tau} + \bar{u}\frac{\partial}{\partial\xi}\right](\varphi) + \bar{u}\frac{\partial}{\partial\xi}(v) = 0 \quad (2.25)$$

$$\left[\Omega\frac{\partial}{\partial\tau} + \bar{u}\frac{\partial}{\partial\xi}\right](v) + \frac{\bar{c}^2}{\bar{u}}\frac{\partial}{\partial\xi}(\varphi) + [2v - (\gamma-1)\varphi - \sigma]\frac{d\bar{u}}{d\xi} = 0 \quad (2.26)$$

$$\left[\Omega\frac{\partial}{\partial\tau} + \bar{u}\frac{\partial}{\partial\xi}\right](\sigma) = 0. \quad (2.27)$$

Figure 2.2, *a-e* shows the ratio of indirect to direct combustion noise η as a function of inlet and outlet Mach number for six reduced frequencies. It is observed that with an increase of the reduced frequency Ω the influence of indirect noise is decreasing. That confirms the hypothesis that in order for entropy noise to be significant the wavelength of entropy perturbation should be large enough compared to the axial dimension of the nozzle entailing that the object of prime interest in the entropy noise investigation is the range of lower frequencies. Noting that reduced frequencies of more than 2 show an increasingly weak acoustic response produced by entropy inhomogeneities it may be concluded that for a typical nozzle of 0.34m axial length entropy noise is influential in the frequency range from 0 to 2000Hz. However, the derived relations are shown to be dependent on the nozzle geometry and subsequently on the acceleration rate of the flow.

2.5 Entropy Noise Generation in a Turbine Stage

The generation of entropy noise in a turbine with one or more stages is a matter of particular interest since it may significantly affect the overall aircraft noise (Cumpsty, 1977). Until recently there were no experimental investigations of the entropy noise generation in a turbine stage configuration and the general research focus was concentrated on analytical and numerical evaluation of entropy noise.

2.5.1 Analytical Investigation of Entropy Noise in a Turbine Stage

A simplified approach for the entropy noise generation was developed by Cumpsty and Marble (Cumpsty & Marble, 1977). It was based on the hypothesis that the flow upstream and downstream of the turbine stage is steady, thus the mass flow rate is constant, and the turbine stage was treated as an infinitely thin discontinuity in the axial direction where static pressure, amplitude and angle of the flow experience a change. Using continuity, momentum and entropy conservation equations the dispersion equations for vorticity, entropy and acoustic modes were derived. The dispersion equations were obtained for two-dimensional flow only, neglecting thermo-diffusion in the radial direction. One-dimensional wave propagation model developed by Marble and Candel (Marble & Candel, 1977) was exchanged with a more advanced spiral model allowing to take into account wave attenuation. The decay time of the wave was relatively small and so these waves were called evanescent or cut-off.

Cumpsty and Marble evaluated the acoustic power downstream of a nozzle guide vane row and a turbines stage produced by entropy waves propagating from the combustion chamber (Cumpsty & Marble, 1977). The results were presented in dimensionless

variables: frequency independent variable fY/a, where f is the frequency in hertz, Y is the wavelength along the cascade and a is the speed of sound. When more than one blade row is being considered the axial spacing δx must be specified, and it is physically more convenient to use $\delta x/Y$. The acoustic power evaluated over non-dimensionless frequency for the NGV section alone and a full turbine stage is presented in Figure 2.3. It can be seen that a proper representation of even a single-stage turbine cannot ignore the strong interaction between the rows (Cumpsty & Marble, 1977). For the left hand waves from the full stage and the right hand waves of a nozzle, it is possible to see a common trend in plots of power against frequency. The power is rising rapidly as frequency is reduced, until, just before the point of cut-off, there is a precipitous fall. Most jet engines have several turbine stages and to investigate this the spectra of non-dimensional acoustic power due to an entropy perturbation into turbines with different numbers of stages were calculated by Cumpsty and Marble (Cumpsty & Marble, 1977). The fall in temperature across each stage, however, leads to a drop in the acoustic velocity, and for this reason the cut-off value at outlet falls with the number of stages. The peak spectral density of acoustic power was shown to increase with the number of stages with a shift towards lower values of independent frequency. The integral of the power with respect to frequency was found, however, to be virtually constant for two or more stages.

Kaji and Okazaki (Kaji & Okazaki, 1970) used the actuator disk approach to evaluate transfer functions over the turbine stage. In one case the blade length was assumed to be negligible, whereas in the developed potential technique it was taken into account. The difference appeared to be insignificant and the conclusion was made that semi-actuator disk theory

provided a good estimate of the entropy noise generation in one stage of the turbine configuration.

Muir (Muir, 1977) extended the work of Kaji and Okazaki for a three-dimensional case. The analytical method of the actuator disk was used for a single and then multiple stage. The averaged frequency was used to avoid the dependence on the wavelength of the incident sound field. According to Muir, the model of Kaji and Okazaki has two restrictions. The radial variations cannot be taken into account due to the two-dimensional nature of the model developed and the fact that the flow must be subsonic. Muir's model resolves the flow limitations to first order and includes the angles of the leading and trailing edge of the blades. Thus, reflection of the wave can be included into the calculation.

2.5.2 Numerical Investigation of Entropy Noise in a Turbine Stage

Leyko (Leyko, 2011) performed Large Eddy Simulation for a numerical model encompassing a combustion chamber followed by stator blades. Vorticity, entropy and acoustic perturbations were calculated in a three-dimensional model of a combustor. Subsequently, a two-dimensional model of a turbine was used to evaluate the acoustic response produced by downstream propagating entropy waves. The acoustic response of a turbine stage by vorticity waves was neglected. The numerical results are in good agreement with the analytical results from Cumpsty and Marble (Cumpsty & Marble, 1977).

Figure 2.4 a, shows that the upstream acoustic wave calculated using a two-dimensional LES procedure is fairly similar to the analytical approach developed by Cumpsty and Marble, entailing that the stator is acoustically compact. Figure 2.4 b, demonstrates the results for the upstream entropy wave. A good agreement is achieved at only the lower

frequencies. This means that the entropy noise investigation requires to take into account the dimension of the blade in order to calculate correctly the entropy mode transfer functions.

2.6 Experimental Investigation of Bake

So far, there were only limited attempts to perform experimental investigation of the entropy noise generation. One of them was carried out by Friedrich Bake from the German Aerospace Centre (DLR) (Bake, 2007). The experimental rig called Entropy Wave Generator (EWG) presented in Figure 2.5 was built to generate entropy inhomogeneities in the flow. The EWG is basically a tube located between the upstream plenum and the convergent-divergent nozzle. The flow generated by a compressed air system is calmed in a settling chamber with a honeycomb straightener before it enters the tube section. The heating module consists of six ring sections with ten plenum wires stretched across. Downstream of the heating module there is convergent section of the nozzle which accelerates the flow before experiencing a shock at the divergent section. The subsonic flow enters a long tube equipped with wall flush microphones along the nozzle, which allow to perform measurements of dynamic pressure fluctuations in the boundary layer of the wall. The flow exits the tube through an anechoic end which minimises acoustic reflections back into the nozzle (Bake, 2009).

To evaluate different parameters of entropy noise in the EWG several tests were conducted with varying mass flow rate to be able to change Mach number in the nozzle area and amplitude of incited temperature perturbations. The amplitude of the entropy wave generated was determined with pressure pulse fluctuations using microphones

located downstream of the convergent-divergent nozzle. The results were evaluated for nozzle Mach numbers 0.15 and 1 with temperature fluctuations rising from 1K to 13K. The temperature perturbations were measured using a bare thermocouple located downstream of the heating device. Figure 2.6 *a*, illustrates the linear dependence of entropy noise generation on the temperature perturbations applied for two Mach number Ma_{nozzle}=0.15 and Ma_{nozzle} =1.

In contrast, Figure 2.6, *b* shows the sound pressure amplitude change with a Mach number variation for two different temperature perturbation amplitudes 7.5K and 9K. For the subsonic nozzle up to Ma_{nozzle}=0.7 entropy noise amplitude increases with Mach number, but for higher Mach numbers the sound pressure level decreases again. This behaviour is explained by Marble and Candel with the acoustic characteristics of a diffuser flow for high inlet Mach numbers.

The theory of Marble and Candel (Marble & Candel, 1977) deals with the entropy noise generation either in a nozzle or in a diffuser separately. The deceleration of an entropy wave in the diffuser downstream and an upstream propagating acoustic wave. The upstream propagating wave is partially reflected in the nozzle throat. The total downstream propagating acoustic wave can be compared to the experimental data measured by microphones downstream of the convergent-divergent nozzle (Bake, 2007).

Figure 2.7 illustrates the comparison of the experimental data with one-dimensional flow theory developed by Marble and Candel. It represents the entropy sound pressure amplitude normalised by the total pressure and relative temperature perturbations over the nozzle Mach number. The presence of several data points for each Mach number

measured is explained by the fact that the experiment was conducted for different temperature amplitudes.

The experimental data shows similarity with the theory only for the nozzle Mach number between 0.6 and 0.7, whereas for lower Mach numbers the experimental results are significantly higher than the theory predicts and for a choked nozzle the measured entropy pressure level is lower than the theoretical value. The possible explanation of such behaviour is the compact assumption used by Marble and Candel in the entropy wave theory as well as a one-dimensional character of the flow.

An aspect which has been neglected is the influence of the acoustic reflections at inlet and outlet of the EWG. Muehlbauer (Muehlbauer, 2008) performed a three-dimensional compressible URANS and showed that these reflections should be taken into account. Figure 2.8 presents the comparison of pressure signals at the fourth microphone located downstream and measured experimentally by Bake and evaluated numerically by Muehlbauer. It is observed that an increase in the flow temperature upstream produces a positive acoustic response which is succeeded by a negative which accounts for the end of the temperature pulse incited at the EWG. The distance between two peaks corresponds to the temperature pulse length. The numerical data shows a good match with the measurements performed.

Despite an audacious attempt to prove the existence of entropy noise and to quantify its influence on temperature and Mach number, the presented experimental investigation can still be considered controversial (Dowling, 2015), since it is not clear how exactly the direct acoustic response produced by the temperature pulse externally increasing the total temperature of the flow was separated from the indirect acoustic response caused by

acceleration of entropy inhomogeneities. Entropy inhomogeneities in Bake's experiment were produced at the moments of a temperature change. The EWG heats the mean flow, thus causing the immediate direct monopole acoustic response determined by the volumetric expansion-contraction of the mean flow. It is propagating downstream at the speed of sound. The temperature changes at the beginning and end of the incited temperature pulse produce shear stresses driven by the mean flow. The net force of these stresses is constant in the flow, entailing that amplitude of the positive and negative signals must be the same. Figure 2.8 suggests that the pressure amplitude at 0.07s might be entropy noise since it is succeeded by a similar negative pulse at 0.17s.

A subsonic nozzle configuration similar to that of Bake was studied by Giauque (Giauque, 2012) and Duran (Duran, 2013). The analytical results presented by Duran were based on a compact nozzle hypothesis for an unchoked subsonic nozzle with throat Mach number of 0.7. The results demonstrate that the strength of indirect combustion noise is two orders of magnitude smaller than the direct combustion noise suggesting that the pressure signal measurements by Bake at the outlet of a convergent-divergent nozzle were not generated by entropy noise but rather by the acoustic waves produced by the heating device (Dowling, 2015).

2.7 Numerical Modelling of the Flow using Large Eddy Simulation

Since the numerical investigation of entropy noise presenting in this thesis was performed using Large Eddy Simulation (LES) as a turbulence model for resolving the unsteady flow with temperature inhomogeneities imposed upstream, an extensive attention was given to LES ability to solve the combustion flow and predict the broadband noise.

2.7.1 Large Eddy Simulation as a Turbulence Model

Numerical investigation of entropy noise required a correct simulation of dynamic pressure fluctuations arising due to temperature variations propagating from the combustor downstream through the nozzle. The turbulence model must be accurate enough to compute entropy noise generated in the model with a complex nozzle geometry. This is compounded by the requirement to model upstream temperature variations in the radial and circumferential directions. Based on this the Large Eddy Simulation (LES) turbulence model was chosen.

Reynolds averaging of the Navier-Stocks equations (RANS) simulates the flow behaviour based on the Reynolds decomposition presenting the solution as being averaged over time or ensembles. Thus, the RANS model provides no explicit information on turbulent structures of the field. To investigate the noise appearing either due to temperature inhomogeneities or rotational kinetic energy, such resolving of the flow is not sufficient. In contrast to RANS, LES explicitly computes the larger scales of motion while the small scales are being modelled (Deardorff, 1970; Nieuwstadt et al., 1991; Mason, 1994; Lesiuer & Metais, 1996). The length scale Δ drawing the border between the direct calculation and simulation cuts off smaller scales to be modelled.

Investigation of entropy noise, generation of which is a product of nonlinear acoustic-entropy interaction, is more convenient to perform when rotational kinetic energy is neglected. That means that all turbulent energy is contained in the dilational modes and the flow can be considered incompressible for the purpose of deriving the sub-grid scale model. The LES modelling involves interaction of turbulence scales of different length. The

energy spectrum for homogeneous turbulence defining the filtering operation is presented in Figure 2.9. The production zone at the lower wave numbers is proceeded by a transferring zone which outscatters the energy from larger to smaller scales, and eventually the dissipation zone at the highest wave numbers. The transfer zone is also called the inertial zone in which the spectral density of energy decreases according to the Kolmogorov law. Moreover, there is an energy transfer from the small to the large scales but with intensity much weaker than that of outscattering. The filter is constructed on the assumption that the cut-off wave number $k_c = \pi/\Delta$ is located within the inertial zone and that the smallest scales are isotropic.

Modelling of the cut-off scales requires filtering of the velocity field performed using a filter (Kleissl, 2004):

$$\bar{u}(x) = \int u(x')\, G(x - x')dx' \qquad (2.28)$$

Where $\bar{u}$ is the filtered velocity field after application of filter function $G(x - x')$. Applying the filter for Navier-Stocks equation for incompressible fluid yields:

$$\frac{\partial\, \bar{u}}{\partial t} + \frac{\partial}{\partial x_j}\left(\overline{u_i}\,\overline{u_j}\right) = -\frac{1}{\rho}\frac{\partial \bar{p}}{\partial x_i} + 2v\frac{\partial}{\partial x_j}\, S_{ij} - \frac{\partial \tau_{ij}}{\partial x_j} \quad (2.29)$$

Where the bar denotes a filtered variable, S_{ij} is strain rate tensor defined as:

$$S_{ij} = \frac{1}{2}\left(\frac{\partial \overline{u_i}}{\partial x_j} + \frac{\partial \overline{u_j}}{\partial x_i}\right), \quad (2.30)$$

And the sub-grid scale stress tensor introduced to account for the commutation error between the filtering and multiplication operator. Following the Boussinesq hypothesis this can be presented as:

$$\tau_{ij} = \overline{u_\iota u_j} - \overline{u_\iota}\,\overline{u_j}. \quad (2.31)$$

The Boussinesq hypothesis is built on the assumption that behaviour of the modelled sub-grid scales is similar to the Brownian motion of particles entailing that energy transfer from the resolved to the modelled scales is akin to the molecular mechanisms represented by diffusion (Stull, 1997). In molecular motion the energy of the flow is extracted by the presence of viscosity, therefore the mathematical structure of sub-grid scales modelling is analogous to that of molecular diffusion but with molecular viscosity replaced by a sub-grid viscosity.

$$\tau_{ij}^{d} = \tau_{ij} - \frac{1}{3}\delta_{ij}\tau_{kk} = -2v_t\bar{S}_{ij} + \frac{2}{3}\delta_{ij}\tau_{kk}\ . (2.32)$$

The most common sub-grid scale model is Smagorinsky model (Smagorinsky, 1963) which defines the sub-grid scale viscosity through resolved strain rate tensor:

$$v_t = C_s^2\Delta^2|\bar{S}|, (2.33)$$

where magnitude of strain rate tensor $|\bar{S}| = \sqrt{2S_{ij}S_{ij}}$ and Smagorinsky coefficient C_s is prescribed on phenomenological theories of turbulence or adjusted empirically in the LES calculation procedure. This model is proven to produce an excessive dissipation especially in the transition region between the laminar and turbulence flows. In additions, the near-wall behaviour requires a use of a dumping function (Meneveau & Katz, 2000). Despite all this, Smagorinsky model remains very popular due to its relative simplicity.

2.7.2 Aerodynamic Sound prediction using Large Eddy Simulation

In recent years a variety of Large Eddy Simulations were performed with a view of modelling the acoustic sources and subsequently evaluating the sound pressure field

(Wagner, 2007). Seror (2000) addressed the problem of evaluating and modelling the contribution of the unresolved scales to the radiated noise production when the Lighthill's acoustic analogy is employed in the LES prediction. To achieve this, they split the Lighthill's tensor into three terms: a high-frequency which is not resolved by the LES numerical prediction used in their study, the filtered Lighthill's tensor, computed from the filtered LES variables, and a subgrid-scale tensor. They performed Large Eddy Simulation and Direct Numerical Simulation of the decaying isotropic turbulence to evaluate the three parts of the Lighthill's tensor for both turbulence modelling methods and estimated the contribution of the subgrid and high-frequency parts to the overall Lighthill's tensor. They showed that subgrid scale influence on the aerodynamic sound production cannot be neglected, and that high-frequency part of the Lighthill's tensor pays only a little contribution to the vortex sound and entropy noise generation.

The evaluation of aerodynamic sound in complex geometries using LES was performed by Kato (Kato, 1991). Kato simulated the turbulent near wake and resulting far-field sound by decomposing the flow field and the resulting acoustic field using a low Mach number flow assumption. The unsteady flow field was resolved using the Smagorinsky model. The complex geometries were treated with overset grids to allow enhanced grid resolution within the near-wall region. The resulted sound pressure field was calculated by employing Lighthill-Curle's equation to evaluate the surface-pressure fluctuations. The agreement between the LES predicted and theoretically estimated sound pressure levels was matched well up to 2500Hz. Kato also showed that the predicted sound pressure level was strongly affected by the grid resolution near the object.

2.8 Chapter Conclusions

Entropy noise is generated due to stresses between layers appearing in non-uniform temperature profile, which when the flow is accelerated fluctuate and generate an acoustic response. Physically, that is similar to a fluctuation of a force applied to a membrane, vibration of the latter being the process of noise generation and transformation of kinetic energy of the flow into the acoustic wave. The mathematical description of the entropy noise generation was achieved by Lighthill who formulated it in an acoustic analogy. Applying the compact Green function technique to Lighthill's acoustic analogy showed that the acoustic strength of entropy noise is proportional to the temperature difference between the 'hot spot' and its environment. In real engines, the unsteady burning of the combustor flame produces a direct noise response determined by volumetric contraction-expansion of the flow and indirect response in the form of entropy noise due to spatial and temporal temperature variations of the combustor exit temperature profile. The analytic estimate of indirect to direct combustion noise ratio was performed by Leyko, showing that entropy noise may be as much as ten times more influential than a direct acoustic response. In addition, the study of Duran showed that the influence of entropy noise diminishes with an increase in frequency. This is anticipated because the entropy noise generation theory is based on the nozzle theory of Marble and Candel which states that the production of entropy noise is most efficient when its wavelength is of the same order as the axial dimension of the nozzle. Cumpsty made an estimate of the generation of entropy noise in a turbine stage, the study found that entropy noise in a turbine stage can be twice as large as in the NGV section alone. An experimental investigation of entropy noise was performed by Bake who used a temperature pulse to heat the flow before

accelerating the temperature inhomogeneities through a simple convergent-divergent nozzle. The acoustic response was measured downstream with a set of microphones. The results show a linear dependence of entropy noise on amplitude of the temperature pulse. The results are still considered controversial since it is not clear how the direct acoustic response due to application of an external temperature pulse was separated from entropy noise.

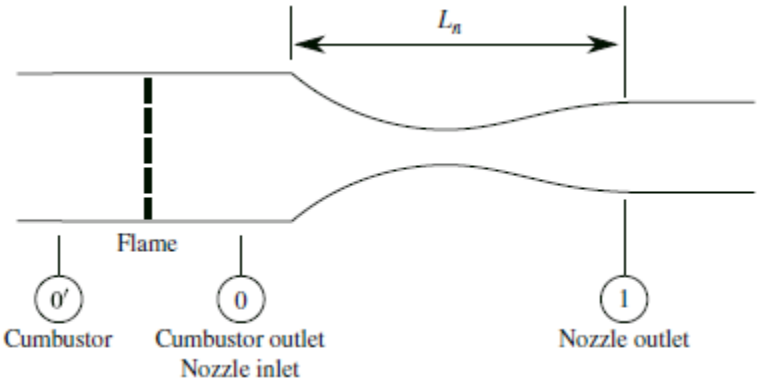

Figure 2.1: Simplified model of combustor-nozzle (Duran, 2013)

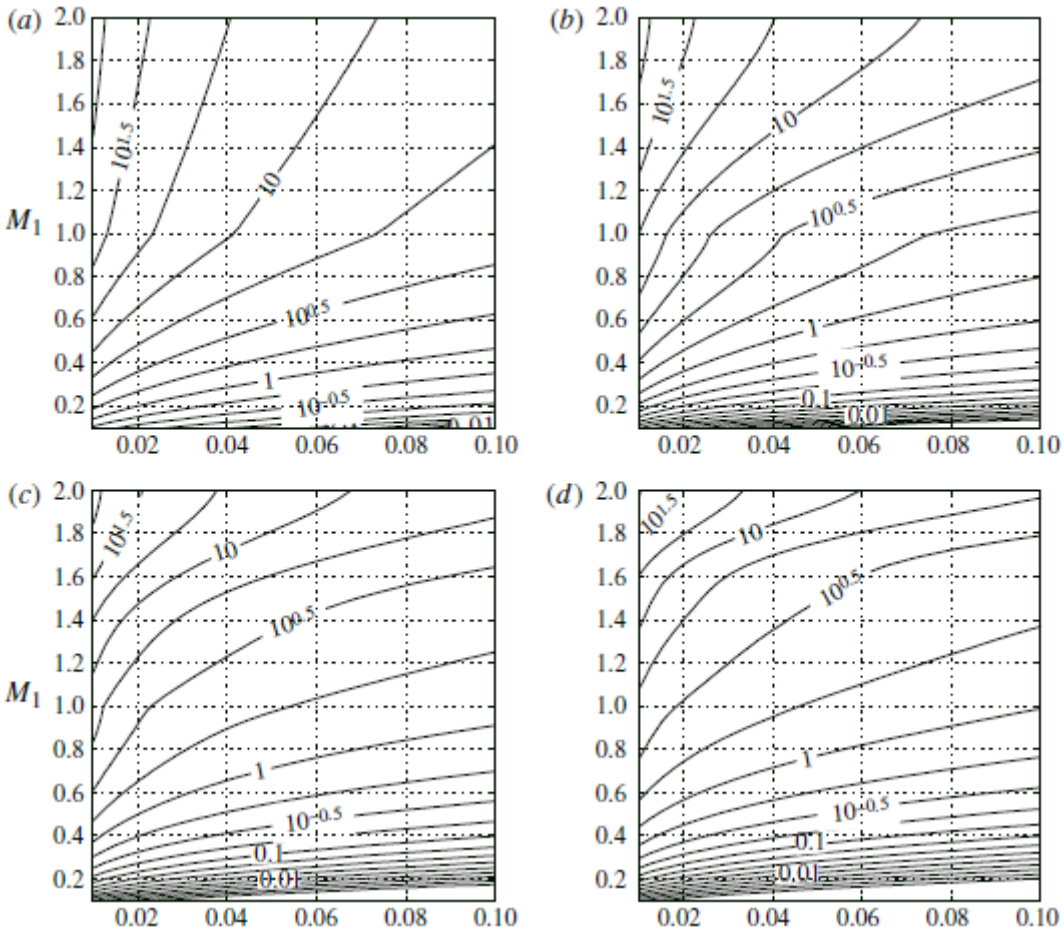

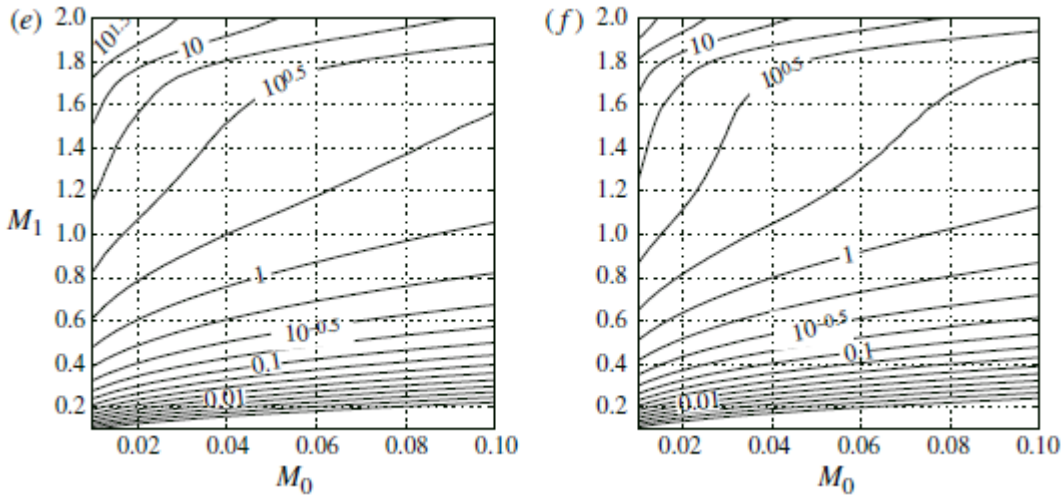

Figure 2.2: Indirect to direct noise ratio calculated using the invariants as a function of the inlet and outlet Mach numbers of the nozzle, M_0 and M_1 for different frequencies: (*a*) η at $\Omega = 0$; (*b*) η at $\Omega = 0.5$; (*c*) η at $\Omega = 1.0$; (*d*) η at $\Omega = 1.5$; (*e*) η at $\Omega = 2.0$; (*f*) η at $\Omega = 2.5$ (Duran, 2013)

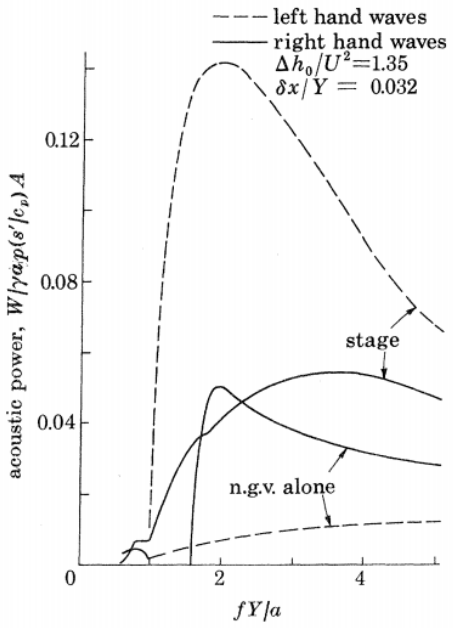

Figure 2.3: Downstream acoustic power due to entropy wave propagating into isolated nozzle guided vane row and a turbine stage (Cumpsty & Marble, 1977)

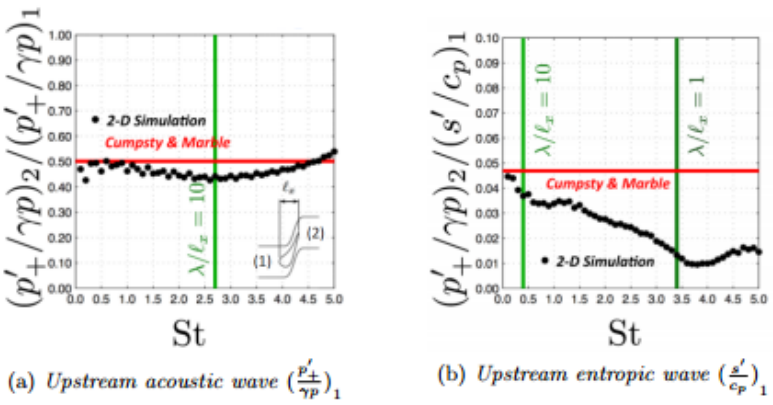

Figure 2.4: Transfer functions by Leyko (Leyko, 2011)

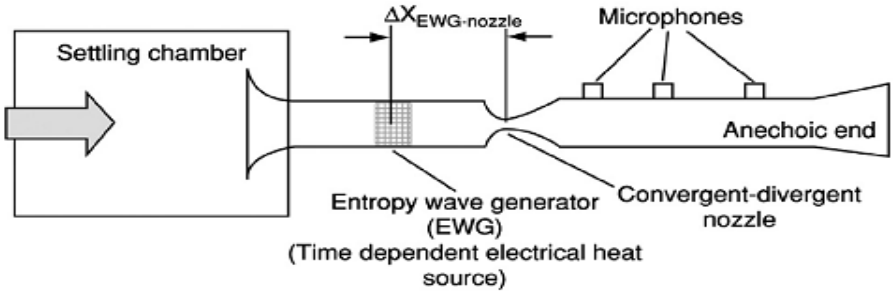

Figure 2.5: Sketch of the DLR Entropy Wave Generator rig (Bake, 2007)

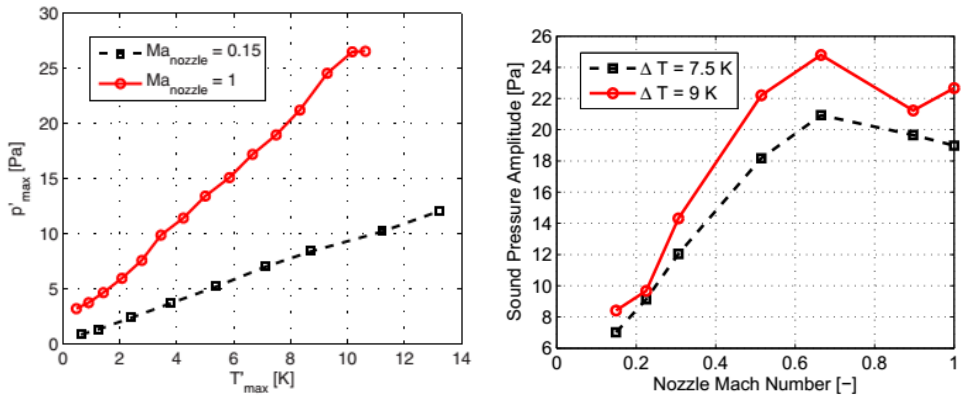

a) *b)*

Figure 2.6: Entropy noise over temperature perturbation amplitude (*a*) and nozzle Mach number (*b*) (Bake, 2009)

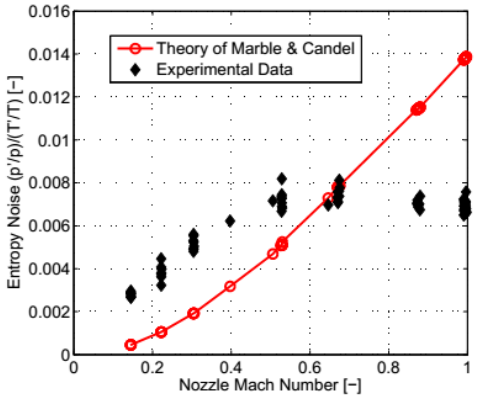

Figure 2.7: Comparison of Bake's experimental data with Marble and Candel theory (Bake, 2009)

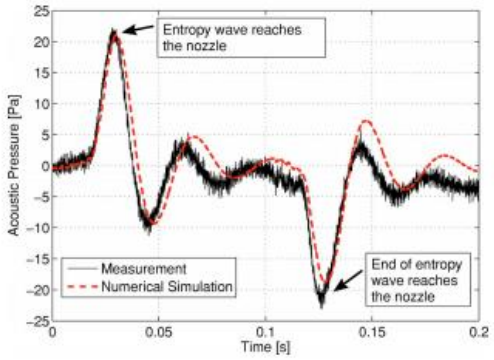

Figure 2.8: Comparison of pressure signal measured experimentally by Bake and evaluated numerically by Muehlbauer (Muehlbauer, 2008)

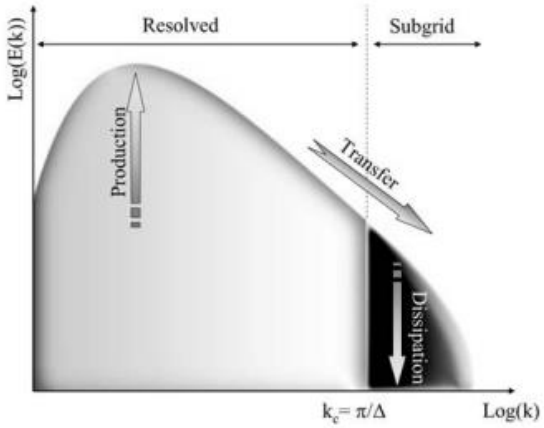

Figure 2.9: Large Eddy Simulation energy spectrum for homogeneous turbulence (Kleissl, 2004)

Chapter 3

Experimental Setup

3.1 Oxford Turbine Research Facility

The entropy noise investigation was carried out in the Oxford Turbine Research Facility (OTRF). The OTRF is a short-duration wind tunnel capable of testing an engine size turbine at the correct non-dimensional conditions for aerodynamics and heat transfer. The unique feature of the facility is the aerodynamic turbobrake, mounted on the same shaft as the turbine, which matches the turbobrake power to the turbine and thus keeps turbine speed constant during the run. Figure 3.1 gives a schematic representation of the facility. A piston is driven along the piston tube by air from a high-pressure reservoir, compressing the working gas inside the tube and heating it isentropically. When the desired pressure is reached, the compressed air is suddenly discharged by means of a fast acting valve through the working section. Typically, steady state conditions are achieved for about 500ms (Chana, 2013).

The pressure ratio across the turbine stage is set by the second throat at the exit from the stage. This is an annular variable area device that maintains axi-symmetry in the exhaust flow, and since it is choked it isolates the turbine from disturbances originating downstream.

The enhanced overall temperature distortion factor (EOTDF) generator is an inlet temperature profile simulator in which cold air of 300K is introduced into the hot gas mainstream.

The design of the EOTDF simulator uses annular slots at the hub and casing wall to create a radial temperature profile, whereas radial baffles were used to generate a circumferential temperature profile of the inlet section. The radial temperature profile is simulated by the injection of cooler air through annular slots at the hub and casing wall. The temperature and mass flow of the hot mainstream can be varied. The design allows adjustment of the coolant injection axial location in order to control the mixing and therefore the profile shape. A more detailed description of the temperature generator is given by Povey (Povey et all, 2007).

A schematic of the generator showing its position relative to the inlet contraction and NGV is shown in Figure 3.2 and, a photograph of the hardware is given in Figure 3.3. This module is comprised of an annular rig at the hub, and at case (pictured green), each with an integral annular plenum to ensure circumferentially uniform pressure, interconnected by 32 steel tubes, which act as radial injectors and feeds to the hub plenum. Flow is admitted to the module through eight hoses, which are connected via a manifold and upstream sonic venturi flow meter to the cold gas reservoir. To ensure excellent periodicity the internal Mach numbers in the feed pipes and plena are kept below 0.1. Two pressure limiters are used at the inlet and outlet of the steel tubes, to allow a certain amount of adjustment, should that be required. The system is designed to operate at high internal pressure to keep the module (and tube diameter) small for a given internal Mach number. The nominal turbine inlet pressure is 4.6bar. The flow is admitted to the annular and radial baffles through small (0.6mm diameter) holes. Sufficient mixing length is allowed to ensure uniform flow at the baffle exit planes. For the radial baffles, an impingement plate is incorporated to encourage mixing.

MT1 is an unshrouded high-pressure research turbine relevant to aircraft applications. The stage contains 32 vanes and 60 rotor blades. The design stage pressure ratio is 3.2 and nozzle guide vanes exit Reynolds number is $2.54 \cdot 10^6$. The annulus containing the NGVs has a contraction section upstream which simulates the exit of the combustion chamber for the uniform inlet temperature condition. The NGV ring consists of 32 vanes, of which 12 can be removed for instrumentation using three removable cassettes. The vanes in the removable cassettes make it easy for instrumented vanes to be fitted, so there is no need to remove the outer casing. The running rotor tip gap at the design speed of 9500rpm is estimated to be 0.56mm. The hub and casing endwalls downstream of the rotor form an extended parallel duct.

3.2 Nozzles Modelling

Investigation of entropy noise in the full turbine stage is a complicated and expensive process that involves consideration of rotor blades rotation and vane aerofoil geometry modifying the flow direction and producing a lot of additional noise sources in the whole range of frequencies. A more simple approach to evaluate entropy noise can be introduced by removing the rotor blades and changing the stator blades with a simple nozzle geometry. This method allows to avoid the appearance of secondary acoustic sources obscuring the real entropy noise produced by acceleration of the flow. The nozzle configuration may be modelled to achieve the Mach number distribution of a typical vane geometry but the flow will be propagating in a simpler manner simplifying the instrumentation and measurements.

3.2.1 Single Nozzle Design

In the OTRF the flow passing downstream from the EOTDF generator experiences a rapid acceleration dictated by the contracting area. The flow speed increases while passing through the NGV section and throat and then decreases at a set of 60 rotor blades. The rotor platform is 28mm long and is proceeded by a two degree diffusion at the casing wall. A duct extension was introduced to allow a required length for seventeen pressure transducers to be fitted in a row.

The NGVs turn the flow by approximately 70 degree and themselves are the sources of additional noise. This is exacerbated by acoustic scattering of entropy noise. Figure 3.4 presents measured results as a sound pressure level against frequency range when the NGVs are present and removed. This illustrates clearly that the presence of the vane leads to an increase of the sound pressure level at the range of frequencies from 200Hz to 5000Hz. Unfortunately, this frequency range is also associated with the largest energy transformation from the total temperature fluctuations into acoustic pressure waves. Therefore, investigation of entropy noise can be carried out more conveniently if several nozzle modifications with different acceleration rate in the NGV section are used with the vane aerofoils removed.

The new investigation approach required removal of the rotor blades and vanes. To simplify the experimental part of the investigation to study the relationship between entropy noise and the contracting geometry configuration a new nozzle was designed and modelled to achieve the same acceleration rate as for the MT1 vanes and to be able to operate from subsonic to transonic flow conditions by changing the pressure ratio across the stage. The nozzle was fitted in a way as to exchange the rotor section gap with a hub

wall of the nozzle. There are a lot of limitations on the possible hardware modification in the OTRF nozzle section. Figure 3.5 presents the OTRF nozzle section of the facility with changeable sections highlighted in green. The vane location and its hub wall section is schematically presented. The design objective was to maintain the mean acceleration in the NGV section over the same axial distance but to be determined not by the aerofoil geometry but by the contracting area of the nozzle up to its throat. In this study we assume that the flow is turbulent with heat conduction neglected, the geometry of the duct is symmetrical in the circumferential direction.

The basic nozzle geometry achieving the MT1 vane acceleration was called nozzle x and was modelled by changing the exit pressure so it could be operated across both subsonic and transonic conditions ranging from Mach number 0.8 to 1.2 at the throat. The comparison of Mach number distribution of the modelled nozzle with that on suction and pressure sides of the MT1 vane is presented in Figure 3.6. For demonstration purposes, the range of axial locations was limited to the NGV section. The subsonic conditions were achieved by adjusting the OTRF second throat area to change the nozzle exit static pressure. The nozzle throat dimension is 14.5mm leading to a mass flow rate increase up to 19kg/s.

Figure 3.7 shows the hardware modifications brought about to reproduce the nozzle design. The hub wall (pictured green), the outer wall of the NGV section (blue) and extension for transducers (magenta) were assembled keeping the inlet section (red) in place. The employment of the extension allows to increase the working length of the axial row of pressure transducers fitted at the outer wall and perform correlation of sound pressure level in the axial direction. The area ratio is kept constant for 139mm starting from

the two degree diffusion at the outer wall downstream of the rotor section to the exit of the nozzle.

3.2.2 Second Nozzle Modelling

With the first nozzle designed to match the mainstream velocity distribution of the original MT1 NGV a second nozzle was modelled. The modelling was performed using the following approach. The existing nozzle configuration was divided into two slices, each of them corresponding to a chosen Mach number value. Subsequently, the axial length x between the throat and the inlet section was multiplied by a length coefficient. For modelling of the second nozzle the coefficient chosen was 1.5. At the new inlet location the same Mach number value has been achieved by adjusting the nozzle annulus geometry using an inverse isentropic design such that the area ratio of the two are kept constant. This procedure has been repeated for several sections. The distribution of Mach number within the NGV section for two modelled nozzles presented in Figure 3.8.

Figure 3.9 shows the hardware configuration for nozzle 1.5x. The index indicates the relative axial length of the vane to which the modelled nozzle corresponds. For the 1.5x nozzle the inlet section, the hub wall and the outer wall of the NGV required to be modified. The area ratio within the NGV section for this nozzle was substantially reduced, thus increasing the flow velocity and making the acceleration process as steady as it was possible to achieve, taking into account the hardware limitations imposed by the facility. The inlet and exit conditions are maintained and the change in acceleration rate is achieved through geometrical changes only. The throat and exit dimensions were kept the same as for nozzle x maintaining the operational flow conditions.

3.3 Turbine Stage Configuration

The unique capacity of the OTRF is that of testing the entropy noise generation through an engine size turbine stage due to a temperature profile similar to that of a real engine combustor. The correct non-dimensional conditions are maintained throughout the test. The full turbine stage is evaluated to produce larger dynamic pressure fluctuations than a annular NGV section (Cumpsty, 1979), and thus serves as an object of preliminary interest to aeroacousticians. The data acquired in such an experiment will allow to make a good estimation of entropy noise influence in the real aero engine with a typical rich-burn combustor system. Carrying out of this kind of experiment is a complicated process which requires consideration of stator blade positioning and rotational speed of the rotor blades. To the best knowledge of the author this is the first entropy noise investigation carried out for a real engine size turbine stage to date.

Figure 3.10 shows the hardware configuration for the turbine stage test. The EOTDF temperature profile being produced at the EOTDF generator propagates downstream with the mean flow speed through the contracting area of the inlet section (pictured red). A set of 32 vanes are located at the NGV section (green). The flow is experiencing a rapid acceleration from Mach number 0.1 to 0.9 and a turning of 70 degree dictated by the aerofoil geometry. The rotation at the speed of 9500rpm, 60 rotor blades follow (blue). The rotor decreases the flow speed to the subsonic condition of Mach number 0.45 in the absolute frame of reference and is numerically evaluated as an additional entropy noise source (Duran, 2013). The rotor tip has a clearance of 0.56mm. Two degree diffusion on the hub and casing walls further decelerates the flow due to an increase in area ratio. The working section ends with the extension section where the pressure transducers are to be

mounted (pink). The employment of the same extension as for the nozzle tests allows to match pressure transducer locations with those of the nozzles. The manufacturing of the hub extension (brown) to match the hub wall length with that of the casing was necessary. The flow conditions for the turbine vane configuration cannot be modified with the second throat and the Mach number distribution in the axial direction was maintained the same for all the tests. Therefore, the only possible test variation for the turbine stage was the mainstream temperature of the flow.

3.4 Nozzle Flow Characteristics

A lot of flow characteristics of the designed nozzles should be evaluated in order to make a realistic assessment of the entropy noise generation. In this regard, CFD simulation was carried out using the commercially available software FLUENT deploying the two equation κ-ε turbulent-viscosity model due to the relatively simple flow behaviour of the nozzles with stator and rotor blades removed. An unstructured mesh was used, tetrahedral with 1.4 million nodes with mesh refinement applied at the wall regions. A more precise description of the numerical setup is presented in Chapter 6. A careful boundary layer thickness investigation for different turbulence models was performed because of the sensitivity at high Mach number in the duct exit. All models confirmed that the total thickness of the boundary layer for the hub and casing walls at the exit of the nozzle does not exceed 0.5mm, which is less than 5% of the annulus height. Experimental measurements in the OTRF were performed using hot wires to measure the turbulence intensity of 5.8%. They show boundary layer thickness of order 0.5mm.

The contour lines of the Mach number distribution are given in Figure 3.11 for the two modelled nozzles. This can give understanding of the Mach number distribution in the axial direction as well as in the radial direction between the hub and casing walls. The nozzles are symmetrical in the circumferential direction. The picture reproduces the working section of the facility from the inlet section to the duct extension. The reason for paying attention to the Mach number distribution within the nozzle confined area is to allow the understanding of the entropy noise generation caused by acoustic/entropy mode interaction and the influence of the geometry configuration in the axial and radial directions. Notably, in Figure 3.9 the Mach number contours for nozzle 1.5x are spread out broader than those of nozzle x, this is particularly evident in the range from Mach number 0.5 to 0.8. The Mach number contours start to coincide downstream of the throat area, whereas nozzle x contours are more curved than those of nozzle 1.5x in the upstream region, determining variations in flow velocity in the radial direction. Thus, the Mach number distribution along the hub wall differs from that of the casing.

Figure 3.12 shows the Mach number distribution for the designed nozzles along the mid-height plane. The beginning of the axial reference point is chosen at the start of the inlet section. The initial Mach number upstream of the inlet section for all nozzles is 0.08, which corresponds to the exit of the EOTDF generator. Further downstream all the nozzles have a different Mach number distribution behaviour until the throat where they reach the same Mach number value. The nozzle 1.5x distribution meets that of nozzle x at the throat with Mach number of approximately 0.7 at the start of the NGV section. The presented Mach number distribution is for the subsonic case of 0.7 Mach number on which the modelling of the nozzles was based on. The adjustment of the second nozzle downstream

of the facility allows a modification of the flow conditions in the desired range, subsonic case with Mach number as low as 0.7 and supersonic of 1.2 Mach number. The steady behaviour of the flow starting from 0.22m is to be noted. The steady behaviour endures more than 70mm up to the duct extension. This is a key factor in the evaluation of dynamic pressure fluctuations since this is the location of the transducer fitting.

It is worth noting that the nozzle 1.5x Mach number distribution shows a significant dependence on the inner wall geometry at the NGV section of the duct, especially on the location of the hub wall profile inflection point. The location of this point was chosen precisely to avoid a double shock at the throat region. The hub wall geometry modification was affected by the presence of the unchangeable inner section of the rig at the location of the rotor disc.

Figure 3.13 presents distribution of area ratio along the mid-height plane for the designed nozzles. Nozzle x is characterised by a constant rate of contraction, while nozzle 1.5x experiences a more rapid contraction at the inlet section and NGV section. Downstream the throat the area ratio behaviour for both nozzles is the same.

Based on the fact that entropy noise is in direct proportion to the static pressure change, noise reduction can be achieved by comparing the rate of Mach number change. Figure 3.14 illustrates the rate of change of Mach number distribution against the axial distance for two modelled nozzles. Nozzle x is characterized by a rapid acceleration close to the throat preceded by a low acceleration, whereas nozzle 1.5x experiences an acceleration in a steady way from the inlet section up to the throat. Analytical prediction can be made that if run with the same inlet temperature inhomogeneities, nozzle 1.5x must be quieter than nozzle x due to a much lower peak value of Mach number rate of change entailing that

there would be no abrupt changes in shear stresses associated with entropy inhomogeneities, fluctuations of which generate entropy noise waves.

3.5 Instrumentation

3.5.1 Pressure Transducers

To perform measurements of dynamic pressure fluctuations with the turbine configuration when the NGV and rotor blade are installed and for two designed nozzles a set of high frequencies Kulite pressure transducers were used.

Kulite XCQ 062 is a miniature pressure transducer with hexagonal head o-ring seal making it easy to mount and simple to perform pressure fluctuation measurements. Pressure variations in time are measured as a fluctuating force applied to a flush metal diaphragm. A solid state piezoresistive sensing element is located immediately behind this metal diaphragm which is protected by a metal screen. Force transfer is accomplished via a non-compressible silicone oil. This sensing sub assembly is welded to a stainless steel body. Use of high temperature materials allows for temperatures up to 232^{o}C.

In order to measure the static pressure change through the NGV section with the simple nozzle configuration two sensors were fitted at the outer wall of the NGV section, one upstream and one downstream. Downstream of the rotor blade and throat of the nozzle static pressure fluctuation behaviour was investigated using 17 consecutive axially located Kulite transducers.

The discontinuity in the area between the working-section duct and the downstream traverse-section cavity results in a reflection at this location. It is therefore desirable to

separate downstream travelling waves from the upstream travelling reflected waves in order to get an accurate measure of the source strength.

To achieve this in an annular duct where there may be higher-order modes present requires an approach similar to beam-forming, in which an array of sensors is used and by considering the phase of the signals recorded at each sensor the sound emanating from a particular direction can be isolated. The aperture (length) of the array and number of sensors required is usually set by the accuracy and anti-aliasing requirements over the target frequency range, however the physical space and number of sensors available places limitations on the array design. Some simulations were performed by ISVR to investigate practical array designs and it was established that an array using all seventeen available sensors distributed over the entire length of the region of the duct where the flow Mach number is reasonably stable would be required. This allows to extend the length of the acoustic aperture up to 0.11m and perform cross-correlation in the axial direction between transducers. The precise axial location of the axial row transducers with regard to the duct is presented in Table 3.1. The reference point was located at the beginning of the inlet section of the facility. Thus, the last 17th Kulite in the axial measurement row is located 0.34m downstream of the working section inlet. A duct extension of 70mm length was manufactured and installed to maximise the space available for the array, but even so it may be difficult to achieve meaningful results at low frequencies.

Figure 3.15 gives a photograph showing the working section and duct extension fitted with Kulites. Notable the 8th Kulite located at the exit of the working section casing wall was glued into the hole as oppose to the rest of the transducers, which are screwed in. This leads to the once only use of this transducer, but will allow to avoid inevitable high

frequency noise associated with flow passing through protruding elements of the Kulite. Entropy noise is proven to have highly unpredictable angular direction of wave propagation (Cumpsty, 1979), so to allow investigation of this effect 18 azimuthally evenly spaced sensors are mounted.

Figure 3.16 shows the working section parts of the facility in relation to the transducers. The location of two pressure sensors in the NGV section are preserved for the nozzle and turbine stage cases. The circumferential fitting for nozzle x and turbine stage may vary but will nevertheless relate to the same Mach number value since the nozzle x configuration was chosen to reproduce the stator blade behaviour. The 18 azimuthally located sensors correspond to the 12^{th} Kulite location of the axial row. To make assessment of the boundary layer noise and evaluate Green's function of the flow 6 evenly spaced Kulites are mounted in the outer cassette outside the working section of the facility.

Figure 3.17 and 3.18 show respectively a 3D CAD model of the duct extension with the Kulite fitting locations in the axial and circumferential directions and the hardware with the holes for Kulites drilled in the extension.

3.5.2 Amplifier Modifications for Kulite Measurements and Gain Characterisation

During the initial set up of the instrumentation difficulties were experienced in taking high quality data for noise measurements using high frequency Kulite pressure transducers. The existing amplification system used high frequency differential amplifiers to boost the Kulite output signal, which was then recorded on a high speed A/D system at 100kS/s. With this system it was not possible to distinguish the low amplitude unsteady noise signals used during the system calibration because of insufficient gain on the signal. As the sound

pressure levels required to be measured for entropy noise are very small in comparison to routine unsteady aerodynamic pressure measurements issues were encountered with external electrical interference, mainly associated with mains power and ground noise. In addition, large dc offsets at the start of the acquisition sequence meant that the gain had to be limited and the A/D range increased, reducing the resolution of the recorded signal.

Overcoming these issues to detect accurate noise signals of the size expected necessitated significant increase in the signal gain and ac coupling of the output signal, allowing maximisation of the available A/D resolution. In addition power to both the Kulites and the amplifiers was switched to batteries which allowed the mains and ground electrical interference to be eliminated to the lowest possible level theoretically possible.

The amplification problems were overcome by designing and implementing modifications to the existing variable gain, inverting amplifier units. The original circuit is shown in Figure 3.19, which allowed for a maximum gain of 100.

The circuit in its original form did not allow for ac coupling but the dc level could be varied by a dc offset part (not shown). Low pass filtering was provided though capacitor C2 and for most of the units was set to have a cut-off frequency of around 500Hz. The modified circuit is shown in Figure 3.20. The first change was to replace the original op amps with higher spec OPA 604 op amps. The dc offset part of the circuit was disabled and the input signal ac coupled by replacing resistor R6 with a 1µF capacitor. This had the additional effect of doubling the maximum gain to 200. The use of a 1µF capacitor gives a cut off frequency of 21Hz. It was necessary to set the cut off frequency for the ac coupling fairly high to ensure that the initial pressure rise at the beginning of the run was filtered out. The

capacitor C2 was replaced with a 220pF capacitor, to give low pass filtering with a cut-off frequency of 100kHz.

Following the modifications to the amplifiers, it was necessary to characterise the gain profile of each of the amplifier channels, as performing a standard static calibration would not be possible because of the ac coupling applied to the Kulite output signal.

The characterisation was carried out by recording frequency sweeps on the high speed A/D at 100kS/s over 10s and then dividing the FFT of the output by the FFT of the input. These data were recorded in sections in order to get a better low frequency characterisation. The sections were then cropped, smoothed and stitched to form the full response curves. Figure 3.21 shows an example of the typical response curve for one of the amplifier channels.

3.5.3 Pneumatic Pressure Tappings

One of the most crucial factor to investigate in the entropy noise test is the steady behaviour of the flow acquired by measuring the static pressure distribution along the axial direction. The measurement is to be performed using simple pneumatic pressure tappings located at the outer wall of the working section. After being filled with air local static pressure value is measured at each of the tappings and the isentropic Mach number distribution is evaluated. Installation of pressure tappings was possible within the outer wall of the facility only.

There are six hardware sections where pressure tappings could be mounted: outer inlet section, proceeded by the outer wall of the NGV, rotor mounting region starting after the throat, followed by the two degree diffusion section, exit section further downstream and

finally the duct extension. One pressure tapping was kept at the outer inlet section. Six pressure tappings were fitted at the outer wall of the NGV section of the nozzles. As shown below this provides sufficient data point to evaluate the isentropic Mach number increase within this region. The location of each tapping was chosen based on numerical prediction as to get the same increase in static pressure value for two contiguously located tappings. The tappings tube fitting was performed using a slot cut at the NGV section outer wall allowing the access to the tappings through a large hole of the main outer wall section.

A set of new tappings were installed at the rotor blade region to improve the flow behaviour understanding. Unfortunately, this was still not sufficient to get a clear, coherent assessment of the peak isentropic Mach number and its distribution in the axial distance. A further update of tappings was required with the total number of tappings reaching 28 in the rotor mounting and diffusion region. This provided the capability to evaluate the flow behaviour along the nozzle including the extension section. Fitting of tappings at the exit section located between the two degree diffusion and extension was not possible. The closely located tappings were introduced at the extension region to catch the possible increase in isentropic Mach number due to the flow acceleration and boundary layer growth. The schematic representation of tapping locations is provided at Figure 3.22. Two originally located tappings are pictured red with the newly introduced tappings pictured blue. Figure 3.23 shows the hardware of two manufactured nozzles with pneumatic pressure tappings glued at the outer walls.

It is worth noting that installation of the hardware cannot be achieved in a way as to avoid appearance of small steps at the border of the two neighbouring sections. The absence of smooth transition at the outer wall of the facility means that the real flow behaviour will

be characterised by the presence of precipitous jumps at bordering locations. The steps are of order 0.1mm.

3.5.4 Thin Film Gauges

Entropy noise is an aerodynamic sound generated by the accelerating entropy inhomogeneities. In real combustors these inhomogeneities are spatially and temporally varying temperature non-uniformities. To match the real engine behaviour the OTRF includes the combustor simulator responsible for generation of the EOTDF temperature profile. The OTRF measurements of unsteady temperature behaviour indicate the presence of substantial temperature fluctuations especially conspicuous at the region of the 'hot spot'. Temperature fluctuations observed belong to the entropy mode of wave field disturbances in the combustor. As shown the Chapter 2 the generation of density fluctuations of entropy noise should be inextricably linked to the dissipation of temperature fluctuations. To prove the generation of entropy noise in the OTRF and to make some angular assessments of its propagation a series of thin film gauges were introduced.

Thin film gauges are thermometers allowing measurement of highly transient surface temperatures. The output represents the time-dependent surface temperature of the gauge measuring part. The measured signal and known thermal properties of the gauges allow to recalculate the time-dependent heat flux. The design of the gauge is such that during a typical time period of about 10ms, the requirements of a body of semi-infinite thickness are fulfilled (Boutier, 1993). The direction of the deduced heat flux is perpendicular to the measuring surface of the gauge. In general, thin film gauges are more

sensitive than thermocouples; they allow a measurement of surface temperature changes in order of 0.1K.

Figure 3.24 shows a makeup of a typical thin film gauge. It consists of a ceramic substrate (zirconium oxide) on this a thin nickel of platinum film is positioned by means of sputtering. Surface temperature change can be measured with a response time in the range of microseconds. The typical diameter of a gauge amounts to 2.3mm with a length of 3.3mm (Kinnear, 1999). Two platinum wires are imbedded by sintering into the substrate. At the rear end wires for electrical power supply and for measuring the resistance change are fixed by soldering. During operation thin film gauges have to be supplied by a constant current in a range of 7mA to 10mA. The unsteady surface temperature change of the substrate during the measurement causes a voltage change in a direct proportion to temperature variation.

The acquired resistance on the thin film gauge as a result of temperature change corresponds to the original resistance as:

$$R = R_0(1 + \alpha \Delta T_s), \text{ (3.1)}$$

where α is a coefficient of temperature sensitivity. Thus, the relation between voltage change and unsteady temperature variation takes form:

$$\Delta T_s(t) = \frac{\Delta u(t)}{\alpha u_0}. \text{ (3.2)}$$

For each thin film gauge a manual calibration was performed. Fitting of the thin film gauges was carried out by gluing a set of gauges on the intended location of measured surface.

Thin film gauges were employed for nozzle 1.5x and the stator blades of the turbine stage configuration after some processing of the data from nozzle x and therefore temperature fluctuations data were not available for nozzle x. Twenty thin film gauges were installed at the outer wall of the NGV section of nozzle 1.5x in two axial rows. Two of the gauges were aligned to the 2 Kulites located upstream and downstream of the NGV section to match temperature and pressure fluctuation measurement points. The distance between the two rows is 20mm in the circumferential direction which accounts for 3.5 degrees. A photograph and a schematic representation of the thin-film gauge positions within NGV section in a two-dimensional projection is presented in Figure 3.25.

The thin film gauges will allow the evaluation of temperature fluctuations to validate the generation of entropy noise and to make a rough estimation of its role on overall noise generation and to check an angle of entropy wave direction in the circumferential direction, attributed to the two-dimensional complex nature of the entropy noise waves. The latter has to be determined by an angle of entropy wave number to the flow direction (Marble & Cumpsty, 1977).

3.5.5 Full HP Stage Test Configuration

The full turbine stage entropy noise investigation required some modifications for transducer measurements. The nozzles were exchanged with the NGV section of 32 fixed vanes succeeded by 60 rotor blades with a rotational speed of 9500rpm. Previous analytical investigation of turbine stage configuration was carried out by Marble and Cumpsty and showed entropy noise to be more influential in comparison with the NGV/nozzle alone configuration.

For the full HP stage the stage exit axial row of Kulite pressure transducers was installed in the exact way as for the nozzles. This was achieved by fitting the outer wall exit extension built for the nozzle to the exit duct of the rotor in the same manner. In addition a hub extension matching the axial length of the casing was manufactured and fitted.

In the simple nozzle configuration two Kulite pressure transducers were fitted on the casing wall upstream and downstream of the NGV section at the locations corresponding to Mach number values of approximately 0.1 and 1.0 respectively. With the stage configuration this section is removed and replaced with the NGV ring. The new Kulites were fitted on the NGV casing platforms at similar Mach number locations.

The presence of blades provides opportunity to evaluate sound pressure level at the central pitch location. In this regard, two additional Kulites were installed on the suction side of the stator blade. The aerofoil Kulites are shown in Figure 3.26, one transducer is located near the leading edge and the second near the trailing edge. A complex fitting of a specifically designed trailing edge Kulite was performed. The data from two mid-span located transducers will help to assess the level of noise generation with the mean temperature of the flow augmented from 300K near the casing wall to 420K at the centre of the blade for the EOTDF case when the ‘hot spot’ is clocked to the area between two vanes.

The schematic positioning of four Kulite pressure transducers (pictured red) at the casing wall of the NGV and at the leading and trailing edges of the stator blade suction side is presented in Figure 3.27. The casing wall Kulites were located 2mm upstream of the leading edge and 3mm downstream of the trailing edge. Thus, the targeted Mach number values

of the Kulite pressure transducers at the NGV section are 0.08, 0.11, 0.76, 0.9 for the full turbine stage configuration.

3.6 Calibration Procedure for Noise Measurement

The relationship between the strength of an acoustic source in the nozzle and the resultant acoustic pressure at another point, including flow effects, can be described as a Green function (Figure 3.28). The acoustic pressures measured at a number of sensors can be used to estimate the strength of a set of acoustic sources in the nozzle providing the Green functions linking the source positions to the sensor positions are known (Holland & Nelson, 2012). The required Green functions are generally not know, so the calibration noise injection source is used to directly measure them in a separate calibration experiment. The described calibration procedure in the OTRF was performed by Keith Holland.

The calibration noise injection source is positioned close to an anticipated site of entropy noise generation. With the rig running, the source is operated with a deterministic signal input and the resultant acoustic pressure is recorded from six Kulite pressure transducers mounted symmetrically at the outer edge of the plenum between the nozzle exit and the secondary nozzle. The outputs from the Kulites, normalised to the strength of the injection source, then represent six Green functions. By assuming axial-symmetry, a further 30 Green functions linking 5 other (symmetrically-spaced) source positions to the six sensor positions can be inferred. Then, under normal running conditions, without the injection source, the strengths of six potential entropy noise sources in the nozzle can be estimated from the output signals of the six Kulites by inverting the (6 by 6) matrix of measured Green functions. If the calibration procedure is repeated with the Kulites rotated through 30

degrees, a total of 12 source strengths can be found from two measurement runs (Holland, 2015).

The source strength of the injection source is estimated during the calibration procedure from the output signals of the four Kulite pressure transducers mounted within the source tube.

If only changes in entropy noise levels, rather than absolute source strengths, are required, a different, more robust calibration procedure can be used. In this case the outputs from the Kulites are used to estimate the strengths of a set of equivalent sources positioned around the nozzle exit (Figure 3.29). The equivalent sources are defined such that they include the effects of flow, thus the acoustic pressures at the Kulites can be thought of as being due to the equivalent sources combined with a set of Green functions evaluated without flow. Here it is assumed that changes in the levels of these equivalent sources are caused by changes in the levels of the actual sources in the nozzle. The no-flow Green functions are measured by blocking the nozzle exit, using a suitable board, and injecting the calibration noise source through a hole in the board. As before, the outputs from the Kulites, normalised to the strength of the injection source, then represent six no-flow Green functions. Again, by assuming axial-symmetry, a further 30 Green functions linking 5 other (symmetrically-spaced) equivalent source positions to the six sensor positions can be inferred (Holland, 2015).

The direct Green function calibration procedure above carries some risk, due to potentially high background noise levels and the effects of flow on the noise injection source. However, the measurement of the no-flow Green functions is expected to be more reliable

as there will be no flow and low background noise during the calibration. To minimise risk, both procedures were therefore carried out.

Figure 3.30 shows the principal mechanism of noise source injection in the facilities. The 18 mm pipe with constant area ratio parallel to the flow direction is to be mounted through an NGV fitted in to a cassette location. Foam is inserted into the end of this tube preventing the wave reflection. Through flanges, this tube is connected to another, the outlet of which is installed into the outer wall of the NGV section. A speaker driver is introduced in order to generate sound waves. Four Kulites are installed inside the second tube; three of them in the inner part of the pipe and one in the Retimet metal foam, used to allow the sound wave to propagate to the working section but not disturb the aerodynamics of the NGV. The small pipe connecting the speaker driver and the main pipe was implemented in order to ensure the driver copes with the sudden increase in pressure level at the start of the experiment. Pictures of the three-dimensional model are presented in Figure 3.30, 3.31 and 3.32. Photos of the source fitted to the cassette of the facility and the Retimet foam are shown in Figure 3.33 and 3.34.

3.7 Noise Sources Analysis

Before proceeding to the experimental part, it is necessary to distinguish all possible noise sources that may arise in the OTRF. These sources must be quantified and all of them with exception of entropy noise should be filtered out.

1) Injection system noise. The comparison of the sound pressure levels distribution will be performed over the range of frequencies for two temperature profiles: uniform with a steady temperature distribution in the radial and circumferential

directions and the EOTDF with a complex distribution of temperature variations similar to a real engine combustor case. The area-averaged mean temperature of the EOTDF temperature profile will be matched with that of the uniform. The uniform temperature profile is generated by injecting the mainstream flow under the chosen temperature conditions. The EOTDF temperature profile generation requires feeding of the coolant air of 300K though slots and baffles. The injection system is a potential noise source. Its influence on the overall noise level will be quantified by comparison the uniform case of 300K with the EOTDF case for the mainstream temperature of 300K.

2) Boundary layer noise. The Kulite pressure transducers are mounted at the outer wall of the facility at the region of the boundary layer. The impact of the boundary layer will be understood by performing measurements at the outer cassette located outside the duct. The boundary layer at this region is thin and laminar but the effect of entropy noise can still be observed.

3) Turbulence noise. This noise might be generated by the turbulent mixing of the flow occurring in the EOTDF temperature profile. It produces larger temporal temperature variation producing an acoustic response different from that of entropy noise since the latter is driven by the mean flow and turns itself into an acoustic source only during the flow acceleration. There is also noise generated by turbulence where the flow from the nozzle annulus is ejected into the traverse cavity. The presence of that noise cannot be neglected. In order to circumvent this noise type, two nozzles with distinct acceleration patterns but the same boundary conditions will be investigated in the OTRF. Injecting the EOTDF temperature profile

and applying the same flow conditions to these nozzles will generate a sound pressure level difference accounting only for entropy noise.

4) Entropy noise. The noise generated by the accelerating temperature inhomogeneities. The precise description is presented in Chapter 2.
5) Vortex sound. The noise generated by rotational kinetic energy present in the flow. It appears as a result of nonlinear interaction between the acoustic and vorticity modal fields. As shown in Chapter 2, it is quadrupole noise source in its nature, whereas entropy noise is dipole. Moreover, its influence in combustors is proportional to the swirl number (Howe, 1975). The swirling of the flow in the EOTDF temperature profile is not substantial, therefore vortex sound can be neglected.

3.8 Chapter Conclusions

This chapter covers the experimental setup of the entropy noise investigation in the Oxford Turbine Research Facility (OTRF). The OTRF is a short-duration tunnel which makes possible investigation of entropy noise due to a unique opportunity to generate a non-uniform temperature profile very similar to that of a typical rich-burn combustor. The Enhanced Overall Temperature Distortion Factor (EOTDF) is a temperature profile produced by injection the coolant air of 300K into the hotter mainstream with varying total temperature. The coolant air is injected through annular slots and circumferential baffles, while the mainstream flow is being driven by a piston of the facility. The non-uniform temperature profile is distinguished by a large difference between the ‘hot spot’ and the endwall temperature, thus allowing to achieve the relative temperature difference of 0.5.

This increases the level of entropy noise since there are only limited facilities capable of sustaining such a large temperature difference.

The generation of entropy noise takes place in the NGV section where the flow is undergoing a rapid acceleration. The initial test measurements in the OTRF showed that the vane geometry has a negative effect on the overall noise production and to avoid appearance of unnecessary acoustic sources, the stator blades are removed and exchanged with a simple nozzle geometry. Two nozzles were designed. The datum nozzle geometry, called nozzle x, was modelled to achieve the same rate of acceleration as a vane blade within the acceleration section of the facility. The second nozzle 1.5x, was designed to prolong the acceleration region thus allowing a steadier Mach number distribution in the axial direction. The coefficient 1.5 determines the relative increase in the axial dimension of a vane required to achieve the proposed acceleration rate. The Mach number, area ratio and static pressure distribution along the axial distance was presented.

The measurements of dynamic pressure fluctuations were performed using Kulite pressure transducers. Seventeen transducers were mounted at the outer wall of the facility to allow the required axial distance necessary to perform cross-correlation. To investigate the generation of entropy noise in the acceleration section, two more Kulites were installed at the inlet and exit of the NGV section. Thin-film gauges were used to make an estimate of total temperature fluctuations and their dissipation within the NGV section, since the generation of entropy noise is inalienably connected to dissipation of total temperature fluctuations as showed in Chapter 2. The calibration procedure for Green functions investigation was performed. The noise source injection was chosen to take place at the NGV section corresponding to the general theory of entropy noise generation.

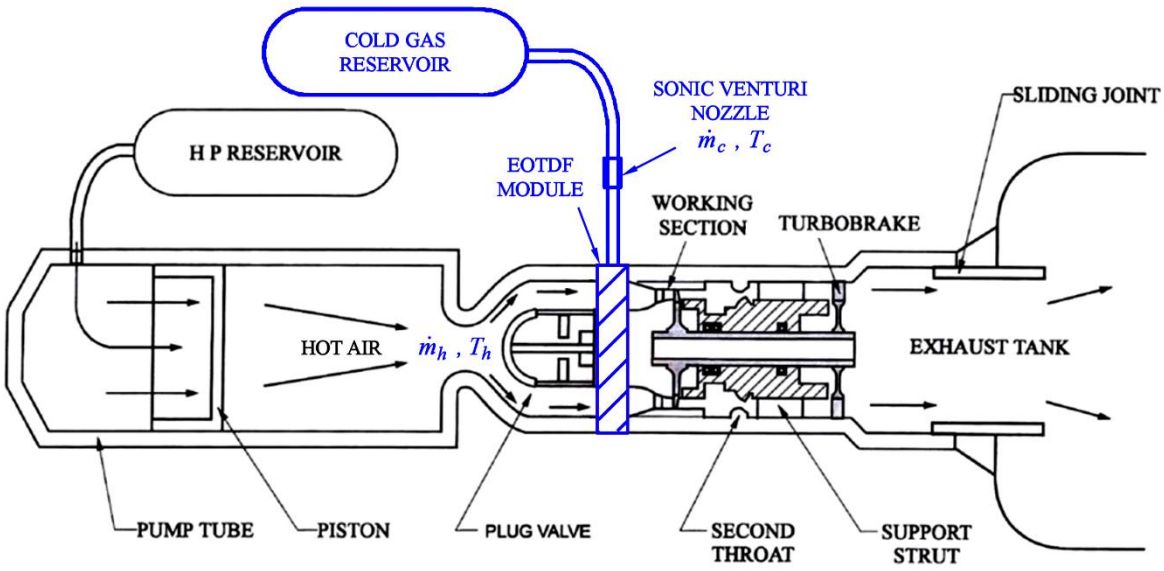

Figure 3.1: Schematic representation of the Oxford Turbine Research Facility

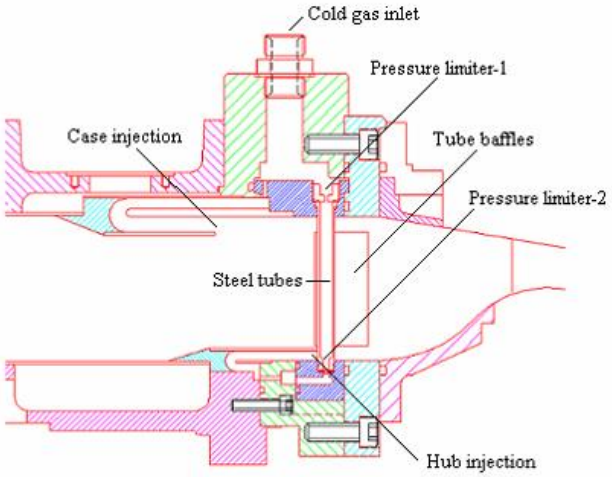

Figure 3.2: Cross-section of the EOTDF generator

Figure 3.3: EOTDF module installed

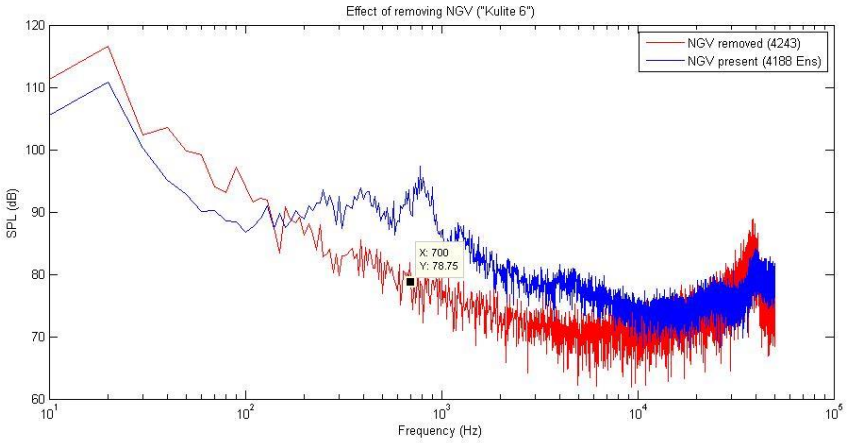

Figure 3.4: Sound pressure level over frequencies with and without the NGVs installed

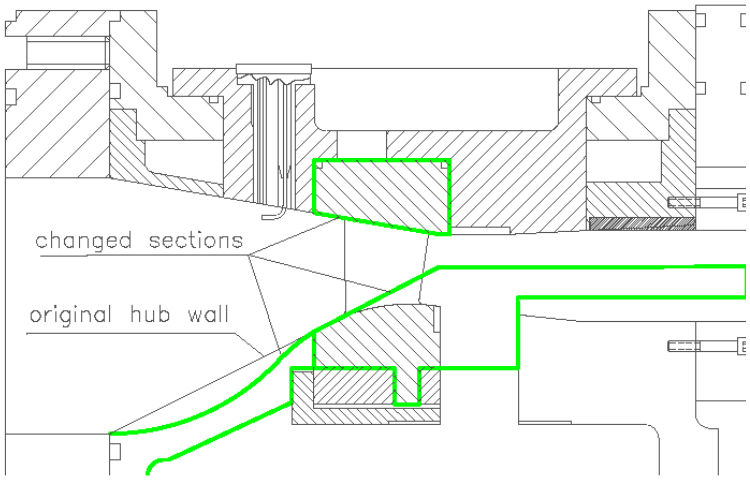

Figure 3.5: Modified sections of the facility

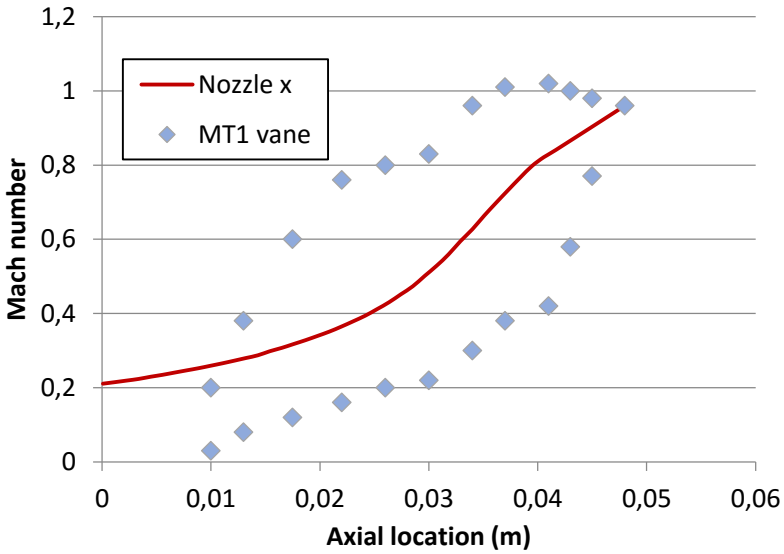

Figure 3.6: Comparison of Mach number distribution for MT1 vane and modelled nozzle

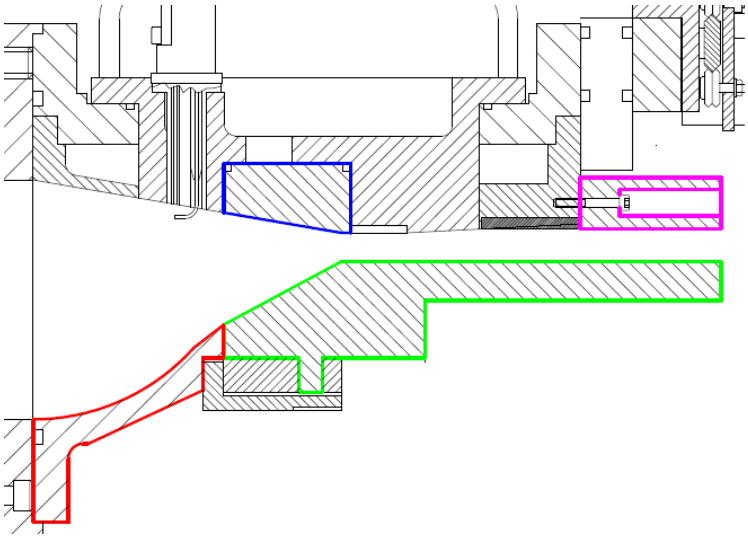

Figure 3.7: Hardware configuration for nozzle x

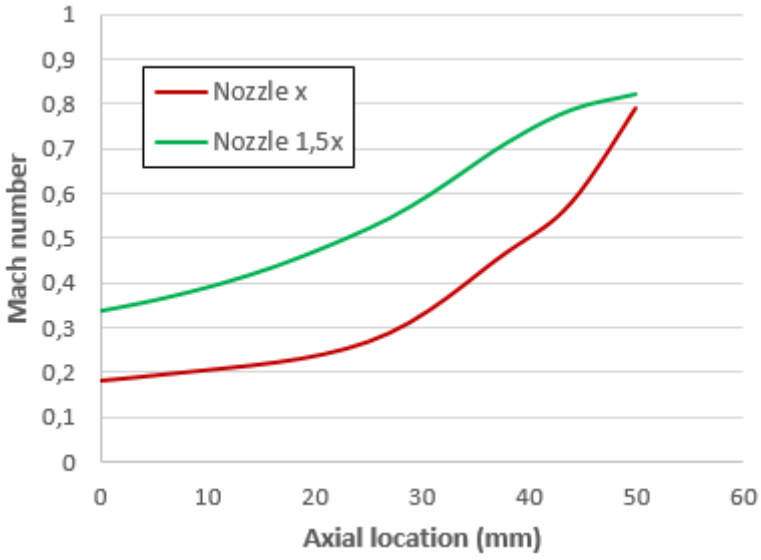

Figure 3.8: Comparison of Mach number distribution for two modelled nozzles in the region of NGV section

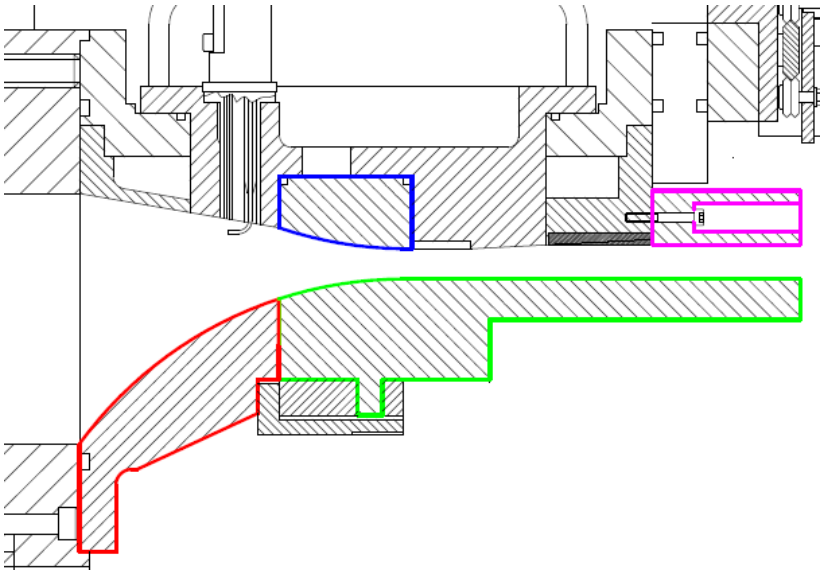

Figure 3.9: Hardware configuration for nozzle 1.5x

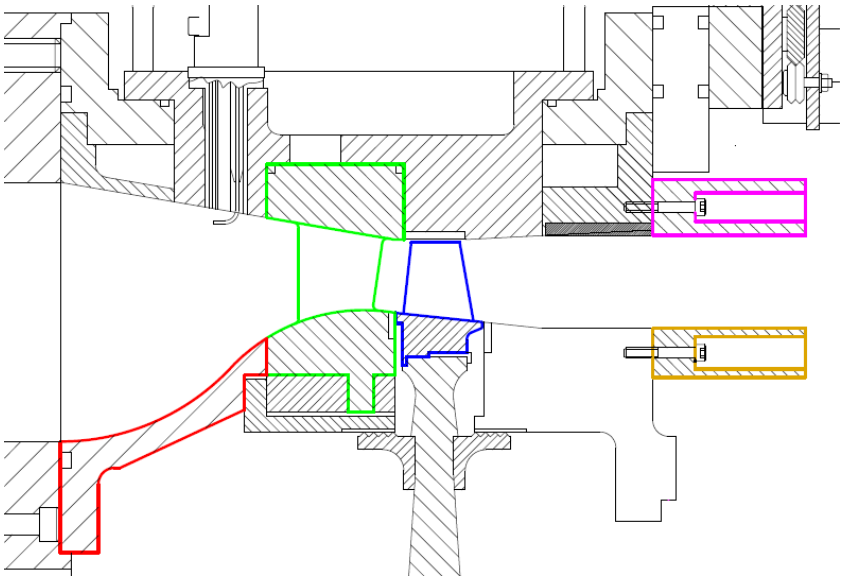

Figure 3.10: Full turbine stage hardware configuration

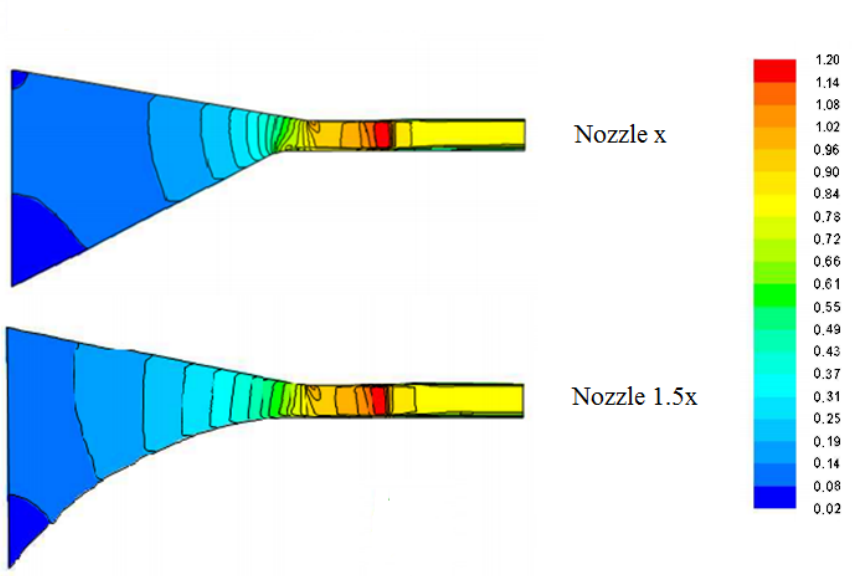

Figure 3.11: Mach number contour lines of two designed nozzles

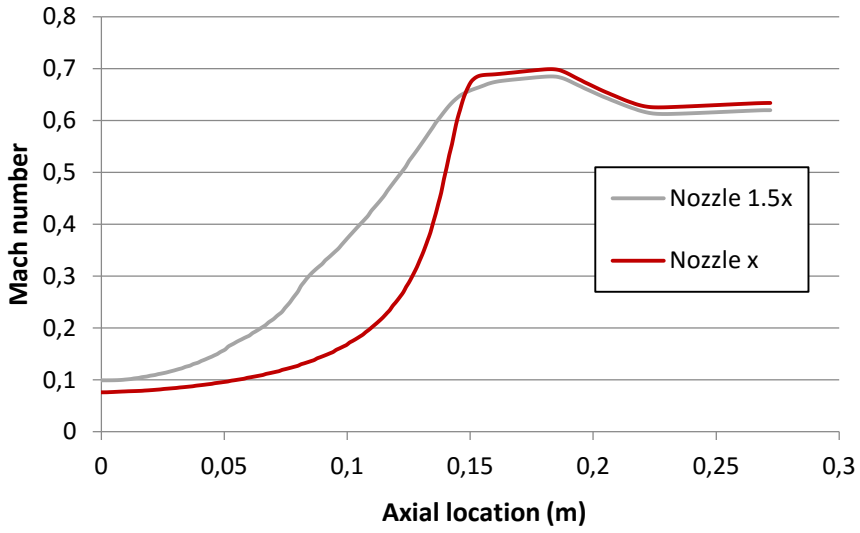

Figure 3.12: Numerically evaluated mid-height Mach number distribution for the two designed nozzles

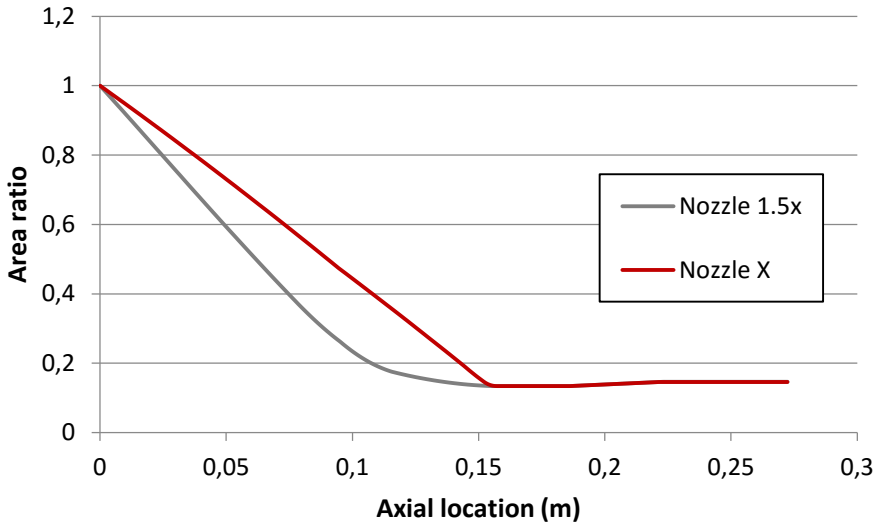

Figure 3.13: Numerically evaluated mid-height area ratio distribution for the two designed nozzles

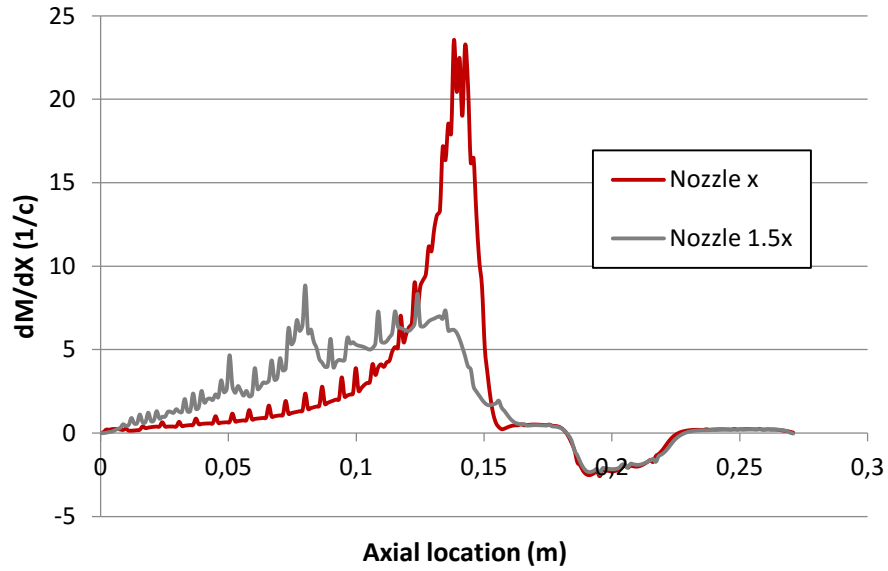

Figure 3.14: Numerically evaluated rate of change of Mach number against axial distance for the two designed nozzles

Model point	Kulite	X location (m)
2052	NGV casing platform	Upstream
2053	NGV casing platform	Downstream
2029	1	0.2300
2030	2	0.2369
2031	3	0.2438
2032	4	0.2506
2033	5	0.2575
2034	6	0.2644
2035	7	0.2713
2036	8	0.2781
2037	9	0.2850
2038	10	0.2919
2039	11	0.2988
2040	12	0.3056
2041	13	0.3125
2042	14	0.3194
2043	15	0.3263
2044	16	0.3331
2045	17	0.3400

Table 3.1: Kulite locations and model points

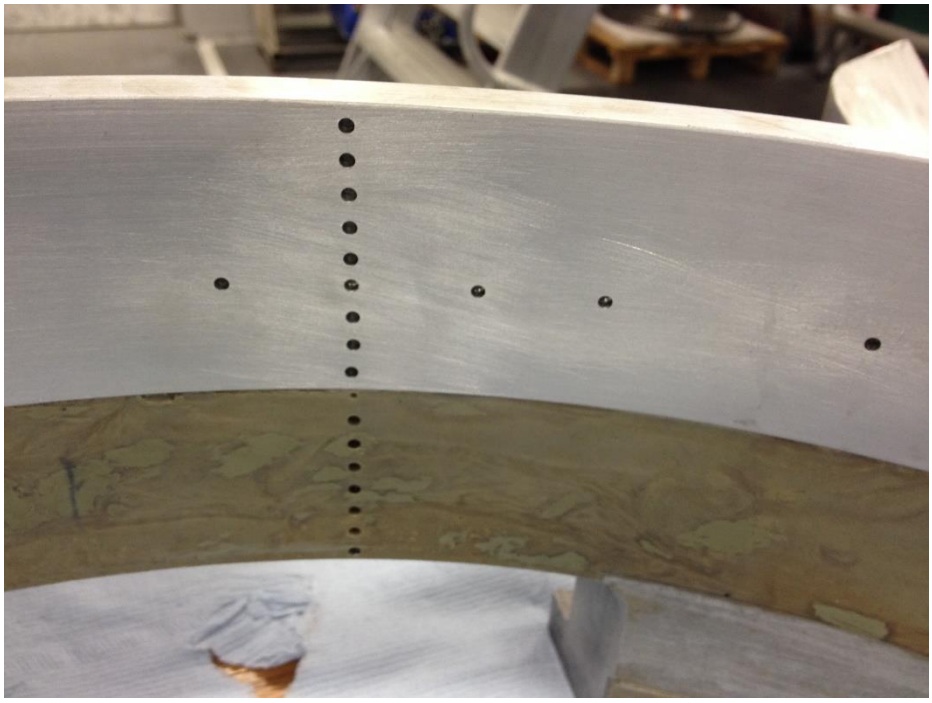

Figure 3.15: Linear Kulite positions

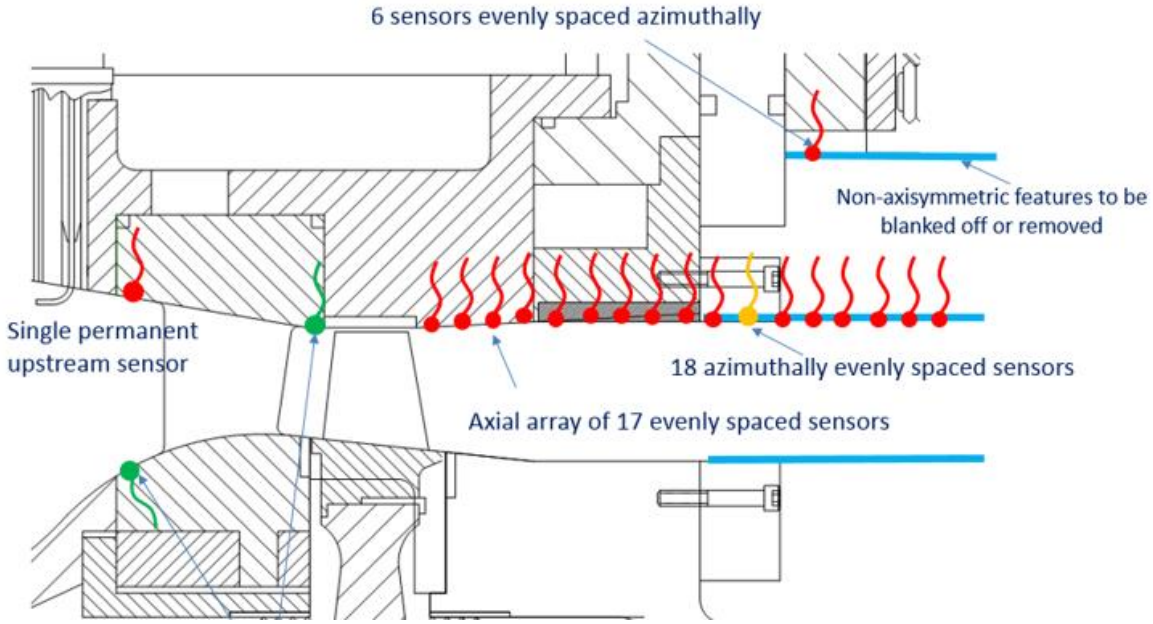

Figure 3.16: Array of Kulites fitted to the working section

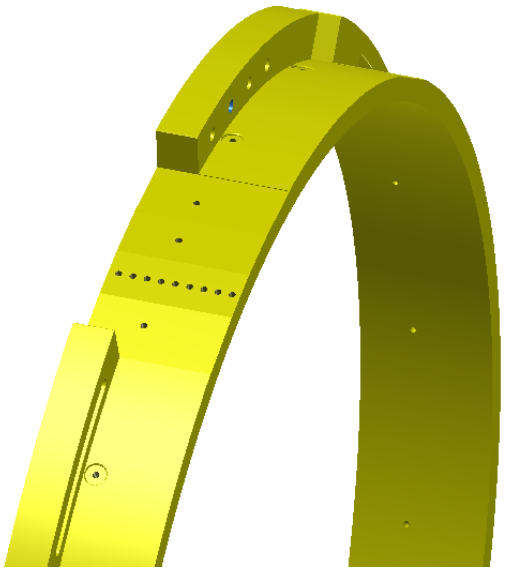

Figure 3.17: Extension duct CAD drawing

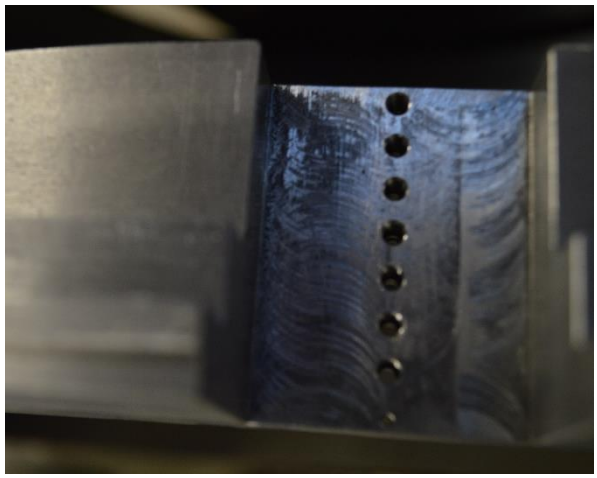

Figure 3.18: Extension duct with transducer holes

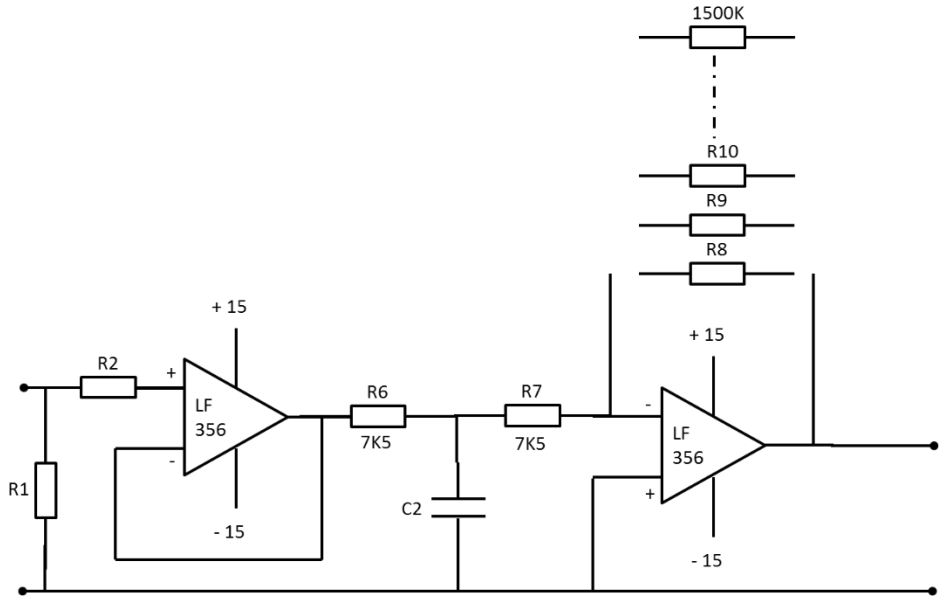

Figure 3.19: Original amplifier circuit with maximum gain of 100

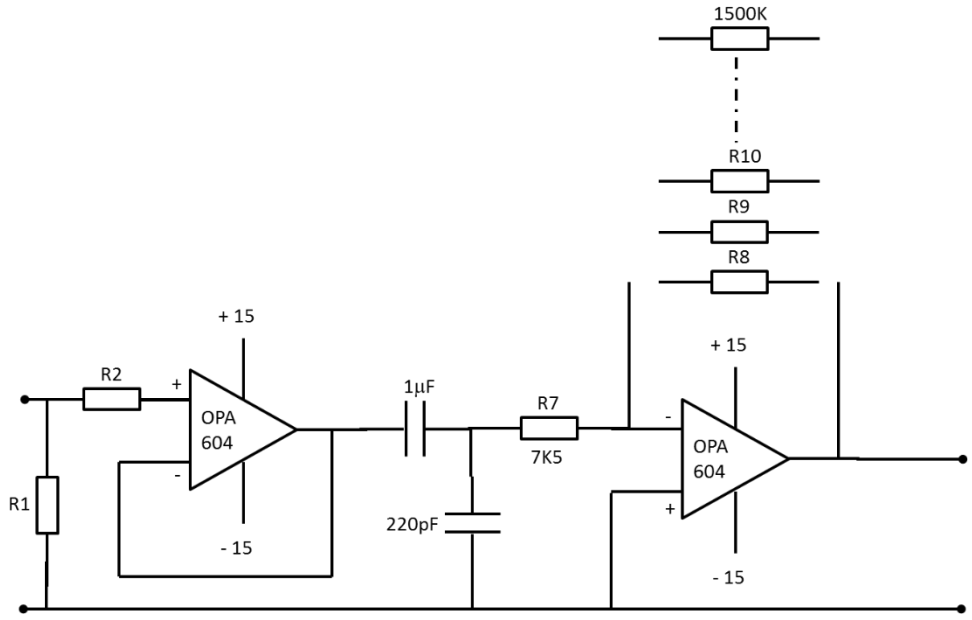

Figure 3.20: Modified amplifier circuit with 200 gain and 100KHz cut-off frequency

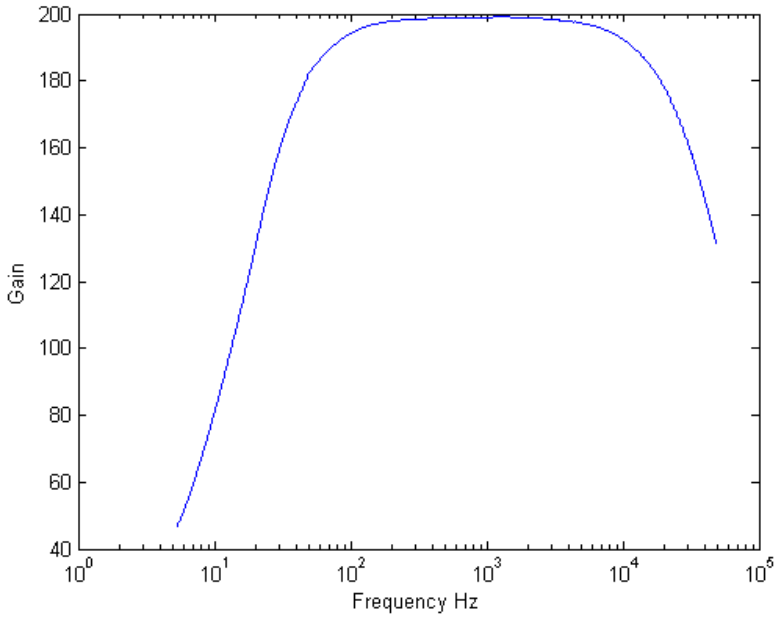

Figure 3.21: Typical response curve for the modified amplifier

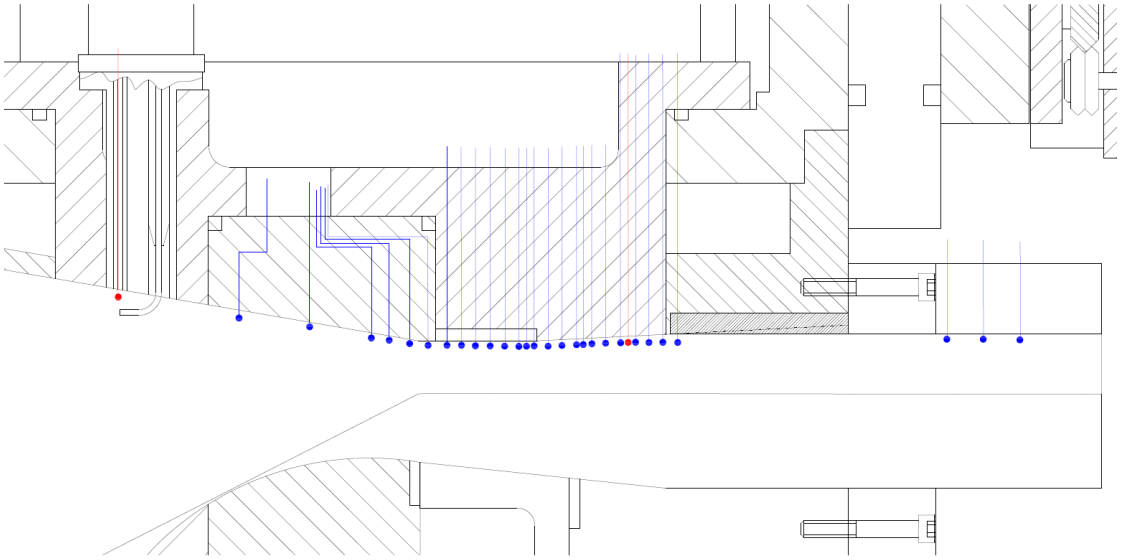

Figure 3.22: Location of pressure tappings along the outer wall of nozzle x

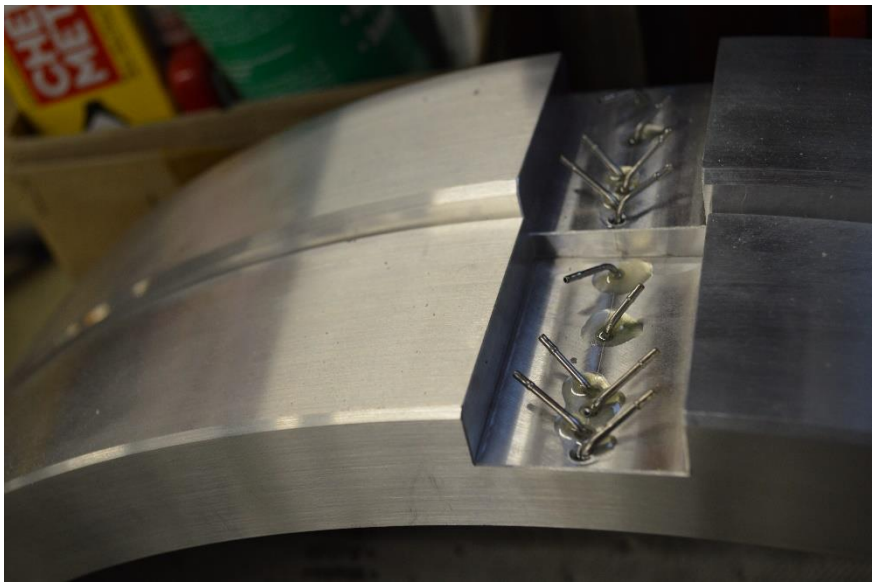

Figure 3.23: Pressure tappings glued at the top sections of two nozzle NGV outer walls

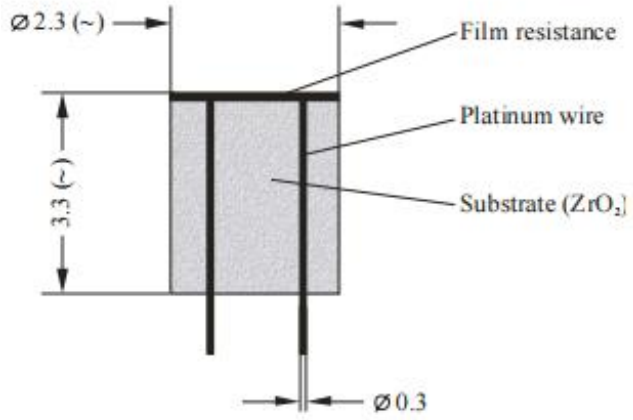

Figure 3.24: Typical thin film gauge makeup

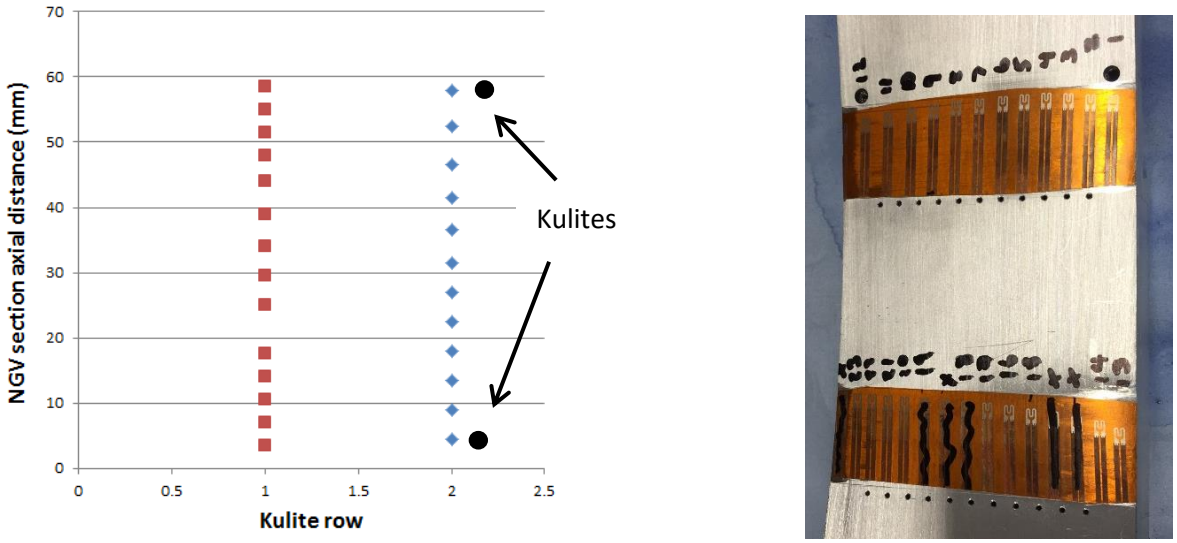

Figure 3.25: Location of thin-film gauges at the NGV section relative to Kulite locations

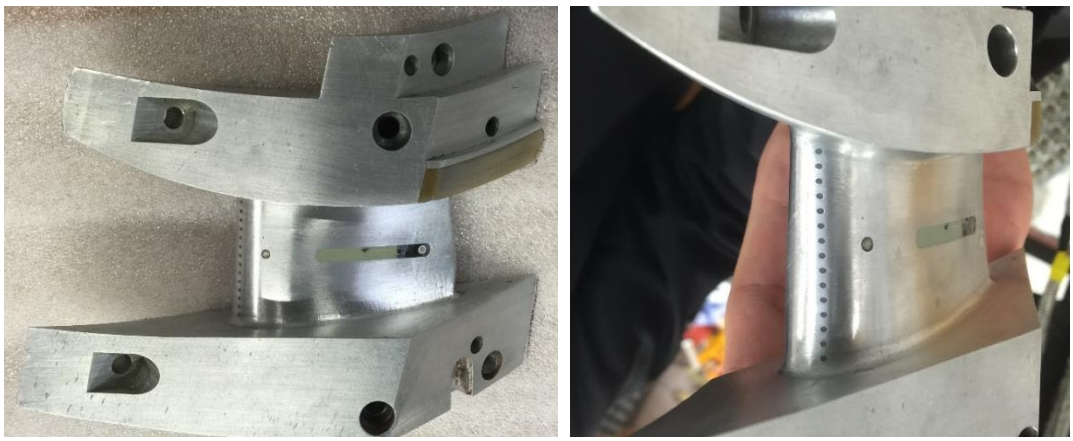

Figure 3.26: Location of Kulite pressure transducers on the stator blade surface

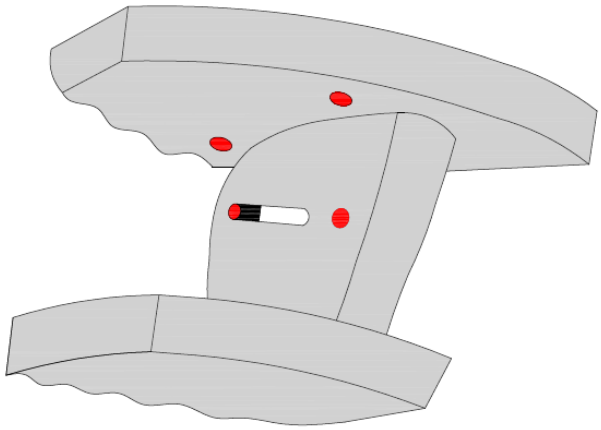

Figure 3.27: Schematic positioning of four Kulites at the NGV section

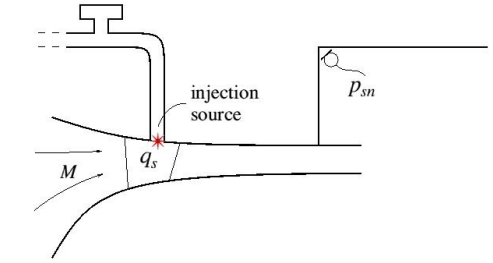

Measure with – flow Green functions $G_n = \frac{p_{sn}}{q_s}$

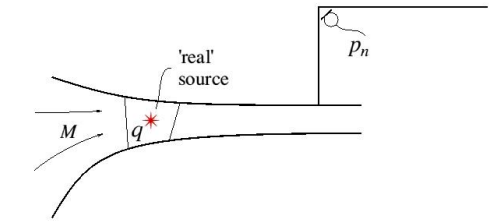

Measure p_n due to source q

then as $\frac{p_n}{q} \approx G_n$, $\boxed{q \approx \frac{p_n}{G_n}}$

Figure 3.28: Direct Green function calibration procedure (only one Green function is shown) (Holland, 2015)

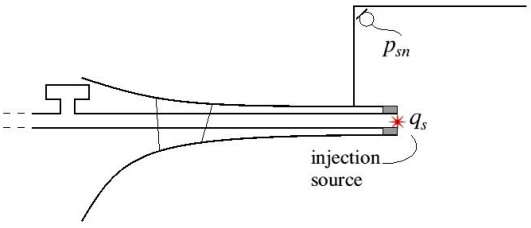

Measure no – flow Green functions $G_n = \frac{p_{sn}}{q_s}$

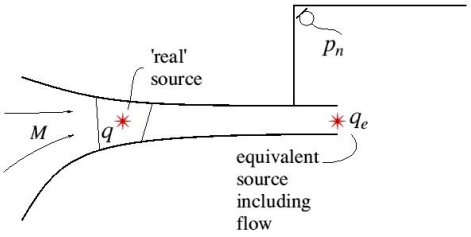

Measure p_n due to source q

then $\boxed{q_e = \frac{p_n}{G_n}}$

Figure 3.29: Equivalent source Green function procedure (only one Green function is shown) (Holland, 2015)

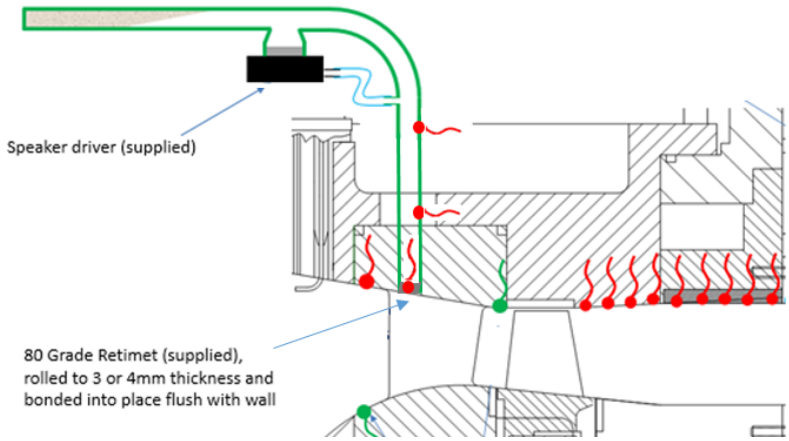

Figure 3.30: Schematic representation of noise source injection

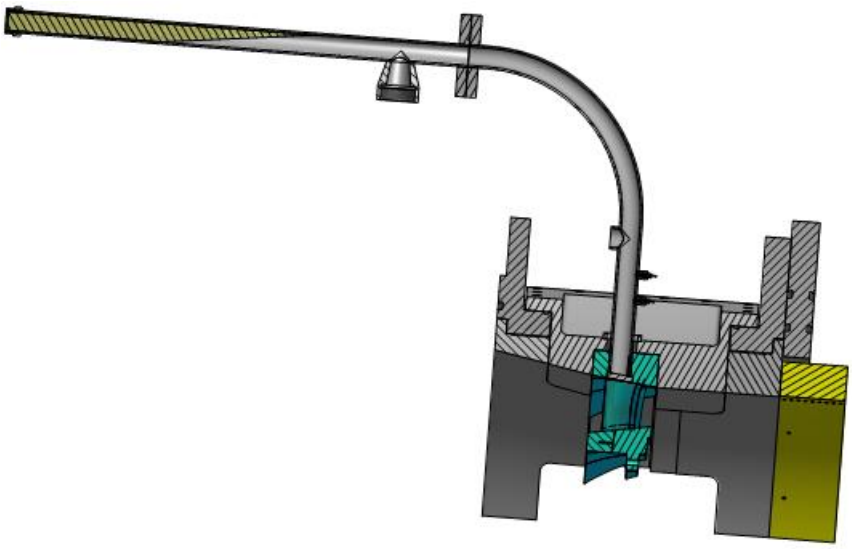

Figure 3.31: Three-dimensional model of the noise source injection

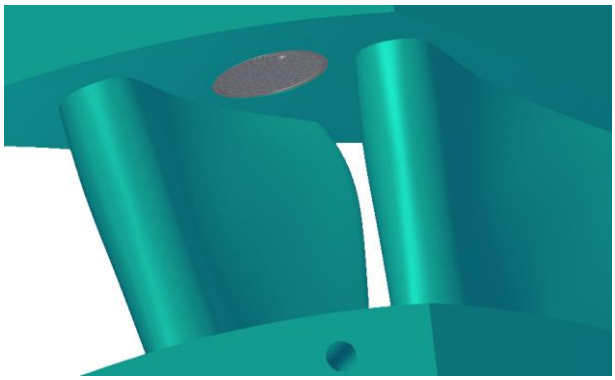

Figure 3.32: Retimet attachment at the case wall of the NGV

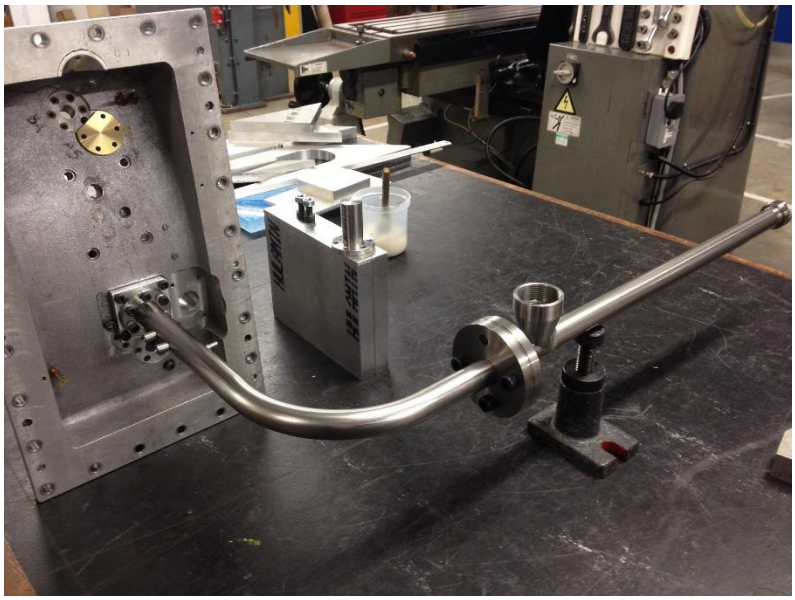

Figure 3.33: Source injection fitted to the cassette of the facility

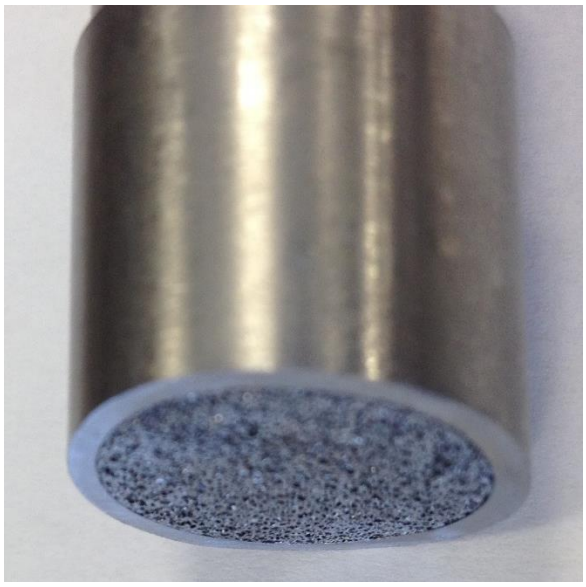

Figure 3.34: Retimet metal foam fitted to the end of the source injection pipe

Chapter 4

Experimental Investigation of Entropy Noise in the First Nozzle

4.1 Experimental Data Processing

4.1.1 Frequency Ranges of Different Noise Sources

Investigation of entropy noise requires to make an estimate of potential noise ranges. Figure 4.1 shows a typical sound pressure level distribution over the frequency range measured in the OTRF. In the lower frequencies the response curve for the modified amplifier as shown in Figure 3.20 is distinguished by a low quality characterisation. That makes acquisition of the correct noise level at frequencies from 10 to 50Hz complicated.

Entropy noise in accordance with Marble and Candel theory is only influential at lower frequencies. This is based on the assumption that wavelength must be comparable with the axial length of the nozzle. Using the reduced frequency Ω as shown in Chapter 2 can make possible to estimate the frequencies where the ratio of indirect to direct combustion noise is significant. Duran (Duran, 2010) showed that entropy noise is generally produced in the reduced frequency range $\Omega = [0; 2]$. Taking the axial distance in the OTRF as approximately 0.34m the range of entropy noise generation covers the frequencies from 10 to 2000Hz.

The fact that the Kulite pressure transducer has a flat face and cannot match the curvature of the outer wall means that additional instrumentation noise will appear. It is estimated

to appear at the higher frequencies approximately from 10 to 50kHz. It is characterised by an additional tone not present when the glued 8th Kulite is evaluated.

4.1.2 Data Consistency and Analysis

This initial analysis is based on 10Hz narrow-band spectra. The time histories have been processed using the Welch method. Data from several runs have been averaged together to reduce the variance in the spectral estimate and improve the clarity of the resulting plots. The frequency response of the measurement system was taken into account using polynomial coefficients for each of the Kulites pressure transducer. The MATLAB function used to process the noise data in a consistent manner is presented in Appendix A.

Figure 4.2 shows consistency of five independent experimental runs carried out in the OTRF for the EOTDF temperature profile generated in the combustor simulator. The sound pressure level is evaluated in decibels against the frequency range determined by the data acquisition instrumentation. The only significant divergence is noticed in the lower frequencies from 10 to 200Hz, where the noise divergence reaches approximately 3dB. At the frequencies higher than 1000Hz the sound pressure level distribution over the frequencies is similar for all runs. That is anticipated because the processed signal is characterised by more repetitions in static pressure corresponding to high frequencies.

The total number of samples needed to achieve a required accuracy is a function of the bandwidth in the frequency domain and the measurement time, given by (Rolls-Royce, 2012):

$$\sigma = \frac{4.43}{\sqrt{B \cdot t}} \quad (4.1)$$

Where σ – standard deviation evaluated in decibels, dB; B – bandwidth, Hz; t – measurement time, s.

Thus, for the chosen bandwidth of 10Hz and taking into account that the experimental investigation in the OTRF was performed to achieve the targeted measurement time of 2s the standard deviation is approximately 1dB.

4.1.3 Run Matrix

One of the main entropy noise test objective is to identify and quantify the influence of key parameters on the entropy noise generation. These key parameters are Mach number at the outlet of the nozzle and the ratio of temperature difference between the 'hot spot' and its environment to the mean temperature of the flow. Figure 4.3 shows the run matrix accomplished for the nozzle x configuration in relation to the varying Mach number in the nozzle and temperature difference. The matrix was applied to the EOTDF and uniform temperature profiles. The flow conditions were varied from as low as Mach number 0.8 to supersonic of Mach number 1.1. The ratio of temperature difference to the mean temperature of the flow corresponds to the 'hot spot' of 450K, 480K and 520K respectively. Five Mach number values of 0.8, 0.9, 0.95, 1 and 1.1 were chosen for the EOTDF temperature profile with the mean temperature of 412K to facilitate the experimental investigation, since the experimental runs with 444K mean temperature can only be maintained for a short period of no more than 0.16s, thus making the entropy noise investigation for such a high temperature challenging. A more precise test matrix with description of inlet mainstream temperature, temperature difference, number of runs and total time is presented in Appendix B.

4.2 Isentropic Mach Number Distribution

Figure 4.4 shows the comparison of isentropic Mach number distribution along the axial distance measured experimentally in the OTRF using pressure tappings and predicted numerically. The isentropic Mach number was measured at the outer wall of the facility. The location of tappings is presented in Chapter 3. The LES numerical prediction was performed for the nozzle x configuration and static pressure distribution along the outer wall within the boundary layer was processed using the isentropic flow relations to make a numerical validation of the experimental data. The initial RANS numerical procedure on which the modelling of the nozzle was performed was exchanged with the more advanced LES prediction in further investigation. The mid-height flow behaviour is matched well for both cases. The subsonic flow conditions were chosen for investigation. A good agreement of the LES numerical prediction with experimental data was achieved. The reference point of the axial distance was chosen at the beginning of the inlet section.

The initial velocity of the flow is Mach number 0.05 at the inlet section corresponding to the exit of the combustor simulator. The nozzle x inlet section contracts the flow area insignificantly, thus the flow speed increases slowly reaching no more than Mach number 0.15 at the inlet of the NGV section. The nozzle x configuration is distinguished by a NGV section with a rapid decrease in area ratio. This causes an abrupt acceleration of the flow, which at the throat region achieves the flow speed of Mach number 0.9. Further downstream the flow is first experiencing a slight acceleration and then a sudden deceleration due to a two degree diffusion at the outer wall, the constant area of the duct extension allows the boundary layer to grow, and therefore the isentropic Mach number shows a constant increase with the exit flow speed of Mach number 0.85.

The LES numerical prediction shows the presence of abrupt step-like changes in flow velocity, this is due to imperfect fitting of the hardware. The installation of the facility hardware is a complicated process and cannot be performed without avoiding small steps at the interface of two neighbouring sections, determined by the manufacture tolerances of order ±0.1mm. The absence of smooth transitions between sections means that at the boundary of the casing wall the flow experiences sudden local velocity changes.

4.3 Entropy Noise Generation in the First Nozzle

4.3.1 Evaluation of Injection Noise

Investigation of entropy noise was carried out for the complex EOTDF temperature profile characterised by temperature variations in the radial and circumferential directions. The generation of the EOTDF temperature profile is achieved by injecting the coolant air of 300K through annular slots and a set of baffles into the mainstream flow of the hotter temperature. In contrast to the uniform temperature profile produced by running the mean temperature through the combustor simulator with slots and baffles out of operation.

Figure 4.5 shows the generation of the EOTDF (a) and uniform (b) temperature profile in the combustor chamber. The EOTDF temperature profile is generated by feeding coolant air through the slots located at the endwalls and baffles located with 11.25 degree steps in the circumferential direction.

Although the mass flow rate and mean area-averaged temperature for both cases are the same, injection of additional flow may lead to the generation of additional noise caused by turbulence mixing within the flow and valves and orifices of the injection system. That

instigates the necessity to estimate the level of influence of the injection system on the overall noise generation. This is achieved by lowering the mainstream temperature down to 300K to match the temperature of the injected air. Thus the first case is that when there is injection of 300K air in the mainstream of 300K, the second case – when there is no injection and the mainstream temperature is maintained at 300K. Two case were tested in the OTRF on the nozzle x configuration.

Figure 4.6 shows the sound pressure level evaluated against frequency spectra for both cases. The measurements were taken at the 8^{th} axial Kulite glued into the outer wall. Sound pressure level of the injection case behaves quite similar to that when there is no injection. The only apparent difference is observed at 620Hz when the injection noise give a precipitous rise in amplitude. The peak at 3900Hz is captured by both cases. The noise levels vary insignificantly at the higher frequencies, while peaks at the lower frequencies are matched. That means that the injection system noise has no effect on the noise level and requires no further investigation.

4.3.2 Generation of Entropy Noise by EOTDF Temperature Profile

The generation of entropy noise as shown in Chapter 2 requires the fulfilment of two conditions. First, the inhomogeneity of entropy field achieved by spatial and temporal variations of combustor exit temperature profile, and second, the acceleration of the mean flow which propagates temperature variations downstream. In the OTRF, it is possible to generate spatial temperature variations of the EOTDF temperature profile by injecting coolant air into the mainstream flow of hotter temperature. The acceleration of the flow is investigated on the nozzle x configuration. The flow is undergoing a rapid acceleration from Mach number 0.1 to 0.9 for the subsonic condition within a short distance of 63.5mm

of the NGV section reaching its maximum value at the nozzle throat. The slight deceleration determined by the diffusion is generally neglected.

Figure 4.7 shows the measured EOTDF and uniform temperature profiles evaluated against radial distance. The measurement plane was located 29.5mm upstream of the stator blade leading edge. The temperature variations were normalised over the area-averaged mean temperature. It is observed that the EOTDF temperature profile is characterised by more than 0.4 temperature variation between the 'hot spot' and the case wall. The uniform temperature profile is on the contrary quite homogenous with minor temperature variations of no more than 0.01 appearing near the walls due to the viscosity effects.

The dynamic pressure fluctuations were measured at the case wall of the duct extension for both temperature profiles with the nozzle x configuration installed. The data from seventeen axial Kulite pressure transducers were processed to make an estimate of the noise level generated by temperature inhomogeneities. Applying Fast Fourier Transform to the unsteady static pressure signal allowed to evaluate the sound pressure level against the frequency domain. The higher frequency limit is 50kHz being imposed by the transducer capabilities. The lower frequency limit was set at 10Hz by the data processing procedure described in section 1 of this chapter.

Figure 4.8 demonstrates the sound pressure level for the EOTDF and uniform temperature profiles over frequency. The measured location was chosen at the 8^{th} axial Kulite. This is because it is glued into the case wall thus avoiding the additional instrumentation noise appearing due to the impossibility to perfectly fit the transducer to match the curvature of the casing wall. The subsonic flow conditions of 0.9 Mach number were maintained for

seven independent facility runs. The averaging of the sound pressure levels for all the runs was performed.

The EOTDF temperature profile is noisier than the uniform. Its estimated sound pressure level is approximately 5dB higher in the range of frequencies up to 4500Hz. The general distribution behaviour of the sound pressure levels along the frequencies is similar for both temperature profiles. The multiple tones are located at the same frequencies.

Notably, the tone at 880Hz appears only in the EOTDF case. It is observed in the background noise data presented in section 3.1, but appears to be shifted to the higher frequency. Its value is approximately 6dB. The tone could be generated by the injection system and its frequency shift to be caused by an increase in the mean temperature of the flow. A substantial tone appears at 4.5kHz in both temperature profiles. The noise difference in the frequencies higher than 4.5kHz is shown to be insignificant. The relatively smooth sloping behaviour of the sound pressure levels measured at such a downstream location indicates that a lot of observed tones and rapid fluctuations amplitude increases can be caused by the boundary layer experiencing a constant growth with the propagation of the flow though the nozzle duct extension.

Figure 4.9 shows the sound pressure level for the EOTDF and uniform temperature profiles measured at the 17^{th} axial Kulite. This is the last pressure transducer upstream of the nozzle exit, thus it evaluates the sound pressure level more likely to be propagating outside the working section of the nozzle. The observed sound pressure level difference is evaluated to increase as the flow propagates downstream and reaches approximately 10dB within the frequency range from 10 to 1500Hz, the frequency range of the entropy noise generation. From 1500Hz the noise difference becomes less significant only drastically

increasing at the frequency range from 10kHz. These are the frequencies at which the instrumentation noise generally appears. Furthermore, as shown in Figure 4.8 the temperature difference produces no noise increase when the pressure transducer is fitted flush with the curvature of the outer wall. The observed rapid amplitude changes can be separated into two groups – those appearing in both temperature profiles and those characteristic to the EOTDF temperature profile only. The first are tones at 1500, 3000, 4500 and 9000Hz. They are evaluated to have a similar sound pressure level with the EOTDF temperature profile being consistently noisier and in addition causing a slight shift in frequencies. The second group tones are those at 880Hz and 3500Hz. These tones appear consistently at the same frequencies and further signify the influence of entropy noise since they are most likely to be produced by a coherent addition of two or more correlated noise sources although their generation must be investigated separately. The rapid noise increase at approximately 35kHz is certain to be caused by imperfect fitting of the transducer and can be neglected.

Taking into account the noise source analysis presented in Chapter 3 as well as background and boundary layer noise estimations performed, it can be concluded that the observed sound pressure level difference is a product of temperature variations engendered in the EOTDF temperature profile and their acceleration through the nozzle causes the generation of entropy noise. It is worth noting that the EOTDF temperature profile is evaluated to have large temperature variations in the circumferential direction produced by the coolant air injected through the baffles. Although these variations are less pronounced than those in the radial direction, they also account for the entropy noise generation. Such a large noise difference in the projected range of entropy noise

frequencies confirms the worries expounded by many aeroacousticians concerning the influence of entropy noise in the real engine and makes the current investigation in the OTRF more significant.

4.4 Influence of Temperature Difference on Entropy Noise

Following the analytical description presented in Chapter 2 it is observed that entropy noise is proportional to the temperature difference between the 'hot spot' and its environment. Moreover, the proportionality of dynamic pressure fluctuations downstream and temperature difference upstream is shown to be linear. Thus, the easiest way to identify and quantify entropy noise is to perform sound pressure level measurements for the EOTDF and uniform temperature profiles with different area-averaged mainstream temperatures.

To generate three different EOTDF temperature profiles the mainstream temperature was varied with a step of 32K keeping the coolant air temperature of the injection flow the same. Figure 4.10 shows three generated temperature profiles for different area-averaged mainstream temperatures. Temperature is evaluated against the radial pitch. The 'hot spot' temperature is lowered from 530K for 444K area-averaged EOTDF temperature profile to 450K for that of 380K. The temperature gradients vary insignificantly near the casing wall due to the maintained coolant air temperature. Applying these temperature profiles and their uniform analogues to the nozzle x configuration will allow a validation of the entropy noise generation in the OTRF. The distribution of temperature against the radial pitch for the uniform temperature profiles was not carried out since it is predominantly uniform.

Figure 4.11 presents the sound pressure levels against frequencies for the EOTDF temperature profiles at three chosen area-averaged temperatures. The subsonic condition of Mach number 0.9 was achieved at the nozzle. The data was processed for the frequency range from 10 to 10 000Hz avoiding the higher frequencies beyond interest. The measurement is taken at the 17th axial Kulite evaluating the noise propagating out of the nozzle.

It is observed that sound pressure levels for three temperatures grow steadily with an increase of the temperature difference. At the low frequency of 100Hz entropy noise is so influential that it leads to generation of additional 10dB when the mean temperature is augmented from 380K to 444K. This trend is noticeable within the frequency range of aeroacoustics interest. The sound pressure level being evaluated in decibels shows an increase that might be following a logarithmic trend when the mean temperature is varied with the constant temperature increase of 32K. That proves the linear dependence of dynamic pressure fluctuations of entropy noise on the temperature difference at the combustor exit.

Moreover, the dynamic pressure fluctuations amplitude increases at 1500, 2900, 4500 and 9000Hz are maintained when the mainstream temperature is varied. An increase in temperature of the 'hot spot' means that it is propagating faster, thus causing a slight shift of these amplitude rises in the frequency domain, from the Strouhal number definition. The sharp amplitude rises at 4500 and 9000Hz for 444K EOTDF temperature profile are visibly contrasting with those of 380 and 412K cases. This may be explained by an increasing predicament to match the chosen boundary conditions in the OTRF at such a high mainstream temperature.

Notably, the rapid amplitude increase at 870Hz is not only intact at the three EOTDF temperature profiles but it also has the similar sound pressure level. Chapter 5 demonstrates the results showing that it is of the same value for both nozzles. When operated with the uniform temperature profile it disappears. The LES numerical prediction as shown in section 6 of this chapter also captures it.

Figure 4.12 shows the sound pressure levels measured for the uniform temperature profiles at the same area-averaged temperatures. The measurements were taken at the same Kulite with the same flow conditions applied to the nozzle. No significant difference is observed in the frequency range implying that a change in the mainstream temperature has no effect on the sound pressure level generation. The frequency and amplitude values of sharp rises are constant for all the temperature profiles.

The investigated uniform temperature profiles are distinguished by an insignificantly small ratio of temperature difference between the 'hot spot' and its environment to the mean temperature, whereas the EOTDF temperature profiles with the mean temperatures of 380K, 412K and 444K are characterized by the temperature difference ratio of 0.28, 0.37 and 0.46 respectively. From figures 4.9, 4.11 and 4.12 It is further observed that the sound pressure level difference associated with entropy noise is substantial only when the temperature difference ratio is getting close to 0.5 and is experimentally evaluated to have little influence on the overall noise level when the temperature difference ratio is less than 0.25. Thus, it might be concluded that in order to carry out a successful experimental investigation of entropy noise the temperature difference ratio should be at least 0.25, entailing that for a flow of, for example, 400K, the difference between the 'hot spot' and the wall region should be of no less than 100K.

The engine turbine stage is often operated with subsonic flow conditions, but the generation of entropy noise in the sonic and supersonic flow is getting particular attention because at such high Mach numbers entropy noise is evaluated to be the most important source of all the aerodynamic sounds. This encompasses vortex sound produced by rotational kinetic energy, entropy noise and a type of the turbine noise generated by thermal viscosity and diffusion.

Not only the OTRF allows a generation of different EOTDF temperature profiles with a possible increase of the temperature difference between the 'hot spot' and its environment, but it also can operate under varying Mach numbers by adjusting the choked second throat located outside the working section of the nozzle.

Figure 4.13 shows the sound pressure levels for the EOTDF temperature profile at three area-averaged temperatures for the sonic flow condition of Mach number 1. The measurements were taken at the 17^{th} axial Kulite evaluating the sound propagating out of the nozzle.

Just like for the subsonic case, the sound pressure level increases with an increase of the area-averaged temperature. The sound pressure level difference of 10dB is observed between the EOTDF temperature of 380K and that of 444K. This difference is maintained in the frequency range associated with entropy noise and at the frequencies higher than 1000Hz it diminishes down to 5dB, providing another proof that entropy noise is particularly influential at the lower frequencies. The similarity of sound pressure levels behaviour is present all along the frequency range from 10 to 50 000Hz including the sharp rise at 1500, 2900, 3800 and 4500Hz. They correspond well to the abrupt amplitude changes observed at the subsonic Mach number conditions. And just like in the Mach

number 0.9 flow condition, the EOTDF temperature profile of 444K gives a slight mismatch. This is determined by the restriction on the facility. The sharp rise at 880Hz is also present. The only significant difference is the sharp rise at 9000Hz, it was evaluated as having the noise level of approximately 93dB at the 0.9 Mach number flow condition, but at the sonic flow it disappears entirely. The measurement sound pressure level at this frequency range is 85dB.

Figure 4.14 demonstrates the sound pressure levels for the uniform temperature profile at three area-averaged temperatures. The flow conditions are sonic of Mach number 1. An approximately 5dB difference is noticeable at the lower frequency region up to 700Hz. At the higher frequencies the sound pressure levels are matched with a slight frequency shift for the 444K case. The amplitude changes are similar to those of Mach number 0.9 condition with one at 9000Hz showing a slight increase. The sound pressure levels match well even at the higher frequencies, proving the validity of the acquired data. There is a substantial difference for the uniform temperature profiles of sonic flow conditions as oppose to the subsonic especially in the lower frequencies. That can be explained by the presence of the shock. Entropy and vorticity inhomogeneities passing the shock experience a change in their intensity and the shock starts emanating entropy and vorticity waves serving a source of entropy noise and vortex sound correspondingly (Landau & Lifshitz, 1987). The sonic conditions in the OTRF were reached with a shock at the region of the throat and the injection system is evaluated to generate a significant vorticity in the flow (Chana, 2013). The vorticity inhomogeneities passing the shock cause an additional noise, vortex sound, propagating downstream. Thus, entropy noise is evaluated to be more influential at the low Mach number flow conditions. This is anticipated because the

acceleration is taking place over a larger distance for the sonic case, entailing that shear stresses determined by entropy inhomogeneities do not experience such an abrupt change as those at the subsonic flow case. Therefore, the smaller fluctuations of shear stresses produce a weaker acoustic response.

4.5 Entropy Noise at Different Mach Number Flow Conditions

The entropy noise investigation in the OTRF was performed not only for different mean mainstream temperatures but also for four different Mach number flow conditions achieved in the nozzle. They were varied from the subsonic of Mach number 0.8 to the supersonic of Mach number 1.1. This was made possible by changing the static pressure conditions at the second throat of the facility.

Figure 4.15 shows the measured sound pressure levels of the uniform temperature profile for four Mach number cases. The measurements were taken at the 17^{th} axial Kulite. The Mach number 0.8 flow condition produces the largest acoustic response with 100dB sound pressure level at 100Hz. When the Mach number is increased to 0.9 the sound pressure level is reduced by approximately 5dB to 95dB at 100Hz and general decrease of the noise level in the lower frequencies is noticeable. When the flow conditions are augmented to the sonic, the general sound pressure level changes slightly, whereas at Mach number 1.1 a significant decrease in noise level follows especially at the frequency range from 10 to 200Hz. The multiple tones at frequencies above 1kHz are shifted slightly at higher values with an increase of Mach number.

Figure 4.16 demonstrates sound pressure levels of the EOTDF temperature profile for the same Mach number conditions. The order in which cases are located in the sound pressure

level domain is the same. The noisiest is the Mach number 0.8 case with a substantial increase in sound pressure level determined by the entropy noise generation compared to that of the uniform case. The sound pressure level at 100Hz is 110dB. The Mach number 0.9 and Mach number 1 fluctuations show a similar acoustic response against the frequencies with only a slight entropy noise generation. Thus, the noise difference between subsonic Mach number 0.8 and sonic Mach number 1 flow conditions is larger for the EOTDF temperature profile than for the uniform. The quietest flow condition is evaluated to be supersonic with Mach number of 1.1. Surprisingly, the noise level at 100Hz is 80dB which is lower than that of the uniform case. This may be explained by the interaction of incident entropy waves with the shock and warrants further investigation. Similar to the uniform cases presented in Figure 4.15, the tones experience a shift with an increase of the flow velocity. The rapid amplitude increase at 880Hz is observed at Mach number of 0.9 and 1.0 flow conditions only.

Thus, it can be concluded that entropy noise is influential at subsonic flow conditions of Mach number 0.8 and 0.9 and is evaluated to diminish with an increase of the flow velocity and thus much less at the supersonic conditions.

4.6 Comparison of OTRF Experimental Data and LES Numerical Prediction

The numerical procedure described in Chapter 6 allows to perform LES numerical predictions of the flow field for the nozzle x configuration with the EOTDF and uniform temperature profile imposed at the inlet. A very good match of the experimentally measured and numerically modelled inlet EOTDF temperature profile was achieved. This

provided a tool for further investigation of sound pressure level produced downstream by the temporal and spatial temperature variations upstream.

To perform a sound pressure level comparison of the LES prediction with the processed OTRF experimental results, the numerical simulation was required to generate a time varying static pressure signal, that can be transformed into the sound level evaluation within the frequency domain using the Fast Fourier Transform. In this regard, LES prediction of the nozzle x computational model with the EOTDF and uniform temperature profiles of the 444K area-averaged temperature of the flow was performed. The Mach number distribution along the computational model was matched with the flow condition achieved in the experiments. The higher frequency limit in the unsteady simulation is determined by the specified time step, while the lower limit is achieved by processing a signal of sufficient time length. To match the frequency limits of the LES prediction with the frequency band of the OTRF experimental data acquired with Kulite pressure transducers, a relatively small time step of 1e-5s for 10 000 consecutive static pressure values was required. Overall, the numerical simulation was performed for 12 000 time steps to allow first a solution convergence to be achieved. This allows the quantification of the sound pressure levels in the frequency range from 10 to 50 000Hz. The unsteady calculation was performed using a CPU of 3.6GHz with 4 cores and required one terabyte of memory. The numerical data was taken at the axial position corresponding to the location of the 12^{th} axial row Kulite pressure transducer to avoid potential flow field disturbances produced due to the exit boundary conditions and mesh skewness.

Figure 4.17 shows the comparison of the sound pressure level measured experimentally in the OTRF with the LES numerical prediction for the EOTDF temperature profile. It is

observed that the LES prediction generally shows the same sound pressure level distribution over the frequency range as the experimental data. The lower frequency band is quite similar up to 200Hz after which LES predicts several sharp static pressure amplitude variations not being measured in the OTRF. The rapid amplitude increase at 880Hz measured in the OTRF for the EOTDF temperature profile is the only one that appears in the LES prediction but, with a larger amplitude value. In addition, the sharp amplitude increase at approximately 4500Hz is captured by LES. The sound pressure level over the frequency band between these amplitude increases also shows a good agreement. The apparent difference at the frequencies higher than 8000Hz can be explained by imperfect fitting of the Kulite pressure transducer. Appearance of some other differences in sound pressure level might be ascribed to the fact that the LES prediction was performed using a computational model which reproduces the hardware working section starting from the measurement plane, and the full combustion chamber with radial slots at the walls and circumferential baffles was discarded preventing a realistic numerical assessment of such important parameters as vortex shedding in the wake of the baffles and flow mixing occurring due to the air injection. These parameters modify the sound pressure fluctuations, the former in particular, since this is vortex sound.

Figure 4.18 shows the comparison of the sound pressure level for the OTRF experiment and LES prediction evaluated for the uniform temperature profile. The numerical prediction shows lower sound pressure level than experimental data in the frequency band of the entropy noise generation with notable sharp amplitude increases measured in the OTRF not being predicted by the LES procedure. In the range of 100-1000Hz where entropy noise is more influential the sound pressure difference is more than 5dB. This discrepancy

in the results might be explained by the absence of the precise two-dimensional experimental data for the uniform profile temperature distribution in the radial and circumferential directions. Another possible explanation is that the experimental measurements were taken at the outer wall of the facility, while in the LES prediction the sound pressure level was evaluated in the mainstream, thus the appearing tones and additional noise is the result of the boundary layer effects. The observed difference of 5dB accounts for less than 1Pa in dynamic pressure fluctuations at such a low noise level. Moreover, the computational model does not fully represent the working section of the facility. The EOTDF temperature profile modelling required the matching of the experimental and numerical temperature profiles at the plane related to the thermocouples location, and thus the modelling of the inlet section of the facility was avoided, preventing a fully realistic reproduction of the flow acceleration. The Mach number distribution for the LES prediction was matched with that of the OTRF experiment.

Figure 4.19 presents the sound pressure level evaluation for the EOTDF and uniform temperature profiles obtained with the LES prediction. This evaluation corresponds to the experimental results presented in section 3 of this chapter. The numerical modelling estimates entropy noise to be quite influential in the frequency range from 10 to approximately 2000Hz. The evaluated difference in sound pressure level is more than 10dB. The rapid pressure fluctuations amplitude increase at 880Hz only present in the EOTDF temperature profile also appears in the LES prediction. Compared with experimentally measured results, the numerical calculation shows an additional noise in the form of sharp amplitude increases being generated from 150 to 800Hz. In addition, the rapid increase at approximately 4500Hz measured experimentally for both temperature

cases is numerically captured for the EOTDF temperature profile only. The sound pressure level in the higher than 10 000Hz frequency band is matched for both temperature profiles, entailing that entropy noise has no effect on such high frequencies and that the observed noise level difference between the experimental and numerical data must account for the appearance of additional instrumentation noise. Neglecting the apparent sound pressure level difference at 4500Hz experimentally shown to be insignificant, it can be concluded that the entropy noise generation is confined to the lower frequency range of 10-2000Hz and can lead to the general sound pressure level increase of approximately 10dB.

4.8 Comparison of Experimental and Theoretical Evaluation of Entropy Noise

Figure 4.9 presents evaluation of entropy noise generated by the EOTDF temperature profile in the nozzle x configuration for the subsonic flow conditions. It is observed that entropy noise is influential at the low frequency range from 10 to 2000Hz. Chapter 2 gives a theoretically evaluated acoustic power of entropy noise generated in a NGV only section. The nozzle x configuration used in the OTRF experimental investigation was modelled from a typical vane with achieving the same rate of the flow acceleration. Thus, a possibility to compare acoustic power generated in the nozzle x configuration in the OTRF experiments with the theoretical evaluation arose. The difference between the sound pressure level observed in the EOTDF temperature profile and that measured for the uniform temperature variation was rearranged to produce an acoustic power estimate.

Figure 4.20 presents the comparison of acoustic power for the OTRF experimentally measured and theoretically evaluated entropy noise. The acoustic power for both cases is generally shows a good match especially considering that the theoretical evaluation was

performed for a generic nozzle. The theoretical evaluation produces less acoustic power at the low frequencies up to 80Hz than that evaluated experimentally. At the frequency range from 100 to 1000Hz, the acoustic powers are generally matched, after 1000Hz theoretical acoustic power is larger than experimental power by approximately 0.01W. The largest acoustic power of entropy noise for both evaluations is approximately 0.05W at observed at approximately 100Hz.

4.7 Chapter Conclusions

The experimental investigation of entropy noise was performed in the Oxford Turbine Research Facility with the nozzle x configuration. The injection noise was evaluated using high frequency pressure transducers and shown to be insignificant. At the same time, the EOTDF temperature profile shows a substantial noise difference compared to the uniform temperature profile. The observed difference is largely confined to the lower frequencies where entropy noise is anticipated. In the frequency range from 10 to 1000Hz entropy noise is evaluated to be of approximately 10dB. Three varying EOTDF temperature profiles were investigated. The general increase in sound pressure level with an increase in the temperature difference between the 'hot spot' and its environment is observed, whereas for the uniform temperature profile, a change in the mainstream mean temperature produces no significant noise difference. The data for the three different mean temperatures were evaluated for subsonic flow condition of Mach number 0.9 and sonic of Mach number 1.

Five different Mach number flow conditions for the EOTDF and uniform temperature profiles were investigated. Entropy noise was proven to be more influential at the lower

flow velocities. The developed numerical method of sound pressure level evaluation against the targeted frequency range presented in Chapter 6 allowed to make a comparison with the experimentally acquired results. Sound pressure levels for the EOTDF temperature profile are quite similar, with the tone at 880Hz being of a larger amplitude for the LES prediction. The LES prediction for the uniform temperature profile gives a lower sound pressure level than that measured in the OTRF. This may be explained by the boundary layer effect.

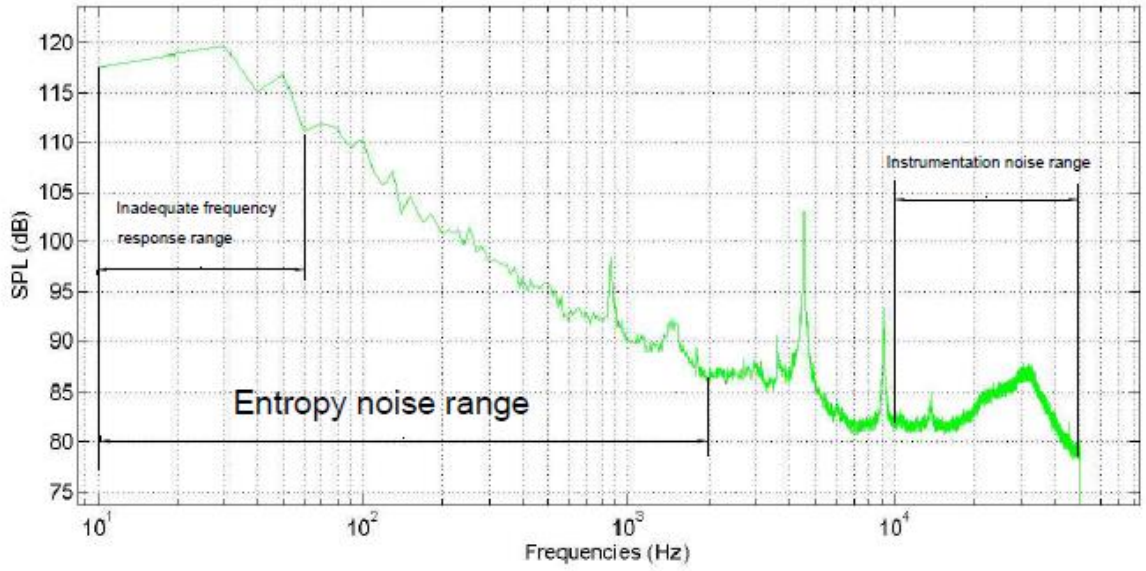

Figure 4.1: Estimated frequency ranges of different noise sources

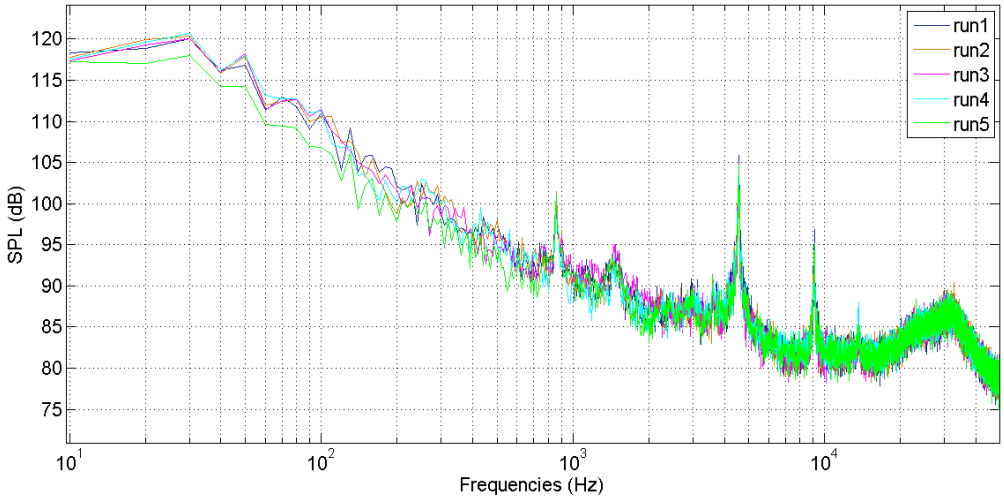

Figure 4.2: Consistency of data for five independent experimental runs

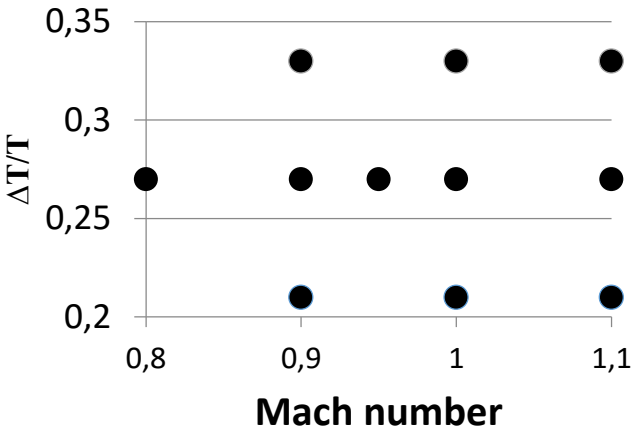

Figure 4.3: Test matrix for the nozzle x investigation

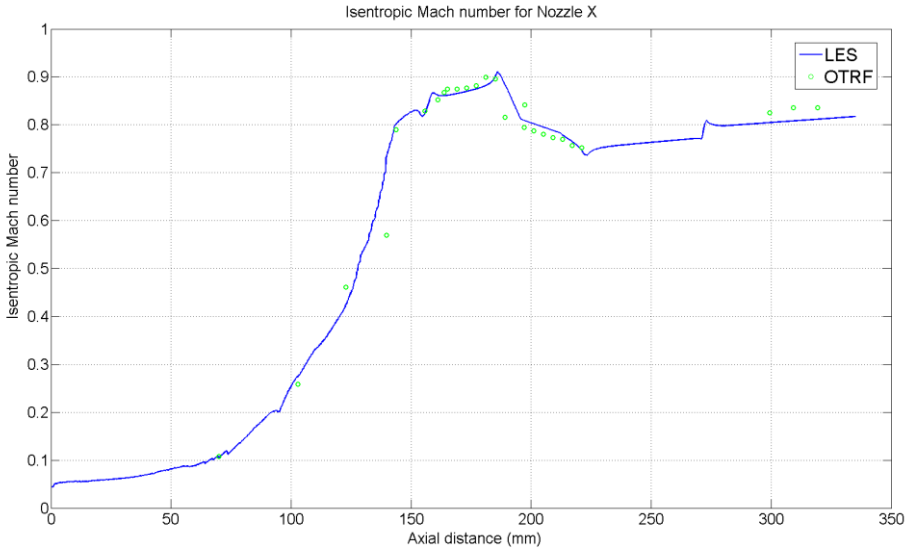

Figure 4.4: Isentropic Mach number distribution along the axial distance

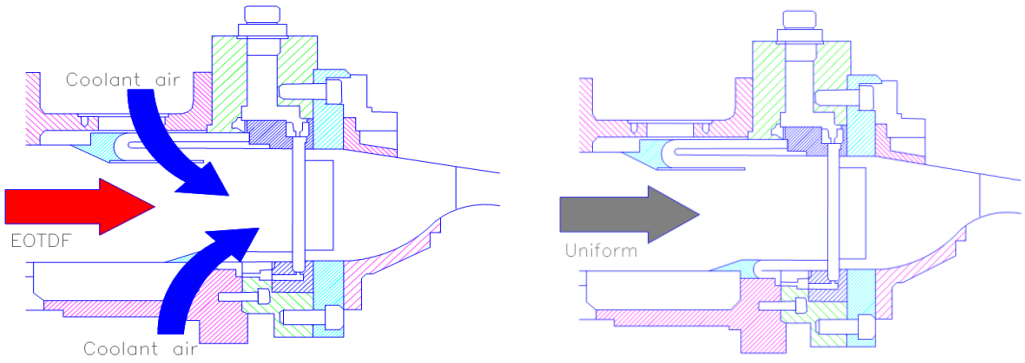

a) *b)*

Figure 4.5: Generation of the EOTDF (*a*) and uniform (*b*) profiles in the OTRF

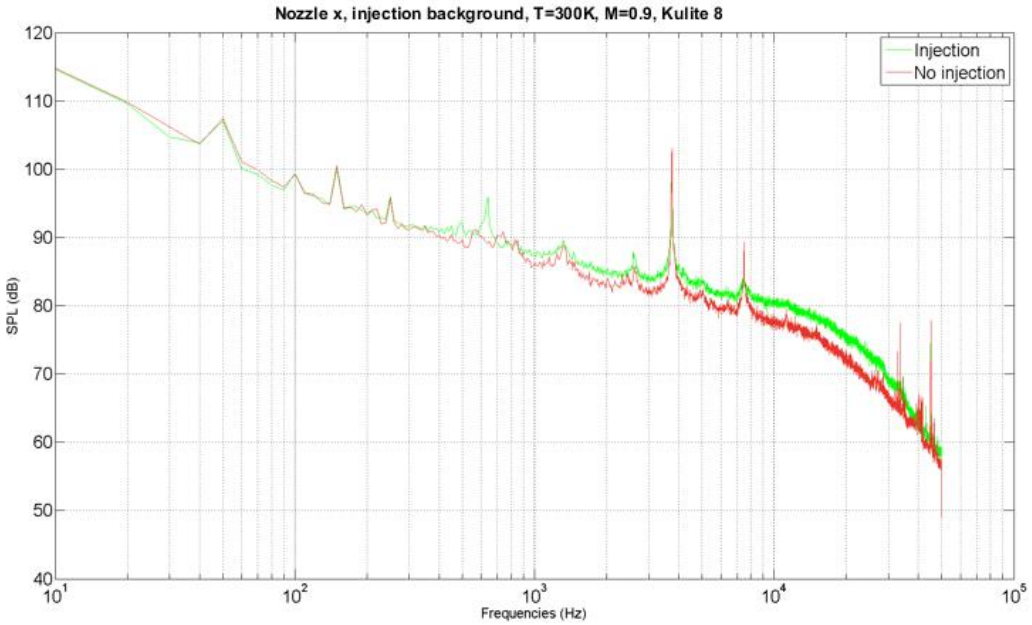

Figure 4.6: Sound pressure level for two background cases

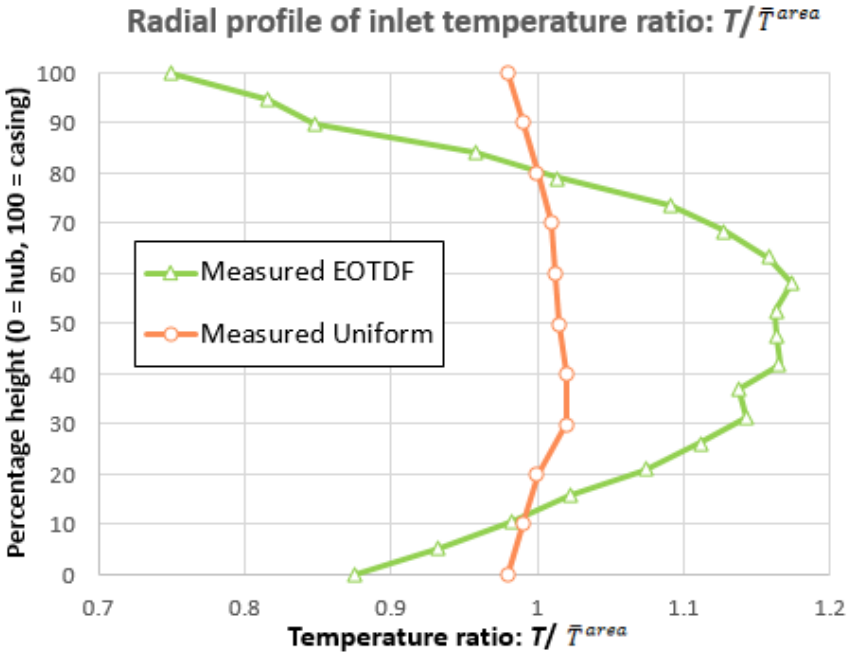

Figure 4.7: Radial EOTDF and uniform temperature profile

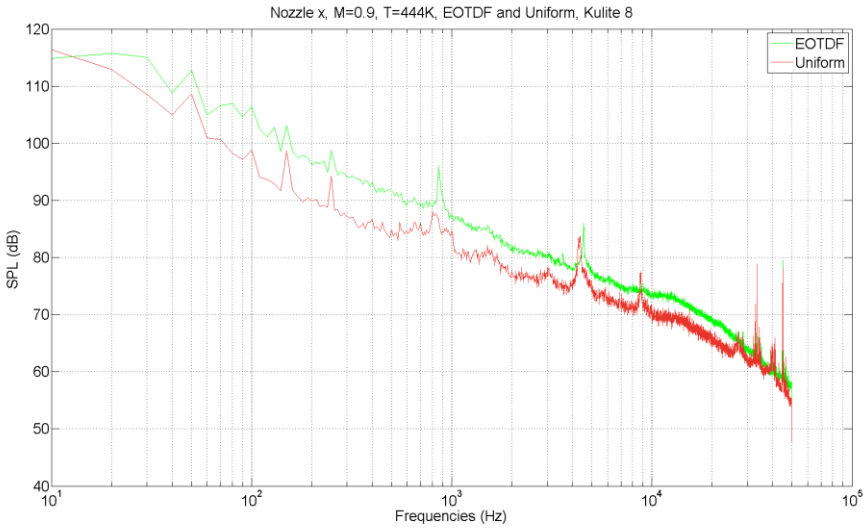

Figure 4.8: Sound pressure level of the EOTDF and uniform temperature profiles at the 8th axial Kulite

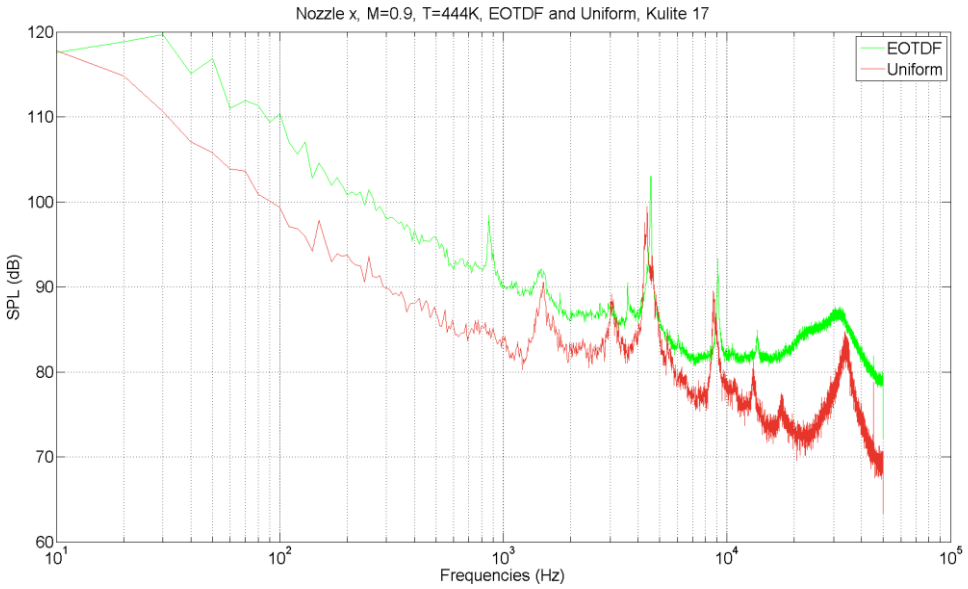

Figure 4.9: Sound pressure level of the EOTDF and uniform temperature profiles at the 17th axial Kulite

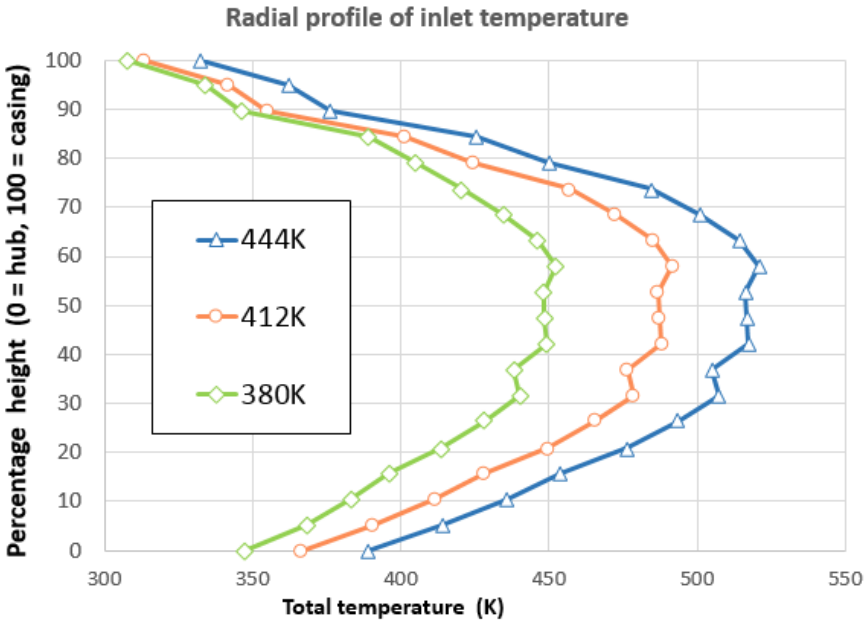

Figure 4.10: Measured EOTDF temperature profiles with different area-averaged mainstream temperature

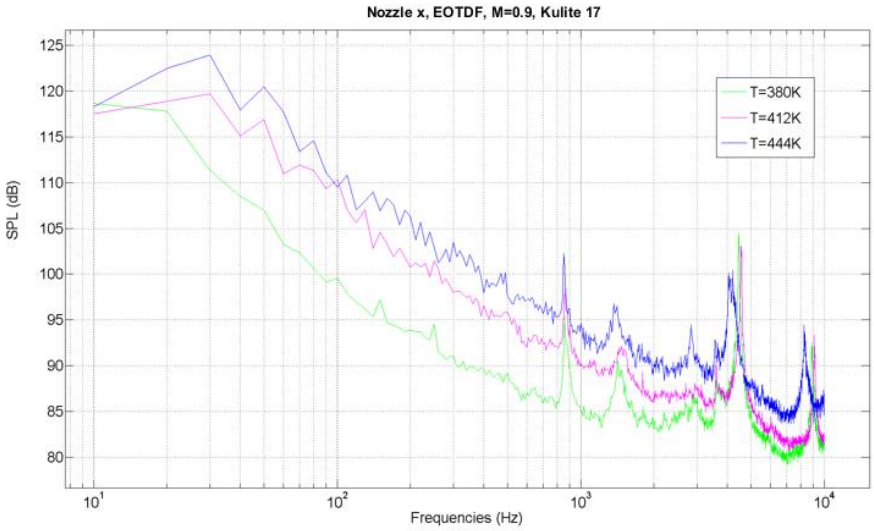

Figure 4.11: Sound pressure levels for the EOTDF temperature profile at three different area-averaged mainstream temperatures for the subsonic flow conditions of Mach number 0.9

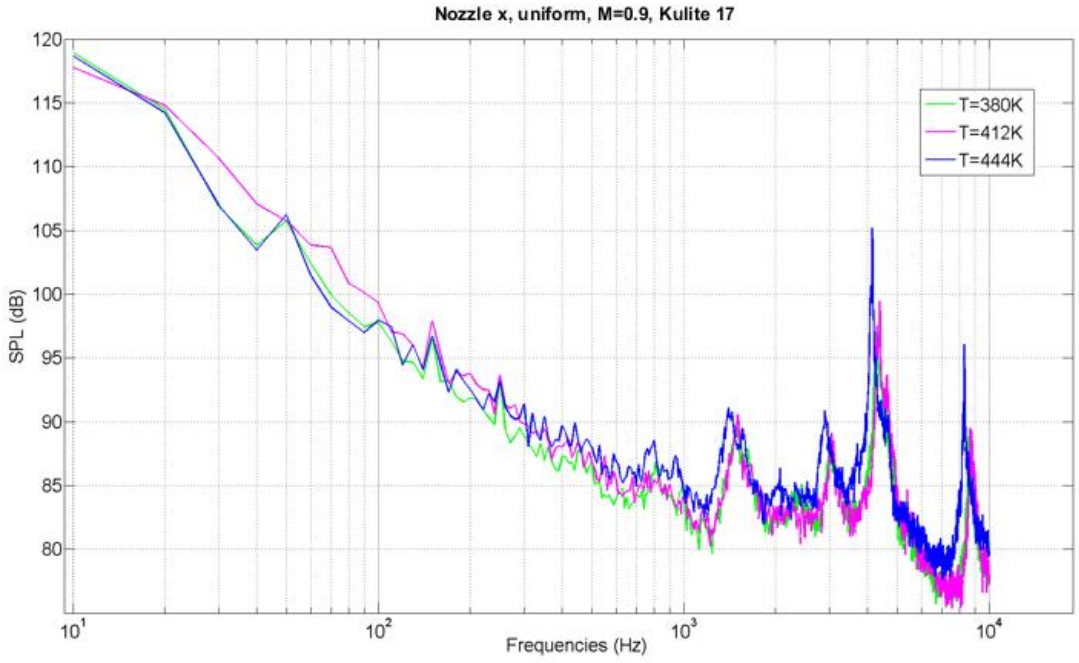

Figure 4.12: Sound pressure levels for the uniform temperature profile at three different area-averaged mainstream temperatures for the subsonic flow conditions of Mach number 0.9

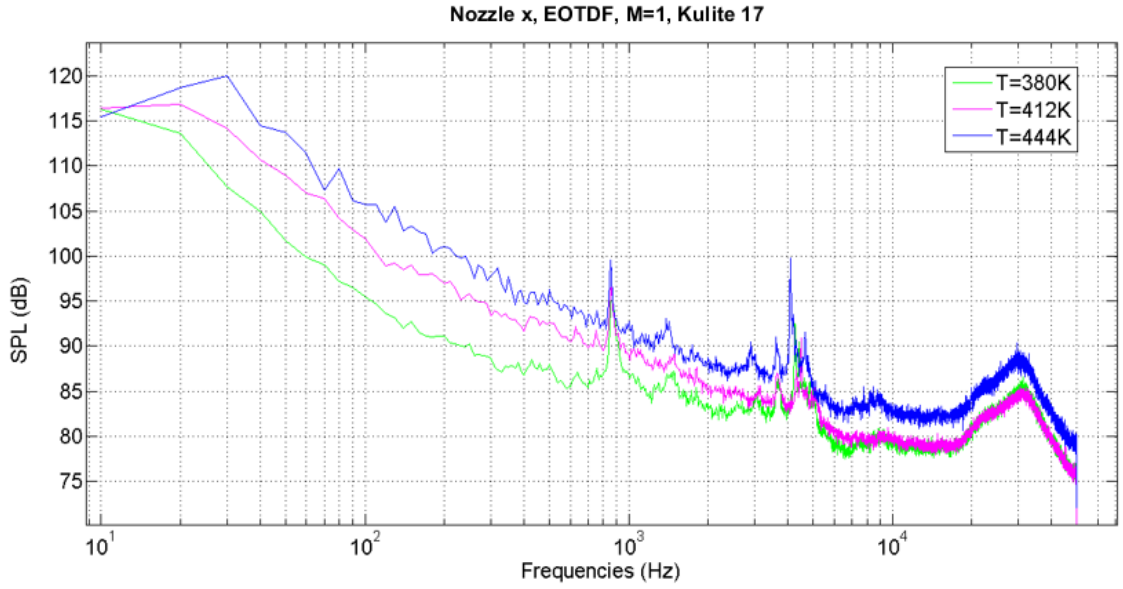

Figure 4.13: Sound pressure levels for the EOTDF temperature profile at three different area-averaged mainstream temperatures for the sonic Mach number 1.0 flow condition

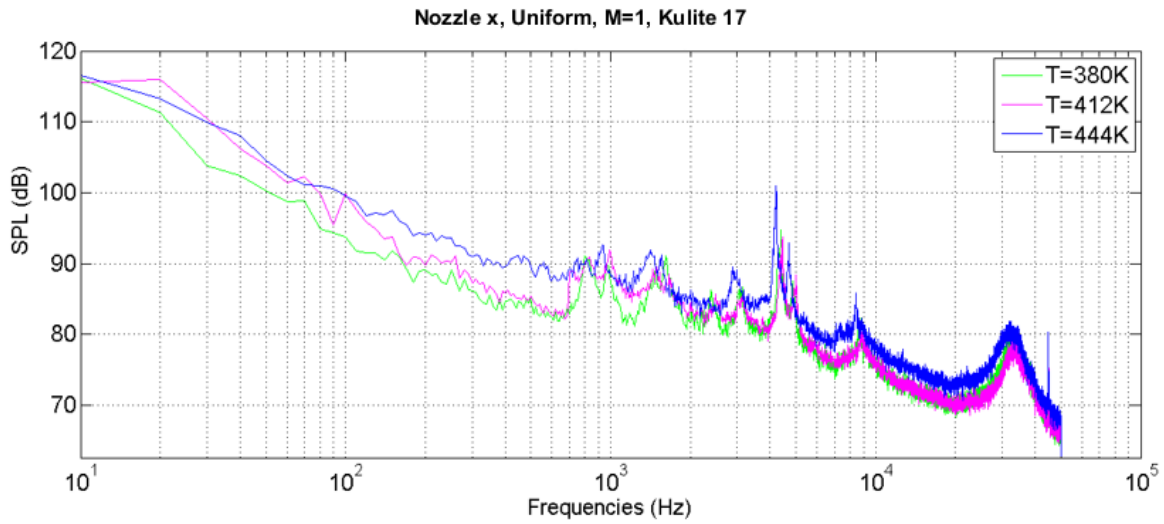

Figure 4.14: Sound pressure levels for the uniform temperature profile at three different area-averaged mainstream temperatures for the sonic Mach number 1.0 flow condition

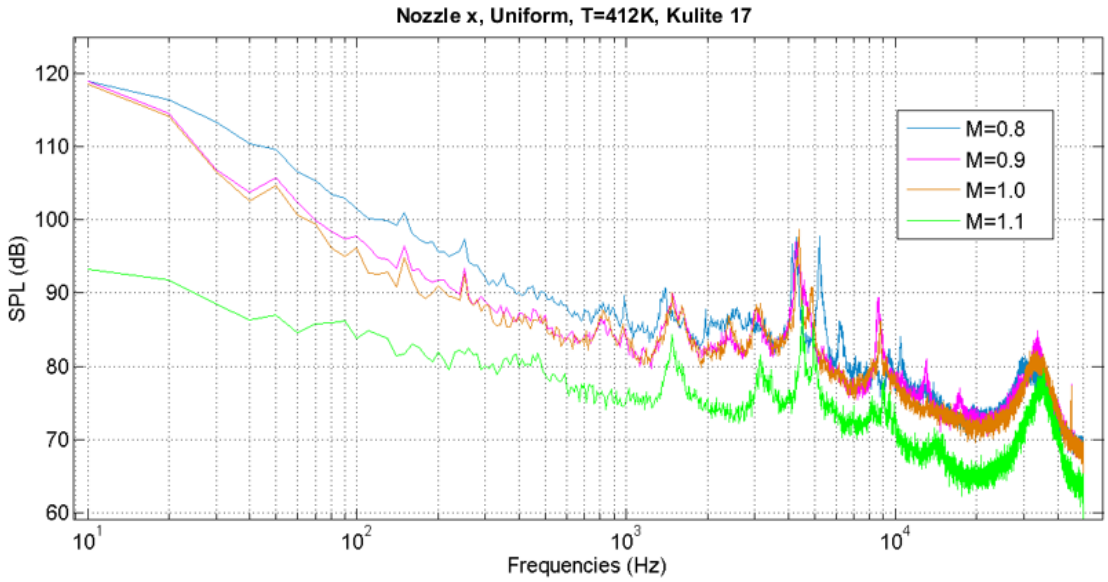

Figure 4.15: Sound pressure levels of the uniform temperature profile for four Mach number cases

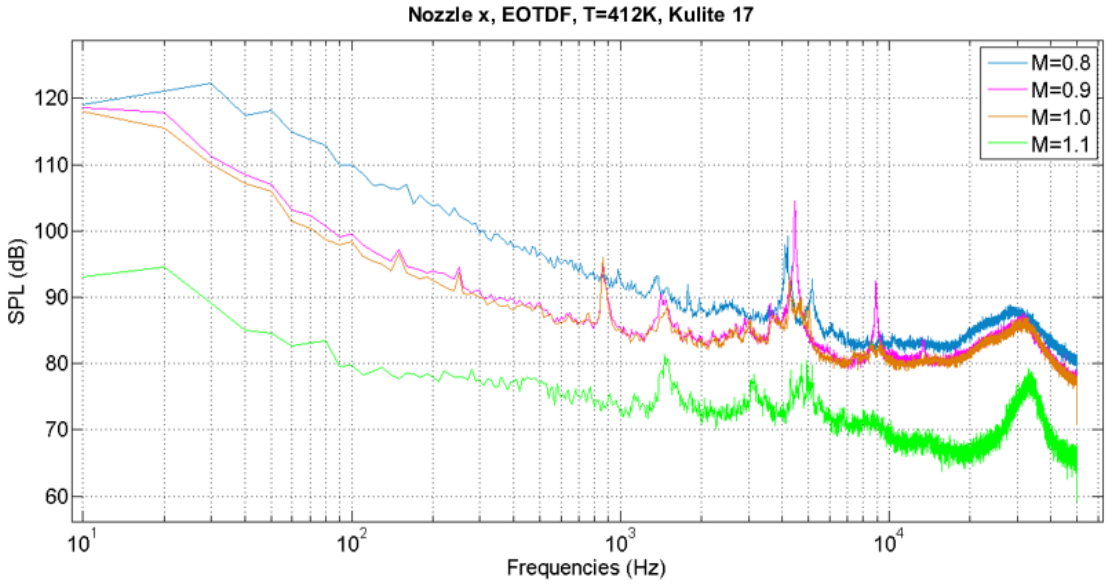

Figure 4.16: Sound pressure levels of the EOTDF temperature profile for four Mach number cases

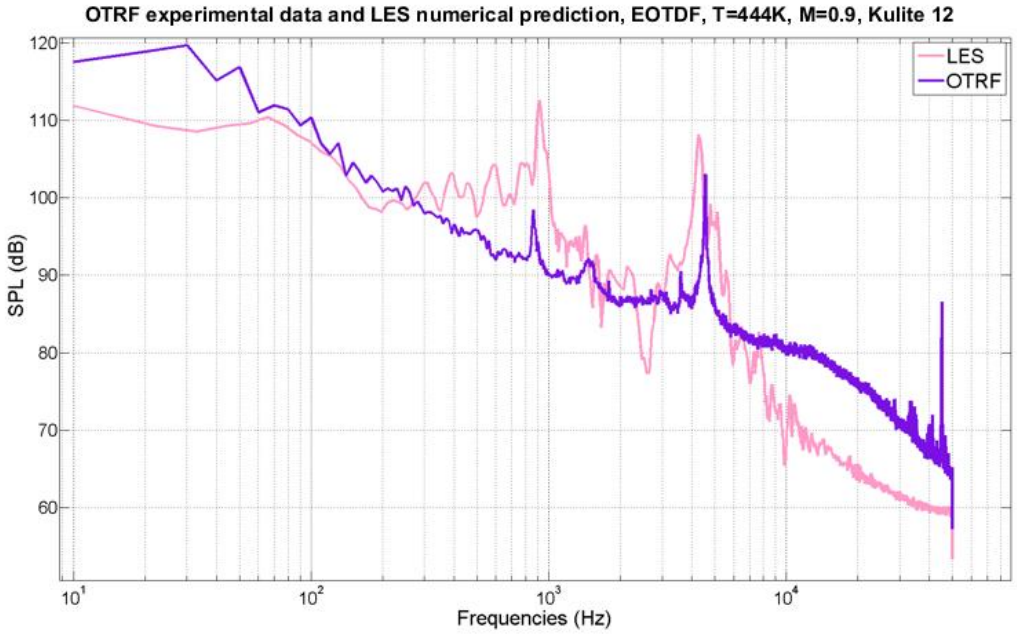

Figure 4.17: Comparison of the OTRF experimental results with LES numerical prediction for the EOTDF temperature profile sound pressure level

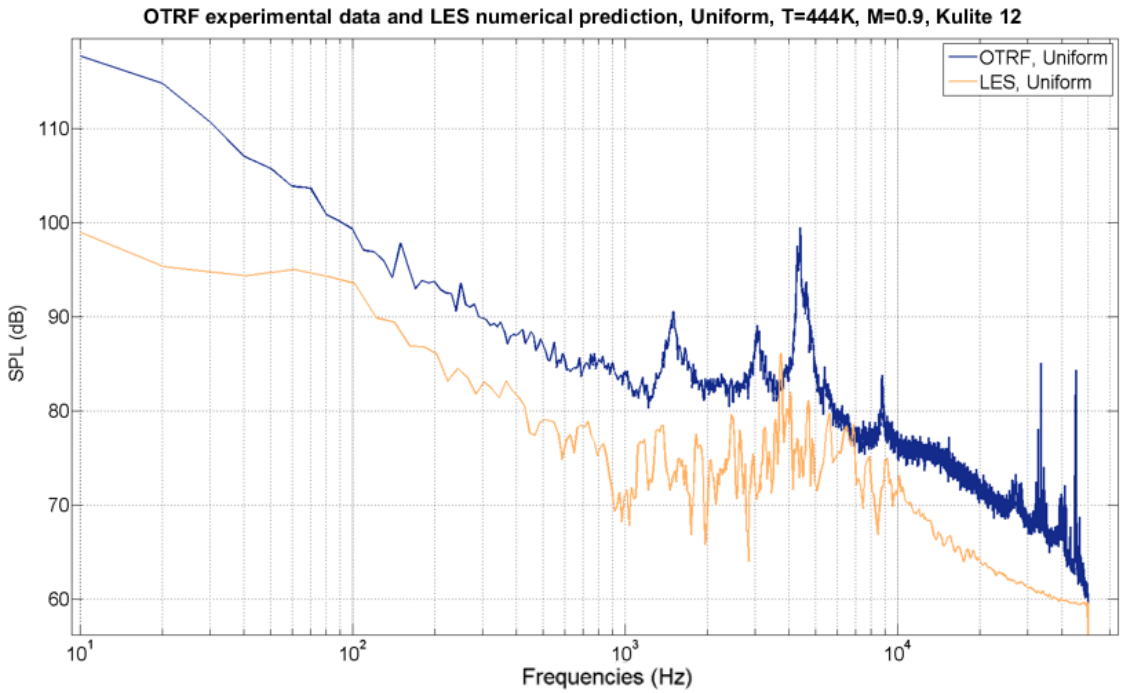

Figure 4.18: Comparison of the OTRF experimental results with LES numerical prediction for the uniform temperature profile sound pressure level

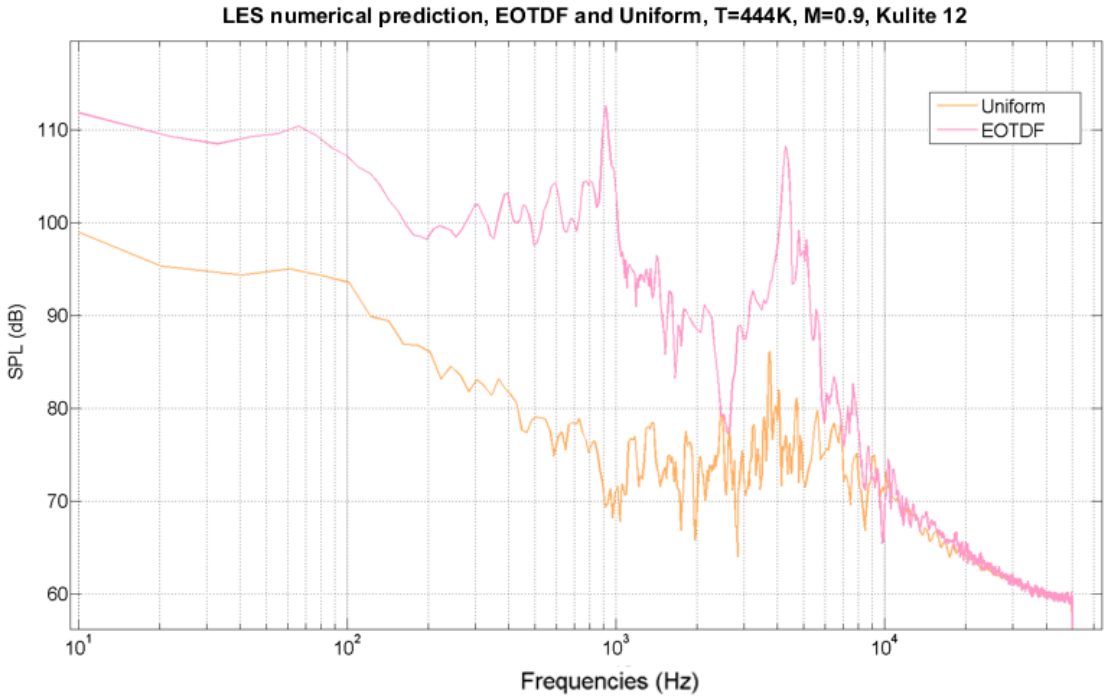

Figure 4.19: Comparison of the sound pressure level of the EOTDF temperature profile with the uniform for the LES prediction

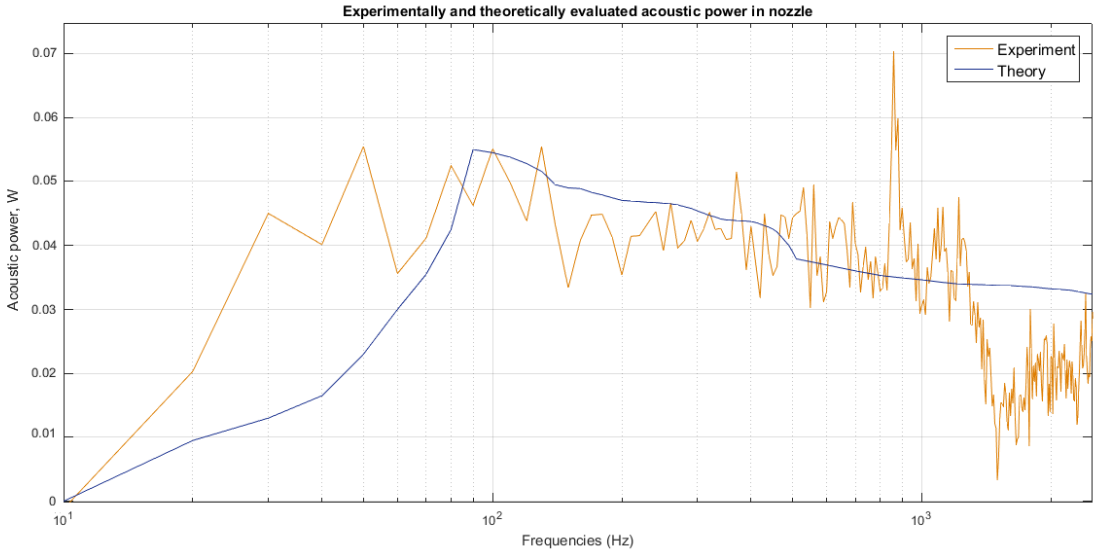

Figure 4.20 Comparison of experimentally and theoretically evaluated acoustic power of entropy noise

Chapter 5

Experimental Investigation of Entropy Noise in the Second Nozzle

5.1 Isentropic Mach Number Distribution for the Second Nozzle

Figure 5.1 shows a comparison of Isentropic Mach number distribution measured at the outer wall for the OTRF experimental results and LES numerical simulation. Experimental data was taken using pressure tappings fitted at the outer wall of the facility. The precise description of their locations is presented in Chapter 3. This allowed to estimate the flow behaviour using the isentropic flow relations. To fully understand the flow behaviour, the same data were taken at the casing wall of nozzle 1.5x using LES predictions. The subsonic conditions were maintained for the nozzle. Figure 5.1 demonstrates a good agreement achieved with the experimental data was achieved. The start of the axial distance measurement was located at the beginning of the inlet section.

The initial Mach number value at the inlet is 0.08 corresponding to the combustor simulator exit value. The NGV region for nozzle 1.5x is characterised by a rapid and steady acceleration. It is worth noting that at the mid-height the flow acceleration is taking place even more quickly because of the nozzle geometry. Figure 3.9 shows Mach number contours for two modelled nozzles with nozzle 1.5x having higher flow velocity value at the mid-height location due to the curved nature of the contours. The measured flow behaviour matches well that the intended Mach number distribution and consequently

nozzle 1.5x modelling was based upon. At the region of the throat the area ratio is constant and flow acceleration stops rapidly, with flow velocity variation being small at the region of the rotor mounting section.

The flow reaches its peak value of 0.9 Mach number within the rotor mounting section before experiencing a sudden deceleration, determined by the presence of the two degree diffusion at the casing wall which increases the area ratio and thus causes a slowing of the flow within a short distance. The constant area measurement duct is located upstream where the flow continues to accelerate in a gradual manner reaching approximately 0.8 Mach number at the exit location.

The LES procedure predicts the presence of abrupt step-like changes in the flow behaviour, this is due to the manufacture tolerances of order ±0.1mm between two neighbouring sections. The absence of smooth transitions between sections means that at the boundary of the casing wall the flow experiences sudden local velocity changes.

Figure 5.2 illustrates the casing wall facility hardware in relation to the Isentropic Mach number distribution acquired with pneumatic pressure tappings. The casing inlet section, the outer wall of the NGV, the rotor mounting section, two degree diffusion, the exit section and extension are installed with tolerance steps of approximately ±0.1mm in the interface region. The reproduction of these features in the CFD shows the unsteady erratic behaviour in these regions. A sudden deceleration at the beginning of the diffusion section is a result of imperfect hardware fitting. Further downstream and within the diffusion section, the flow continues to decelerate, although this slowing of the flow velocity is determined by the area ratio increase. This takes place at the casing wall only, since the hub wall consists of a one piece section extending from the inlet section of the nozzle up

to its exit. The Isentropic Mach number distribution at the mid-height location is not influenced by these imperfect hardware fitting steps; the only affected region is the local casing wall boundary layer.

The successful nozzle 1.5x experiments allow to compare the flow behaviour for both investigated nozzles. Figure 5.3 shows comparison of the isentropic Mach number distribution along the axial distance for nozzle 1.5x and nozzle x. Both measurements were performed for the same subsonic flow condition of Mach number 0.9 using the same pressure tappings located at the casing wall.

The flow behaves the same way for the two nozzles starting from the throat as it propagates downstream. The only apparent difference is within the NGV section where the two nozzles are characterised by different rates of flow acceleration necessary to investigate the dependence of entropy noise sound pressure level on the acceleration rate. The initial Mach number at the exit of the combustor simulator is 0.08, while the first pressure tapping located 70mm downstream of the inlet section shows that the flow in nozzle 1.5x is accelerated to isentropic Mach number of approximately 0.23 propagating twice as quick as in nozzle x. The flow in both nozzles experiences the same small acceleration at the extension region before exiting the working section at a Mach number just above 0.8.

5.2 Entropy Noise in the NGV Section of Two Nozzles

Two Kulite pressure transducers were mounted at the leading and trailing edge of the NGV section. Since in the nozzle configuration the vanes are removed, the notation leading and trailing edge denote the locations where the leading and trailing edge would be located

were the vanes installed. At the NGV section the flow is undergoing a rapid acceleration dictated by a significant change in area ratio. Figure 5.4 presents the sound pressure levels measured at the leading and trailing edge of the NGV section for the nozzle x and nozzle 1.5x configuration. The measurements were taken for the EOTDF temperature profile. There is no change in the noise level for nozzle x at the frequency range where entropy noise is anticipated. The only observed difference is in the higher frequencies, and may be explained by imperfect fitting of the downstream transducer or boundary layer growth. The absence of significant difference can be explained by the geometry of the nozzle x configuration and the locations of Kulite transducers. The nozzle x is design to experience a rapid acceleration at the end of the NGV section upstream of the throat. This is the region where the most rapid acceleration is taking place, and thus entropy noise is generated.

Nozzle 1.5x shows an increase in sound pressure level within the NGV section in the frequencies from 600Hz. The increase in noise is approximately 5dB at 1000Hz and increases at higher frequencies. Moreover, the tone at 880Hz is present in both nozzles even at such an upstream axial location, it is particularly visible at the nozzle 1.5x configuration. At the trailing edge the tones for both nozzles are evaluated to have the same noise level. The presence of noise difference in the nozzle 1.5x configuration is anticipated because the nozzle was designed to have a steady acceleration dictated by a decreasing area of the working section. At the axial distance between leading and trailing edge some entropy noise is being generated.

It can be concluded that a noise difference appears at the NGV section between two nozzle configurations. This is due to different flow acceleration rates achieved in two nozzles. The

observed sound pressure level difference is approximately 10dB at the lower frequencies. This is potentially entropy noise.

Figure 5.5 shows the sound pressure levels for two investigated nozzles evaluated at the leading and trailing edge pressure transducers with the uniform temperature profile generated in the combustor simulator. The nozzle x configuration shows only a slight increase within two tones at the frequency range from 500 to 1000Hz and generally produces no additional noise. The generation of the uniform temperature profile at the nozzle x configuration predictably gives no entropy noise because in this case not only there is no temperature difference in the flow but also the geometry of the nozzle prevents to generate any additional noise in the distance between two Kulites.

Nozzle 1.5x configuration gives a substantial increase in sound pressure level in frequencies higher than 600Hz, the behaviour is similar to that for the EOTDF temperature profile. At the tones region the sound pressure level increase within the NGV section is evaluated at a 10dB level. The tone at 880Hz is predictably absent. Notably, the general sound pressure levels are similar and at the trailing edge location the noise difference becomes insignificant in all the frequency ranges. The observed difference for the uniform temperature profile is only confined to the region of two tones and can be explained by the additional noise generated by the rotational kinetic energy.

Notably, the general sound pressure level difference between two nozzles is less at the trailing and leading edge altogether for the EOTDF temperature profile than for the uniform entailing that entropy noise is generated in this region.

5.3 Entropy Noise Generation due to Different Acceleration Rate of the Nozzles

Two investigated nozzles are characterised by different acceleration rates confined to the NGV section with mass flow rate at the outlet being the same. As shown in Chapter 2 the generation of entropy noise requires two prerequisites: first, the spatial or temporal temperature variations accounting for the appearance of additional stresses, fluctuation of which produces an acoustic response; second, a change in static pressure distribution allowing temperature fluctuations in the entropy mode to transform themselves into the acoustic mode and generate noise. The change in static pressure distribution is caused by acceleration of the flow occurring in the NGV section. Thus, two nozzles investigated having different acceleration rates when operated with a non-uniform temperature profile should produce a difference in the noise level corresponding to the entropy noise optimization achieved by a change in acceleration rate of the flow. Alternatively, when operated with a uniform temperature profile two nozzles are supposed to generate the same sound pressure level. The experimental investigation was based on two temperature profiles, EOTDF and uniform, generated upstream of nozzle x and nozzle 1.5x configuration.

Figure 5.6 shows the sound pressure levels generated by two investigated nozzles against frequency. The uniform temperature profile was generated upstream of the working section of the nozzles. The evaluation was performed based on measurements taken at the 17^{th} axial Kulite and the flow mean temperature of 444K. It is observed that no difference appears in all the frequency ranges. The sloping behaviour of the sound pressure levels is the same for both nozzles in the range from 10 to 1000Hz. From 1000 to 10 000Hz five

tones are matched well in their frequency value and dynamic pressure fluctuations amplitude. Even the higher frequencies allocated to instrumentation noise range are well matched. The uniform temperature profile gives no noise difference for both nozzles.

Following on, the EOTDF temperature profile was generated at the combustor simulator and tested for nozzle x and nozzle 1.5x. Figure 5.7 shows the sound pressure level evaluated for both nozzles with the EOTDF temperature profile. The data were processed at the 17th Kulite. This transducer is located at the furthest downstream position allowing to make an estimate of the sound pressure level propagation from the nozzle working section. It is noticeable that nozzle 1.5x configuration allows to achieve a decrease in the overall measured noise level. The noise level improvement is confined to the frequency range from 10 to approximately 3000Hz where the nozzle 1.5x modification is quieter than nozzle x. Moreover, the observed difference diminishes as the frequency increases. The fact that two sound pressure levels meet at 10Hz can be explained by the inability to apply the correct frequency response, the more precise description of this impediment is presented in Chapter 3. At the low frequency of 100Hz the measured difference reaches approximately 10dB, this is a substantial improvement for such an important frequency range. The observed sound pressure level difference at 1000Hz is approximately 5dB. In addition, the tone at 880Hz appearing for both nozzles is of the same noise level. A small tone at 4500Hz for nozzle x matches that of nozzle 1.5x. The sound pressure levels meet at the frequency of 4000Hz and at the higher frequencies show the same behaviour.

To validate the observed difference data from the 8th Kulite, the glued pressure transducer better matching the curvature of the outer wall, was processed. Figure 5.8 illustrates the sound pressure levels for nozzle x and nozzle 1.5x measured in the OTRF with the EOTDF

temperature profile at the inlet of the working section. The subsonic flow condition of Mach number 0.9 was maintained in both nozzles. The mean temperature of the flow was 444K.

The sound pressure level difference of 10dB at 100Hz is noticeable. It decreases to 5dB at 1000Hz and almost disappears at 3000Hz. Generally, the overall sound pressure level behaviour for two nozzles is similar to that evaluated at the 17th Kulite. That demonstrates that the measured noise difference is consistent. The tone of 880Hz appears with the same noise level for both nozzles. The nozzle 1.5x configuration, although evaluated as a quieter modification, generates the same dynamic pressure fluctuations amplitude at this tone as the nozzle x configuration. The precipitous increase is taking place immediately before the tone in contrast to the nozzle x configuration where the general increase in sound pressure level led to a less abrupt change in tone noise level. The general behaviour of the two nozzles at the higher frequencies is the same.

Two designed nozzles were investigated with the uniform and EOTDF temperature profiles generated upstream at the combustor simulator. The mean flow temperature and flow Mach number conditions were maintained for all the investigation cases. The uniform temperature profile is evaluated to produce the same noise response for both nozzles, while the EOTDF temperature profile shows an improvement as large as 10dB at the important frequency of 100Hz for the nozzle 1.5x configuration. The observed difference in sound pressure level is confined to the frequency range from 10 to 3000Hz, the frequencies where entropy noise is evaluated to be influential due to the wavelength and the axial dimension of the nozzle being of the same order. At the higher frequencies the difference disappears thus leading to the conclusion that the measured difference is

entropy noise. That means that in order to optimize the general noise level of aero engine the stator blades at the first turbine stage should be of an increasing axial distance, thus making the acceleration of the flow steadier. Following the described procedure the optimized noise level may be reduced by up to 10dB.

The observed results may have an analytical explanation. The modelling of nozzle 1.5x, as described in Chapter 3, was performed to achieve the steadiest Mach number distribution in the NGV section that was possible considering the limitations imposed by the facility hardware. The modelled nozzle 1.5x is characterised by a smaller rate of area contraction from the combustor exit to the throat than that of nozzle x. The steady acceleration means that the entropy noise stresses appearing due to spatial temperature variations experience a steady fluctuation all along the NGV section. That means that no abrupt change in static pressure is observed in the nozzle 1.5x modification in opposite to that of nozzle x where these stresses experience an abrupt fluctuation at the throat region. The fact that entropy noise stresses in the nozzle 1.5x configuration fluctuate steadily does not allow a large acoustic response to be generated. Thus, the experiments performed are validated by the theoretical acoustic analogy developed by James Lighthill. Its precise description is presented in Chapter 2.

5.4 Chapter Conclusions

The experimental investigation of entropy noise was performed in the OTRF for the nozzle 1.5x configuration. This nozzle is distinguished by a steady Mach number distribution within the NGV section, and therefore a more constant acceleration than that of nozzle x. The sound pressure level of two nozzles was investigated at the leading and trailing edge

of the NGV section. It was observed that the EOTDF temperature profile at the nozzle 1.5x configuration produced approximately 10dB noise difference compared to nozzle x, while the uniform temperature profile generated the same sound pressure level for both nozzles. That means that a change in acceleration rate of the flow when the non-uniform temperature profile is operated can optimise the sound pressure level in a turbine stage. The observed noise difference was described as entropy noise since it was determined by the difference in the flow acceleration rate within the NGV section only. Thus, it can be concluded that in order to decrease entropy noise in a nozzle configuration the distance over which the change of Mach number of the flow occurs should be prolonged.

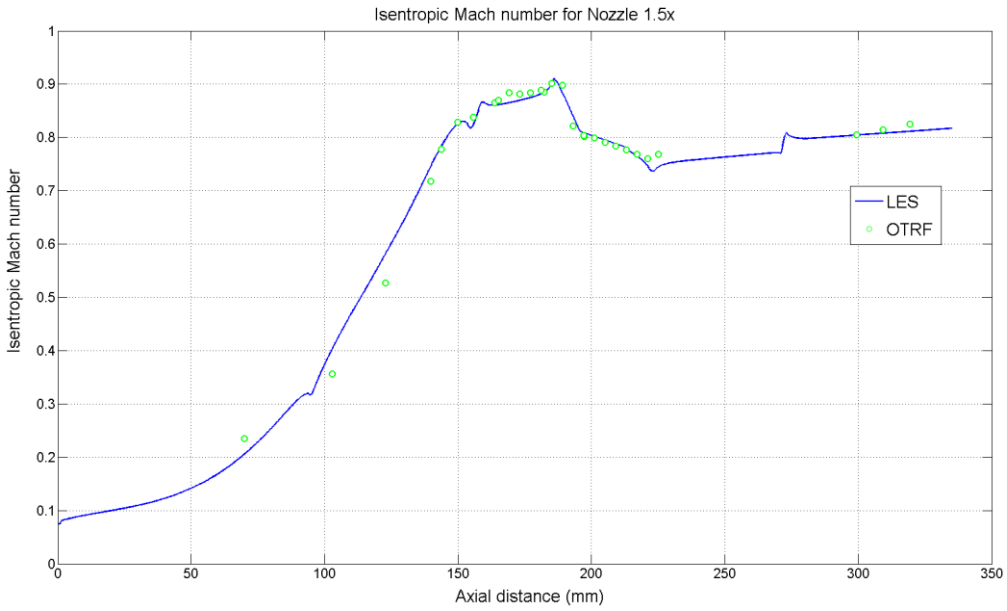

Figure 5.1: Comparison of isentropic Mach number distribution along the outer wall from measurements in the OTRF and numerical simulation using LES prediction

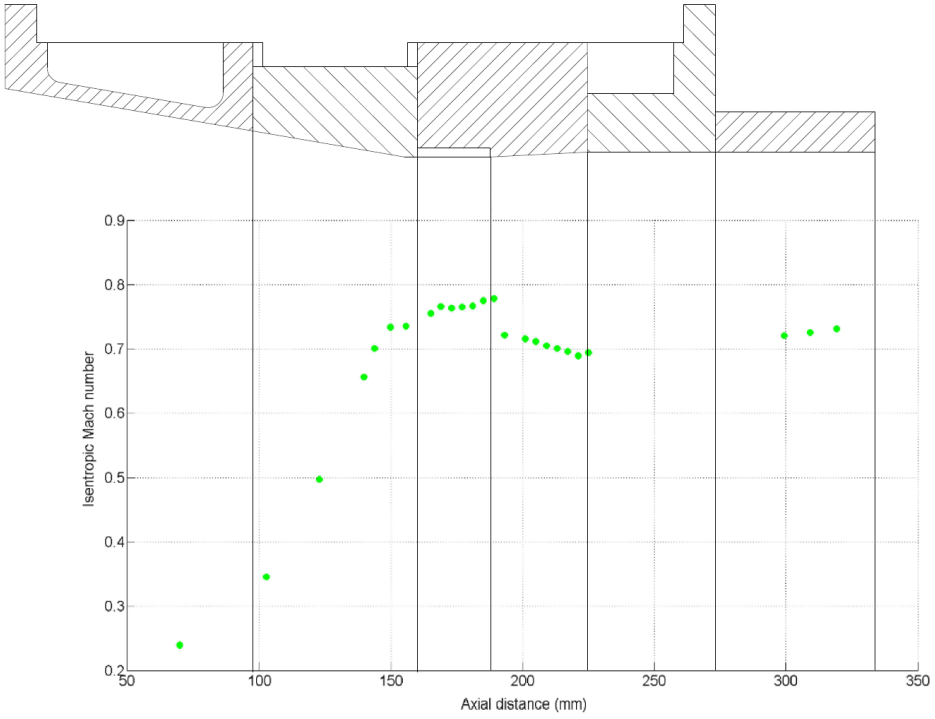

Figure 5.2: The outer wall hardware in relation to the isentropic Mach number measured in the OTRF

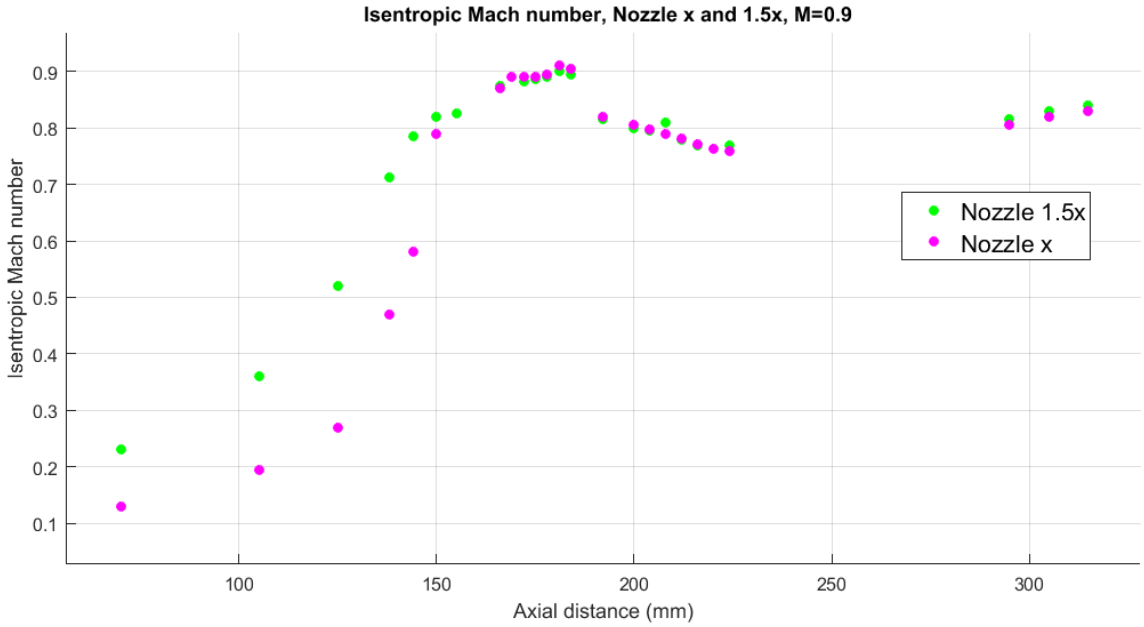

Figure 5.3: Comparison of isentropic Mach number for nozzle x and nozzle 1.5x

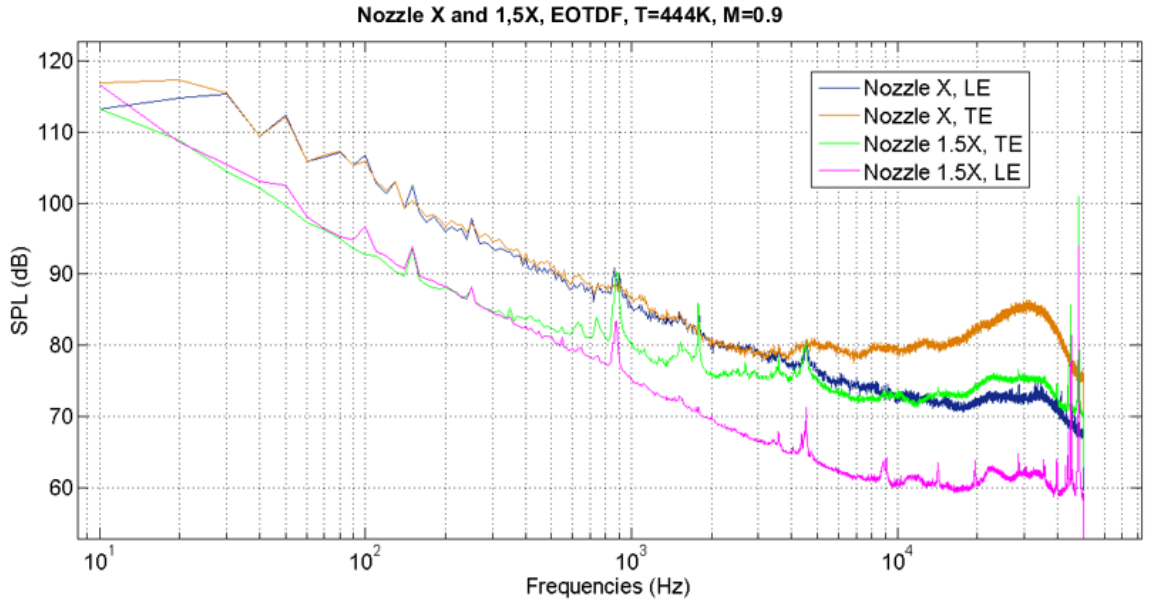

Figure 5.4: Sound pressure levels at the leading and trailing edge of the NGV section of two nozzles for the EOTDF temperature profile

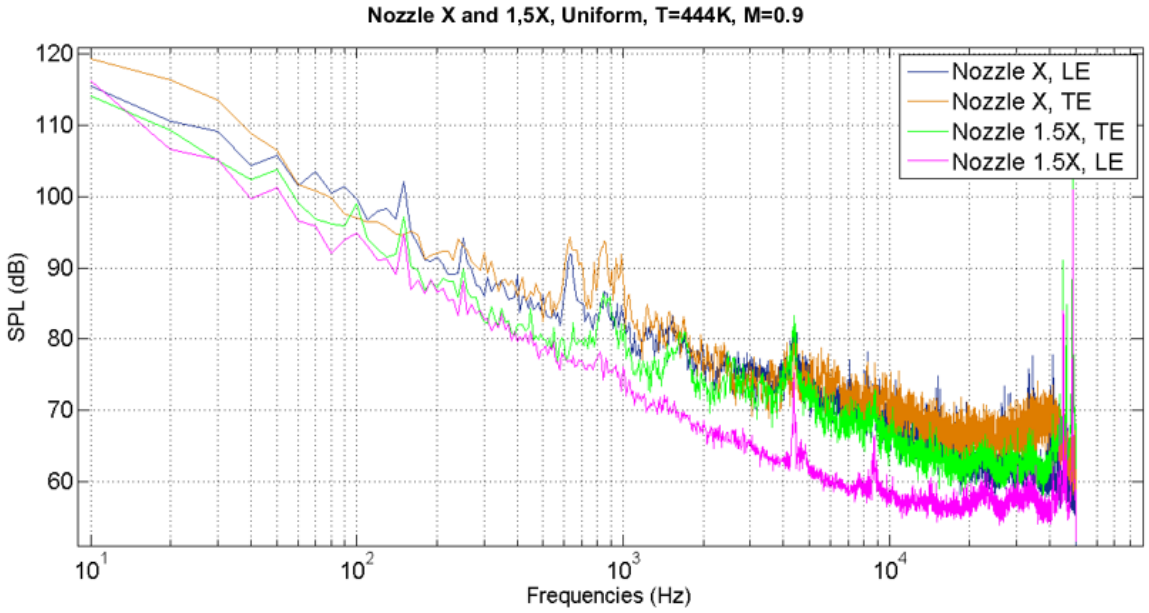

Figure 5.5: Sound pressure levels at the leading and trailing edge of the NGV section of two nozzles for the uniform temperature profile

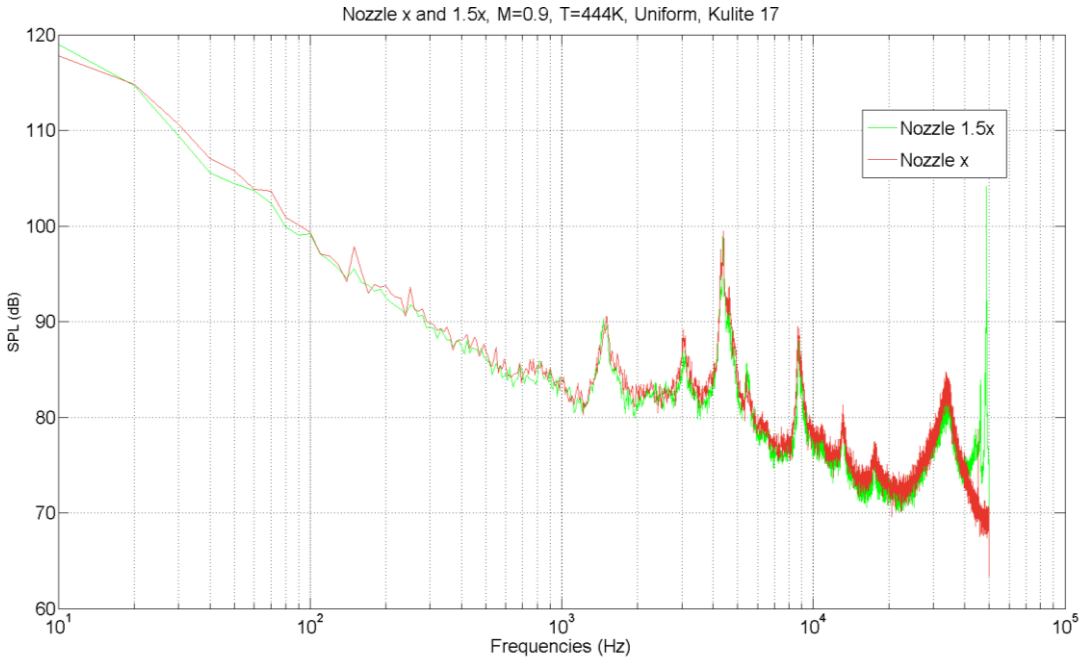

Figure 5.6: Sound pressure levels for two nozzles with the uniform temperature profile

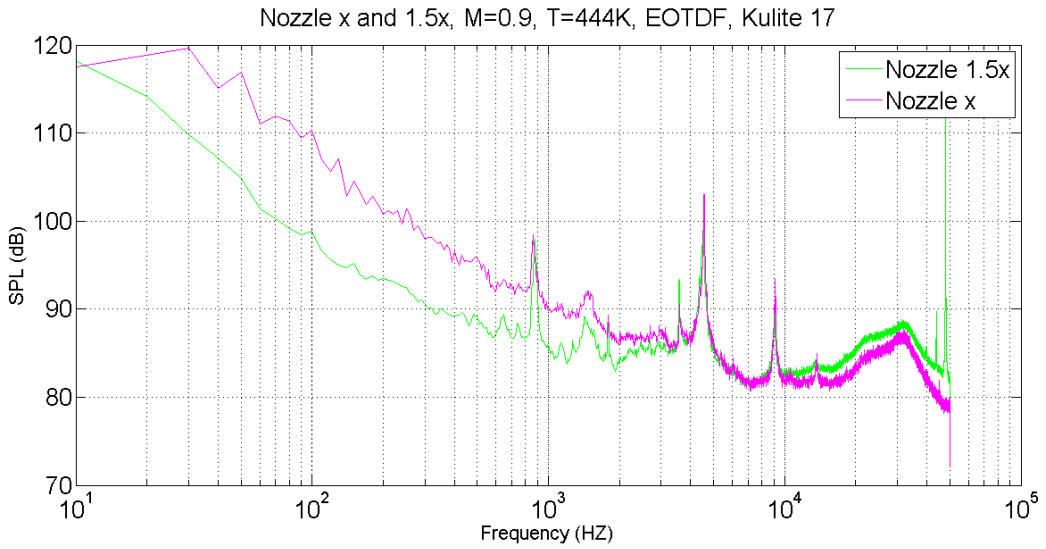

Figure 5.7: Sound pressure levels for two nozzles with the EOTDF temperature profile measured at the 17th Kulite

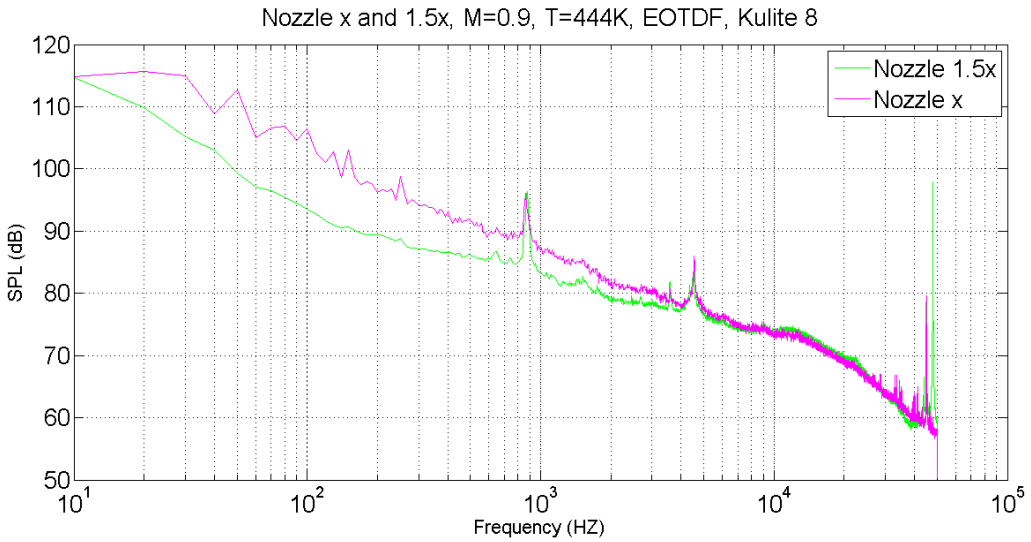

Figure 5.8: Sound pressure levels for two nozzles with the EOTDF temperature profile measured at the 8th Kulite

Chapter 6

Numerical Investigation of Entropy Noise in the Nozzle Configuration

Entropy noise is generated in a turbine stage due to acceleration of temperature inhomogeneities. To simplify numerical and, subsequently, experimental investigation of the entropy noise generation in a turbine stage consisting of an NGV and rotor can be exchanged with a nozzle geometry reproducing the acceleration of the flow taking place in the first stator blade row. This will allow to avoid the appearance of additional noise sources arising, for example, due to the trailing edge noise or wake-rotor interaction. The prerequisite for a successful numerical investigation is the accurate modelling of a complex EOTDF temperature profile used in the OTRF. The EOTDF temperature profile is characterised by spatial and temporal temperature variations. The experimental measurements of these variations were required in the modelling.

6.1 Numerical Setup

Chapter 3 presents the objectives of the entropy noise investigation in the OTRF using two nozzles with different flow acceleration rates. Flow characteristics of the nozzles, Mach number distribution, area ratio and rate of change of Mach number, were evaluated. To perform a numerical evaluation of the entropy noise generation the working part of the facility should be reproduced and investigation of noise generated by spatial and temporal

variations carried out. This makes possible a comparison of the numerical and experimental data.

6.1.1. Outline of CFD Simulation

The CFD simulation was carried out using commercially available simulation package ANSYS FLUENT, version 12.

The modelling of the flow field was performed by the following procedure:

1) The model of the computational domain was produced and then divided into discrete control volumes, cells, using a mesh generation package. These volumes store information that can be total temperature, static pressure, density, velocity components, etc. in faces and nodes within each volume. The fluid property values within the volume were assigned during the CFD calculation.
2) A turbulence model was selected to simulate the flow motion, heat transfer and other phenomena. Fluid and material properties of the computational model should also be specified. For the modelling of entropy noise the most important aspect of the turbulence model is its capacity to model the additional shear stresses caused by entropy inhomogeneities, since fluctuation of these shear stresses is responsible for the generation of an acoustic response.
3) The boundary conditions of the computational model such as inlet static pressure, total temperature variations at the inlet and wall boundaries were specified to represent correctly the hardware of the facility and match the boundary condition of the experiment when applicable.

4) The chosen turbulence model and boundary conditions were assigned to the computational model in the FLUENT package. This software uses a control-volume based method to discretise the incompressible flow governing equations to algebraic equations that could be solved numerically. For the combustor with half a turbine stage model segregated solver with SIMPLE pressure-velocity coupling algorithm with 2^{nd} order upwind discretisation for density, momentum, turbulent kinetic energy, turbulent dissipation rate and energy was used.

6.1.2 Computational Model

The computational model reproducing the geometry of two nozzles starting from the inlet section of the facility to the duct extension was meshed using the commercially available ICEM ANSYS package. To increase the accuracy of the numerical prediction taking into account a relatively simple geometry representation of the model structured mesh was chosen. Figure 6.1 shows boundary conditions applied to nozzle x (a) and nozzle 1.5x (b). The inlet zone was specified as pressure inlet with the static pressure boundary condition applied uniformly within the inlet frame. To describe the symmetric nature of the flow, periodicity, pictured blue, was enforced for both sides. The outlet boundary conditions were chosen for the pressure exit plane (pictured red). The hub and case wall, shown green, are non-slip. This relatively simple but efficient computational model will provide a good background for further investigation. The structured mesh with resolution of approximately 7 million grid cells and aspect ratio of 1.2 achieved for both nozzle models leads to an accurate numerical prediction of the flow field. Temperature boundary conditions are imposed at the inlet zone. The Large Eddy Simulation based on this

computational model was carried out. The acquired data is presented in section 4 of this chapter.

6.2 Temperature Fluctuations Modelling

The EOTDF temperature profile is generated by injecting cold air at 300K into the mainstream flow at 530K. The interaction between the hot and cold streams produces a profile of a complex steady and unsteady nature. Apart from having a region of the 'hot spot' and a gradually cooling flow closer to the walls, unsteady total temperature fluctuations are detected and evaluated to have their own profile with a larger amplitude at the centre of the 'hot spot'.

Unsteady inlet temperature fluctuations were measured at the OTRF rig with a set of rakes located circumferentially with a step of 1.5 degree (Figure 6.2). Measurements were taken at 27 inlet locations with temperature sensors located 29.5mm upstream of the NGV leading edge. Figure 6.3 shows a relative position of the measurement plane for the nozzle x configuration. The values presented is the radius of the hub and casing wall border lines of the measurement plane. Figure 6.4 gives an example of three experimentally measured traces of total temperature fluctuations at three different heights during the run time. It is observed that the amplitude of temperature fluctuations varies depending on the radial location. Figure 6.5 illustrates the range of the EOTDF temperature variations evaluated against the radial location. At the 'hot spot' location temperature variations cover the range from 480K to more than 550K. At the location distanced from the 'hot spot' temperature variations diminish and at the hub and casing walls they almost disappear. An

accurate modelling of these temperature variations was necessary in the entropy noise investigation since similar variations are generated in the real engine combustor.

Due to a highly complex nature of the temperature distribution in the radial and circumferential directions and the fact that these are unsteady temperature fluctuations, the reproduction of these features in the numerical simulation presented a major challenge. In order to reproduce these features the temperature profile frame was split into 135 sectors, 9 in the circumferential and 15 in the radial direction of the flow. This profile frame represented the flow field between two baffles.

The design of the datum nozzle x was chosen for the first simulation. The configuration of this nozzle was based on the original inlet section of the facility and specifically designed outer wall of the NGV section. The stator and rotor were removed and exchanged with the hub wall.

The combustion chamber section was terminated at the location of the measurement plane, and part of the model representing the hardware was enlarged with a chamber of constant cross-sectional area intended to straighten the flow passing downstream from the set of tubes stretching out of the inlet part of the chamber. Each one of these tubes was set to represent a sector of the total temperature profile. The flow with specified boundary conditions is injected through these tubes, then entering the constant area chamber and finally passing downstream through the nozzle. The inlet boundary conditions of each tube correspond to the conditions of the measurement plane sector allocated to it. Different tube modifications were considered (Figure 6.6). The criteria for these tubes were the dissipation level of the total temperature fluctuations and the possible meshing resolution of them. The most eligible modification was proven the third modification of

rectangular prisms with section area progressing in the radial direction. As particle tracking showed later this configuration allowed to preserve temperature fluctuations with dissipation rates not exceeding 5% of the fluctuation amplitude even in the region of the 'hot spot'. This can be further improved by adjusting the inlet pressure boundary conditions with respect to the varying area of each tube. Such a complicated design configuration was proven to be the only efficient method to numerically model not only the steady temperature distribution within the measurement plane but also unsteady temperature fluctuations measured in the OTRF.

Figure 6.7 illustrates the mesh of the model near the tubes. The mesh is multi-zones with tetrahedrons and prism mapped mesh type with refinement along the hardware reproducing part. This is shown to be the most effective method to prevent the energy contained in the sub-flows from dissipation and transfer when entering the main flow zone of the constant area chamber. A grid of 10.4 million cells was generated in order to achieve the maximum accuracy.

Later on, each one of these sections was defined as an inlet of the nozzle with boundary conditions of the overall inlet part and user-defined functions prescribing the unsteady total temperature fluctuations. Total temperature fluctuations in this section were modelled as a sinusoidal function with mean value being the mean value of the temperature in this particular section of the flow and amplitude of fluctuations accounting for half the peak-to-peak value of the total temperature fluctuations measured in the rig. The frequency of fluctuations was chosen at 350Hz for all cases since this is the predominant frequency measured experimentally as shown in Figure 6.27. Figure 6.8 presents the FLUENT generated picture of user-defined functions applied at each of the

sections. Periodic boundary conditions were applied for the model sides along the nozzle. Symmetrical boundary conditions with no friction were chosen for the tubes and the chamber of constant area, since these elements are not of real nature. The casing and hub walls, and the inlet section of the facility were specified as no-slip walls with 300K constant temperature. To include in the simulation acoustic waves propagating back into the combustion chamber a fully-reflective boundary condition was set at the outlet plane of the nozzle.

The numerical model was run with an unsteady density-based solver. Large Eddy Simulation with Smagorinsky sub-grid-scale model was used for all cases. This allowed successful modelling of all possible temperature field instabilities along the nozzle as well as a more precise calculation of the energy dissipation along the nozzle and energy transformation from the entropy into acoustic mode. Implicit solution method with explicit transient formulation of turbulence was used. This will increase the reliability of the model by achieving the best possible quality of turbulence generation. The time step of 1e-4 seconds was used for 350Hz fluctuations. This provides roughly 20 data points for one period of fluctuations. The run time was taken as 2000 time steps.

Figure 6.9 shows the comparison of the unsteady peak-to-peak total temperature fluctuations between the experimental and numerical data. The numerical measurements were taken at the exact location as during the experiment. The accurate modelling of the temperature profile in both radial and circumferential directions is noticeable. Some minor differences can be attributed to the fact that the numerical modelling is set for 9 sectors in the circumferential and 15 in the radial direction, whereas the experimental data was

obtained with 10 rakes in a row with 9 sensors installed. Moreover, some of these sensors were out of order and interpolation of the data was required.

Figure 6.10 presents the evolution of the EOTDF temperature profile in half a time period domain at the location of measurement plane. Conspicuous temperature variations of the 'hot spot' have an amplitude of up to 80K and represent the major noise source. That means that not only the real aero-engines have a complex steady temperature profile with cold air at the endwalls and a 'hot spot' in the centre, but the hotter region is fluctuating with a larger amplitude than the colder region.

This successful modelling allows an improved investigation of the entropy wave generation and propagation in the nozzle configuration and modelling of a vane configuration with a view to increasing entropy noise. Investigation of the vane configuration with the temperature fluctuations imposed upstream using the developed method is presented in Chapter 7.

6.3 Numerical Modelling of the EOTDF Temperature Profile

The modelling of the EOTDF temperature profile is an important part of the entropy noise numerical investigation. It is imperative for validity of the numerical data to achieve a very good matching with the experimentally measured EOTDF temperature profile. The numerically modelled profile should reproduce the temperature variations generated in the facility in both radial and circumferential directions.

6.3.1 Modelling Procedure

The three-dimensional Large Eddy Simulation (LES) with Smagorinsky sub-grid scale using commercially available software ANSYS FLUENT was used in this study. The numerical

algorithm used in the three-dimensional computation consists of the time-matching, implicit, finite-difference scheme. The procedure is third-order spatially accurate and second-order temporally accurate. The viscous fluxes are calculated using standard central differences. For efficiency reasons, an implicit time integration is employed to deal with the very small grid size encountered near the wall. The large discrepancy between the speed of an acoustic wave and the advection velocity at the low Mach number flow conditions makes explicit time integration inefficient. This occurs because numerical stability considerations impose small time steps on the acoustic waves, whereas the physical entropy wave is mainly driven by the solenoidal part of the flow, whose time step, being associated with advection, is larger. In addition, Newton sub-iterations are used in each time step to increase stability and reduce linearization errors. One Newton sub-iteration was performed for each time step. Usually LES requires high-order centred schemes for the Euler fluxes discretization to minimize dispersive and dissipative numerical errors. However, such numerical schemes cannot be applied easily in complex geometries. Thus, getting a high-order method is a time consuming task owing to the high-order quadrature need to resolve fluxes along the boundaries. Wu (Wu, 1999) showed that LES can be carried out with a low-order centred scheme in case of the sufficient mesh resolution and that a second-order accurate scheme can produce a good numerical prediction of the sound pressure level emanated by the flow field. Taking into account the fact that a typical wavelength of acoustic waves in turbulent flows is generally larger than the Kolmogorov scale, the mesh for the entropy noise investigation is well adapted and the investigation of entropy noise and aerodynamic sound generation using a second-order scheme is rendered possible.

At the inlet, the static pressure, the total temperature boundary conditions and location of the face-type zones are specified using user-defined functions written in C code and applied at the inlet zone of the computational model. The complex Riemann invariants for compressible flow with regard to entropy variations are extrapolated upstream.

Simulation of the 'hot spot' and its environment required modification of the flow temperature conditions within this region. Thus, the inlet velocity components defining the 'hot spot' behaviour will be in a square root proportion to the temperature variations:

$$u_{hs} = u_{444}\sqrt{\frac{T_{hs}}{T_{444}}} \quad , (6.1)$$

where T_{hs} represents total temperature within the 'hot spot' and T_{444} is the total temperature of the spatially and temporarily uniform inlet profile with 444K being the area-average value for both the EOTDF and uniform case. The static and total pressure at the inlet of the EOTDF profile are assumed to be equal to that of the uniform case (Butler, 1989). The temperature profile was specified in zones assigned to match the location of the thermocouples used in the OTRF experiment. This gives variations of axial velocity component within the inlet section, but neglects to take into account velocity variations in the circumferential and radial directions, as well as flow angles entailing that the numerical modelling allows an evaluation of entropy noise but eschews to calculate rotational kinetic energy and the associated noise produced by vorticity inhomogeneities.

The modelling of the EOTDF temperature profile at the inlet was performed using experimentally obtained data from the OTRF. The EOTDF profile is generated by injecting coolant air of 300K through slots located at the endwalls and baffles in the equidistant position along the circumferential direction.

Based on the fact that the nozzle and the combustion chamber are symmetrical in the circumferential direction, only one section of the real facility was modelled. The circumferential angle of the simulated section is 11.25 degree, since the flow is symmetrical for each of the sections located between 32 uniformly located baffles. The pressure ratio was specified at mid-span of the computational exit with non-reflective boundary conditions. Periodicity is enforced along the outer circumferential sides. No-slip boundary conditions are applied at the hub and casing wall of the model.

In the OTRF the baffles and the hub/casing annular slots create the temperature fluctuations and the temperature profile in the radial and circumferential directions respectively due to the injection of colder air through them, but in the LES prediction these temperature fluctuations are prescribed using user-defined functions. The nozzle x modification with the duct extension at the outlet was chosen in order to make a comparison with the experimental data. The mesh is multi-zones with tetrahedrons and prism mapped mesh type (Figure 6.11). This is shown to be the most effective method to prevent the energy contained in the sub-flows from dissipation. Additional mesh improvement was performed to minimize the aspect ratio. The total number of grid points used to discretize the turbulent flow of the nozzle was 7.4 million.

The investigation of the entropy noise generation requires to employ the compressible flow in order to allow solenoidal fluid modelling of acoustic waves. The acoustic waves of interest are located in the low frequencies, especially for the entropy noise investigation, and thus have large wavelength which are easy to capture by a mesh of relatively medium quality for the aerodynamic sound investigation purposes. Grid used in this study are characterised by the following mesh spacing characteristics: $\Delta x^+ = 15.4$, $\Delta y^+ = 15.4$,

$\Delta z^+ = 7.5$. The first estimate of the size of the turbulent structures in the form of the integral length scales can be calculated. Length scales in streamwise and spanwise directions are $L_{uu}^x = 85.2$, $L_{uu}^z = 22.3$. Thus, quality of discretization of turbulent structures can be estimated from ratios of integral length scales to the corresponding mesh spacings. In the streamwise direction, the length scale is discretized by more than 5.8 points of the mesh spacing. In the spanwise direction, the length scale is discretized by more than 3 points. Considering that acoustic wavelengths shorter than approximately 4 points pre wavelength are estimated to be damped by the relaxation filter (Kremer, 2013), it can be concluded that the generated mesh allows resolving the turbulent structures in the streamwise direction, but might give some unsolved scales in the spanwise direction. The time scale resolved in the streamwise direction $\tau_{uu}^x = 13{,}4$.

In order to further validate the LES procedure and prove that the generated mesh is capable of resolving the turbulent flow with the specified boundary conditions, normalised spectrum of energy for different Mach number values of the nozzle x configuration was evaluated. Figure 6.12 shows the distribution of normalised energy along the normalised wave number for three Mach number values. The evaluation was performed at the mid-height location of the NGV section. It is observed that the energy cascades are showing an increasing behaviour for low wave numbers similar to a slope of 2 for the energy containing region. Afterwards, energy cascades are sloping down with an approximate level of slope 5/3. This corresponds with the Kolmogorov's theory of energy cascade behaviour. The dissipation region is observed at the higher wave numbers for all cases. Notably, for Mach number of 0.67 the dissipation region appears earlier entailing that energy is starting dissipating and being dumped and thus predicting a correct turbulence resolving. This is

anticipating considering the discretisation analysis presented above. However, this does not mean that the acoustic field is not being resolve. Firstly, the acoustic wavelength is much larger than a mesh spacing and length scale; secondly, the entropy noise generation is taking place during acceleration, thus a lot of entropy/acoustic energy transformation is taking place at the lower Mach numbers, and thirdly, the resolved energy range even for Mach number of 0.67 is sufficient to correctly predict the general flow behaviour and model the transformation of kinetic energy contained in the non-uniform temperature profile into an acoustic response.

Figure 6.13 shows the two-dimensional EOTDF temperature profile for one model sector confined between two contiguous baffles obtained experimentally using thermocouples (a) and numerically with LES (b). The positioning of temperature contours evaluation in the numerical simulation is matched with those measured experimentally in the nozzle. Figure 6.14 illustrates the comparison of the numerically evaluated and experimentally measured EOTDF temperature profile evaluated along the radial pitch taken at the circumferential centre of the working section. That further validates the good modelling agreement that has been achieved. The only insignificant difference appears within the 'hot spot' region. The measurement plane was located 29.5mm upstream from the leading edge of the NGV section. The computational model reproduces the working section of the facility from the measurement plane where the temperature profile was imposed to the exit of the duct extension. This does not allow to include into the computation such important flow parameters as vortex shedding due to baffles and flow mixing upstream in the combustion chamber, but this technique provides an opportunity to quantify the sound pressure level produced by a well modelled EOTDF temperature profile.

This technique of temperature profile modelling allows an extensive investigation of the noise level generated by varying temperature profiles in the nozzle, turbine stage as well as evaluation of noise emanated by the rich-burn and lean-burn combustor exit temperature profile.

6.3.2 Data Processing

Figure 6.15 shows the computational model with the EOTDF temperature profile imposed upstream. The data processing location is marked with an arrow corresponding to the axial location of the 12th Kulite installed at the outer wall of the duct in the OTRF experiment. Figure 6.16 presents an example of the transient waveform for dynamic pressure fluctuations versus time acquired in the measurement location of the 12th Kulite. In order for the $p(t)$ waveform to be evaluated in the frequency spectrum, the Fourier transform $\hat{p}(w)$ was introduced.

$$\hat{p}(w) = \frac{1}{2\pi} \int_{-\infty}^{\infty} p(t) e^{iwt} dt \quad (6.8)$$

The Fourier transform has real and imaginary parts and determines the frequency limits of the processed waveform for the chosen time step t_s as:

$$\left[\frac{1}{nt_s}; \frac{1}{2t_s}\right], \quad (6.9)$$

where n – number of time steps forming the static pressure signal. The choice of the time step and length of the calculation was made with consideration of the computational costs incurred.

Although this provides the sound pressure amplitude spread over the targeted frequency range, and thus is sifficient to make an assessment of the entropy noise generation, it is

customary to measure and report a quantity varying linearly as the decimal logarithm of pressure (Pierce, 1989). This quantity is said to be a sound pressure level and is defined as:

$$L_p(w) = 20 \log\left(\frac{\hat{p}(w)}{P_{ref}}\right), \quad (6.10)$$

the resulting value having the units of decibels. The denominator factor P_{ref} presents a reference pressure, which usually taken 2e-5Pa for airborne sound.

6.3.3 Validation of the Developed Method and Consistency of Results

A very good match of the numerical and experimental EOTDF temperature profile requires validation of the developed method, since the spectrum of temperature fluctuations observed in the OTRF may differ from that modelled in the LES prediction using turbulence intensity distribution. Moreover, the received signal at the chosen location may vary due to uncertainties arising in the numerical procedure caused by imperfect solvency of the scales, necessity to use a sub-grid scale model and turbulence intensity imposed. In addition, the computational cost often prohibits to perform a long simulation necessary to acquire a waveform of samples long enough to cover the frequency range achieved during the experiment.

In this regard, a series of independent LES predictions were carried out; firstly, to estimate the matching of the sound pressure level acquired from the experiment and numerical modelling, secondly, to investigate the influence of uncertainties on the numerical results, and thirdly, to quantify the change of sound pressure level due to a shorter frequency range targeted by the LES procedure.

Figure 6.17 shows sound pressure levels of four independent numerical simulations evaluated in the chosen frequency range. The numerical data was processed at the location of the 12th axial Kulite for the nozzle x configuration with the EOTDF temperature profile generated upstream. The subsonic flow conditions of Mach number 0.9 were maintained in the nozzle. The numerical bandwidth was shortened to cover the frequency range from 10 to 4000Hz. It is observed that despite possible turbulence uncertainty in the LES prediction, the sound pressure levels are matched very well. Four independent numerical predictions are quite consistent especially at the higher frequencies showing only an insignificant discrepancy at the lower frequencies. This is explained by the repeatability error occurring in the lower frequencies.

Numerical prediction at a shorter frequency range can be compared with numerically predicted and experimentally measured sound pressure level for the same nozzle configuration and flow conditions (Figure 4.17). Two rapid amplitude increases are noticeable to appear in the LES prediction for the shorter frequency range. The first at 880Hz matches in the frequency value with that measured experimentally, the second at approximately 1150Hz appears only in the numerical modelling. This may be explained by shortening of the targeted frequency range and subsequently energy transformation within the frequency domain. The experimental data shows another amplitude increase at 4500Hz having the frequency range from 10 to 50 000Hz, whereas the LES modelling predicts an increase at 1150Hz with the frequency range from 10 to 4000Hz. The general behaviour of the sound pressure level curves and even tone peaks at the low frequencies are similar in value. This entails that the temperature uncertainties produced at the inlet

of the computational domain do not prevent a good simulation to be performed. Thus, the developed method is validated.

Thus, the developed method of sound pressure level evaluation based on the EOTDF temperature profile modelling with exception of the spectrum of temperature fluctuations is validated using the available experimental data, the consistency of the LES prediction is showed to be sufficiently confident, while the chosen frequency range is recommended to match that of the instrumentation used in the OTRF experiment.

6.4 Entropy Noise Reduction in a Nozzle based on Other Common Numerical Technique

There are many numerical techniques currently in use to evaluate the generation of entropy noise. One of the most common technique used by many other researchers (Leyko, 2011) is a simplified numerical approach based on modelling of a 2D nozzle and reduction of noise generated by the 1D temperature inhomogeneities propagating downstream from the combustion chamber. As mentioned in section 2 of this chapter the real combustor exit temperature profile is characterised not only by spatial temperature variations but also by large temporal temperature fluctuations within the profile frame. Optimisation of sound pressure level in a nozzle configuration requires to account for these temperature fluctuations. The performed experimental investigation and successful modelling of 2D temperature variations developed in this study allows validating the most common technique used by other researchers and modelling of a ‘quiet’ nozzle based on 1D temperature fluctuations.

The study of the modelled nozzles was used to validate the common numerical technique. In order to model the engine temperature instabilities propagating from the combustion chamber downstream though the turbine stage, a numerical code to describe spatially and temporally uniform temperature fluctuations was written. Artificially generated total temperature fluctuations were applied at the inlet of each nozzle. Large Eddy Simulation (LES) with Smagorinsky subgrid scale modelling for different nozzles was applied with the boundary conditions described in Table 6.1.

The pressure ratio corresponds well to the experimentally measured exit pressure set using the second throat. Non-reflective boundary conditions were imposed at the exit plane. Amplitude of temperature fluctuations was chosen based on the available measurements in the OTRF. Amplitude values were averaged within the profile frame to perform the numerical evaluation corresponding to the other common numerical technique.

To perform a more extensive investigation two new nozzles 0.8x and 0.6x were numerically modelled. They geometries were modelled based on the procedure described in Chapter 3. Figure 4.18 shows designs of the nozzle 0.8x and 0.6x configurations. The nozzles are presented as possible hardware configurations for the OTRF testing.

The sound pressure level for the four nozzles was evaluated at the mid-height 5mm upstream of the exit plane of the nozzle. Since the inlet temperature fluctuations were modelled as a sinusoidal function, the acoustic response of the pressure field was also sinusoidal and the value of sound pressure level at the chosen location can be calculated by applying FFT to the acquired dynamic pressure fluctuation signal. Figure 6.18 shows the evaluation of sound pressure levels for the chosen frequencies for four investigated nozzles. The chosen range of frequencies is 100-4000Hz, because these are frequencies

that are likely to be propagating through the turbine stage and where entropy noise is evaluated to be more influential.

The results in Figure 6.18 show clearly that the nozzle 0.6x produces lower noise levels across all the targeted frequencies. Nozzle x shows an improvement over 0.8x for frequencies below 280Hz but is noisier at the higher frequencies. The nozzle which gives the highest noise levels in all the frequency range is nozzle 1.5x with approximately 3dB sound pressure increase in the lower frequencies and substantial difference of 10dB at 1000Hz. At the higher frequencies of 4000Hz the sound pressure levels are coming close.

The nozzle hardware configurations vary only within the NGV section and are the same downstream of the throat. The throat and exit duct dimensions are kept the same. Different rates of geometrical contraction of a nozzle give different levels of entropy noise. Temperature fluctuations imposed downstream described as:

$$\frac{T'}{T} = \left(\frac{\gamma-1}{\gamma p}\right)_0 p' + \left(\frac{1}{c_p}\right)_0 s'. \quad (6.2)$$

The incitement of temperature fluctuations at the inlet plane of the nozzle produces an acoustic response generated by the acoustic and entropy mode. The acoustic mode is a result of volumetric expansion-contraction of the flow arising due to the imposed temperature fluctuations, the acoustic response of the acoustic mode is described by the first term on the right hand side of equation (6.2) and is monopole in its nature. The entropy mode is described by the second term when density is constant. The acoustic response of the entropy mode is caused by temperature variations within the flow leading to the appearance of shear stresses at the border region where the temperature of the flow changes. When accelerated, these shear stresses produce an acoustic wave. Since

temperature fluctuations upstream, mass flow rate and Mach number value downstream of the throat are the same for each case, acoustic mode excitations due to temperature fluctuations should be of the same value. Therefore, neglecting acoustic-boundary interaction the sound pressure difference presented in Figure 6.18 is attributed to the entropy noise generation alone. As noted in Chapter 2, generation of entropy noise is only possible when the acceleration of the flow is taking place and Chapter 4 and 5 provides an experimental and numerical proof that a quieter nozzle is characterized by a slower change of Mach number value. This is owing to the slower change of the local static pressure in the nozzle 1.5x configuration than in that of nozzle x and thus less noise level being emanated. Data presented in Figure 6.18 contradicts the numerical, experimental and theoretical conclusions and arguments regarding the entropy noise generation. Therefore, it might be concluded that the numerical model with only temporal temperature fluctuations specified uniformly across the inlet sector give an erroneous results, and thus this procedure is rendered incorrect.

It is worth noting that the proposed procedure is based on the temporal temperature variations only and does not allow the modelling of the spatial temperature variations in the radial and circumferential directions. Moreover, the temperature fluctuation amplitude was imposed upstream within the entire measurement plane. This is a simplified approach most easily implemented in numerical simulation, since the imposed temperature fluctuations might be regarded as being one-dimensional and the nozzle configuration as a two-dimensional model. This is currently the most common numerical approach in the entropy noise investigation (Leyko, 2011).

As shown in Chapter 4, a more precise LES prediction based on the numerical procedure developed in Chapter 6 gives a more reliable sound pressure level data since entropy noise is being generated by an accurately modelled spatially and temporally varying temperature profile. Although the proposed method is computationally expensive, it is shown to be a better approach in the entropy noise investigation, which defies many other entropy noise investigation approaches currently in use.

6.5 Influence of Frequencies on Entropy Noise Generation based on Temperature Fluctuations

Entropy noise is considered to be important in the frequency range of 10-2000Hz. Numerical evaluation of dynamic pressure fluctuations generated downstream by temperature fluctuations incited upstream of a nozzle described in previous sections provides a good background for investigation of the rate of change of static pressure for different flow conditions and frequencies.

The LES numerical procedure described in section 3 of this chapter is used for investigation. Sinusoidal total temperature fluctuations with amplitude of 7K were imposed at the inlet plane of the two modelled nozzles. The generated dynamic pressure fluctuations determining the acoustic response due to the flow acceleration were evaluated for different Mach number values.

Figure 6.19 shows normalised static pressure over temperature fluctuations plotted against Mach number values for the nozzle x configuration. Frequencies of 100, 500, 1000 and 2000Hz were chosen to cover the frequency range of interest. The ratio $\frac{p'}{p}\frac{T}{T'}$ of normalised static pressure at the chosen location over normalised temperature

fluctuations at the inlet plane is used to evaluate entropy noise since it gives a non-dimensional characteristic. The LES prediction was performed for the same temperature fluctuations and following equation (6.11) the direct combustion noise is described with the term $\frac{\gamma-1}{\gamma}\frac{p'}{p}$ and must be decreasing with an increase of Mach number. Thus, the appearance of a precipitous rise in the ratio presented in Figure 6.22 accounts for the generation of entropy noise. The observed behaviour corresponds well with the theoretical assumptions presented in Chapter 2. Entropy noise for 100Hz frequency is the largest with the fluctuations amplitude increasing significantly after 0.3 Mach number. The curve for 500Hz wave frequency shows a constant growth of entropy noise, whereas those of 1000Hz and 2000Hz are evaluated to have a small drop in the noise amplitude with an increase of Mach number. A decrease in the static pressure amplitude for these high frequencies means that entropy noise is no longer influential.

Figure 6.20 shows the same ratio evaluated against Mach number for the nozzle 1.5x configuration. The general behaviour of entropy noise preserves but 100Hz wave frequency is marked by a more severe increase in amplitude of dynamic pressure fluctuations. This is confirmed by the sound pressure level evaluated in section 3. The 500Hz wave frequency shows a constant growth of the entropy noise level, while 1000Hz curve starts sloping down after 0.4 Mach number. Notably, entropy noise for the nozzle 1.5x configuration at higher frequency of 2000Hz is similar to that of the nozzle x configuration, entailing that the nozzle geometry and subsequently area ratio makes no difference on the entropy noise generation at high frequencies.

6.6 Dissipation of Total Temperature Fluctuations along the Nozzle

The modelling of total temperature fluctuations measured in the OTRF presented in section 3 allows to perform a numerical evaluation of their dissipation in the direction of the flow motion. A very good match of the experimentally acquired and numerically modelled total temperature fluctuations within the measurement plane reinforces the validity of the chosen procedure. Measurement of the unsteady fluctuations propagating downstream through the nozzle was performed using the user-defined functions inciting the correct temperature fluctuations, the latter were rearranged to generate fluctuations of the predominant frequency of 350Hz. This simplifies the processing of the data.

Figure 6.21 presents an analysis of total temperature fluctuation dissipation performed for the nozzle x configuration along the centreline. The reference point for the axial distance was chosen as the measurement plane. The axis of total temperature fluctuation evaluates the peak-to-peak value of the total temperature fluctuations. The sloping pink line is the temperature amplitude dissipation of the 'hot spot' total temperature fluctuations along the axial distance. It starts with an amplitude of 30K then it experiences a slight increase, this may be explained by the contraction of the generated acoustic front and the influence of the entropy mode velocity driving the temperature fluctuations to the 'hot spot'. The chosen frequency of 350Hz is relatively low, thus allowing the possibility that the fluid moves from the colder to the hotter region within the temperature profile increasing the amplitude of total temperature fluctuations. The entropy mode velocity arises because the colder region, as measured experimentally in the OTRF, fluctuates with lower amplitude while the 'hot spot' is characterised by much larger temperature fluctuations. The diffusion equation (2.12) dictates that temperature fluctuations at the local temperature maximum,

the ’hot spot’, are decreasing with time and it happens quicker than at the colder region. The dynamic pressure fluctuations are absent in the entropy mode demanding density at the ‘hot spot’ to increase thus causing the flow to compress in the direction of the ‘hot spot’. After a certain period the dissipation of total temperature fluctuations begins and it takes place in a constant manner reaching peak-to-peak total temperature fluctuation value of 36K at the exit of the nozzle.

The region of the NGV section where the acceleration of the flow takes place is marked in Figure 6.22. Neglecting an insignificant diffusion downstream of the throat region entropy noise is generated in the NGV section and propagates undisturbed with the speed of sound. The assumed behaviour of the entropy noise generation is presented with the pink line. The supposed dissipation behaviour of total temperature fluctuations when the entropy mode velocity is absent is plotted in green. The behaviour of total temperature fluctuations under the linear acoustic approximation is shown in blue.

As noted in Chapter 2, fluctuations of temperature can be decomposed as a sum of the linear and entropy terms. The linear acoustic medium when pressure is proportional to density with the speed of sound value dictates that the incited total temperature fluctuations generate the direct acoustic response due to volumetric expansion-contraction of the fluid produced by temperature fluctuations. It has no effect on the dissipation of temperature fluctuations. In the entropy mode total temperature fluctuations are converted into density fluctuations, the latter when accelerated serves as an acoustic source in the acoustic mode of the Kovasznay decomposition described by Lighthill’s acoustic analogy. Once generated, entropy noise propagates with the speed of sound and total temperature fluctuations might be regarded as being departed into the

external system. Further downstream when the flow velocity is constant the conversion of total temperature fluctuations into density fluctuations continues, but the appearance of density fluctuations do not turn themselves into an acoustic source because there is no acceleration of the flow. They are being driven by the mean flow and stay in the entropy mode.

If the linear acoustic approximation is considered only and the entropy term is neglected, the dissipation of total temperature fluctuations does not take place. Neglecting the dissipation through Brownian motion of molecules the fact that the LES prediction captures the dissipation of temperature in the axial direction means that the generation of entropy noise is well modelled in the numerical prediction.

Figure 6.23 presents the comparison of the dissipation of the 'hot spot' total temperature fluctuations along the axial distance for nozzle x and nozzle 1.5x. The EOTDF temperature profile fluctuations were applied upstream for both cases. The dissipation of total temperature fluctuations for nozzle 1.5x happens in a steady way with the peak-to-peak fluctuations decreasing down to 27K. In comparison to nozzle x, nozzle 1.5x is characterised by a higher amplitude at the inlet measurement plane entailing that the fluid was compressed upstream in the direction of the 'hot spot'. That can be caused by the geometry of nozzle 1.5x which is characterised by a quick contraction of the area at the inlet section, whereas nozzle x was modelled to experience a steady area ratio decrease within the NGV section, while the inlet section only slightly accelerates the flow. This means that entropy noise is generated in nozzle 1.5x predominantly in the inlet section of the facility, while in nozzle x it happens within the NGV section. The fact that the dissipation value at the exit plane for nozzle 1.5x is less than that for nozzle x does not mean that the

resulting entropy noise is larger for nozzle 1.5x since its generation requires acceleration of the flow.

6.7 Modelling of Temperature Fluctuations with Phases

Total temperature fluctuations arising in the combustor due to the flow mixing are generated in the OTRF by injection coolant air of 300K through annular slots and baffles to the mainstream of a hotter temperature. These fluctuations are characterised by a mean total temperature, amplitude of fluctuations, chosen frequency of temperature fluctuations and phase shift. The burning of the flame in the real combustor happens in an unsteady way requiring the investigation of phase influence on the sound pressure level. To get a further insight into the phase shift the unsteady total temperature fluctuations were measured in the OTRF with thermocouples mounted on a set of rakes acquiring the history of temperature variations over time with a step of 1.5 degree in the circumferential direction. There are nine thermocouples at each rake evaluating the flow behaviour from the casing to hub wall.

Several thermocouples were chosen for investigation. Their location within the nozzle computational domain is presented in Figure 6.24. The thermocouples were chosen at the casing wall and centre of the temperature profile with a circumferential step of 7.5 degree covering two contiguous sectors, one sector between two baffles with 4 thermocouples and the second with another two thermocouples. The second and fourth thermocouples represent the case extremities since they provide an evaluation of temperature fluctuations at the ’hot spot’ where the amplitude of temperature fluctuations is the largest and at the cooler region at the hub wall. The measurement was performed with

three rakes located at the chosen circumferential step to get consistent data for several sectors over the same time, thus avoiding possible phase uncertainties arising due to turbulence. The EOTDF temperature profile is generated with 32 equidistantly installed baffles, the sector therefore has a circumferential dimension of 11.25 degree.

Figure 6.25 shows time histories of total temperature fluctuations for the chosen thermocouples. The data were taken at the same experiment at the time period from 1.4 to 1.55 second. The plot of the total temperature fluctuations over the entire run duration is presented in section 3. It is observed that the behaviour and amplitude of total temperature fluctuations for 0 and 7.5 degree rakes are similar and may be assumed as sinusoidal. Assuming the Strouhal number in this region as 0.02 and taking into account the speed of the flow at the location of the measurement rakes and the circumferential dimension of the baffles, it might be concluded that the observed sinusoidal temperature fluctuation of 350Hz can be a result of periodic coolant air injection of the circumferentially installed baffles. In contrast, the 15 degree rake gives more uncertain data. The slight sloping behaviour of temperature fluctuations is explained by the imperfectly maintained static pressure boundary conditions at the inlet of the OTRF.

The uncertain behaviour of total temperature fluctuations necessitated to perform a Fast-Fourier Transform (FFT) to evaluate the spread of energy contained in these fluctuations across the frequency range, this is presented in Figure 6.26. It is observed that for 0 and 7.5 degree rakes the predominant frequency is approximately 350Hz, while the 15 degree rake gives a more steady spread of the temperature fluctuations. Thus, the frequencies of total temperature fluctuations for the following nozzle sector are not in phase with the first sector. That means that temperature fluctuations show a similar phase shift behaviour

within one sector of the nozzle but vary in the circumferential direction. The sound pressure level being generated by the total temperature fluctuations and propagating downstream can be affected by these phase shifts. The LES numerical prediction was performed to investigate the influence of phase shift on the sound pressure level of the generated noise. The different phase distribution was imposed at the inlet section of the nozzle sector.

Figure 6.27 shows comparison of the Fast-Fourier Transform applied to the unsteady temperature fluctuations evaluated against the targeted frequency range of 10-10 000Hz at the 4th thermocouple located at the 7.5 degree rake for the OTRF and LES data. It is observed that the LES prediction managed to achieve a good match with the experimental data. The difference between the LES prediction and OTRF experiment does not exceed 20K with both graphs getting down to approximately 140K at frequency of 1000Hz. In the low frequencies the LES prediction is evaluated to produce a larger temperature fluctuations level than OTRF experiment. This tendency persists up to 1000Hz. The LES temperature fluctuations level is experiencing an increase in the frequencies from 150Hz getting up to 170K before starting to decrease at 700Hz matching the OTRF temperature fluctuations level at the frequency slightly higher than 1000Hz with 140K. The OTRF temperature fluctuations level also shows a similar pattern but with a lower temperature fluctuation level. At the higher frequencies LES prediction gives less temperature fluctuations level than that generated in the OTRF. There is no rapid temperature fluctuations level increase in the frequency of 880Hz.

Figure 6.28 shows Mach number contours of the injection tubes into the constant area chamber. The flow passing through the chamber is characterised by the presence of

velocity traces at the wall region. A difference in their length at the chosen moment of time means that the phase shift modelling was successful. The multi-zone mesh of 9.7 million cells for the nozzle x configuration of supersonic conditions was run according to the procedure described in section 3 of this Chapter. To understand the influence of the phase shifts on the noise generation, the case with uniform distribution of phase shifts was performed as well.

To evaluate the influence of phase shifts on the noise generation LES numerical prediction was performed for the predominant frequency of 350Hz only. For purposed of simplification, the precise modelling of the temporal temperature variations was exchanged with only a sinusoidal temperature fluctuation of 350Hz. The spatial temperature variations were neglected in this study. Figure 6.29 shows sound pressure level against axial distance of the nozzle x configuration run for uniform and multiphase model. The noise level for the uniform case is visibly larger by 2-3dB in the chosen axial distance range. The emitted noise level at the exit plane is about 165dB entailing that the phase shift makes very little difference on the overall noise level. The general sound pressure level for the numerically predicted nozzle is larger than observed when performing a more precise modelling of spatial and temporal temperature variations due to a simplification procedure not allowing a good match of temperature fluctuations with those observed in the OTRF.

The noise is being generated at the NGV section of 0.05m in length, at the throat where the area of the nozzle is changing drastically a sharp rise in dynamic pressure fluctuations amplitude is observed. After levelling off further downstream, the flow experiences a shock determined by the chosen flow conditions. At the duct extension region of the constant

cross area the noise level is experiencing a sinusoidal behaviour, which is similar to the Direct Numerical Simulation for the sound pressure level generated in a nozzle by the entropy fluctuations presented by Gatski (Gatski, 2013).

6.8 Chapter Conclusions

In this chapter, the generation of entropy noise was investigated on a nozzle configuration reproducing the acceleration rate of half a turbine stage. Large Eddy Simulation was chosen as a turbulence model to achieve the best accuracy of results and resolve the flow field. The experimental measurements carried out in the OTRF showed that the 'hot spot' is characterised by a larger temporal temperature variation than its environment. The range of spatial and temporal variations was numerically modelled and matched very well that of the facility.

In order to investigate the entropy noise generation, the necessity to model temperature variations was resolved using user-defined functions with total temperature variations matching very well those observed in the measurement plane of the facility. The LES numerical prediction requires to acquire a waveform of several thousand time steps in order to cover the frequency range of interest. The validation of the numerically obtained data and its consistency was performed using the available experimental data.

Since there are two types of temperature variations observed in an engine combustor exit profile: spatial, determined by temperature difference between the flame and the cooling endwalls, and temporal, temperature fluctuations generated by turbulence due to unsteady burning of the flame. The modelling of a 'quiet' nozzle based only on the temperature fluctuations was performed.

The LES numerical prediction was carried out to evaluate the influence of frequency on the level of entropy noise. The data was evaluated against Mach number showing a constant increase of entropy noise for lower frequencies below 500Hz and less entropy noise generation for higher frequencies. That shows that entropy noise is influential in the lower frequencies.

Investigation of temperature dissipation along the nozzle was performed as well. It confirmed the LES prediction of entropy noise and showed the presence of the entropy mode velocity. Temperature dissipations for the nozzle x and nozzle 1.5x configurations along the axial distance were compared. A quicker dissipation rate along nozzle 1.5x was observed. The phase shift modelling of the temporal temperature variations was carried out showing that the noise level decreases insignificantly when the phase shift is considered.

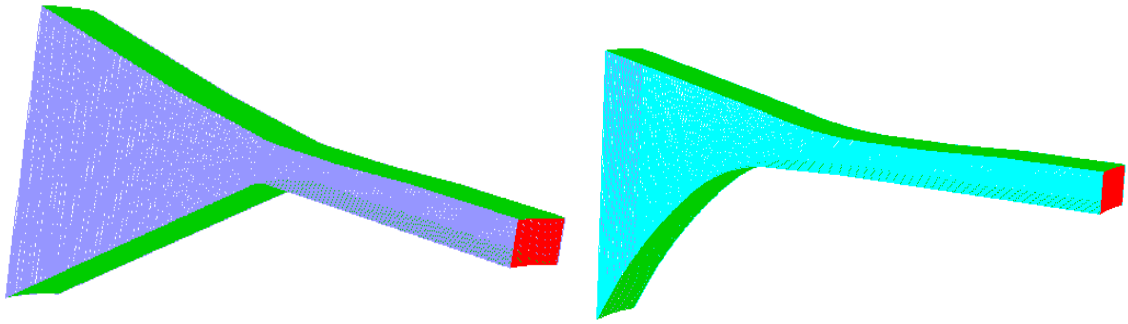

a) *b*)

Figure 6.1: Boundary conditions applied to nozzle x (*a*) and nozzle 1.5x (*b*)

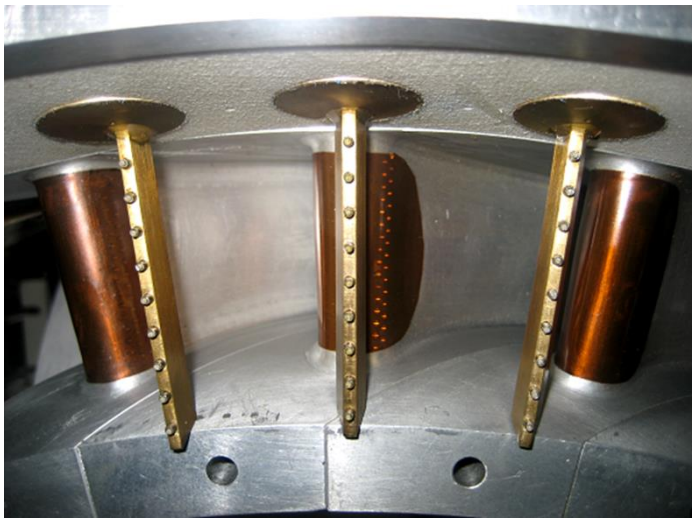

Figure 6.2: Temperature sensors at the NGV

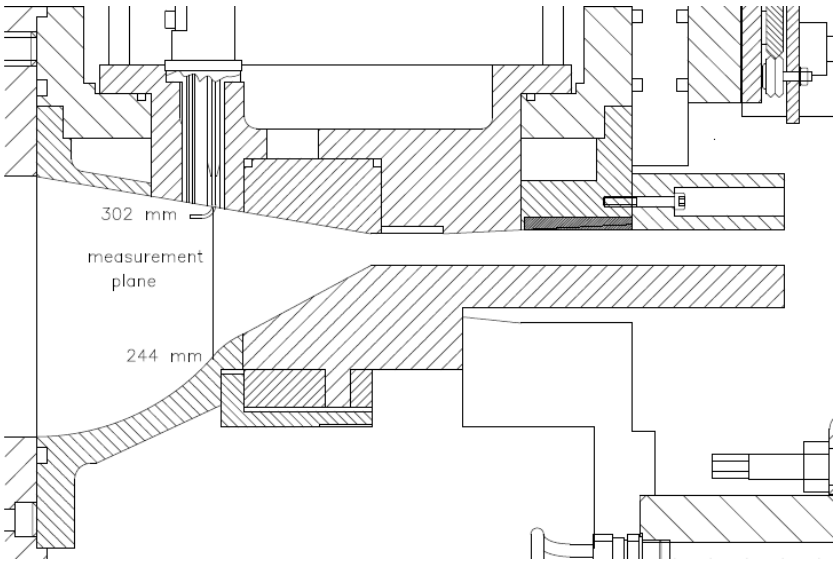

Figure 6.3: Location of the measurement plane

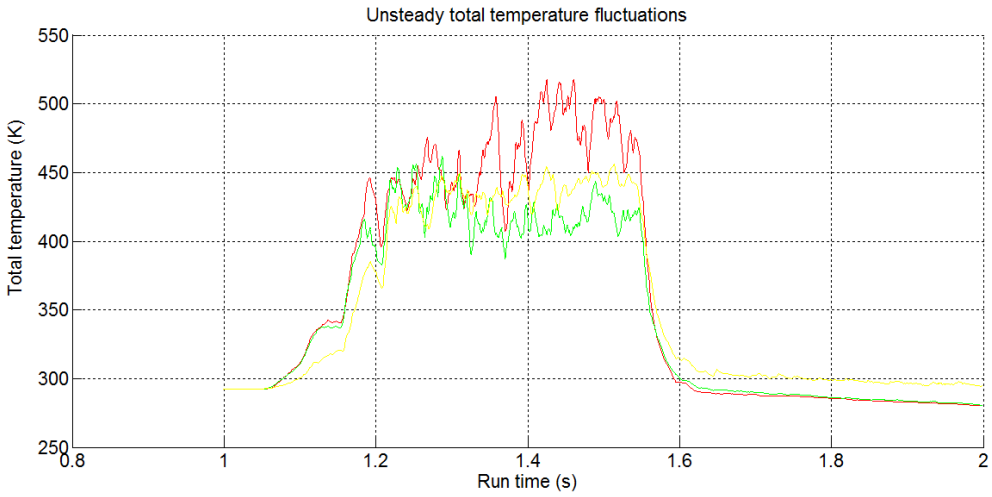

Figure 6.4: Total temperature fluctuations over run time

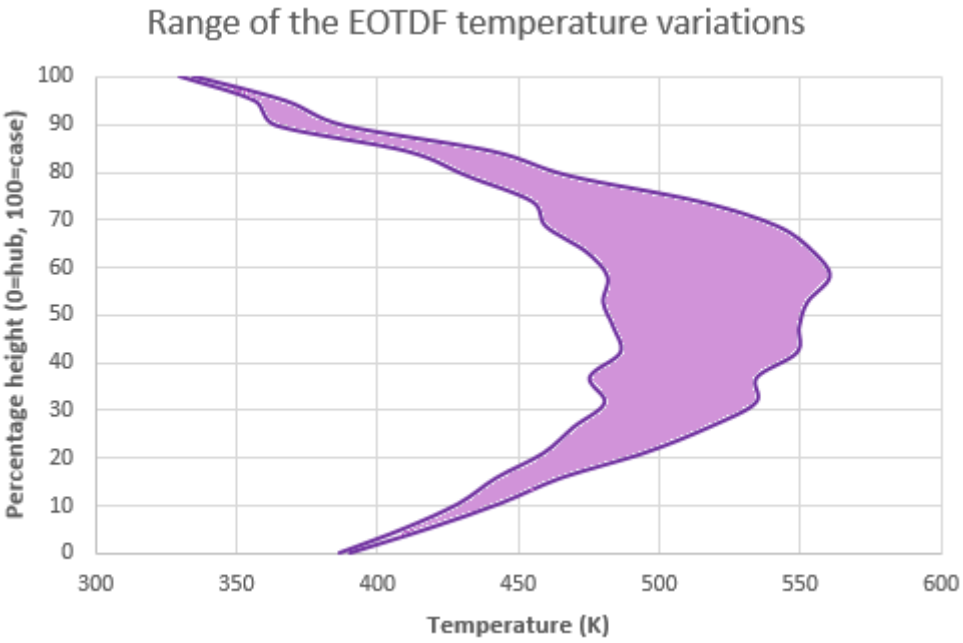

Figure 6.5: Range of the EOTDF temperature variations

Figure 6.6: Tube modifications investigated

Figure 6.7: Mesh of the model with the tubes and constant area chamber

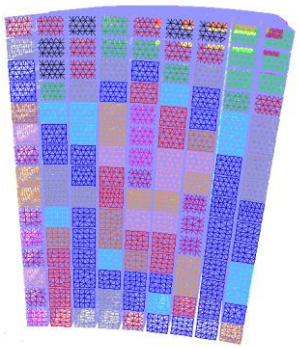

Figure 6.8: User-defined functions applied at each of the inlet sections

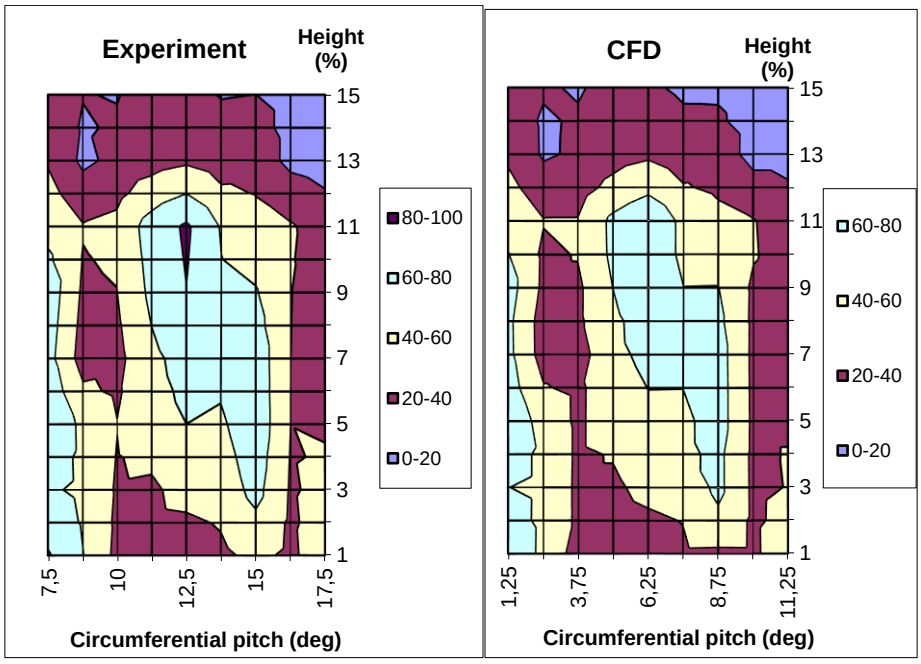

Figure 6.9: Comparison of the experimentally measured in the OTRF and numerically modelled unsteady total temperature profiles evaluated at the location of the measurement plane

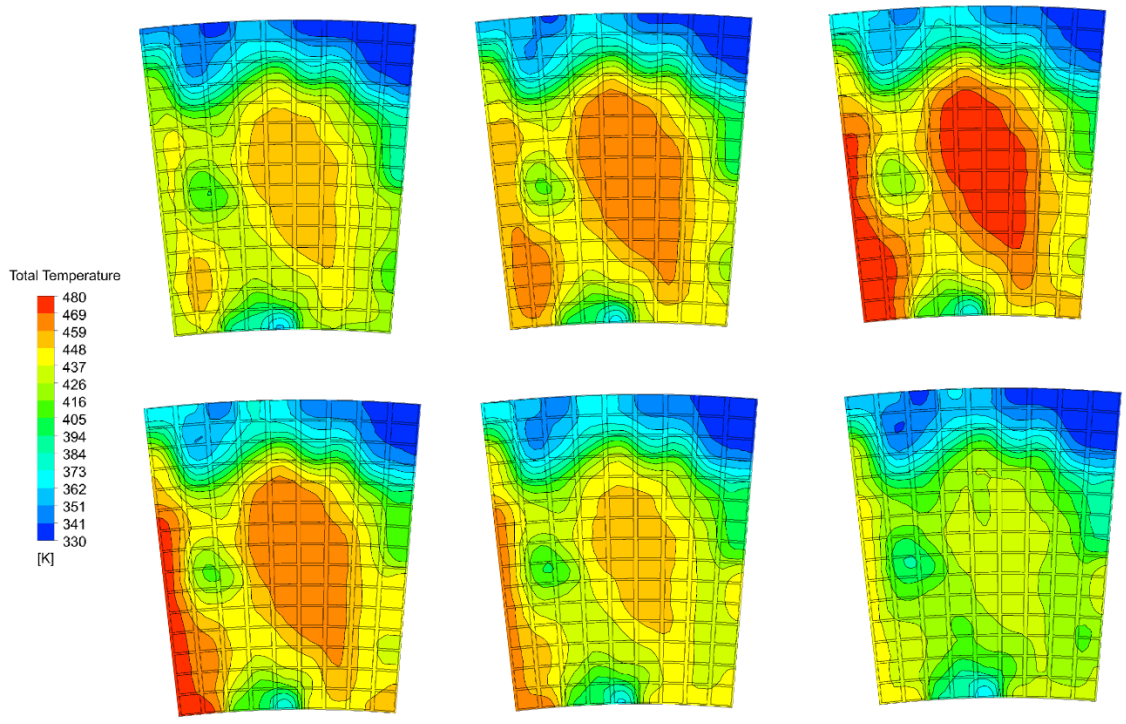

Figure 6.10: Evolution of the EOTDF temperature profile evaluated at the location of the measurement location

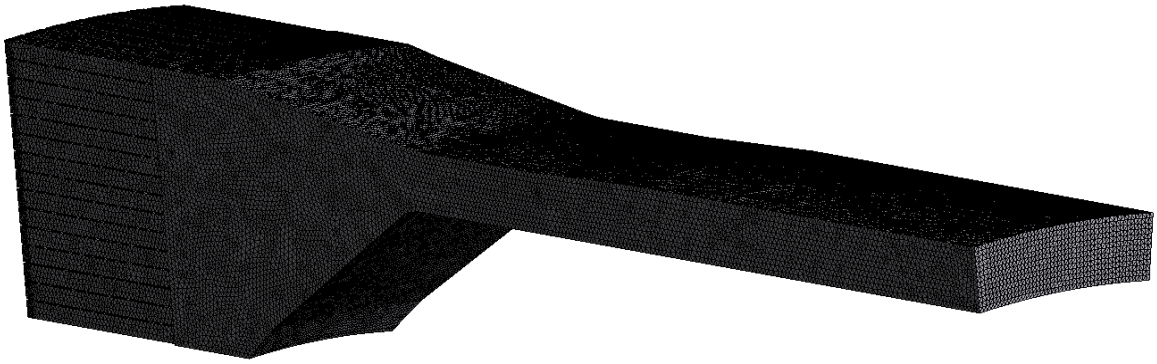

Figure 6.11: Mesh of the computational model

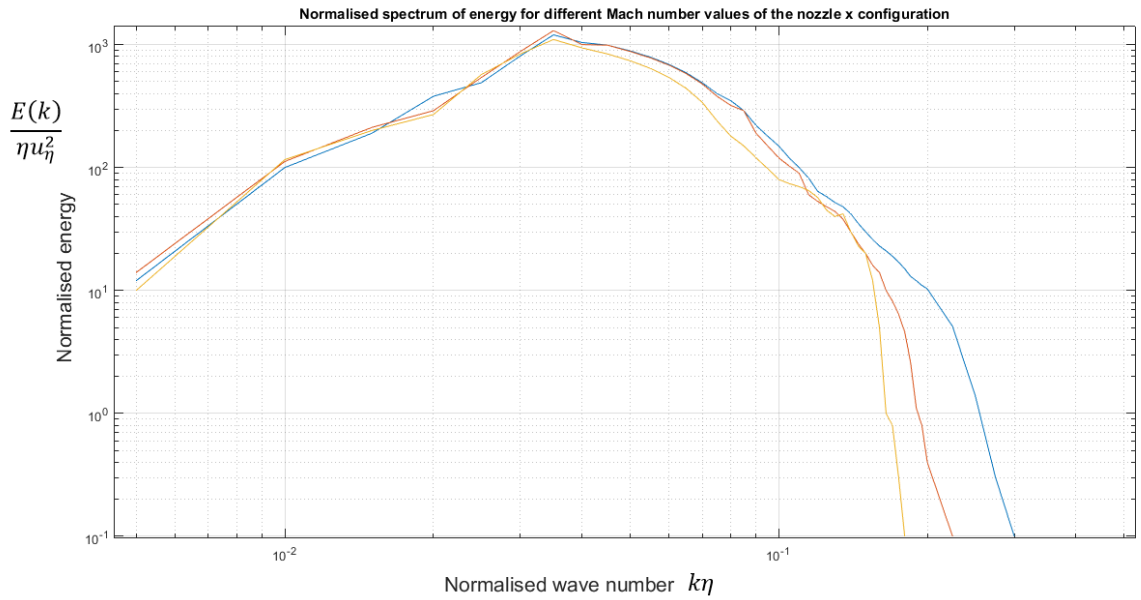

Figure 6.12: Normalised spectrum of energy for different Mach number values of the nozzle x configuration

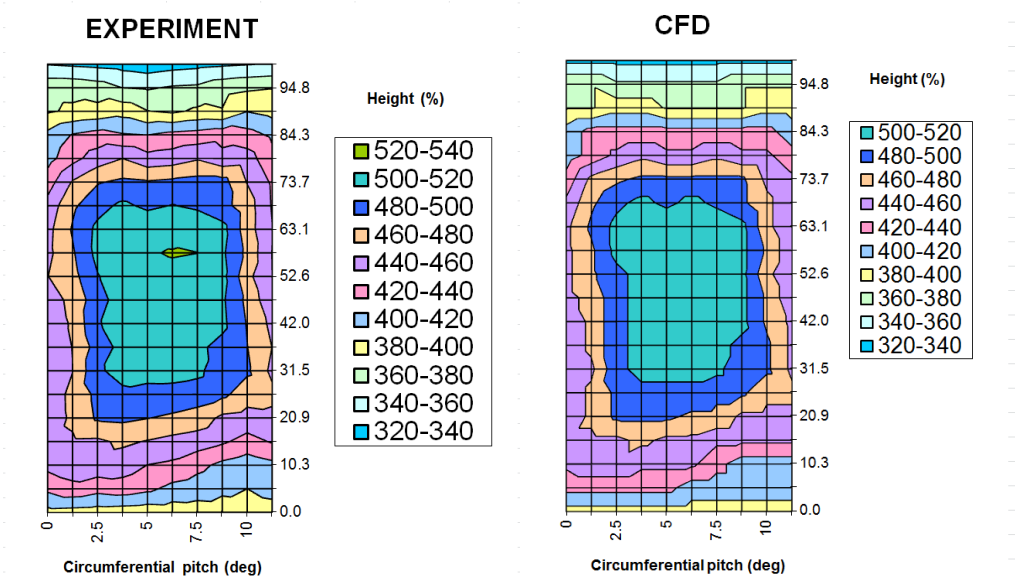

Figure 6.13: Comparison of the two-dimensional EOTDF temperature profile measured in the OTRF and obtained with LES numerical predictions evaluated at the location of the measurement plane

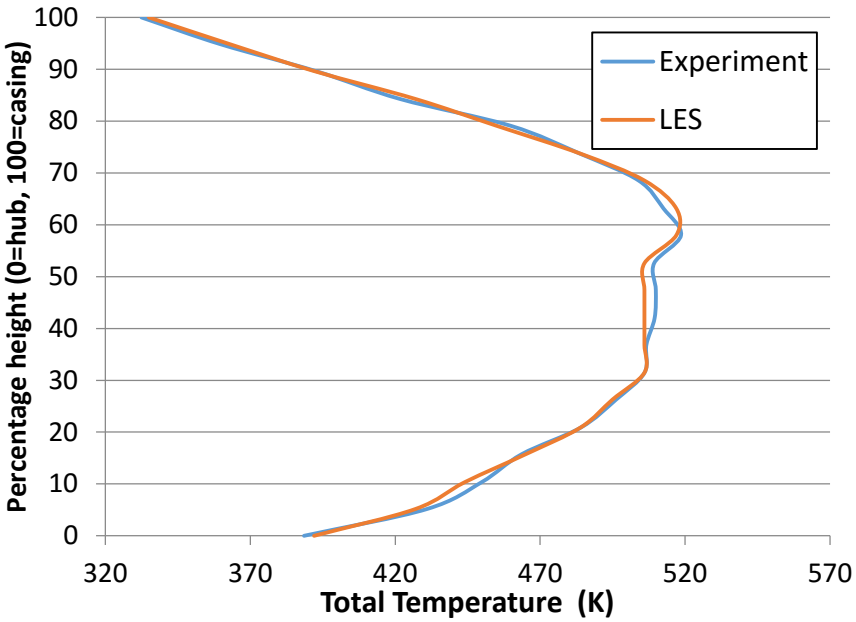

Figure 6.14: Comparison of the EOTDF temperature profile against radial pitch for the OTRF experimental and LES numerical case evaluated at the location of the measurement plane

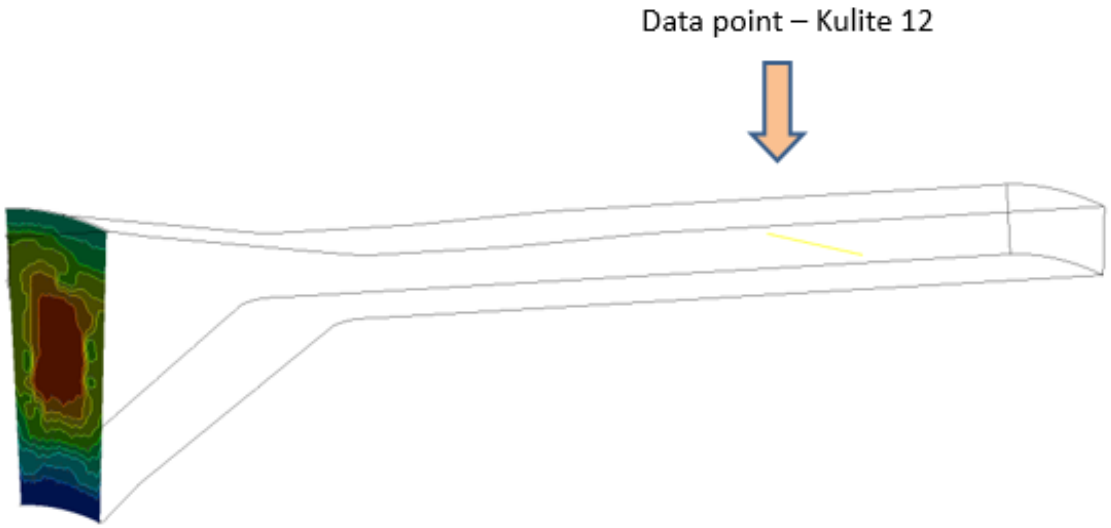

Figure 6.15: Computational model with the EOTDF temperature profile imposed upstream and data processing location marked with an arrow

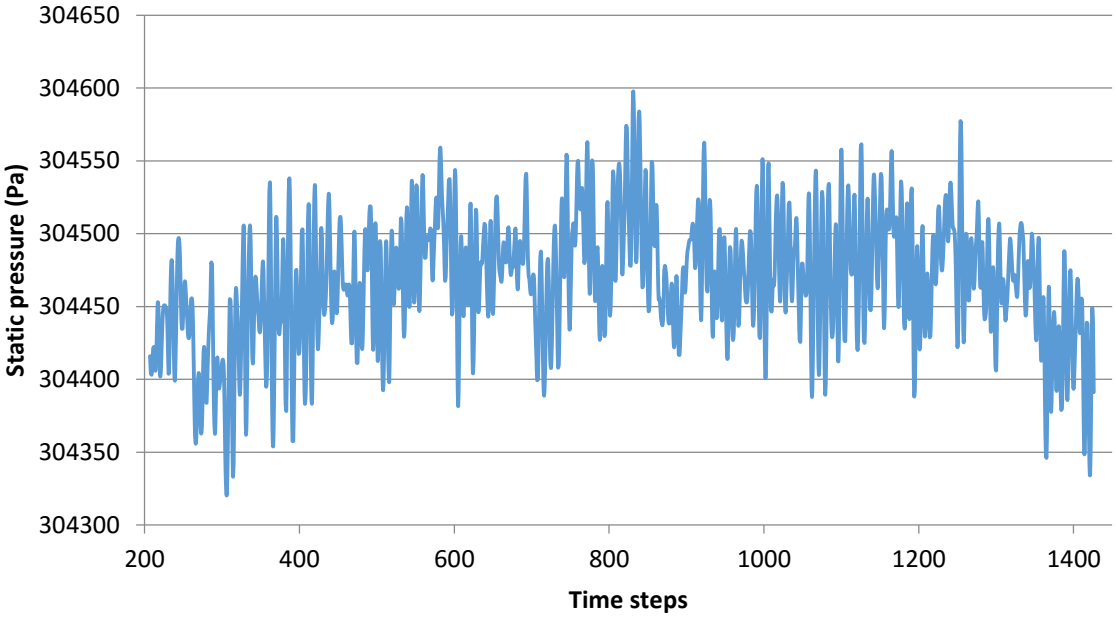

Figure 6.16: Waveform of the numerically acquired dynamic pressure fluctuations versus time steps at the measurement location of the 12th Kulite

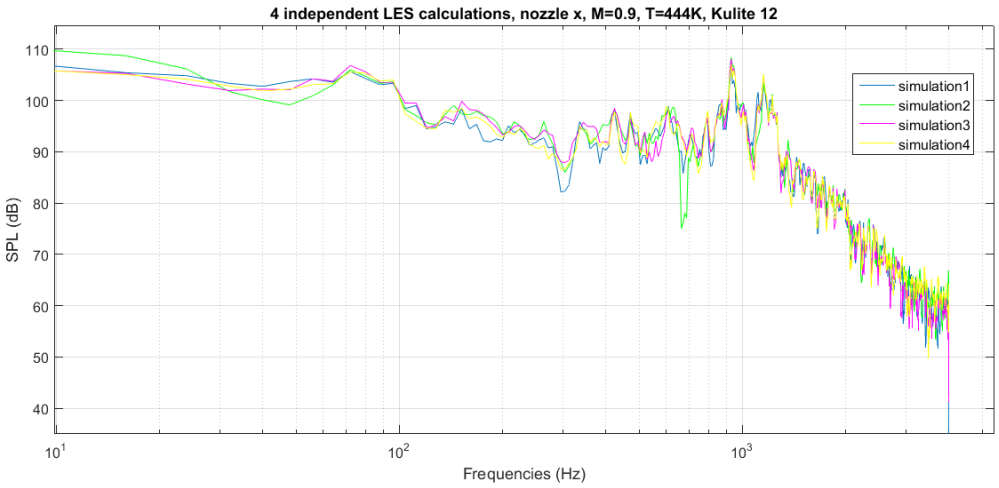

Figure 6.17: Sound pressure levels of four independent numerical simulations evaluated in the chosen frequency range

Boundary conditions	**Values**
Static pressure (outlet/inlet)	3.0bar/4.6bar
Mean total temperature	444K
Temperature fluctuation amplitude	7K
Frequency range	100-4000Hz

Table 6.1: Boundary conditions applied to the fluctuations model

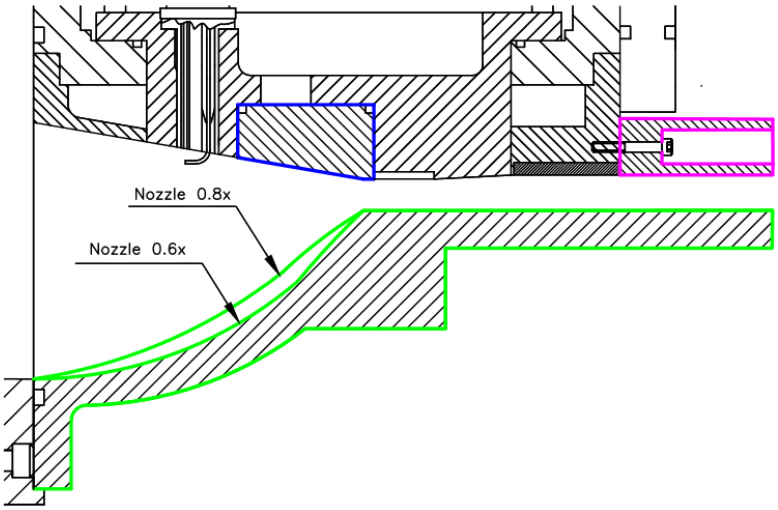

Figure 6.18: Design of the nozzle 0.8x and 0.6x configurations

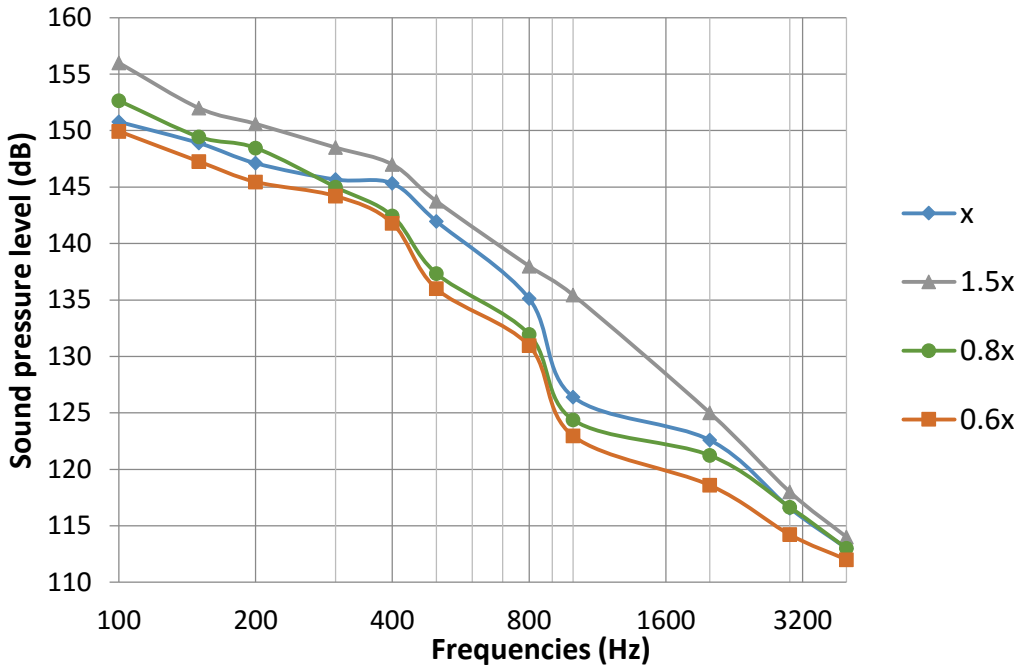

Figure 6.19: Sound pressure levels over frequencies for four nozzle modifications

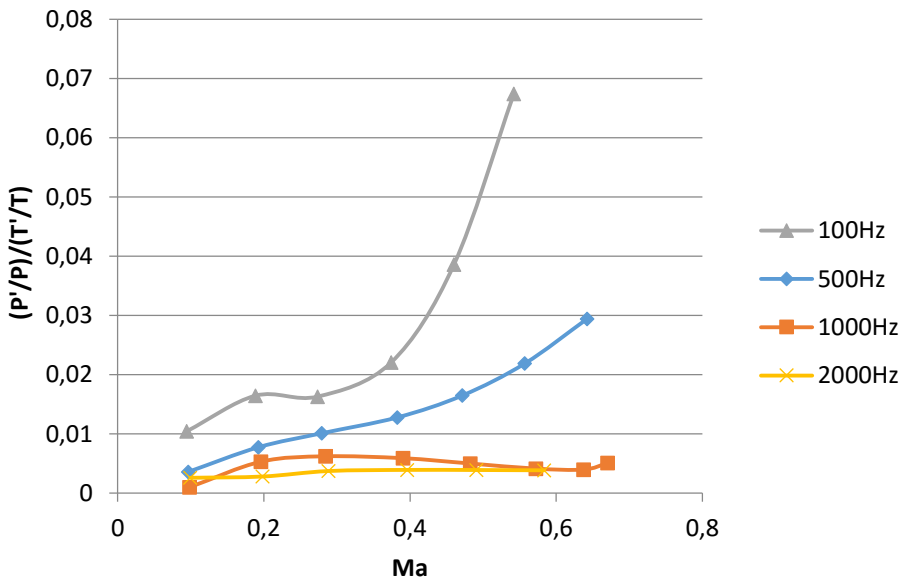

Figure 6.20: Normalised static pressure over temperature fluctuations against Mach number for the nozzle x configuration

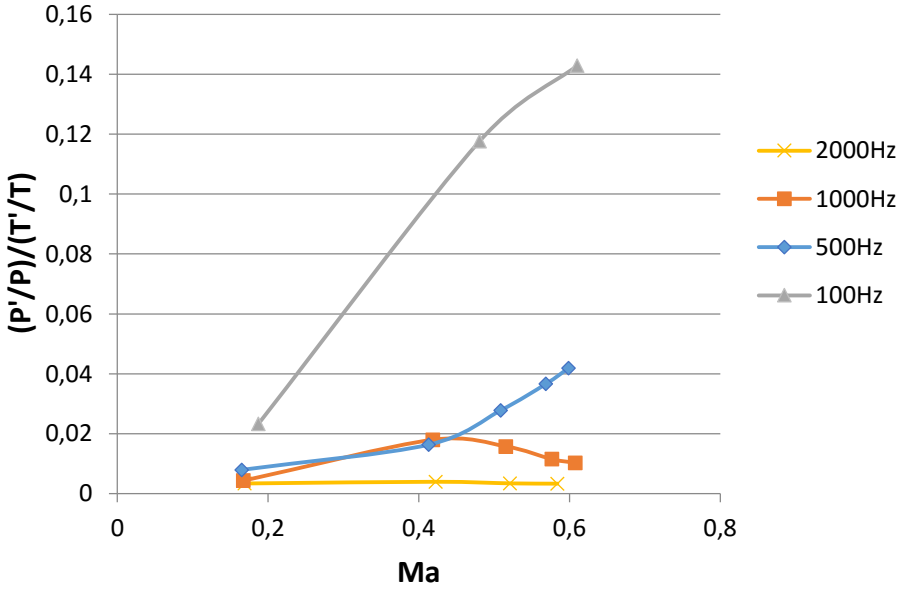

Figure 6.21: Normalised static pressure over temperature fluctuations against Mach number for the nozzle 1.5x configuration

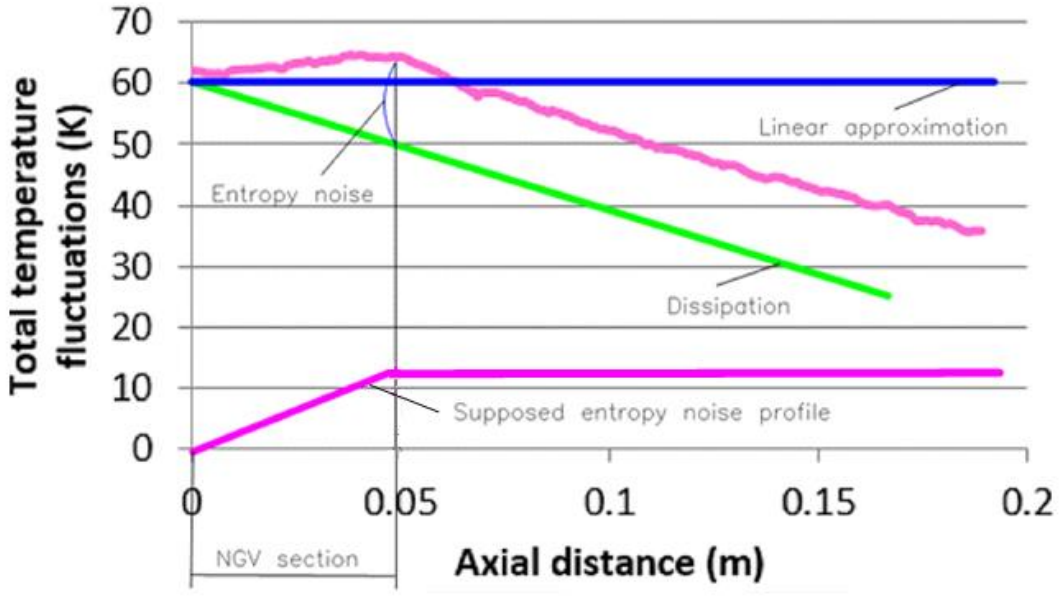

Figure 6.22: Analysis of dissipation of total temperature fluctuations in nozzle x

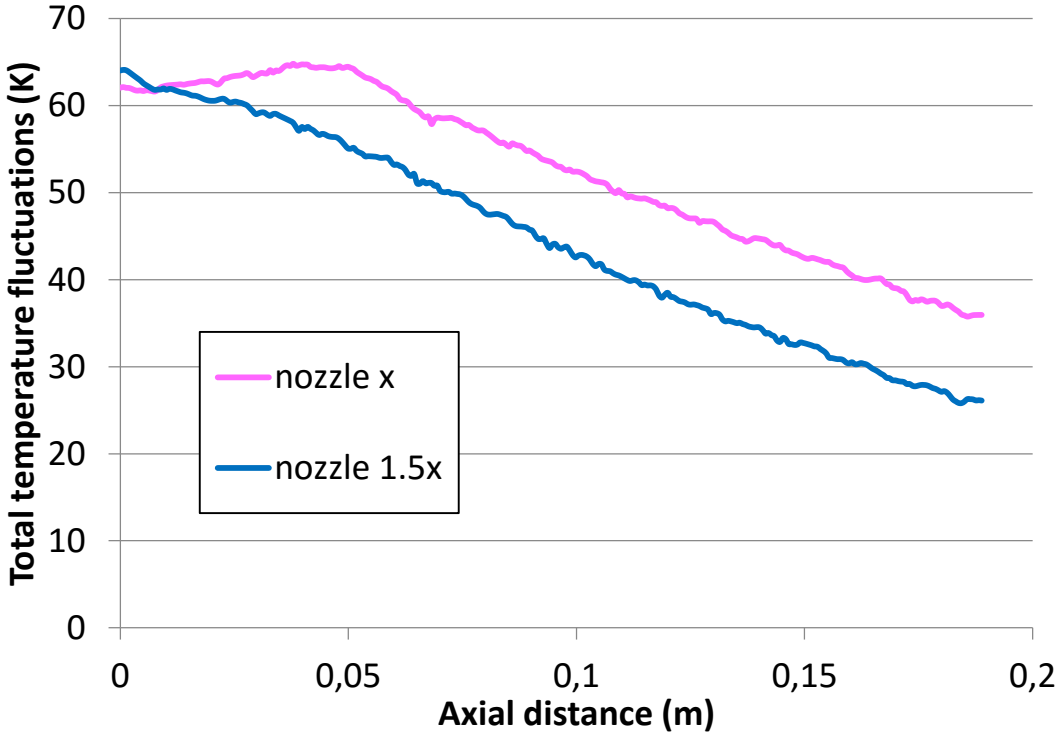

Figure 6.23: Dissipation of total temperature fluctuations in nozzle x and nozzle 1.5x

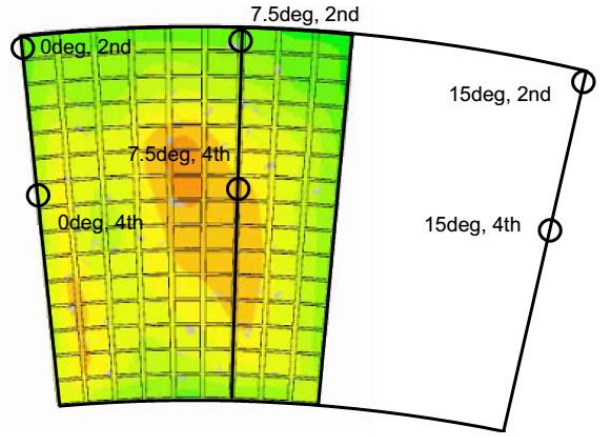

Figure 6.24: Location of the chosen thermocouples within the nozzle computational domain

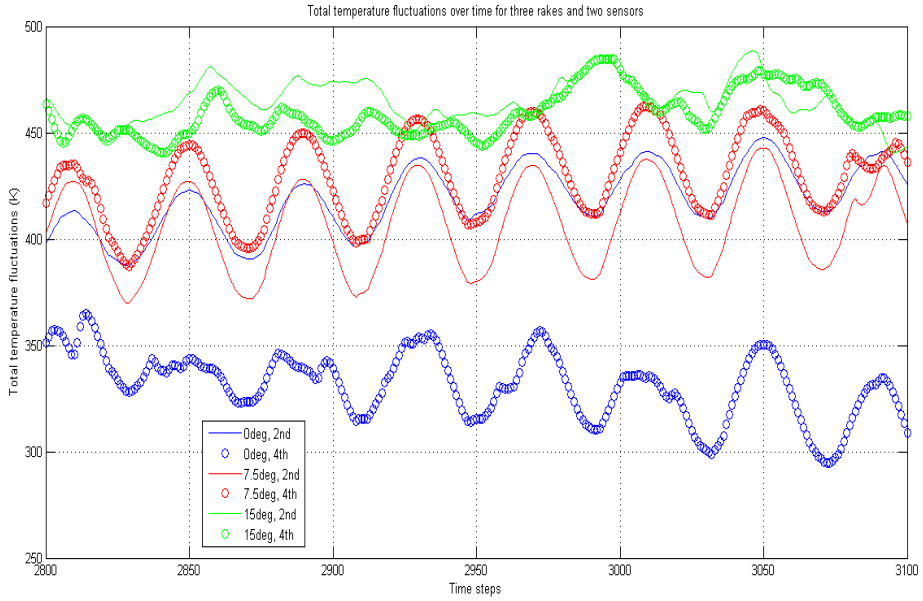

Figure 6.25: History of total temperature fluctuations for the chosen thermocouples over time steps

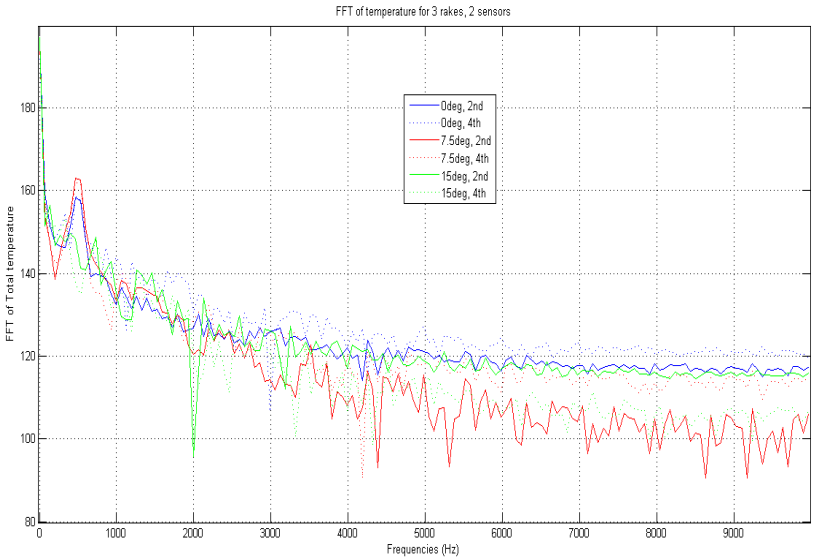

Figure 6.26: FFT of temperature fluctuations for the chosen thermocouples

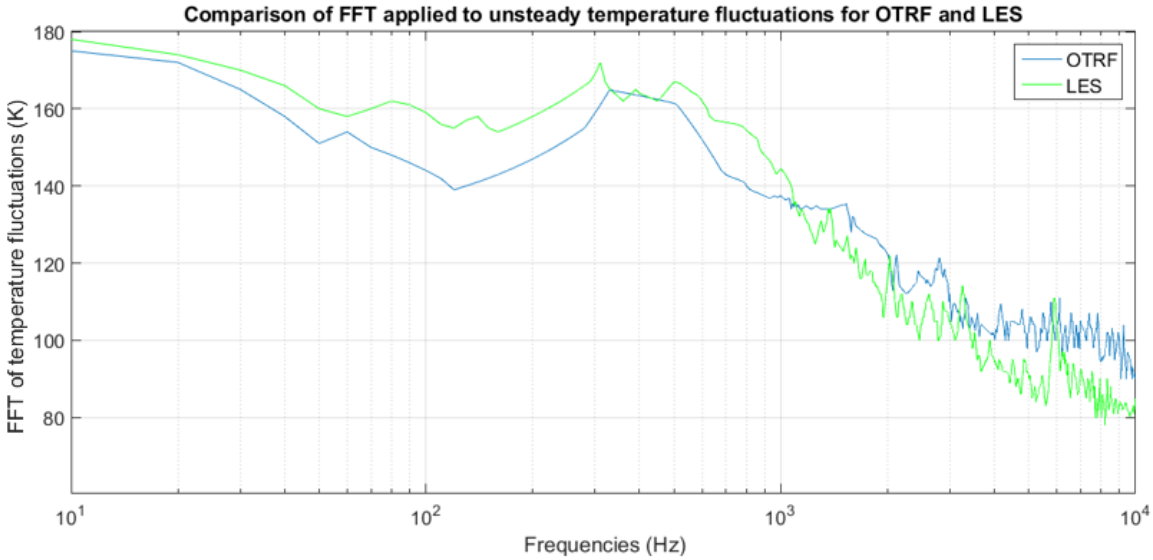

Figure 6.27: Comparison of the Fast Fourier Transform of temperature fluctuations evaluated against the targeted frequency range at the 4th thermocouple located at the 7.5 degree rake for the OTRF and LES data

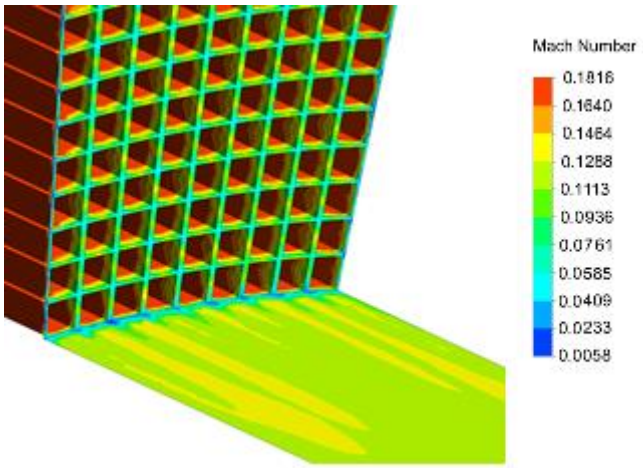

Figure 6.28: Mach number contours of the flow injecting inlet sections

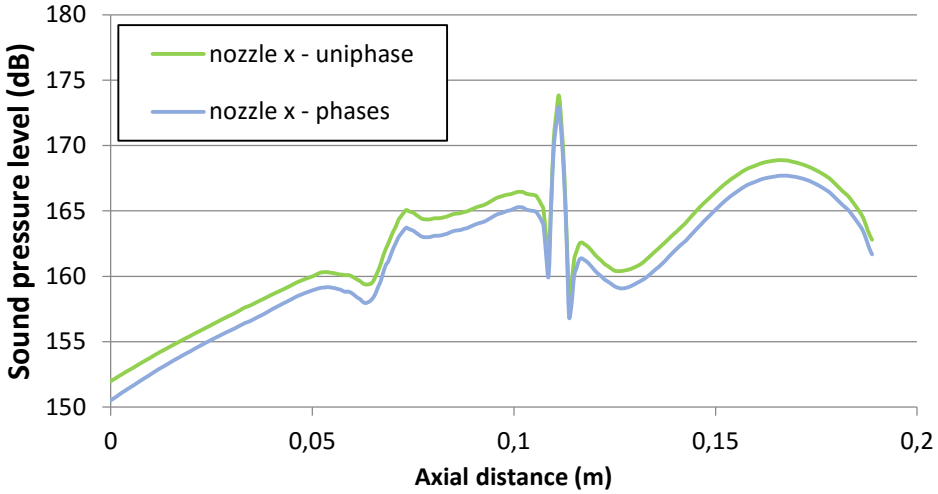

Figure 6.29: Sound pressure level along the nozzle for the uniform and multiphase temperature model

Chapter 7

Numerical Investigation of Entropy Noise in half a Turbine Stage

Entropy noise in a turbine stage is generated by accelerating inlet temperature variations which are spatially and temporarily varying at the exit of the combustor. A lot of unsteady numerical computations were performed to investigate such crucial parameters as heating of the first-stage rotor (Dorney, 2011), thermal fatigue, migration of the hot streaks (Dring, 1989) and other issues arising from a non-uniform distribution of temperature in the combustion chamber, but only limited attention was paid so far to the generation of unsteady dynamic pressure fluctuations by these temperature variations.

7.1 Investigation of Entropy Noise at the Exit Combustor and half a Turbine Stage Configuration

The numerical modelling of the combustor exit temperature profile requires not only a good agreement of the modelled temperature variations with the experimental data at the location of the measurements but also encompassing such important characteristics as rotational kinetic energy, turbulent flow behaviour determined by mixing, vortex shedding in the wake of the baffles, flow interaction with solid boundaries and others. In this regard, the most viable method of reproducing temperature instabilities observed in the OTRF is to model the combustion chamber inlet section hot mainstream air and radial slots at the

hub and casing and circumferential baffles responsible for injection of coolant air to generate the and temperature profile in the radial and circumferential directions.

The non-uniform temperature profile modelled this manner is characterised by intrinsic temperature variations in the spatial and temporal domains. Later, these temperature variations propagate downstream and accelerate at the region of the nozzle guide vanes, thus generating entropy noise. Attachment of half a turbine stage section to the combustor simulator allows to model accurately the generation of entropy noise in the region of the stator blades and quantify its dependence on Mach number. Validation of the data might be performed by comparing the Isentropic Mach number distribution along the pressure and suction sides of the blade.

7.1.1 Meshing

Numerical simulation of entropy noise was carried out for the MT1 NGVs preceded by the original inlet section. The NGV section contains 32 stator blades located uniformly around the circumference. Figure 7.1 shows a three-dimensional model of the working section of the facility with the rotor blades removed. The geometry, location and angular orientation of the blade matches exactly those of the MT1 vane. The casing wall was left intact.

To generate the inlet temperature profile the working section of the facility was fitted with the non-reacting combustor simulator starting from the section responsible for the injection of hot air to the radial slots at the endwalls and baffles feeding coolant air. Figure 7.2 illustrates a section of the combustion chamber accounting for two ‘hot spots’. The chamber contains 32 circumferential baffles located equidistantly. They are aligned to

NGVs to avoid clocking, variation of the 'hot spot' in the circumferential direction, implying that the 'hot spot' will enter the vane section between two baffles.

Based on the fact that the nozzle and combustion chamber are symmetrical in nature in the circumferential direction, only one passage section of the model was required to be meshed. The NGV aerodynamic design is for an axial flow inlet angle and the mean exit angle from the NGV at around 70 degrees.

The circumferential angle of the simulated section is 11.25 degree accounting for one sector between two baffles. This choice of angular dimension is explained by the fact that the flow simulation is more accurate if the mesh represents the fluid motion in the passage between the suction and the pressure side of the blade and between two baffles at the combustion chamber. Figure 7.3 illustrates the span view of the assembled model, the baffles and vanes were schematically reproduced. The computational domain was extended along the turbine sector for a full axial chord length downstream of the blade trailing edge to enable a good match with the Mach number distribution of the experimental data. Figure 7.4 shows the front view of the meshed model. Vane and baffles were schematically reproduced at their locations. The mesh represents the flow field within the specified geometry discretised with grid cells to achieve the resolution required to reproduce the geometrical and physical flow features. Unstructured hexahedral mesh containing approximately 4.2 million grid cells was generated.

7.1.2 Turbulence Model

The simulation of the combustor and half a turbine stage computational model requires to resolve the flow field in a relatively simple configuration with boundary conditions not of

an engine case, but of the OTRF. The EOTDF temperature profile is much lower than that of a typical rich-burn combustor. In addition, the numerical simulation requires to achieve a mixing and temperature distribution within the operational range with minimal computational costs. Hence, the Unsteady Reynolds Averaged Navier-Stokes (URANS) turbulence model was chosen.

The spatial and temporal averaging in the URANS turbulence modelling is based on the Reynolds decomposition presenting a fluid quantity as:

$$f(x,t) = \bar{f}(x,t) + f'(x,t). \quad (7.1)$$

It expresses an idea that instantaneous values of fluid quantity *f* can be decomposed as a sum of its ensemble average value $\bar{f}$ and its turbulent fluctuation value f'. The ensemble average value is defined as:

$$\bar{f}(x,t) = \lim_{n\to\infty}\left(\frac{1}{n}\sum_{k=1}^{n} f^{(k)}(x,t)\right). \quad (7.2)$$

Physically $f^{(k)}$ represents the value of the fluid quantity *f* at time *t* and position *x* during realisation of k^{th} experiment. Mathematically this is a random value of quantity *f*. The chosen averaging method takes the mean values at a fixed position x with the time span large enough for ergodicity principle to apply, thus making the averaging independent of time:

$$\bar{f}(x,t) = \lim_{T\to\infty}\left(\frac{1}{T}\int_0^T f(x,t)dt\right). \quad (7.3)$$

The ensemble averaging operator filters out the contribution of turbulence fluctuations and the Navier-Stokes equation can be rewritten in terms of averaging variables:

$$\frac{\partial \overline{u_i}}{\partial t} + \frac{\partial \overline{u_i u_j}}{\partial x_j} = -\frac{1}{\overline{\rho}} \frac{\partial p}{\partial x_i} + \frac{\partial \overline{\tau_{ij}}}{\partial x_j} - \frac{\partial}{\partial x_j} (\overline{u_i' u_j'}). \quad (7.4)$$

The last term on the right hand side of equation (7.4) results from time-averaging and can be a dominant part in the total shear stress. Since the term appears only due to the Reynolds averaging it is called Reynolds stress. It physically represents the averaged motion if i-component of the momentum in j-direction caused by fluctuations in the turbulent flow. Modelling of this tensor is one of the most direction in numerical methods.

The modelling of the Reynolds stress tensor $\overline{\tau_t}$ is based on the Boussinesq hypothesis:

$$\overline{\tau_t} = 2 v_t \overline{S_{ij}} - \frac{2}{3} v_t \delta_{ij} \frac{\partial \overline{u_k}}{\partial x_k} \quad (7.5)$$

The closure of the system of equations is thus concentrated on the definition of v_t turbulent kinetic viscosity. In the present study unsteady Reynolds-averaged Navier-Stokes computation with $k - \epsilon$ turbulent model was used. It is a usual model in low and high Reynolds number formulations. The turbulent kinetic viscosity v_t is expressed as:

$$v_t = C_\mu \frac{k^2}{\epsilon}, \quad (7.6)$$

where k and ϵ represent turbulent kinetic energy and its dissipation rate respectively.

The validation of results will be carried out by comparing the isentropic Mach number distribution along the suction and pressure sides of the vanes measured during the experiment in the OTRF and predicted numerically. Hence, the modelling of the boundary layer for the URANS turbulent model became an important issue.

The modelling of the flow behaviour within the boundary layer is performed by employing wall functions. The use of wall functions significantly reduces the number of computational

points required in the boundary layer region for resolving the flow motion. The boundary layer thickness δ is defined as the distance from the wall where the fluid velocity is 0.99 of the free-stream velocity. Inside the boundary layer regions are distinguished, the inner and outer layer. The outer layer resides usually in the region between 0.2δ and δ. The outer layer is affected by the free-stream velocity and pressure gradients. The inner layer can be decomposed into three sub-layers: the logarithmic region, the buffer layer and the linear sub-layer. Almost all turbulent flows in the inner layer exhibit a universal velocity distribution behaviour referred as the law of the wall.

The flow velocity and distance from the wall might be presented through their non-dimensional analogues as:

$$y^+ = \frac{\overline{u_w} y}{v} \quad u^+ = \frac{\bar{u}}{\overline{u_w}}, \text{ (7.7)}$$

where $\overline{u_w}$ is skin friction velocity,

$$\overline{u_w} = \sqrt{\frac{\overline{\tau_w}}{\bar{\rho}}} \text{ (7.8).}$$

It is observed that the linear sub-layer usually resides between the wall and values of y^+ close to 5, the buffer layer between y^+ around 5 and 40, and the logarithmic layer above 40. The non-dimensional velocity in the linear sub-layer and in the logarithmic layer can be analytically presented as follows:

$$u^+ = y^+, 0 < y^+ < 5 \text{ (7.9)}$$

$$u^+ = \frac{1}{k} ln y^+ + C, y^+ > 40. \text{ (7.10)}$$

The law of the wall is applied at the logarithmic layer, while the computational domain must be generated with sufficient grid resolution so the sub-layer be modelled according to the principle of linearity between the dimensionless flow velocity and distance.

7.1.3 Boundary Conditions

Computation of the meshed model was performed in the FLUENT software package. The specification of the air and solid wall conditions was required. The computational domain was used to simulate two temperature profiles: uniform of 444K and EOTDF with the area-averaged temperature of 444K. Figure 7.5 and 7.6 show boundary conditions applied to the model zones for the EOTDF and uniform temperature profile respectively. Five zones were specified as pressure inlet (pictured blue) for the EOTDF case – the mainstream, two slots at the hub and casing wall and two contiguous baffles; one inlet zone was maintained for the uniform temperature profile generation. Fully reflective boundary condition was chosen for the outlet (red) to allow reflection of the acoustic wave to take place and reproduce the correct features of the flow field. Periodicity was enforced along the model sides (yellow), whereas the baffles, vane sides and walls were defined as no-slip walls (black).

Table 7.1 shows the value of boundary conditions applied at the inlet and outlet of the model for the EOTDF temperature profile. The uniformly distributed temperature and pressure conditions were enforced at the inlet sections. To generate the EOTDF temperature profile the inlet total temperature conditions for two slots and two baffles were lowered to 300K, thus generating temperature non-uniformities leading to the

production of entropy noise in the blade section. For generation of the uniform temperature profile the mainstream temperature was maintain at 444K.

7.1.4 Results

7.1.4.1 Temperature Profile Comparison

Figure 7.7 shows the comparison of the EOTDF temperature profile generated experimentally and numerically as a percentage height of the radial pitch. The measurement plane is located 29.5mm upstream of the vane leading edge. The numerical prediction matches well with the experimentally measured profile achieving the same minimum-to-maximum total temperature ratio. The hub and casing wall temperature values are similar in both cases. The CFD prediction is characterised by a higher temperature gradient producing a larger 'hot spot' area than the experimental measurements. Thus, the 'hot spot' in the numerical prediction, although matching the measured position in the radial direction, spreads over more than half a pitch height. The largest discrepancy nonetheless does not exceed 30K and being confined to the wall region represents the experimental range of the EOTDF temperature profile.

Figure 7.8 presents percentage difference of temperature between measured experimentally and obtained numerically EOTDF temperature profile evaluated at the location of the measurement plane. It can be noted that temperature difference does not exceed 10% with the largest difference being observed at the 20 and 80% of the radial height and diminishing to less than 1 percent at the region of 'hot spot' and near the walls. Thus, it can be concluded that the temperature profile generated numerically is not only

within the experimental range of the OTRF, but achieves the same temperature difference between the 'hot spot' and the 'cold spot'.

It is worth noting that the modelling of the temperature profile the way it is generated in the combustor simulator allows to make a realistic assessment of the flow field and include in the calculation such important parameters as the flow mixing and vortex shedding in the wake of the baffles. These all are showed to be crucial factors in the indirect combustion noise modelling (Dowling, 2015). The modelled uniform mean temperature profile matches experimental data very well since the flow is injected through the mainstream inlet sector only.

7.1.4.2 Isentropic Mach Number on the Blade Surfaces

To validate the numerical data the distribution of isentropic Mach number on the stator blade has been compared with the available experimental data from the basic MT1 NGV. Figure 7.9 shows the comparison of the CFD prediction with experiment data along the suction and pressure sides for three pitch heights of the blade: 10, 50 and 90% span.

The isentropic Mach number is defined as:

$$M = \sqrt{\frac{2}{\gamma-1}\left[\left(\frac{p}{p_t}\right)^{\frac{1-\gamma}{\gamma}} - 1\right]} \quad (7.11)$$

The CFD prediction shows a good agreement with experimental data for the pressure side, whereas some regions of an excessive acceleration are notable at the suction side, especially near the trailing edge of the blade. The numerical simulation struggles to predict the flow behaviour in this region. This might be resolved by a better grid resolution as well as a more accurate geometry modelling of the trailing edge. As noted, the isentropic Mach

number distribution does not experience a serious discrepancy between two cases, thus the aerodynamic behaviour of the flow is well predicted by the numerical simulation (Gundy-Burlet & Dorney, 2011).

7.1.4.3 Entropy Noise at the Stator Blade Section

The overall aim of the entropy noise investigation is to quantify the dependence of the sound generated by inlet temperature inhomogeneities which are spatially and temporally varying at the inlet of the test section with a turbine stage installed. By changing the injected temperature profile from the uniform to EOTDF, the entropy field is disturbed, thus entropy waves propagating downstream with the mean flow should produce an acoustic response during acceleration within the stator blade section. This acoustic response is possible to evaluate by injecting different temperature profiles to the combustor simulator. The inlet temperature profile generator was simulated and compared to measurements from the OTRF with the generator installed. The numerical predictions have been performed for the uniform profile of 444K and EOTDF temperature profile.

Figure 7.10 presents the comparison of normalised dynamic pressure fluctuations evaluated 3mm downstream of the trailing edge of the NGV at mid-height for EOTDF and uniform temperature profiles. The simulation shows no noise being generated along the stage for the uniform case, whereas the temperature difference for the EOTDF temperature profile leads to fluctuations of static pressure of approximately 120Pa, entailing that acceleration of the flow field with entropy inhomogeneities at half a turbine stage produced an additional acoustic response. The performed comparison with the

uniform temperature profile proves that this acoustic wave is not caused by the boundary layer and it propagates downstream of the stage. It is reasonable to assume that the observed acoustic response is entropy noise.

The observed entropy noise is produced by temperature inhomogeneities accelerated in the blade section. To evaluate the generated noise level the dynamic pressure fluctuations over time for the EOTDF temperature profile have been evaluated at the mid-height position of the blade section starting from the leading edge downstream to the trailing edge. This region is characterized by a rapid acceleration of the flow associated with the aerofoil geometry. Several points on the streamline of the 'hot spot' located at the mid-height were chosen at different Mach numbers. Figure 7.11 shows normalized dynamic pressure fluctuations against time evaluated at the mid-height along the stator blade. The dynamic pressure fluctuations were measured at several chosen locations with Mach number increasing and local pressure decreasing as the flow propagates downstream. The location of the Mach number data lines is presented at the top left side with colours corresponding to the local Mach number values. The amplitude of dynamic pressure fluctuations increases as the 'hot spot' propagates downstream, while the Mach number value increases. That would contradict the theory of acoustic noise propagation governed by the linear acoustic equations if only the acoustic mode were considered, and can only be explained by the generation of an additional noise at the stage during the acceleration period. A description is presented in Chapter 2 implying that this is entropy noise produced by the temperature difference between the 'hot spot' and its environment.

Figure 7.12 presents evaluation of the peak-to-peak difference of dynamic pressure fluctuations against Mach number for the EOTDF temperature profile. As shown here,

pressure fluctuations experience a rapid increase with an increase in Mach number as the 'hot spot' propagates through the NGV section. The acoutic response relates to the lower frequency case of 100Hz confirming that entropy noise is influential at the range of low frequencies. With the increase of frequency the intensity of entropy noise is shown to diminish significantly.

The pressure fluctuations are evaluated for one and a half cycles and observed to have a positive acoustic pulse succeeded by a negative. This effect may be because of the acquired stretching distance between the 'hot spot' and the 'cold spot'. If represented as an 'entropy dipole' (Figure 7.13), the 'hot spot' and 'cold spot' at the inlet section of the computation flow field are distanced only in the radial direction, the 'hot spot' at the centre and the 'cold spot' near the wall. The 'entropy dipole' accounts for generation of entropy noise since it is characterized by a density and entropy difference of the EOTDF temperature profile. Due to the fact that the 'hot spot' is propagating at a faster rate than the 'cold spot', the 'entropy dipole' is experiencing a stretching in the axial direction causing the appearance of additional shear stresses. When accelerated, the 'hot spot' is emitting an entropy noise wave, while the 'cold spot' being driven by the flow is lagging behind. The accelerated hot particle is emitting a positive sound wave, whereas the cold particle appearing later will behave as a negative acoustic source in regard to the mean temperature value since the net force of the flow field is constant within the computational volume.

More specifically, the positive pulse of the entropy wave is generated by the 'hot spot' when the latter reaches a certain noise front where the density fluctuations due to the difference between the 'hot spot' and the mean temperature is converted into an acoustic

response propagating downstream off the stage at the speed of sound, the generation of the negative acoustic signal occurs slightly later because the 'cold spot' of the 'entropy dipole' being propagated at the speed of the flow requires a certain amount of time to reach the same entropy noise front. Taking the stretching added through the vane as insignificant and neglecting the turbulent mixing the time length of the pulse will diminish as the 'entropy dipole' passes through the stage. It is observed in Figure 7.15 that the time length of a positive-negative pulse decreases by 2.5ms between the inlet and outlet of the NGV section, which corresponds well to the reduction in the axial stretching of the 'entropy dipole' calculated analytically. Figure 7.14 shows normalised against the maximum value dynamic pressure fluctuations P/Pmax for the leading (M=0.18) and trailing edge (M=0.87) of the NGV section. The change in the length of the positive-negative pulse is evident. Furthermore, Figure 7.15 presents a plot of the pulse length of the pressure signal with regard to the Mach number value of the flow. The trendline is sloping downwards as the flow accelerates.

To further validate the 'entropy dipole' mechanism, the acquired stretching between the 'hot spot' and 'cold spot' observed with URANS was compared with the analytically calculation of the stretching change along the blade. The latter was evaluated using the known geometrical characteristics of the facility and flow parameters. The velocity difference between the 'hot spot' and the 'cold spot' was calculated using equation (6.1) presenting variations of velocity as a square root proportion to the temperature variations. The acquired 'entropy dipole' stretching along the blade obtained numerically and analytically is presented in Table 7.2. It is observed that the general trend of stretching diminishing is noted for worth the URANS prediction and analytical calculation. The

difference in stretching may be ascribed to the imperfect URANS simulation and the presence of rotational kinetic energy, also having a stretching and producing an acoustic response.

The change in the length of the pulse furnishes the proof that these fluctuations are not caused by an acoustic response of any kind, but by a complicated nature of entropy noise.

This clearly validates the hypothesis that the sound pressure level for entropy noise is increasing as the turbine stage entropy waves propagate downstream and that this increase is governed by entropy non-uniformities of the temperature profile.

7.2 New Vane Modelling Procedure

The improved modelling of the EOTDF temperature fluctuations varying spatially and temporally described in Chapter 6 extends the possibility to improve the design of the stator blades in order to reduce the sound pressure level. Originally there are 32 stator blades located uniformly around the circumference. The NGV configuration was designed to let the flow exit the NGV section under a 70 degree angle. This is a complicated case for a numerical investigation since it requires prohibitively expensive computational costs arising due to a change in the flow motion and because the blade geometry may serve as an additional acoustic source presented with flow-boundary interaction. With regard to computational simplification, a new vane modelling approach was introduced.

Several possible modifications were considered. The first was a vane half as long in the axial direction with 64 blades. This was based on the nozzle hypothesis of the faster acceleration-deceleration region and its effect on the noise level in the nozzle. Unfortunately, this may not result in the desired effect due to the increase in the noise

generated within the boundary layer. A significant increase in the number of blades will definitely affect the noise level. The second modification was a vane shifted upstream as much as the facility restrictions allowed, this way letting the acceleration occur earlier and to achieve the noise decrease similar to that of the nozzle 1.5x configuration.

Because the flow experiences a 70 degree turning within the vane, the noise generation is increasingly complicated. The acoustic sources, whether located in the passage between two vanes or at the boundary layer near the trailing edge, may propagate the acoustic wave in the different directions simultaneously. That means that entropy noise is neither generated at the straight line beyond the trailing edge of the vane, nor along the flow direction. This is further complicated by the possible computational costs of running the model with all set of vanes.

As long as the noise generation within a nozzle provides reliable data and the generation of entropy noise occurs along a straight line, the following approach was applied. The original MT1 vane should be redesigned in a computational domain, thus instead of experiencing a 70 degree turning it should be straightened out along the axial distance. This way the blades will look like a set of aerofoils. Since the primary goal is to achieve a reduction in entropy noise level as compared to the current noise level in the vane, the absolute values of the sound pressure level are not of a crucial importance. If shown with a numerical simulation, a new modification can be applied for manufacturing a new vane. The noise generated in the vane was split into two categories; the noise level generated due to the aerodynamic shape of the vane and the one produced by a 70 degree flow turning. As described above the flow turning is to be excluded. Thus the only category to

investigate is the entropy noise level due to the aerodynamic shape of the blade and the influence of a new vane geometry on the entropy noise generation.

Figure 7.16 shows the original stator blade (*a*) and the modified version (*b*). The area and the perimeter of the aerofoil was kept the same. Due to the symmetrical nature of the modified aerofoils acoustic sources are located at the same regions and the entropy noise generation and propagation takes place in a simple manner.

The developed procedure allows not only to numerically evaluate the sound pressure level generated by a new vane geometry, but more importantly it proves that the experimental investigation in the OTRF based on two nozzle geometries can be further extended for vane investigation. Figure 3.4 shows that the presence of the NGVs produces an additional noise. Thus, it was imperative to prove that noise reduction achieved in nozzle modelling can be applied to the real vane designs.

The LES numerical prediction was performed according to the procedure described in section 2, Chapter 6. The EOTDF temperature profile was imposed upstream of the model at the measurement plane with total temperature fluctuations correctly representing those measured in the OTRF. The approach of temperature fluctuations rather than that used to reproduce the radial and circumferential temperature variations is justified by the emerging opportunity to evaluate the sound pressure level along the model axial direction since the temperature fluctuations as noted in Chapter 6 have a predominant frequency of 350Hz.

Two computational models were modelled following the developed noise optimisation method. The vanes were designed to represent the two manufactured nozzles. The

aerofoils were straightened but the acceleration rates of the flow were kept similar to those achieved in the designed nozzles. The unsteady computation was processed for two full cycles of temperature fluctuations following which the sound pressure level of the generated acoustic waves was acquired using the amplitude value of the dynamic pressure fluctuations. The frequency of the evaluated dynamic pressure fluctuations downstream was the same as the frequency of total temperature fluctuations imposed upstream. That means that the evaluated sound pressure level was produced by the temporal variations in temperature and can be classified as entropy noise.

Figure 7.17 shows sound pressure levels for the two modelled straightened vanes evaluated along the axial direction. The vanes were named after the corresponding nozzle geometries. The starting reference of the axial dimension was chosen as the leading edge of the straightened vane. The radial location of the presented data is the mid-height plane.

The nozzle x configuration is noticeably noisier than that of nozzle 1.5x. The sound pressure level difference at the exit of the computational model reaches approximately 7dB. Moreover, the straightened vane model corresponding to the nozzle x configuration experiences a sudden increase in sound pressure level amplitude at the trailing edge location. That may be explained by the imperfect numerical modelling of the trailing edge. The modelling of the trailing edge is a complicated process and slight geometries variations can’t be avoided. A sudden decrease and then increase in local static pressure value can be evaluated. The temporal temperature variations propagate downstream and at the region of the trailing edge experience a sudden change, thus generating an additional noise peak. Further downstream the sound pressure level becomes steady propagating through the duct extension with the same noise level and exiting with the noise level of 167dB.

Nozzle 1.5x is quieter overall, starting with the same sound pressure level at the inlet section, propagating steadily through the vane section. Nozzle x shows a slight noise decrease proceeded by a region of minor unsteadiness and finally generating 160dB at the duct extension. Based on the data observed, it can be concluded that the real vane with the acceleration rate of the nozzle 1.5x generates less noise all along the working section of the facility. In addition, the vane representing the nozzle x geometry shows a rapid increase in sound pressure level at the trailing edge of the vane warranting a more careful hardware modelling to avoid such a significant noise increase of more than 20dB. This makes nozzle 1.5x the recommended configuration not only because of the desired decrease in the general noise level, but also due to safety considerations.

It is worth noting that the evaluated sound pressure levels are hardly representative of the correct sound pressure levels in the nozzles or half a turbine stage since the vane geometries were modified in order to simplify the numerical simulation and the imposed total temperature fluctuations require further validation with experimental data. Nonetheless, this approach can be justified due to its relative simplicity, possibility to evaluate the sound pressure level not at the chosen location but along the axial distance, and to make an estimate of entropy noise in the real half of a turbine stage configuration. Furthermore, the developed approach proves that entropy noise reduction achieved experimentally in the OTRF can be applied to vane modelling, because no change in the laws governing the generation of entropy noise was observed, entailing that although there is a noise difference evaluated with and without NGVs it does not impede the entropy noise optimization developed.

The developed method of entropy noise evaluation is a useful approach to model a quieter stator blade in the turbine stage. It allows to supress the acoustic sources associated with the turning of the flow and complicated vane geometry and to perform an estimate of the noise level all along the working section. It is advantageous since the engine aerofoil geometry is used and the appearance of detrimental increases in noise levels can be predicted.

7.3 Chapter Conclusions

The generation of entropy noise in a turbine stage represents the most crucial aspect of the indirect combustion noise, since the propagation of entropy noise through the real aero engine can significantly affect the overall noise.

The numerical modelling of the combustor simulator terminated by half a turbine stage was performed. The modelled combustor simulator correctly reproduces the geometry of the OTRF combustor with coolant air introduced into the mainstream flow of hotter temperature. The modelled EOTDF temperature profile is within the experimental range, while the simulated mean flow allows to take into account such important flow parameters as vortex shedding in the wake of the baffles, rotational kinetic energy of the flow and turbulent mixing. The URANS turbulent model was chosen to achieve the required accuracy with acceptable computational costs.

Two temperature profiles were investigated: EOTDF and uniform. The numerical results show the generation of additional noise due to temperature variations of the EOTDF temperature profile. The noise increases as the flow accelerates through the blade section. That means that temperature variations in the entropy mode are being converted into an

acoustic response. The observed pulse of dynamic pressure fluctuations was investigated. The length of the pulse is shown to be dependent on the Mach number value entailing that the positive acoustic response is being succeeded by a negative due to the velocity difference between the 'hot spot' and 'cold spot'. That demonstrates that the observed dynamic pressure fluctuations represent the acoustic response of entropy noise.

The new vane modelling procedure was proposed. The aerofoil of the blades was modified to straighten the flow direction maintaining the area and perimeter of the blade. This approach allows to avoid unnecessary noise sources appearing due to the flow turning and scattering of the acoustic source of entropy noise. The geometry configurations of the designed nozzles were simulated using LES prediction. Total temperature variations observed in the OTRF were imposed upstream of the model. The numerical results show a significant decrease in the noise level along the nozzle distance for the vane model related to the nozzle 1.5x configuration. In addition, the nozzle x configuration is evaluated to produce a rapid noise increase at the region of the trailing edge.

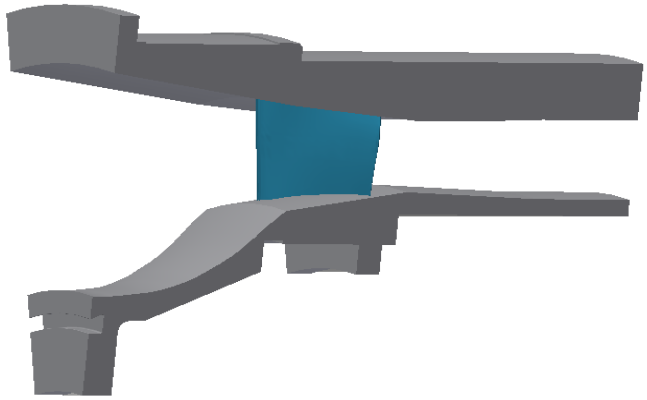

Figure 7.1: Three-dimensional model of the working section of the facility

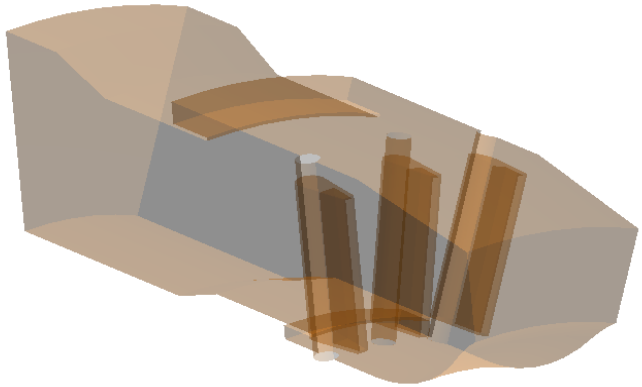

Figure 7.2: Three-dimensional model of the combustor

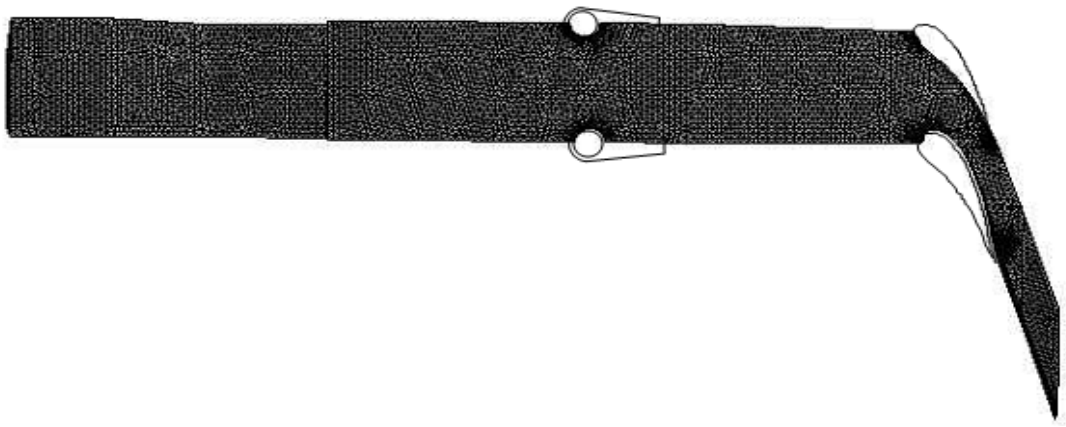

Figure 7.3: Span view of the assembled model of the combustor and vane passage with baffles and airfoil surfaces schematically present

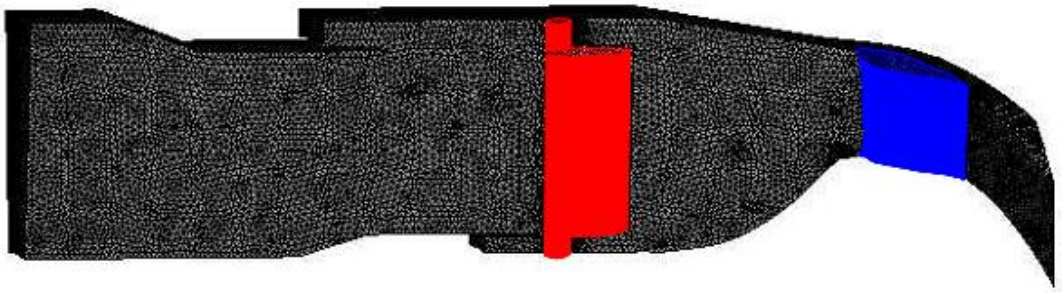

Figure 7.4: Front view of the meshed model with vanes colours blue and baffles red

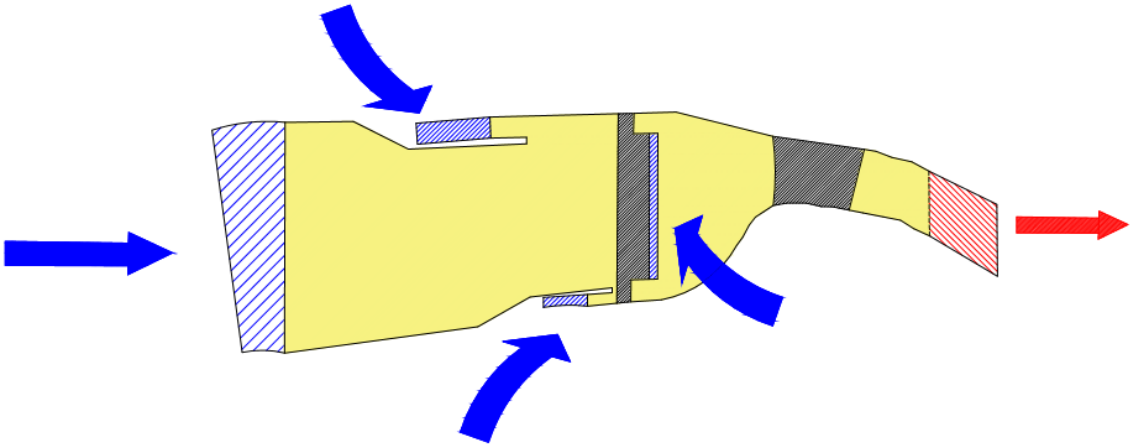

Figure 7.5: Boundary conditions applied for the EOTDF temperature profile generation

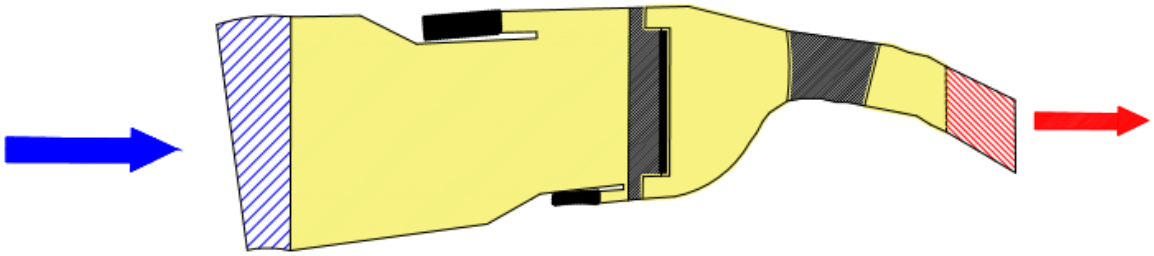

Figure 7.6: Boundary conditions applied for the uniform temperature profile generation

Boundary conditions	**Values**
Mass flow rate	14.3kg/s
Static pressure (outlet/inlet/slots/baffles)	2bar/4.6bar/4.6bar/4.6bar
Total temperature	300K/520K/300K/300K
Inlet turbulence intensity, *Tu*	12%

Table 7.1: Boundary conditions applied to the model

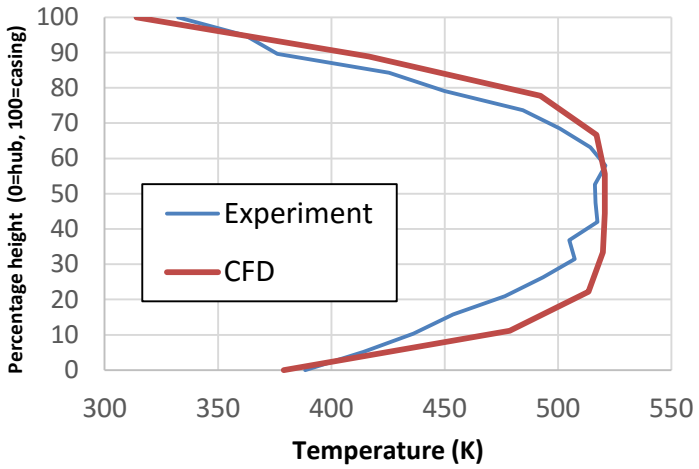

Figure 7.7: Experimentally measured and numerically obtained EOTDF temperature profile along the radial pitch evaluated at the location of the measurement plane

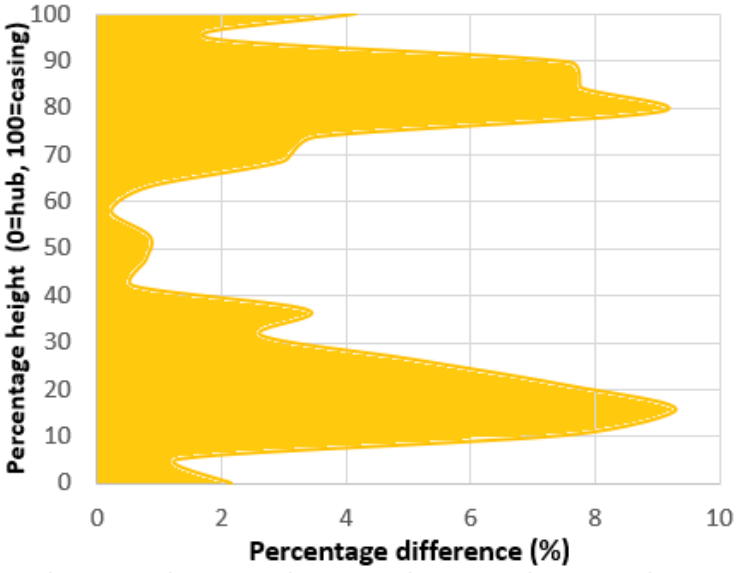

Figure 7.8: Percentage difference of temperature between measured experimentally and numerically obtained EOTDF temperature profile along the radial pitch evaluated at the location of measurement plane

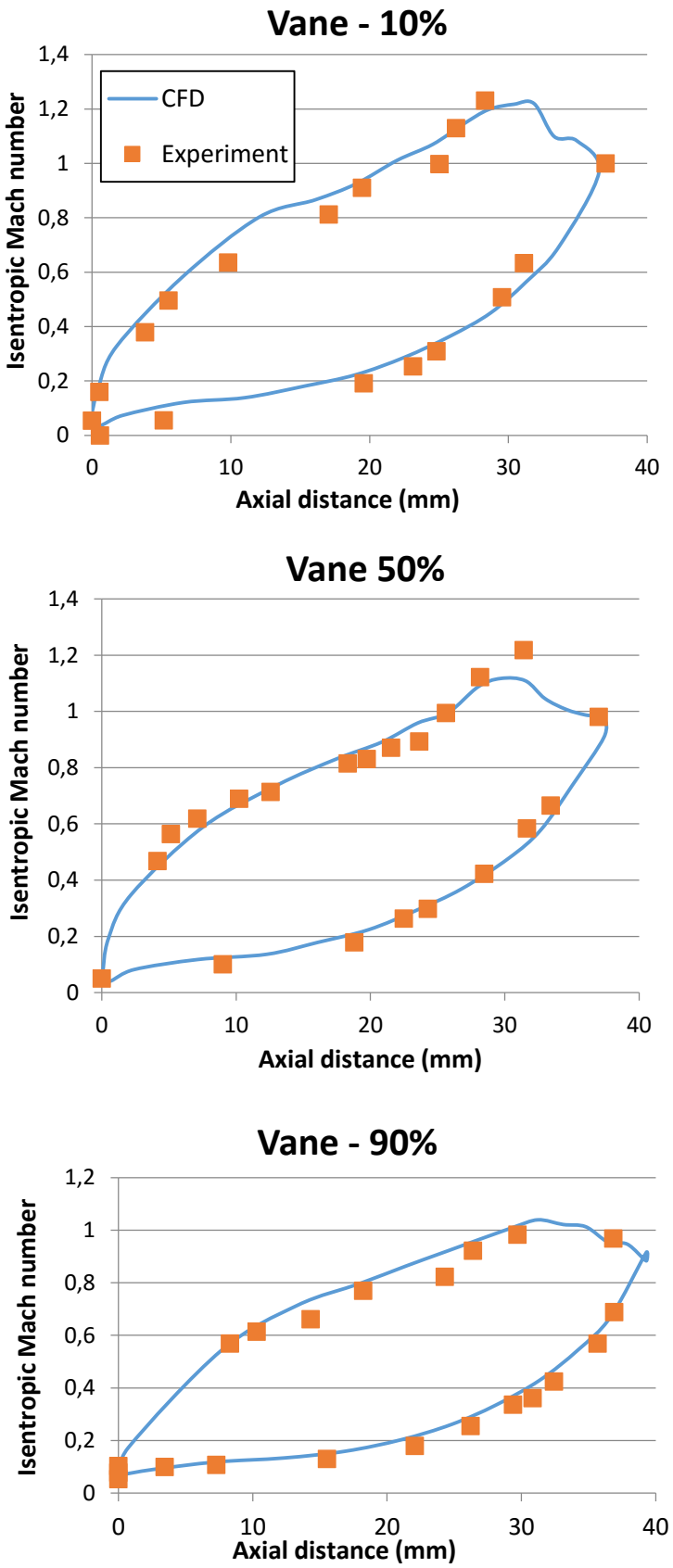

Figure 7.9: Isentropic Mach number distribution along the blade surface for three radial heights

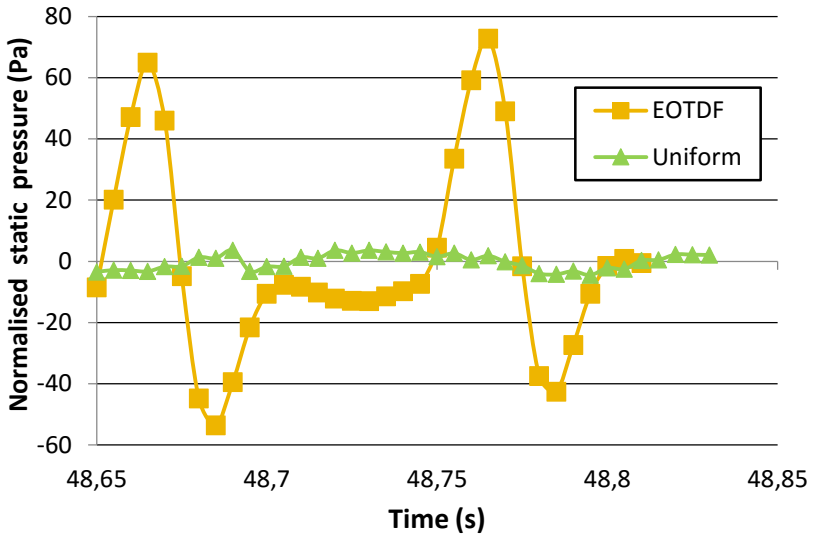

Figure 7.10: Comparison of normalised dynamic pressure fluctuations for uniform and EOTDF temperature profile evaluated 3mm downstream of the vane

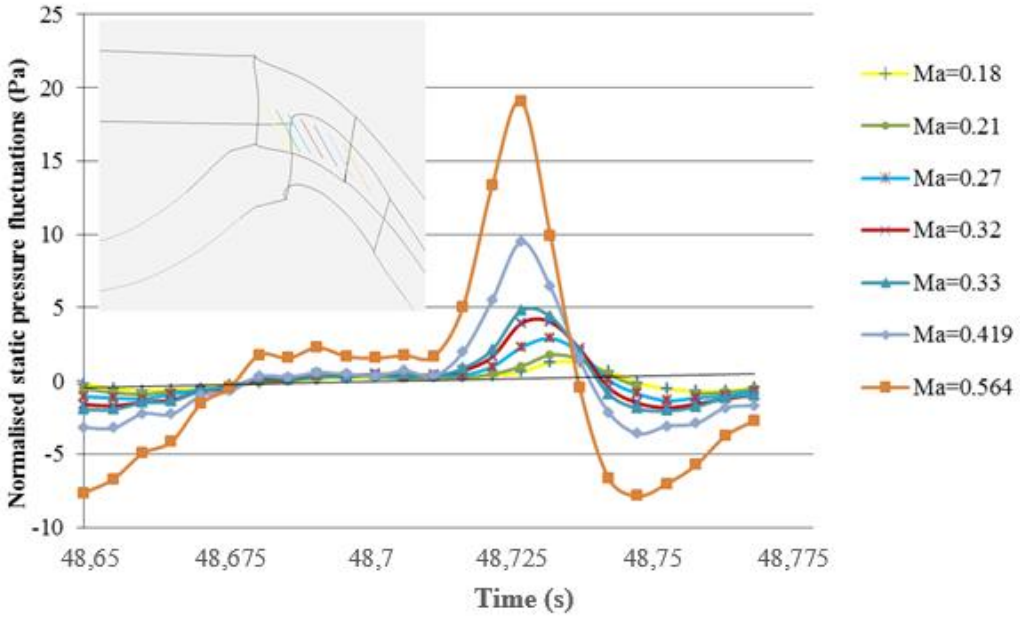

Figure 7.11: Normalized dynamic pressure fluctuations over time for different Mach numbers with data line locations

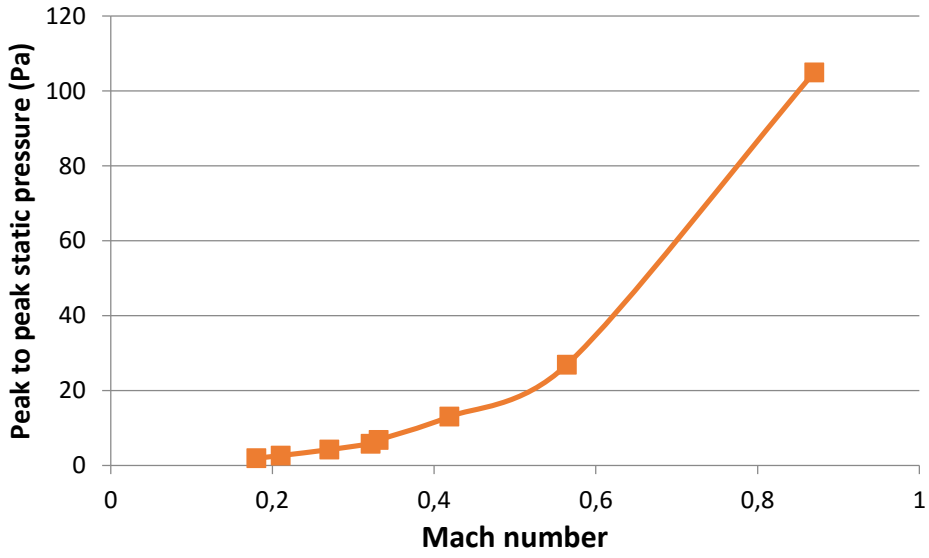

Figure 7.12: Peak to peak static pressure over Mach number for the EOTDF temperature profile

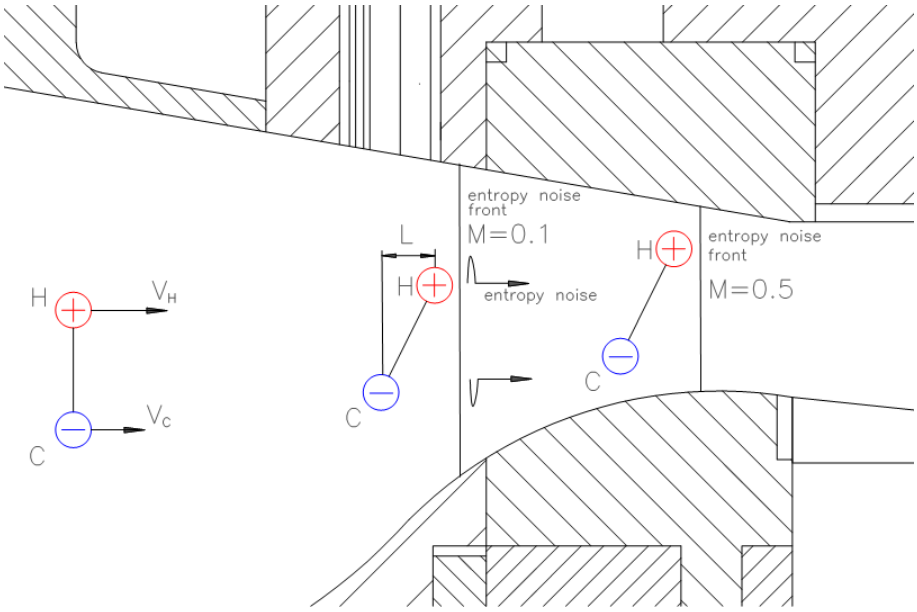

Figure 7.13: 'Entropy dipole' as a representation of the 'hot spot' and 'cold spot' of the EOTDF temperature profile

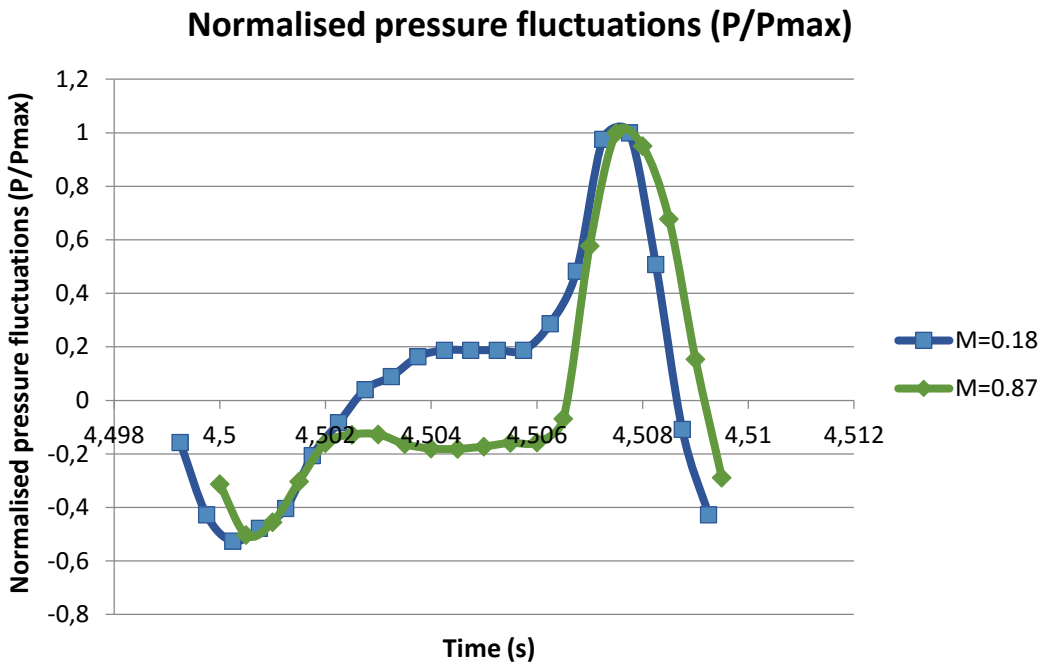

Figure 7.14: Normalised dynamic pressure fluctuations for the leading and trailing edge

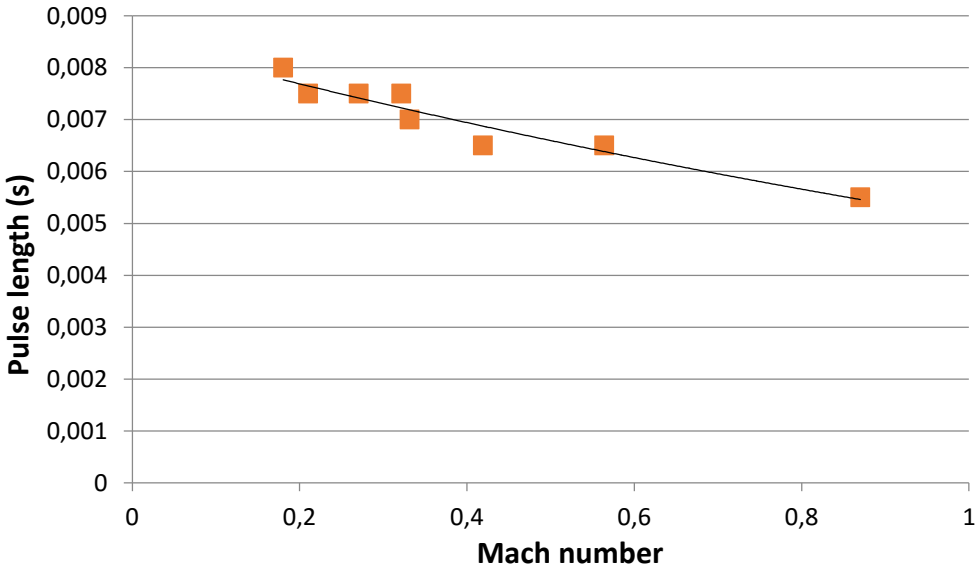

Figure 7.15: Pulse length of the pressure signal over Mach value with trendline

Mach number of the flow	**Analytical evaluation**	**URANS evaluation**
0.18	0.0539 (m)	0.05 (m)
0.21	0.0532 (m)	0.05 (m)
0.27	0.0524 (m)	0.05 (m)
0.32	0.0502 (m)	0.0475 (m)
0.33	0.0489 (m)	0.0475 (m)
0.419	0.0467 (m)	0.044 (m)
0.564	0.0429 (m)	0.038 (m)
0.87	0.0378 (m)	0.036 (m)

Table 7.2: Comparison of the acquired stretching of the 'entropy dipole' evaluated analytically and numerically for different Mach number flow conditions

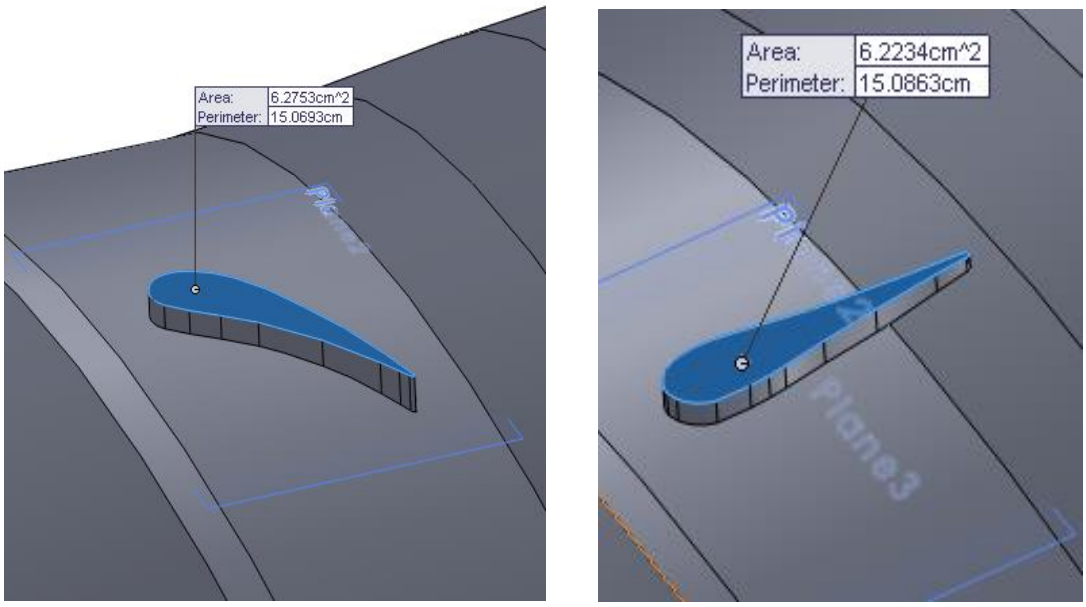

a) *b*)

Figure 7.16: The original (*a*) and modified (*b*) vane aerofoil with area and perimeter indicated

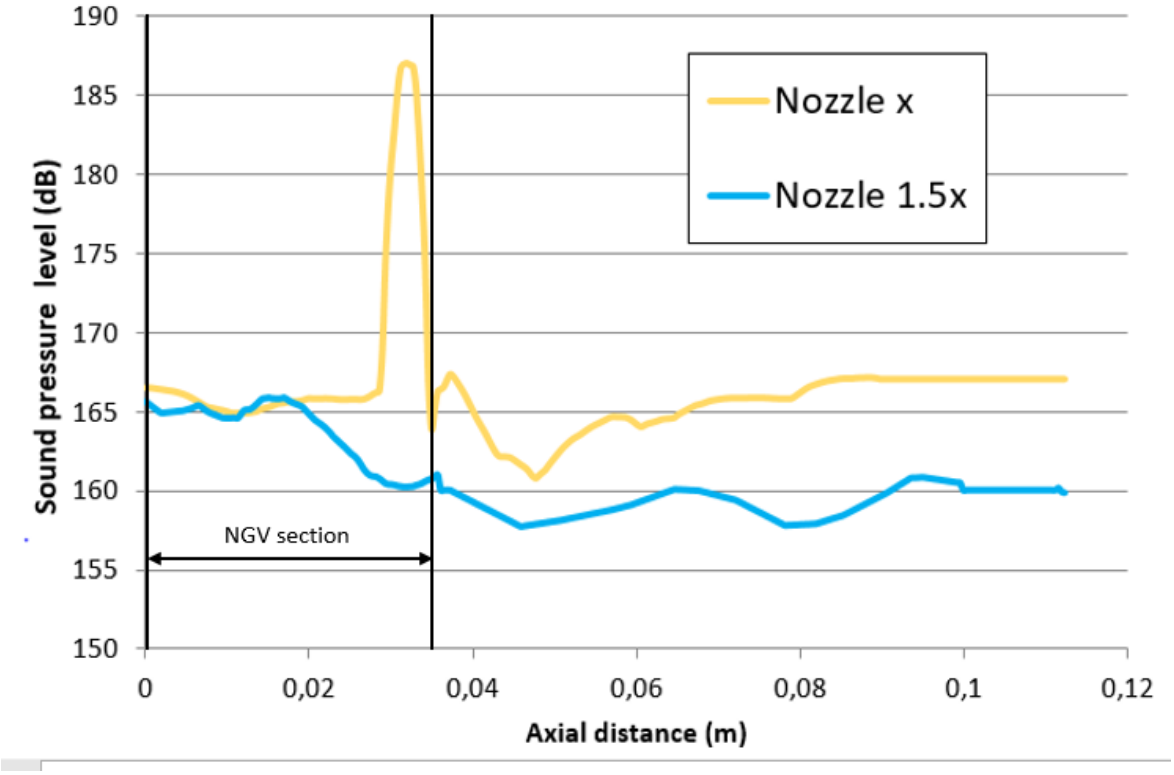

Figure 7.17: Sound pressure levels along axial distance for the two modelled vanes

Chapter 8

Entropy Noise Optimisation in Lean-Burn Combustors

8.1 Types of Combustors

The primary purpose of the combustor is to increase enthalpy of the working fluid through ignition. Lean direct injection and rich-burn, quick-quench, lean-burn (RQL) are two most used concepts for gas turbines. The RQL combustors are designed to employ an excessive cooling air for dilution after the primary zone. This results in strongly mixing flow at the combustor exit. In contrast with the RQL design, lean-burn combustors inject more air in the primary zone to decrease the NOx emission at the expense of less air available for cooling. Figure 8.1 shows the effect of stoichiometric air-to-fuel ratio on NOx emission (Lefevbre, 1999).

As a result of new cooling systems operating in lean-burn combustors, temperature profile at the exit of the combustion chamber tends to have a larger temperature gradient near the wall regions. The decrease in NOx emission is achieved by lowering the temperature peak. The lean-burn design also allows to prevent local quenching. Figure 8.2 shows radial temperature profiles of typical RQL and lean-burn combustors evaluated at the combustor exit (Koupper, 2015). Lean-burn combustion is characterised by a rapid temperature increase and flatter ‘hot spot’ area. Moreover, the flame producing the ‘hot spot’ is burning more unsteadily in the lean-burn system, thus generating larger temporal temperature variations.

As shown in Chapter 2 temperature differences account for the generation of entropy noise, which might be large in modern lean-burn combustors. The OTRF provides a unique opportunity to investigate the entropy noise generation since the EOTDF temperature profile matches well the temperature profile of a typical rich-burn combustor. The comparison of the EOTDF temperature profile with that of a typical rich-burn combustor is presented in Figure 8.3. Temperature was normalised over the mean value using a temperature factor (TF).

8.2 Analytical Modelling of Rich-Burn and Lean-Burn Combustor Temperature Profiles

The next generation aero-engines are projected to operate with the lean-burn combustion chambers destined to replace those used since the 1980s, Rich-burn, Quick-quench, Lean-burn (RQL) combustors. Thus, the possible noise sources and their optimisation draw extensive attention of engineers. The lean-burn combustor is distinguished by a flatter region in the centre, a larger 'hot spot' area, and by a lower temperature peak than the rich-burn.

The flow field at the exit of the combustor is highly unsteady producing large turbulent vortices, this is further exacerbated by the unsteady burning of the flame and mixing with coolant air taking place. The temperature profile of such a combustor is spatially and temporally varying.

To demonstrate the effect of temperature fluctuations on the noise level increase in the next generation engine two combustor exit temperature profiles were modelled analytically: first – the one of a typical rich-burn combustor and second – the one of a lean-

burn combustor distinguished by a more rapid temperature increase at the hub and casing walls and a cooler central region. Figure 8.4 shows the circumferentially-averaged temperature profiles modelled over the radial percentage height. The lean-burn temperature profile modelling was based on the available published data on the temperature distribution along the radial pitch for the lean-burn combustor (Koupper, 2015). The lean-burn combustor has a higher temperature value for approximately 25% of the radial span at the wall regions. At the 'hot spot' region the lean-burn combustor temperature is lower and flatter than the rich-burn. The real temperature value has been rearranged using temperature ratio (TF) as relations of the local temperature value against the mean temperature value. The modelled temperature profiles are chosen to be symmetrical over the mid-height pitch. This is to simplify the numerical calculation.

The unsteady heat release has been shown to result in the generation of temperature fluctuations superimposed on the combustor temperature profile with the largest fluctuations occurring in the region of the 'hot spot'. Evaluated working temperatures of the combustor prevent an accurate measurement of temperature fluctuations to be taken. Due to the lack of real measurement on rich-burn and lean-burn temperature fluctuations within the combustor chamber, these fluctuations were assumed based on the data achieved in the OTRF with numerical and experimental approaches.

Figure 8.5 shows evaluation of the assumed temperature fluctuations for the rich-burn and lean-burn combustors along the radial distance (Rolls-Royce, 2012). A temperature fluctuations factor (TFF) was applied. The experimentally obtained temperature fluctuations produced by the EOTDF temperature profile are shown. The lean-burn combustor is assumed to generate temperature fluctuations in the 'hot spot' region of 50%

more than those of a rich-burn combustor. This may be explained by a smaller temperature difference within the flatter central region of a lean-burn combustor allowing turbulence fluctuations to increase. The temperature fluctuation span-wise gradient for both combustors is similar with the lean-burn combustor having a larger fluctuation near the wall regions. This is determined by a more advanced cooling system being introduced. The EOTDF temperature profile although similar to a typical rich-burn combustor cannot accurately reproduce temperature fluctuations appearing in the real combustor. At the 'hot spot' region its fluctuations are substantially lower than in the engine case.

This allows to estimate the range of spatial and temporal temperature variations in the modelled rich-burn and lean-burn combustors. Figure 8.6 presents the estimated range of circumferentially-averaged temperature variations in the modelled rich-burn and lean-burn combustors evaluated against the radial percentage height. The temperature factor was used. The shaded area of the lean-burn combustor temperature variation is apparently larger than that of the rich-burn. Although the temperature peak of the lean-burn combustor coincides with the temperature peak of the rich-burn, temperature fluctuations are nonetheless significantly increased in amplitude. This is despite a considerable decrease in temperature peak for the steady temperature profile. The hub and casing walls fluctuations are similar with the lean-burn combustor experiencing a more rapid temperature increase in the direction of the 'hot spot'.

This is crucial data to make an estimate of the noise generation in engine turbines due to temperature fluctuations emanated from the combustion chamber. The rapid temperature gradient and larger fluctuations at the 'hot spot' region make lean-burn combustors potentially noisier in the range of lower frequencies and warrant further investigation.

8.3 Evaluation of Sound Pressure Levels Emanated by the Modelled Rich-Burn and Lean-Burn Combustors

A good agreement of the OTRF experimental data with the LES numerical prediction for the nozzle x configuration as presented in Chapter 4 provides an opportunity to numerically evaluate sound pressure levels in the range of the chosen frequencies for the modelled rich-burn and lean-burn combustor system. The unique feature of such a prediction are the realistic complex temperature profiles of the combustor systems varying in the radial and circumferential direction. The numerical calculation will allow to make an assessment of the sound pressure level produced not by simplified temperature fluctuations imposed all within the temperature profile or circumferentially-average temperature variations, but by the temperature variations, and subsequently velocity and density variations, of the mean flow representing the real engine conditions.

The first step was to rearrange the radial temperature profiles of the modelled rich-burn and lean-burn combustors into two-dimensional profiles with correct temperature variations in the radial and circumferential directions. The OTRF EOTDF temperature profile is similar to a typical rich-burn combustor, based on the experimentally acquired temperature variations the modelling of the rich-burn temperature profile was possible by scaling the local temperature values.

Figure 8.7, *a* shows the achieved temperature profile of the modelled rich-burn combustor. The modelled symmetric radial temperature profile was exchanged with a more realistic temperature distribution near the hub and casing walls. The hub wall is cooler than the casing, thus representing the real engine case. A ‘hot spot’ of more than 2000K is located

in the centre of the profile which is surrounded by a lower temperature region. The temperature difference between the 'hot spot' and 'cold spot' reaches 740K.

Figure 8.7, *b* presents the modelled temperature profile of the lean-burn combustor. The two-dimensional variations were achieved by imposing relative circumferential variations of the EOTDF temperature profile to the analytically modelled radial temperature profile of the lean burn combustor. The lean-burn temperature profile is distinguished by a larger 'hot spot' area in the centre with a lower value of the peak temperature than that of a rich-burn combustor. The flatter profile behaviour is maintained the same as for the modelled radial temperature variations. The colour legend for both case was kept the same allowing a comparison of the temperature gradient. As shown in Figure 8.1, *b* the lean-burn temperature contours spread broader than those of the rich-burn, whereas at the wall regions the temperatures experience a rapid change. This being the characteristics of a typical lean-burn combustor. The modelled lean-burn combustor was maintained symmetrical in the radial direction over the mid-height plane. The endwall temperatures are similar as opposite to the rich-burn case, with the difference between the 'hot spot' and 'cold spot' not exceeding 580K, entailing that the modelled lean-burn combustor should be showing lower entropy noise values than the scaled EOTDF temperature profile.

To evaluate the sound pressure levels emanated by these combustor systems the modelled temperature profiles were imposed upstream of the nozzle x configuration. The computational model and LES numerical prediction procedure were chosen the same as those described in Chapter 4, with the nozzle contracting area modelled to achieve the flow acceleration of an engine stator vane. The pressure boundary conditions at the inlet section were augmented to match the real engine case value of 50bar at the combustor

exit. The pressure drop over the stage was kept the same maintaining subsonic flow conditions. The unsteady numerical simulation produces data of dynamic pressure fluctuations as a function over time. Fast Fourier Transform performed rearranges it as the sound pressure level over the frequency range. The higher limit of the frequency range being determined by the chosen time step of the numerical modelling. Due to a higher expensive computational cost, the frequency band was limited to the range from 10 to 4000Hz since this is the frequency range where entropy noise is more influential. The dynamic pressure fluctuations were evaluated at the mid-height position of the mean flow in the axial location of the nozzle x numerical predictions.

Figure 8.8 shows the sound pressure levels evaluated for both the rich-burn and lean-burn combustors over the chosen frequency range. The OTRF EOTDF temperature profile evaluation was included to make an estimate of the general sound pressure level increase in the real engine combustor. Predictably, the rich-burn combustor produces higher noise levels than the EOTDF temperature profile. This is due to a fourfold increase in the scaled total temperature values, eleven time higher pressure boundary conditions and an increase in temperature fluctuations generated by turbulence. The noise behaviour of a rich-burn combustor is less abrupt than that of the EOTDF temperature profile with two rapid increases in pressure amplitude near 1000Hz disappear.

The lean-burn combustor exhibits a persistently higher sound pressure level than the rich-burn within the chosen frequency range. The general behaviour of the sound pressure level is more gradual for the lean-burn peaking at approximately 145dB at the lower frequency and experiencing a constant smooth noise level decrease at the higher frequencies. Notably, the noise difference between the lean-burn and rich-burn combustor increases

reaching scarcely more than 20dB at 4000Hz. Considering that entropy noise is influential only up to 1000Hz, the appearance of an increase at the frequencies from 1000 to 4000Hz should be explained by some other acoustic processes taking place.

It should be noted that the developed procedure although evaluating the sound pressure level generated by a non-uniform temperature profile of a real combustor with the flow and boundary conditions corresponding to a real engine values, the LES modelling didn't take into account the influence of other combustor flows features as reaction in the combustion chamber which potentially can distort temperature fluctuations, additional turbulence levels and swirls in the combustor flow can increase the general sound pressure level because the rotational kinetic energy developed by the swirl in the flow when accelerated will produce an additional noise.

If the modelled temperature profile of the lean-burn combustor is within the correct temperature distribution range, and arising temperature fluctuations are predicted correctly by the LES simulation, the general increase in sound pressure level for the next generation lean-burn combustor is about 10dB compared with the currently in use rich-burn combustors. The rich-burn combustor used in LES prediction corresponds well to the real combustor, showing sound levels of 130-140dB in the region of lower frequencies up to 200Hz. At the same time, the modelled lean-burn combustor generates a larger noise level of 140-147dB. Although, the modelled lean-burn combustor is characterised by a lower temperature difference between the 'hot spot' and the endwalls than the real rich-burn, it experiences a more abrupt temperature change within the hub and casing wall regions, leading to the appearance of stronger shear stresses and a potentially higher entropy noise level. The LES prediction was confined to a narrow frequency band, but

nonetheless showed that the modelled lean-burn combustor is noisier than a typical rich-burn. This further signifies the ever growing importance of entropy noise.

8.4 Lean-Burn Combustor Parametric Modelling

The observed difference in the sound pressure level for the modelled rich-burn and lean-burn combustors provides a good background for a better insight into the entropy noise generation and its influence in a real engine combustor. The additional noise is shown to be a result of a larger and flatter area of the 'hot spot' located at the centre of the temperature profile. The noise optimisation of the combustor exit temperature profile can be indispensably useful for modelling of the next generation lean-burn combustors, as stricter noise emissions regulations are being imposed. In order to optimise entropy noise in the lean-burn combustor, the sound pressure level was investigated on several modelled combustor temperature profiles.

8.4.1 Optimisation Process

The modelling of a new lean-burn combustor with a quieter noise generation rate requires to modify the analytically modelled lean-burn profile presented in Figure 8.4 using varying temperature profile parameters within the range of possible reproduction in real engine.

In this regard, the modelled lean-burn combustor temperature profile can be optimised using the following parameters:

8.4.1.1 Temperature Peak

One of the characteristic mark of the lean-burn combustor is a lower temperature peak of the 'hot spot'. This allows a decrease in the NOx emission due to the excess air, but the

precise temperature peak value may vary. The temperature peak is dependent on the mixing of air and fuel in the lean-burn combustion process and thus is one of the most important parameter of the combustion process itself.

Figure 8.9 shows circumferentially-averaged radial temperature profiles of three lean-burn combustors in relation to the typical rich-burn. Since the numerical modelling of a lean-burn combustor can be augmented by the two-dimensional temperature profile of the OTRF EOTDF temperature profile similar to a real rich-burn combustor, the referencing of the temperature peak parameter was performed from the peak value of a typical rich-burn combustor. The latter, as shown in Figure 8.3, is quite similar to the EOTDF temperature profile. The delta temperature values of 60K, 80K and 100K were chosen for the optimisation process. The endwall temperature at the hub and case, the temperature gradients and the area of the 'hot spot' were maintained allowing an unimpaired quantification to be performed. The symmetrical nature of the modelled lean-burn combustors is to be noted. The lowering of the temperature peak in the real combustor will require employment of more air and introduction of a more advanced cooling system.

8.4.1.2 Temperature Gradient

The second optimisation parameter was chosen as the gradient of temperature at the hub and casing walls. Figure 8.10 presents three circumferentially-averaged radial temperature profiles for the modelled lean-burn combustors differed by the temperature gradients. The lean-burn combustor is characterised by a more pronounced temperature gradient than that of a typical rich-burn combustor. The angles of temperature increase α_1, α_2, and α_3 are chosen from consideration that these are the temperature gradients most easily achieved in the real engine combustion chamber by increasing the mass flow rate of the coolant air

and mixing of the air. The flat 'hot spot' region at the centre of the profile is preserved, but the area ratio is substantially diminished with a decrease of the temperature gradient. The smoothest temperature transition produces the temperature profile similar to that of a real rich-burn combustor, but with a lower and flatter 'hot spot'.

Employment of these two optimisation parameters produces nine different lean-burn combustor temperature profiles, reproduction of those is achievable in real engine conditions.

8.4.2 The modelled Lean-Burn Profiles

To simplify the numerical evaluation the nine modelled lean-burn temperature profiles were labelled as presented in Table 8.1. The modelled temperature profiles are one-dimensional, circumferentially averaged temperature profiles evaluated as a function of the temperature value for a radial pitch location. To perform a complex three-dimensional numerical computation a readjustment of the modelled temperature profiles was required. This was achieved using the available experimental data from the OTRF.

The EOTDF temperature profile is evaluated as a scaled typical rich-burn combustor. The experimentally measured two-dimensional EOTDF temperature profile provides a realistic temperature distribution in the radial and circumferential directions and was used to obtain the rich-burn combustor temperature profile. Following that, the modelled lean-burn combustors were assigned with the circumferential variations of the scaled EOTDF temperature profile. This explains the necessity to refer the temperature peak optimisation parameter to the temperature peak of a typical rich-burn combustor. In the EOTDF temperature profile the modelled lean-burn profiles are characterised by the hub wall

being cooler than the casing wall. The readjustment led to insignificant deviations in the radial temperature variations. The modelled profiles are no longer symmetrical in the radial direction since the real rich-burn combustor temperature profile is also not symmetrical, thus allowing a reproduction of as much realistic lean-burn temperature variations in the radial and circumferential directions as was possible.

Table 8.2 shows two-dimensional temperature profiles of the modelled lean-burn combustors. The legend values are maintained the same for all the cases and are presented at the bottom of the table.

Notably, comparing three temperature profiles for the same temperature gradient, the red 'hot spot' contour is diminishing and splits with the decrease of the temperature peak, whereas the near-wall regions are kept the same. For the temperature profiles with the peak temperature of 2020K the red 'hot spot' contour effectively disappears with only minor elements of it being present. Meanwhile, the yellow contour of 1860K is kept intact because the temperature decrease has no effect on lower profile temperatures.

Three temperature profiles for the same temperature peak are distinguished by a diminishing 'hot spot' region in the radial direction and an increase in the spreading of the lower temperature contours with a decrease in the temperature gradient. The temperature gradient α1 is characterised by the red 'hot spot' contour disappearing and the contours being concentrated around the remaining part. With an increase of temperature gradient the temperature contours recede further to the near wall regions, while the hotter region spreads in the radial and circumferential directions.

Since the computation simulation for all the temperature profiles is performed for the same boundary conditions of the flow, the area ratio of the 'hot spot' becomes an important parameter in the entropy noise optimisation because, as shown in Chapter 2, the entropy noise level is proportional to the temperature difference between the 'hot spot' and its environment.

To optimize the sound pressure level emanated by the nozzle, two parameters of the temperature profile were chosen for investigation. The first parameter, the ratio of the 'hot spot' for each of the modelled temperature profiles to the overall area of the modelled circumferential section of the combustor. The ratio is evaluated as the area of the 'hot spot' contour with total temperature exceeding 2010K divided by the area of the temperature profile. The parameter is crucial to estimate the influence of the 'hot spot' on the noise generation because largest temperature fluctuations appear in this region due to lower density. The second parameter, the temperature difference between the coldest and hottest spot, can give an insight into the noise impact of the cooling system and air injection. The 'hot spot' for a typical lean-burn combustor is lower than that of a rich-burn due to additional air introduced, whereas the 'cold spot' appears because of the endwall cooling. Table 8.3 presents the chosen parameters for the modelled combustors.

8.4.3 Numerical Procedure

The numerical modelling was carried out using commercially available ANSYS FLUENT package. Smagorinsky sub-grid scale model was chosen for the LES calculation. The modelled two-dimensional temperature profiles were imposed at the inlet section of the nozzle x configuration. The precise modelling of temperature variations, dynamic pressure

fluctuations evaluation and data processing are described in Chapter 6, section 3. The unstructured tetrahedral mesh of 6.8 million cells was generated using ICEM ANSYS and applied for all the modelled temperature profiles. Grid used in this study are characterised by the following mesh spacing characteristics: $\Delta x^+ = 15$, $\Delta y^+ = 15$, $\Delta z^+ = 10$. Length scales in streamwise and spanwise directions are $L_{uu}^x = 75$, $L_{uu}^z = 21$. The length scale is discretized by 5 points of the mesh spacing. In the spanwise direction, the length scale is discretized by more than 2 points. Thus, the generated mesh allows resolving the turbulent structures in the streamwise direction, but might give some unsolved scales in the spanwise direction.

The computational model extends from the measurement plane downstream to the duct extension exit. The overall length is 0.314m. The chosen boundary conditions were adjusted to match those of an engine turbine. They are presented in Table 8.4.

The chosen pressure ratio corresponds to the supersonic condition of Mach number 1.2. Figure 8.11 shows the static pressure distribution from the inlet to exit plane taken at the mid-height plane. The axial position was presented as a relative axial length evaluated over the length of the nozzle. Static pressure decreases in an exponential way from 50bar at the inlet down to 28bar in the location of the throat. Downstream the flow continues to accelerate experiencing a shock after which it propagates steadily through the duct extension. Figure 8.12 presents the static pressure distribution along axial distance for the numerically modelled nozzle x configuration. It is observed that the static pressure behaviour in the lean-burn combustor optimization process is similar to that achieved in the nozzle x configuration.

The nozzle x configuration was designed to produce the same rate of flow acceleration as that of the first stage stator blades in an engine turbine. Therefore, the performed numerical simulation allows to make an estimate of the level of entropy noise generated in a lean-burn combustor terminated by half a turbine stage configuration. The time step of 5e-5s and static pressure signal length of 2000 consecutive time steps for the performed LES prediction were required to cover the frequency range from 10 to 10,000Hz. The acquired static pressure signal is of 0.1s time length.

8.5 Investigation of Entropy Noise in the modelled Lean-Burn Combustors

8.5.1 Lean-Burn Combustors with the Temperature Peak of 2020K

The LES predictions performed allowed to evaluate dynamic pressure fluctuations at the chosen location as a signal versus time step, later processed using Fast Fourier Transform applied to the acquired waveform. This technique allows to evaluate the sound pressure level generated over the targeted frequency.

Figure 8.13 shows the comparison of sound pressure levels emanated by the three modelled lean-burn combustors with the chosen temperature peak of 2020K. The circumferentially averaged temperature profiles evaluated against the radial position are presented on the left. It is observed that the general sound pressure level increases with a decrease of the temperature gradient, for example, ‘α1-2020’ combustor produces the highest acoustic response having the longest temperature transition region near the walls. This combustor shows large amplitude tones in the frequencies from 1000 to 2000Hz. Moreover, the peak at 2500Hz is also the noisiest among the investigated combustors. The second quietest combustor is ‘α2-2020’, although showing the noisiest acoustic response

at the higher frequencies from 5 to 10kHz, which may be explained by imperfections of the numerical calculation performed, it generates less noise than ‘α1-2020’ in the important range of frequencies from 800 to 3000Hz. ‘α3-2020’ is evaluated as the quietest combustor.

8.5.2 Lean-Burn Combustors with the Temperature Peak of 2040K

Figure 8.14 shows the sound pressure level against frequencies for three modelled lean-burn combustors with the temperature peak of 2040K. Depending on the temperature gradient they were called ‘α1-2040’, ‘α2-2040’ and ‘α3-2040’. The circumferentially averaged temperature profiles of them evaluated against the radial position are presented on the left. It is observed that temperature gradient plays a dominant role in the lean-burn combustor noise generation. The rapid temperature increase at the near-wall region produces less noise than that of a smoother temperature transformation. In addition, the sound pressure levels spread quite similar at the frequencies higher than 3000Hz implying that entropy noise is the most important noise source, since all the difference is confined to the lower frequency range.

At the lower frequencies up to 1000Hz ‘α3-2040’ lean-burn combustor shows a noise improvement of 10dB compared to the other two modelled combustors. It generates the noise level of approximately 123dB at 10Hz and 120db at 100Hz, whereas ‘α1-2040’ and ‘α2-2040’ both produce a similar acoustic response of 136-137dB at 10Hz and 133dB at 100Hz. At the frequencies from 100 to 1500Hz ‘α2-2040’ is conspicuously better than ‘α1-2040’ while at the lower frequencies the latter shows some improvement. The ‘α2-2040’ sound pressure level slopes quicker than ‘α1-2040’ and almost levels with ‘α3-2040’ at

300Hz, making ‘α1-2040’ the noisiest combustor at such an important frequency range as 100-1500Hz.

Two rapid amplitude increases are observed, at approximately 1600 and 2500Hz. Again, ‘α3-2040’ lean-burn combustor is the quietest with a substantial improvement of 10dB over the two other combustors at 2500Hz. The first amplitude rise appears at the higher frequency of 1800Hz with the noise level of 123dB. ‘α1-2040’ and ‘α2-2040’ produce the same sound pressure level at the first amplitude increase with ‘α2-2040’ getting a sharper rise at the second increase. Generally, ‘α2-2040’ and ‘α1-2040’ are quite similar starting from 1200Hz.

The quietest lean-burn combustor in the chosen frequency range is ‘α3-2040’ producing as much as 13dB less than ‘α2-2040’ and ‘α1-2040’ in the range from 10 to 800Hz and approximately 5dB from 800 to 10,000Hz. That means that an increase in the temperature gradient allows minimization of the noise level emanated by the lean-burn combustor with a targeted temperature peak of 2040K. Moreover, a change of temperature gradient from $\alpha 1$ to $\alpha 2$ minimises substantially the noise level in the frequencies from 100 to 1200Hz only, while temperature gradient increase for $\alpha 2$ to $\alpha 3$ gives a lower noise level at 10 to 300Hz.

8.5.3 Lean-Burn Combustors with the Temperature Peak of 2060K

Figure 8.15 shows comparison of three modelled lean-burn combustors with temperature peak of 2060K. Once again, the observed at other temperature peaks dependency preserves with ‘α1-2060’ being the noisiest combustor due to the lowest temperature gradient with sound pressure level from 100 to 1000Hz frequency range reaching 130dB.

'α2-2060' and 'α3-2060' are quieter in this region with average sound pressure levels of 125 and 120dB respectively. In addition, 'α1-2060' is characterised by a larger amplitude at 2500Hz and 10dB more noise generated at the higher frequencies from 5 to 10kHz. 'α2-2060' combustor is noisier than 'α3-2060' at the lower frequencies, only being surmounted by 'α3-2060' at the tone of 2kHz. 'α2-2060' is the quietest combustor in the region from 1000 to 2000Hz, matching well the sound pressure level of 'α3-2060' at the higher frequencies.

8.5.4 Lean-Burn Combustors with α1 Temperature Gradient

Figure 8.16 shows the sound pressure levels for 'α1-2060' and 'α1-2040' combustors evaluated against the targeted frequency range. It is observed that 'α1-2060' produces larger noise levels than 'α1-2040' in the frequency range from 1000 to 10,000Hz, while at the lower frequencies the sound pressure level of two combustors is very similar. The mean temperature of 'α1-2040' is 0.5% lower than that of 'α1-2060' and despite this insignificant difference an increase of the 'hot spot' temperature leads to the noise difference of approximately 5dB at higher frequencies. It might be concluded that at temperature gradients approaching a typical rich-burn combustor, the developed LES procedure predicts a sound pressure level increase only in frequencies higher than 1000Hz.

8.5.5 Lean-Burn Combustors with α2 Temperature Gradient

Figure 8.17 demonstrates the sound pressure levels of the modelled combustors with α2 temperature gradients. Overall, the sound pressure levels are quite similar within the investigated range of frequencies. 'α2-2060' combustor despite being distinguished by a higher temperature peak for the α2 temperature gradient produces lower noise then 'α2-

2020' within the frequencies from 100 to 1000Hz. All the investigated combustors have large tones at 1500Hz and 2500Hz. All the combustors have approximately the same noise level. At the frequencies from 3kHz the sound pressure level distribution for three combustors is spread similar along the frequency spectre with 'α2-2020' generating a larger noise level at the highest frequencies. This may be explained by an imperfect acquisition of static pressure signal in the numerical simulation. At the lower frequencies the sound pressure levels are similar, although it is unreasonable to make an estimate for these lower frequencies since the signal was acquired to cover the chosen frequencies with a time length providing only one measurement point for such a low frequency as 10Hz.

8.5.6 Lean-Burn Combustors with *α*3 Temperature Gradient

The sound pressure levels of the three modelled temperature profiles with *α*3 temperature gradient and varying temperature peaks were evaluated against the targeted frequency range. They are presented in Figure 8.18. Their circumferentially averaged temperature profiles with the names assigned are shown on the left. The temperature peak value is shown to be an influential parameter modifying the noise level up to 10dB at the lower frequencies. 'α1-2060' lean-burn combustor with temperature peak of 2060K is the noisiest producing sound pressure levels of approximately 138dB at 2100Hz and 130dB at the 10-100Hz frequency range. 'α3-2020' combustor although having the lowest temperature peak of 2020K generates a larger noise level than 'α3-2040' with 2040K temperature of the 'hot spot' region. The amplitude peak of 'α3-2020' is 130dB at 2500Hz, while that of 'α3-2040' is only 120dB. Therefore, at the frequencies from 10 to 250Hz 'α3-2020' is slightly noisier than 'α3-2060'.

Overall, 'α3-2040' gives noise optimization in the whole frequency range. The difference in sound pressure levels is insignificant at the higher frequencies concluding that the temperature peak value is a predominant entropy noise parameter. Such a confusing behaviour of the modelled combustors when with an increase in the temperature peak from 2020K to 2040K the noise level is reduced can be explained by looking at the two-dimensional temperature profiles presented in Table 8.2. 'α1-2060' lean-burn combustor is modelled to have one large 'hot spot', whereas that of 'α3-2040' is split into two parts and 'α3-2020' combustor is represented by a series of small 'hot spots'. That means that in 'α3-2020' there are more temperature variations at the centre of the profile determined by the difference in temperature between the 'hot spot' and its environment. That causes generation of additional entropy noise sources and thus increases the sound pressure level.

That shows that sound pressure level is dependent on the temperature peak of the lean-burn profile. An increase in temperature value does not necessarily lead to the generation of a larger noise level owing to the fact that the temperature difference between the 'hot spot' part and its environment can produce more entropy noise. The general improvement observed is 10dB lower sound pressure level at the lower frequencies.

8.5.7 Lean-Burn Combustors with Different Temperature Peaks and Gradients

The modelling performed of the lean-burn combustors allows to make an estimate of the sound pressure levels generated by temperature profiles with different temperature peaks and gradients. This is to get a further insight into the entropy noise optimisation and to model a new combustor exit temperature profile which will produce less noise.

Figure 8.19 shows sound pressure levels emanated by 'α3-2060' and 'α2-2040' combustors and their circumferentially averaged radial temperature profiles. It is observed that 'α3-2060' produces 5-10dB less noise in 10—300Hz range while having a larger amplitude peak at 2100Hz than 'α2-2040'. At the higher frequencies from 2500-10,000Hz the sound pressure levels match well proving that the noise difference is being determined by entropy noise. That means that by increasing the temperature peak and making the temperature gradient more pronounced at the near-wall region entropy noise optimisation becomes possible.

Figure 8.20 presents sound pressure levels produced by 'α2-2040' and 'α3-2020' lean-burn combustors and their radial temperature profiles. 'α2-2040' appears to be noisier than 'α3-2020' at 10-100Hz frequency range and quieter at 100-400Hz. At the higher frequencies the sound pressure levels are quite similar with the rapid fluctuations amplitude increase at 2500Hz being of the same value for both combustors. After 2500Hz a very good match of the noise levels is noticeable. Overall, two combustors can be assessed as generating the same noise levels. That means that with an increase of the temperature peak by 20K and making the temperature gradient less pronounced the sound pressure level remains the same.

Figure 8.21 illustrates the comparison of sound pressure levels for 'α2-2040' and 'α1-2060' combustors. 'α1-2060' is characterised by a smaller 'hot spot' and higher temperature peak than 'α2-2040' and produces more noise especially at 1000 – 10,000Hz range. The noise difference reaches 5dB at the lower frequencies from 100 to 1000Hz, while when compared with 'α3-2020' 'α2-2040' shows no difference in this range. The tones at 2500Hz appear at both combustors with 'α1-2060' having a larger amplitude. The sound pressure

level difference preserves at the higher frequencies. These two combustors are characterized by the same mean temperature of their temperature profiles. Despite having the area-averaged temperature the same, the sound pressure levels are different in the targeted range of frequencies.

Figure 8.22 demonstrates the evaluated sound pressure levels for 'α1-2020' and 'α2-2040' combustors. 'α1-2020' combustor has lower temperature peak and smaller area of the 'hot spot', the mean temperature of it is lower than that of 'α2-2040'. Nevertheless, it is noisier by approximately 2-5dB within all the frequency range. That means that the lower area of the 'hot spot' and subsequently the larger temperature difference between the 'hot spot' and its environment causes, as shown in Figure 8.21, a substantial increase in the sound pressure level.

8.5.8 General Entropy Noise Optimisation Conclusions for Lean-Burn Combustor

Based on the presented numerical results of the modelled lean-burn combustors some conclusions can be drawn.

It is observed that the rapid, more pronounced temperature gradient produces lower noise level as it tends toward the walls. This pattern maintains for all the temperature peaks investigated.

The temperature peak value shows a large effect on the general sound pressure level of the modelled lean-burn combustors. Unfortunately, it is evaluated to be highly sensitive on the temperature gradient. For example, the modelled combustors with $\alpha 2$ temperature gradient are showing similar sound pressure levels for all the evaluated temperature peaks. For $\alpha 3$ temperature gradient the quietest lean-burn combustor is evaluated to be that of

2040K, while that of 2020K is noisier. That means that a lower temperature peak, the characteristic mark of lean-burn combustor, does not necessarily generate less noise.

The chosen temperature peaks and gradients are reproducible in real lean-burn combustors. Although the modelled combustors represent only the limited range of possible temperature profiles, they can provide valuable understanding and good background for further entropy noise generation and optimisation of the temperature profile characteristics.

8.6 Chapter Conclusions

The next generation lean-burn combustors are characterised by a larger 'hot spot' area with the lower temperature peak. Temperature fluctuations at the 'hot spot' are predicted to increase in the lean-burn system architecture as compared with the rich-burn. The estimated range of spatial and temporal temperature variations for a modelled rich-burn and lean-burn combustors are evaluated along the radial pitch. The sound pressure levels of these combustors are predicted using a LES procedure. An accurate modelling of the targeted temperature profiles was based on the developed numerical procedure described in Chapter 6. The target frequency range was limited to 4kHz in order to decrease computational costs. The evaluation of the EOTDF temperature profile was included in the comparison since the typical rich-burn combustor was modelled by scaling the EOTDF temperature profile. It was observed that a typical lean-burn combustor produces larger sound pressure levels.

Based on this estimate, the necessity to evaluate the influence of lean-burn combustor temperature profile on the sound pressure level of entropy noise emanated by a turbine

configuration has emerged. In this regard, two optimisation parameters were chosen: temperature peak and temperature gradient. Thus, nine lean-burn temperature profiles were designed. The boundary conditions were augmented to match those of a real engine. The nozzle x configuration was operated using the developed LES procedure within the frequency range from 10 to 10,000Hz.

Predictions show that temperature gradient plays an important role in sound pressure level optimisation in lean-burn combustors, with an increase in temperature gradient at the near-wall region, the general level of noise is diminished in all three investigated temperature peaks. The temperature peak is numerically evaluated to be highly dependent on the temperature gradient. The more pronounced near wall temperature gradient shows that for three modelled temperature gradients, the less noise is generated by a temperature peak of 2040K and not that of 2020K.

The developed method of entropy noise evaluation and optimisation in lean-burn combustors is certainly advantageous due to the possibility of modelling the chosen combustor exit temperature profile very accurately in both the radial and circumferential directions. The imposed temperature variations are typical for those of a lean-burn combustor.

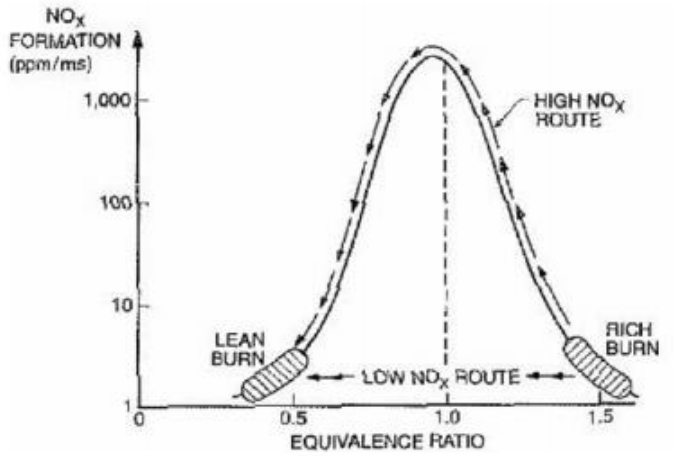

Figure 8.1: Effect of stoichiometry on NOx emission in RQL combustor (Lefevbre, 1999)

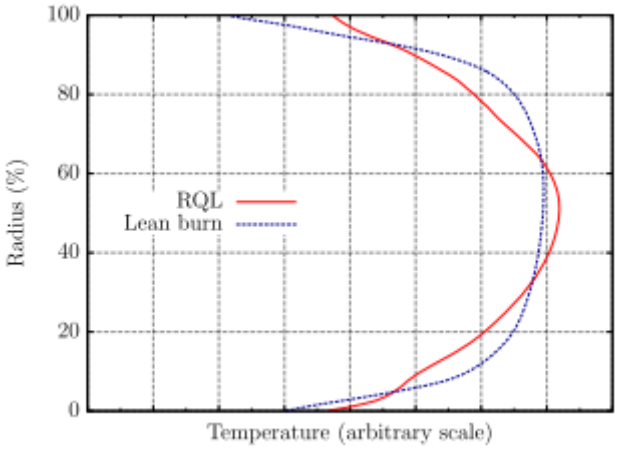

Figure 8.2: Typical circumferentially averaged temperature profiles at the combustor exit (Koupper, 2015)

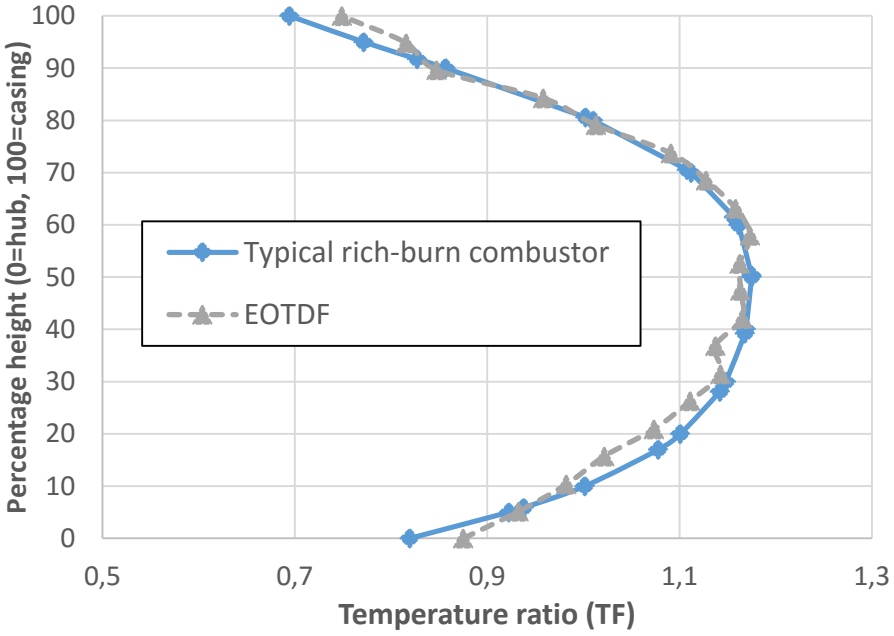

Figure 8.3: Comparison of the EOTDF radial temperature profile with a typical rich-burn combustor profile

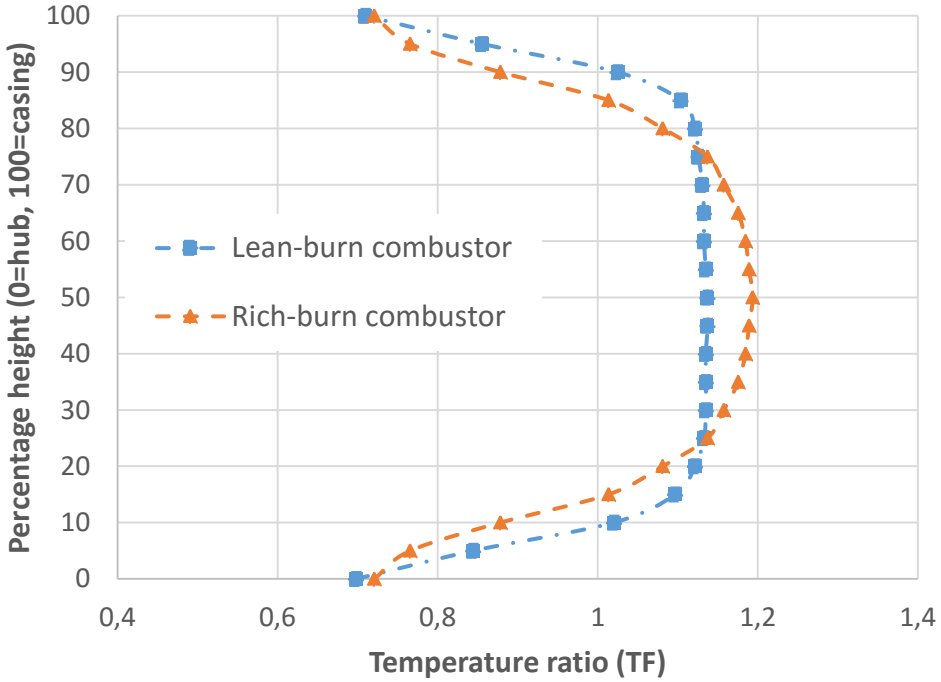

Figure 8.4: Analytically modelled radial temperature profiles of a rich-burn and lean-burn combustors

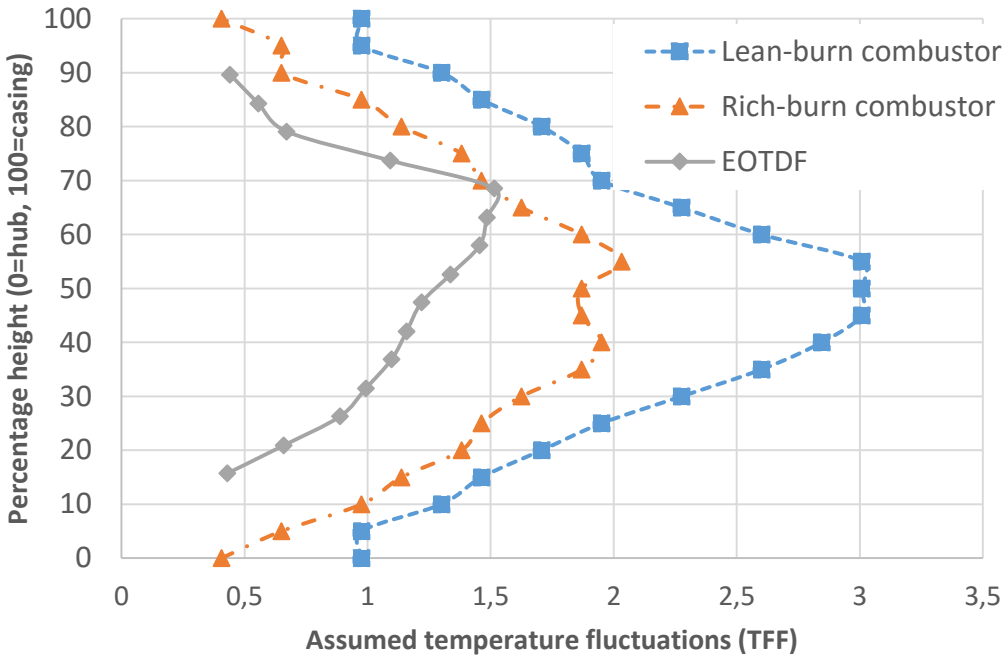

Figure 8.5: Assumed radial temperature fluctuations for modelled rich-burn and lean-burn combustors

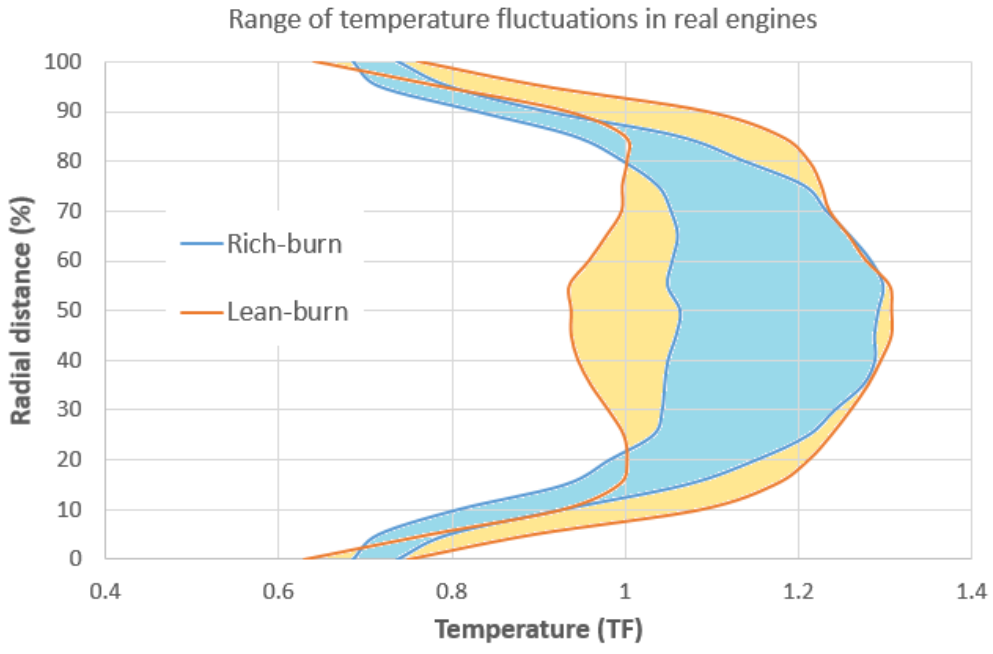

Figure 8.6: Estimated range of temperature fluctuations in the modelled rich-burn and lean-burn combustors evaluated against radial percentage height

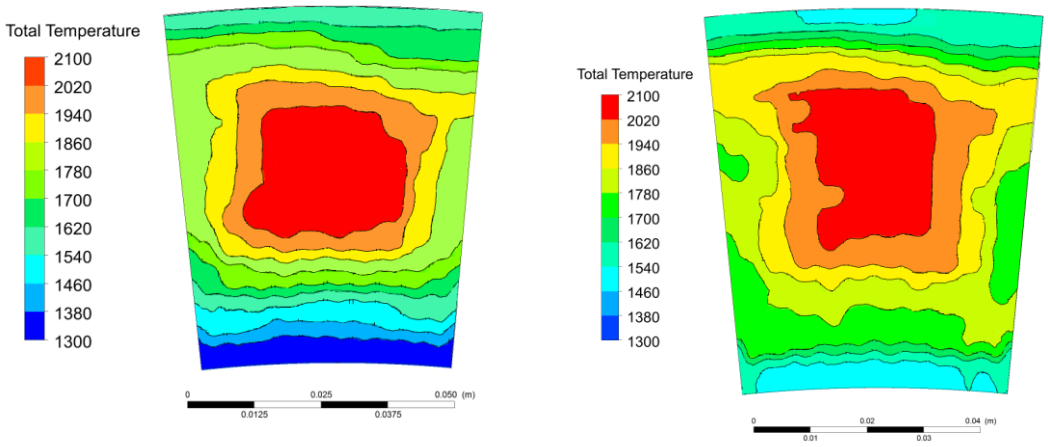

a) *b*)

Figure 8.7: Two-dimensional temperature profiles modelled for the rich-burn (*a*) and lean-burn (*b*) combustor

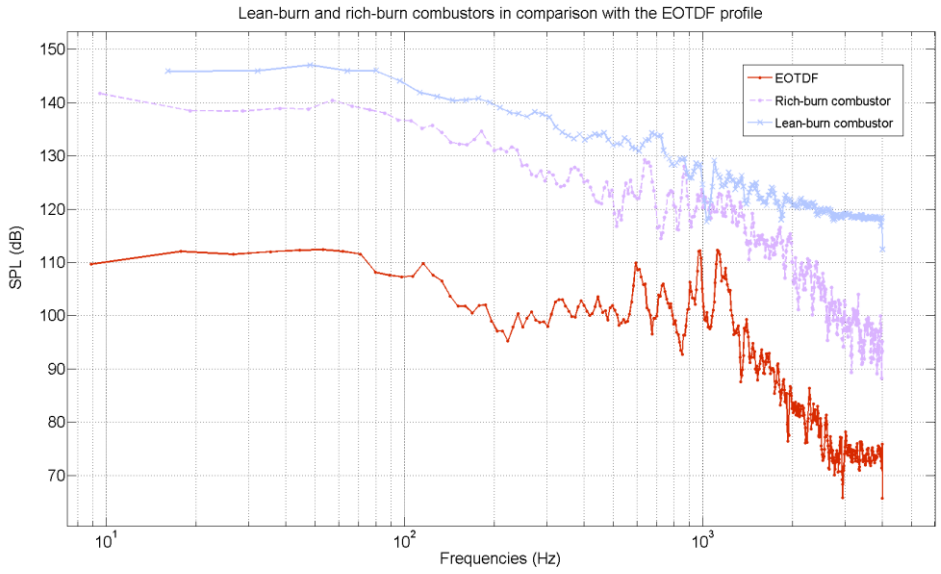

Figure 8.8: Sound pressure level evaluated numerically for the modelled rich-burn and lean-burn combustors in comparison with the EOTDF temperature profile

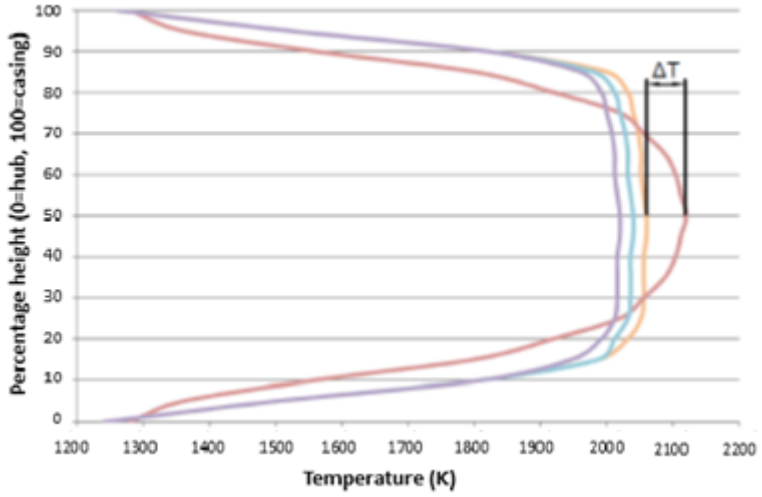

Figure 8.9: Temperature peak as an optimisation parameter

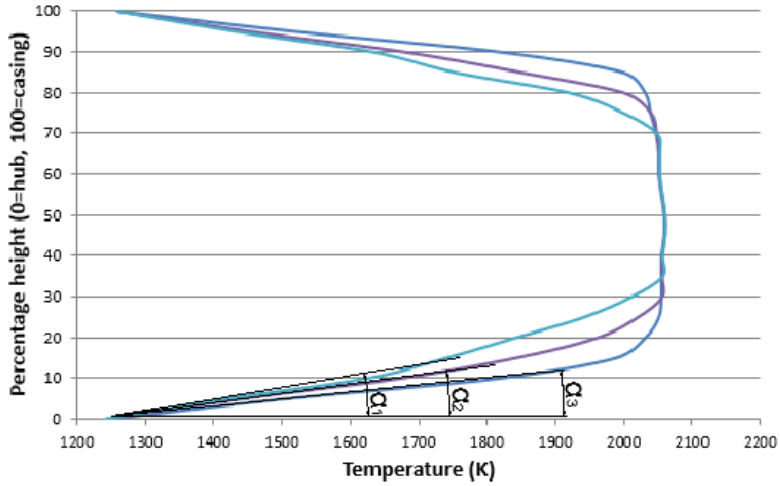

Figure 8.10: Temperature gradient as an optimisation parameter

ΔT / α	2060K	2040K	2020K
α1	'α1-2060'	'α1-2040'	'α1-2020'
α2	'α2-2060'	'α2-2040'	'α2-2020'
α3	'α3-2060'	'α3-2040'	'α3-2020'

Table 8.1: Assigned names of the modelled lean-burn combustor temperature profiles

	2060K	2040K	2020K
α1	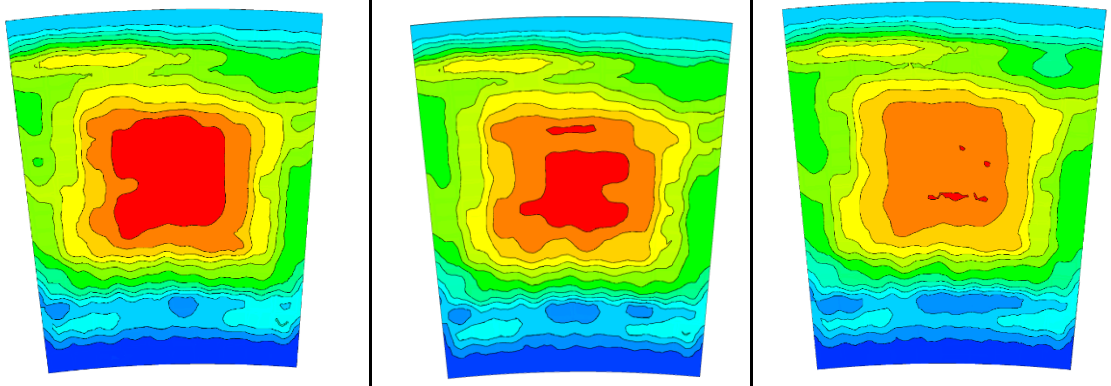		
α2	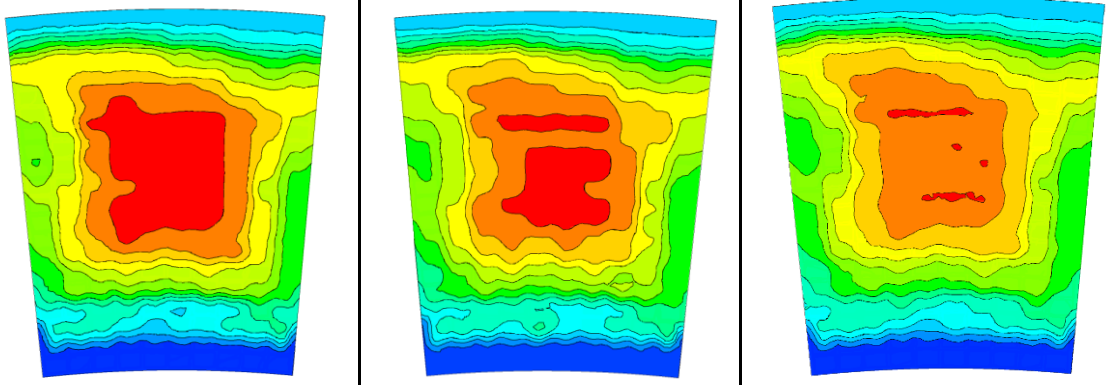		
α3	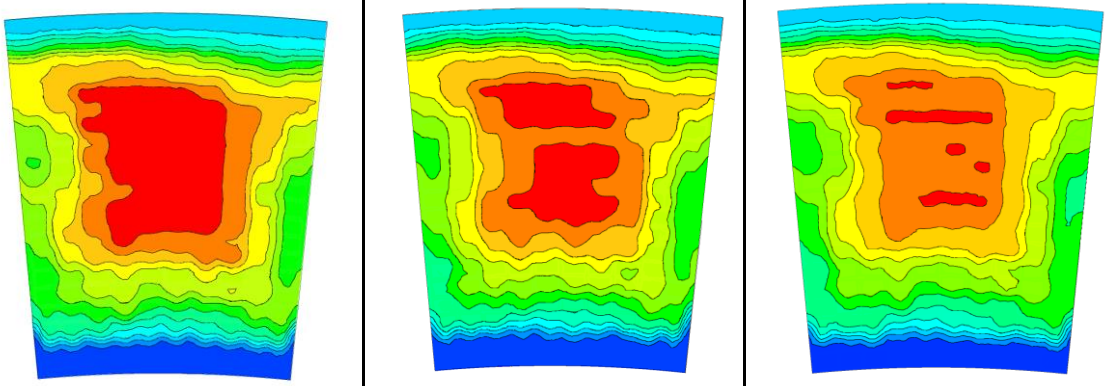		

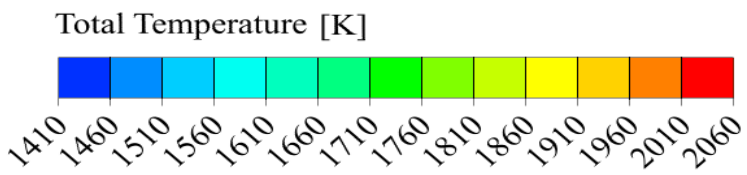

Table 8.2: Two dimensional temperature profiles modelled

ΔT / α	2060K	2040K	2020K
α1	0.136 /653K	0.088 /633K	0.026 /613K
α2	0.157 /662K	0.099 /642K	0.058 /622K
α3	0.196 /662K	0.138 /643K	0.064 /623K

Table 8.3: The 'hot spot' area ratio and temperature difference for the modelled combustors

Boundary conditions	Values
Inlet static pressure	50bar
Pressure ratio	1.53
Mass flow rate	19.1kg/s
Turbulence intensity	12%
Frequency range	10-10 000Hz

Table 8.4: Boundary conditions of the lean-burn combustor model

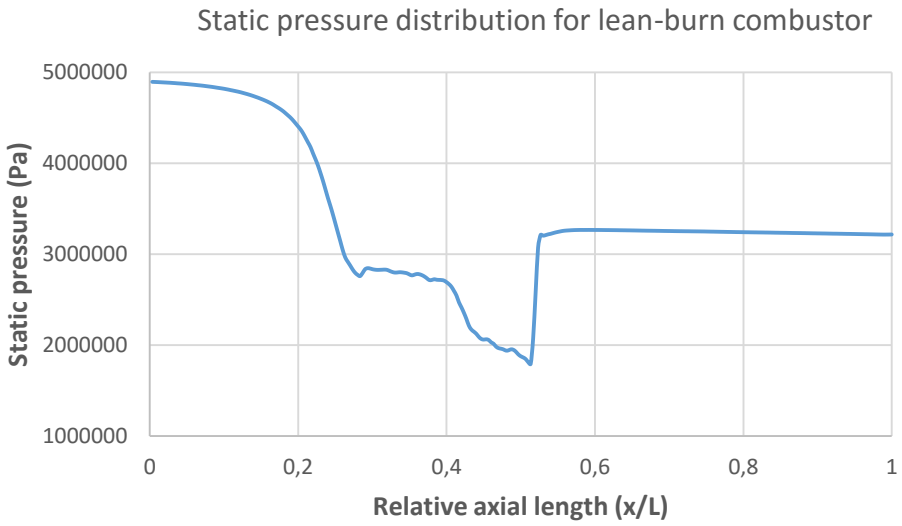

Figure 8.11: Static pressure distribution along the axial length for the lean-burn combustor

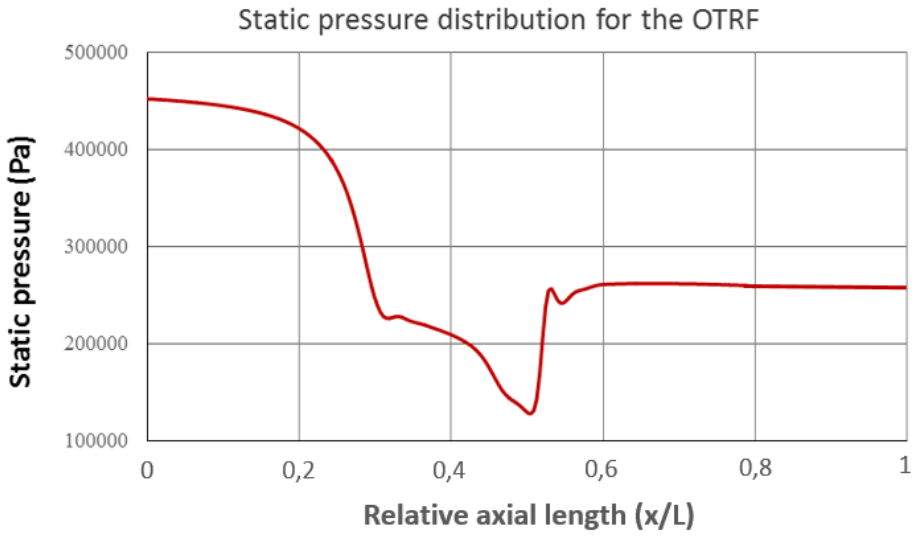

Figure 8.12: Static pressure distribution along the axial length for nozzle x

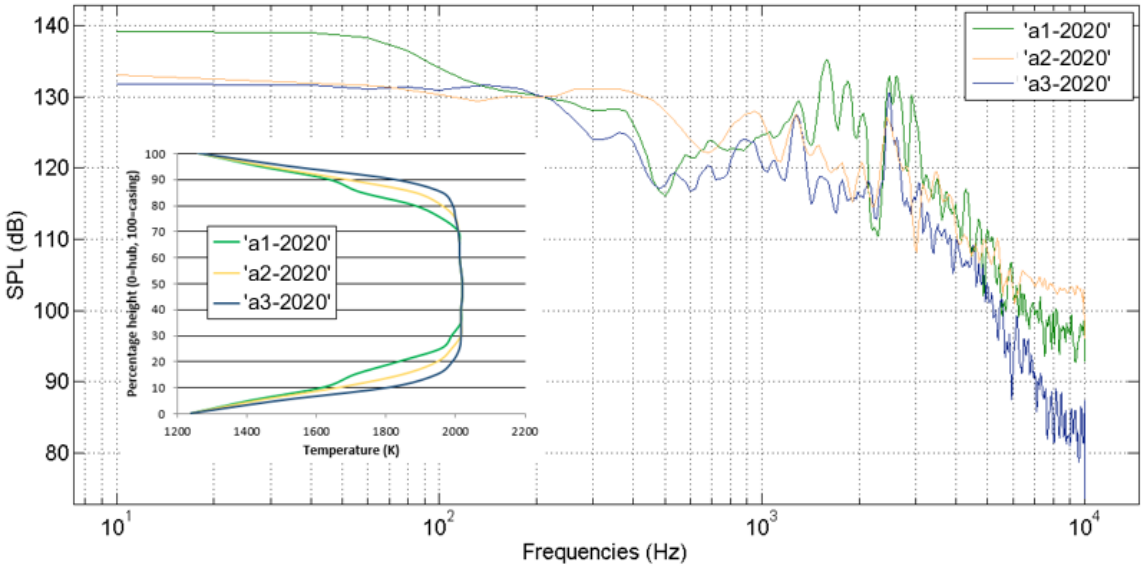

Figure 8.13: Sound pressure levels of the three modelled lean-burn combustors with temperature peak of 2020K

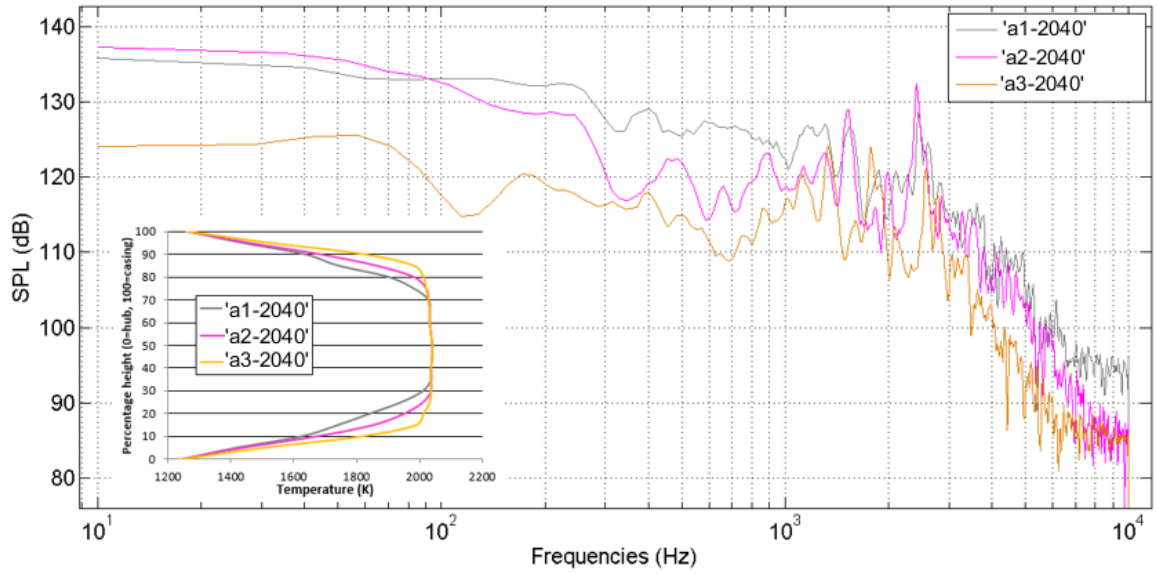

Figure 8.14: Sound pressure levels of the three modelled lean-burn combustors with temperature peak of 2040K

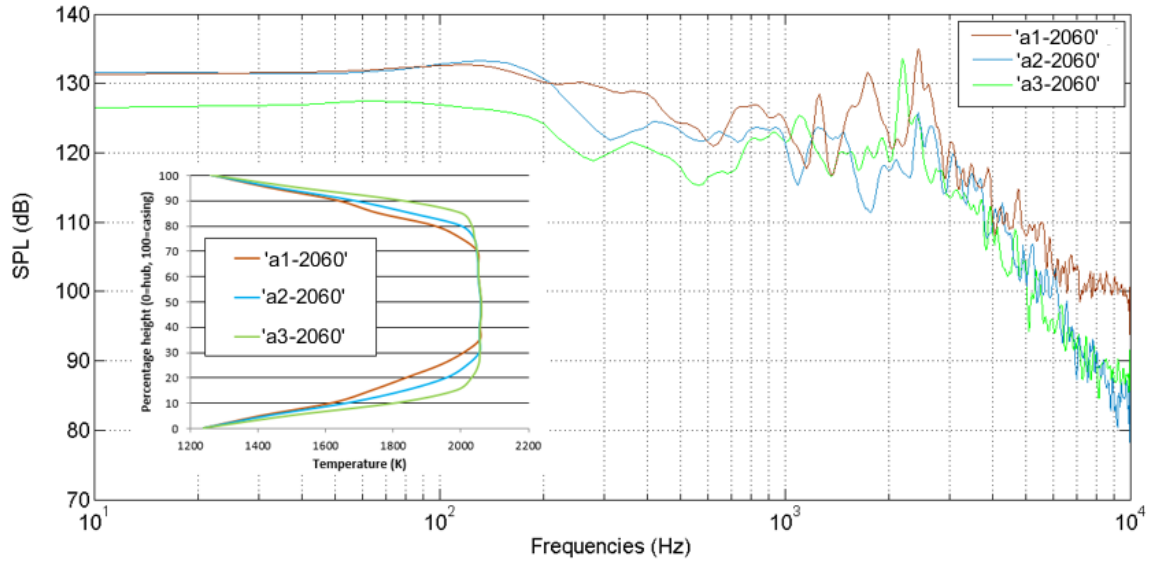

Figure 8.15: Sound pressure levels of the three modelled lean-burn combustors with temperature peak of 2060K

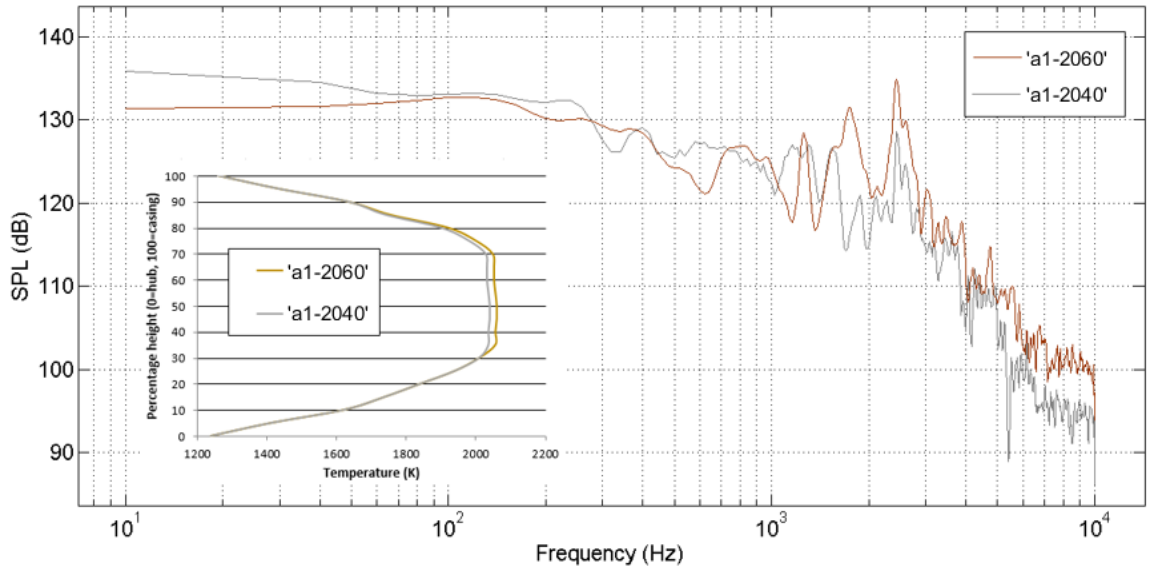

Figure 8.16: Sound pressure levels of 'α1-2060' and 'α1-2040' combustors with a1 temperature gradient

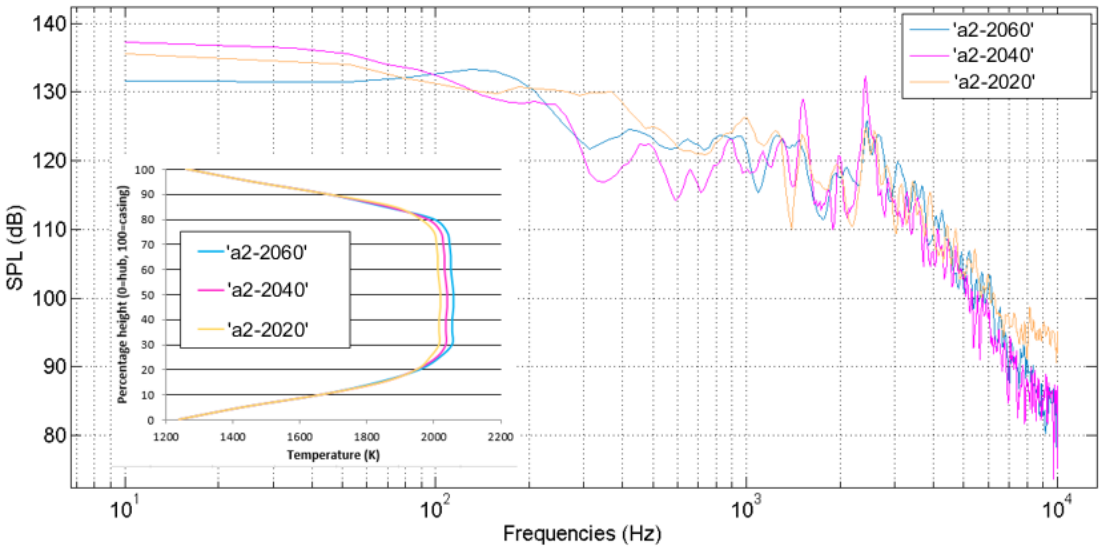

Figure 8.17: Sound pressure levels of the three modelled lean-burn combustors with $\alpha 2$ temperature gradient

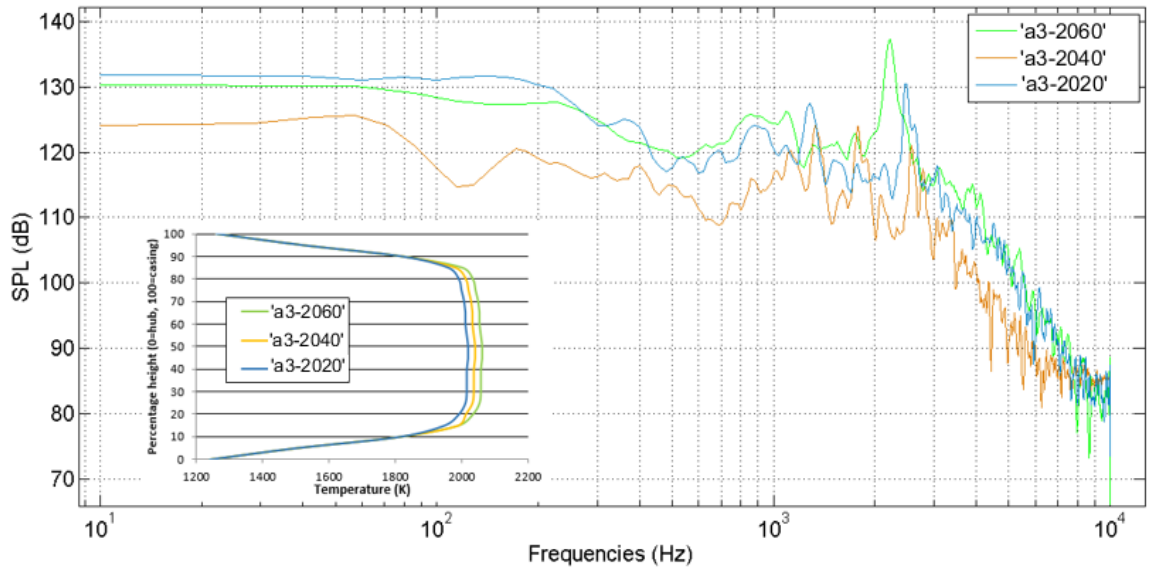

Figure 8.18: Sound pressure levels of the three modelled lean-burn combustors with α3 temperature gradient

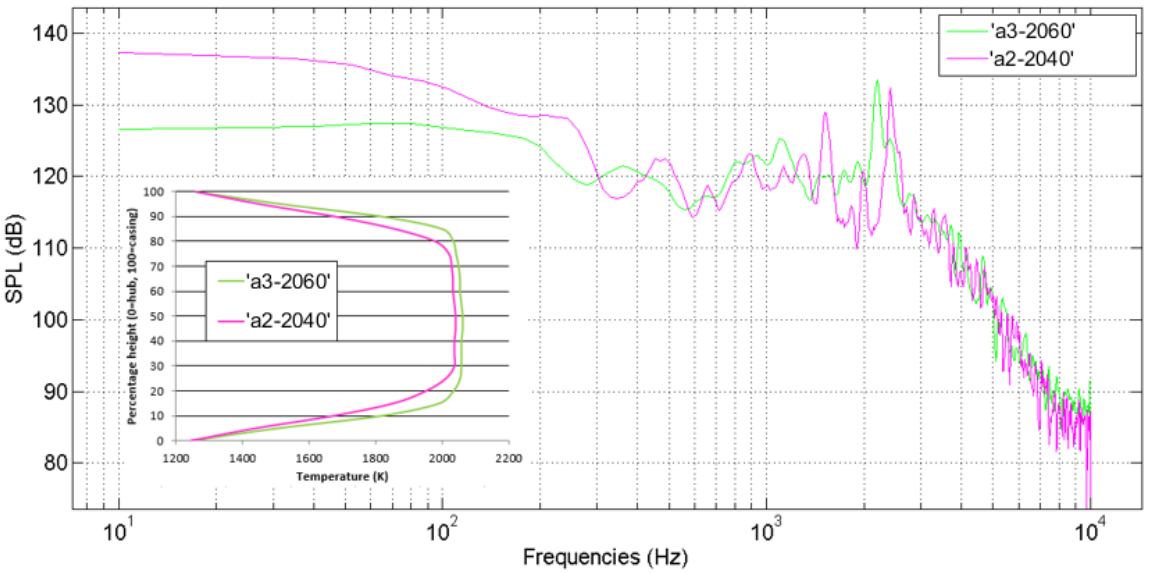

Figure 8.19: Sound pressure levels of 'α3-2060' and 'α2-2040' combustors

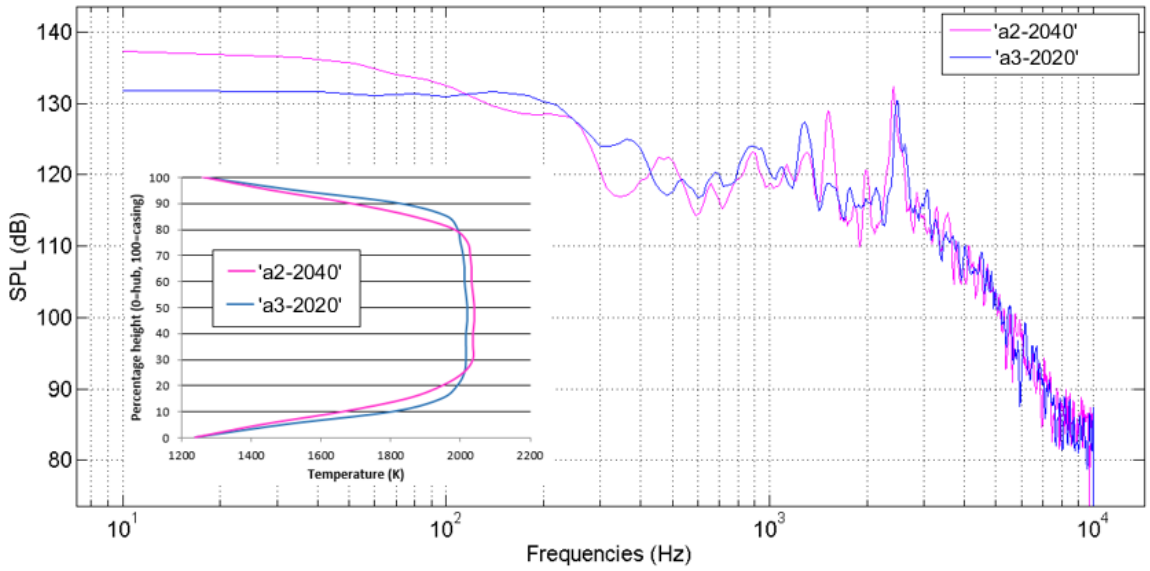

Figure 8.20: Sound pressure levels of ‘α2-2040’ and ‘α3-2020’ combustors

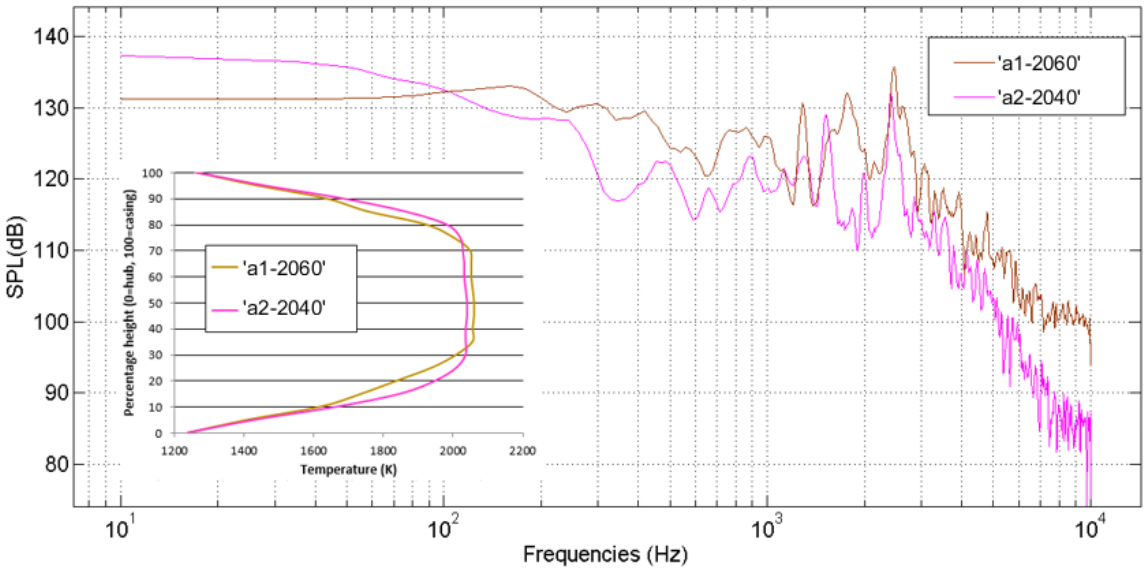

Figure 8.21: Sound pressure levels of ‘α1-2060’ and ‘α2-2040’ combustors

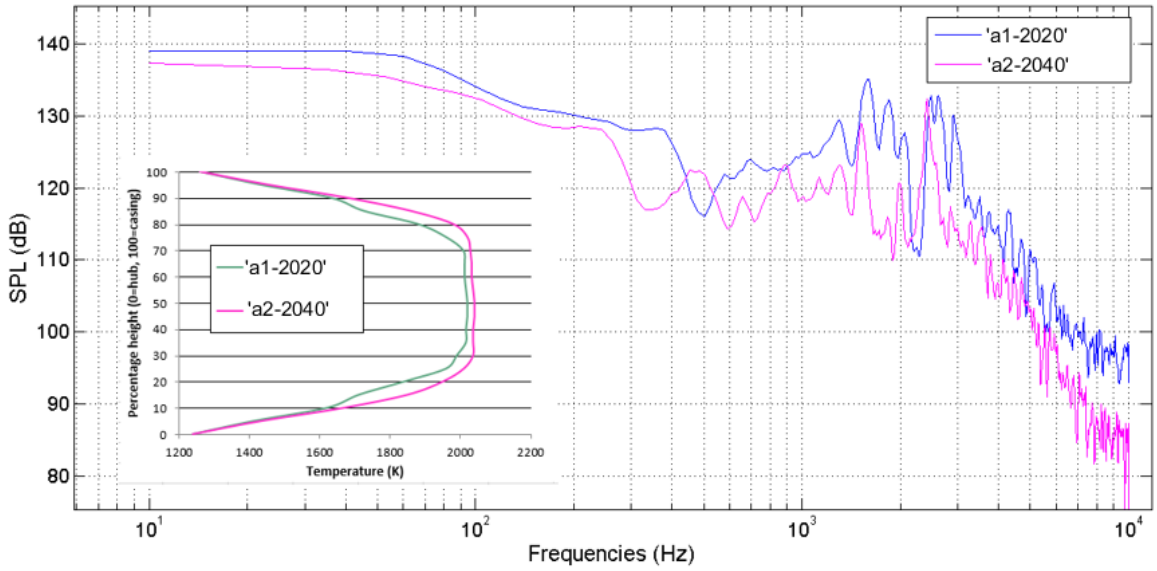

Figure 8.22: Sound pressure levels of ‘α2-2040’ and ‘α1-2020’ combustors

Chapter 9

Conclusions

9.1 Overall Conclusions

The goal of this thesis has been to investigate the generation of entropy noise in the Oxford Turbine Research Facility. The investigation required to make an estimate and perform a quantification of entropy noise due to temperature inhomogeneities propagating from the combustor chamber. In order to generate entropy noise two requirements should have been met: the presence of temperature inhomogeneities in the flow and its acceleration. In this regard, two simple nozzle geometries were modelled to have different Mach number acceleration rates confined to the NGV section. The first nozzle, called nozzle x, was designed to achieve the same acceleration rate as a typical stator blade. The second nozzle 1.5x was modelled to extend the acceleration region, thus allowing a steadier Mach number distribution in the axial distance. The coefficient 1.5 determines a relative increase in the axial dimension of the vane required to achieve the proposed acceleration rate. Numerical modelling was performed to investigate and optimise entropy noise.

Entropy noise investigation in the first nozzle. The aim of this study was to investigate and evaluate the potential entropy noise arising due to temperature inhomogeneities. First, the influence of injection system on the overall noise was investigated. The tunnel was operated with the mainstream temperature of 300K with and without injection of the coolant air. It was observed that injection makes an insignificant influence on the overall noise propagating out of the nozzle. Following that, the uniform and EOTDF temperature

profiles were generated at the inlet section of the facility. The experimental data showed an increase of approximately 10dB at the low frequency of 100Hz. Later, three EOTDF temperature profiles with varying 'hot spot' temperature were investigated. The EOTDF temperature profiles show a constant increase in the sound pressure level, while the uniform temperature profile with the same mean temperatures of the flow gave no noise increase. That makes the temperature difference between the 'hot spot' and its environment an influential parameter in overall noise optimisation.

Entropy noise investigation in the second nozzle. The generation of entropy noise may also be investigated by varying the acceleration rate of the flow within the NGV section. To investigate the generation of entropy noise on a different Mach number distribution, the second nozzle was designed. The experimental investigation showed that the uniform temperature profile generates the same sound pressure level within the targeted frequency range for both nozzle geometries. Then the EOTDF temperature profile was generated upstream the general sound pressure level was reduced by approximately 5-10dB in the low frequencies for the nozzle 1.5x configuration. The generation of entropy noise within the NGV section was investigated on two pressure transducers mounted at the outer wall.

Numerical investigation of entropy noise in a nozzle configuration. A more simple approach to investigate entropy noise is to exchange stator blades with a nozzle configuration. In this regard, two modelled nozzle configurations were remodelled in the numerical simulation. Large Eddy Simulation was chosen as a turbulence model since it allows explicit resolving of the larger scales, and the non-linear interactions of vorticity, entropy and acoustic modes are modelled well with relatively little computational costs.

The precise temporal and spatial temperature variations as measured in the OTRF were modelled numerically for further investigation. LES prediction of the two-dimensional EOTDF temperature profile with precise modelling of radial and circumferential temperature variations was achieved. The influence of wavelength on entropy noise was investigated on two nozzle geometries, it was shown that entropy noise diminishes with an increase of wave frequencies which corresponds to the general theory of the entropy noise generation. A dissipation study was performed based on temperature fluctuations. The temperature amplitude was decreasing along the nozzle while at the region of the flow acceleration entropy noise was generated.

Numerical investigation of entropy noise in half a turbine stage. Numerical investigation was performed for a computational model encompassing the combustor simulator responsible for generation of the EOTDF temperature profile and half a turbine stage. The numerical approach was validated by comparing the Isentropic Mach number distribution along the suction and pressure side of stator blades with the available experimental data. The numerical EOTDF temperature profile, as compared to that measured in the rig, is characterised by a more pronounced temperature gradient although being in the experimental range nonetheless. The EOTDF temperature profile is evaluated to generate additional noise of approximately 120dB at the exit of the vane, whereas the uniform temperature profile at the same axial location gives only minute dynamic pressure fluctuations corresponding to the sound pressure level of no more than 106dB. Moreover, the amplitude of dynamic pressure fluctuations is shown to increase as the flow is accelerated through the turbine stage. In addition, the ‘hot spot’ is projected to produce a positive acoustic response, proceeded by the ‘cold spot’ as a negative acoustic source. The

pulse length of the static pressure signal diminishes with the flow acceleration, entailing that the observed noise is not a direct acoustic noise of any kind, but entropy noise complicated in its nature.

Entropy noise optimisation in lean-burn combustor. The combustor exit temperature profile for a lean-burn combustor is distinguished by a more pronounced temperature gradient at near-wall regions and lower temperature peak as compared to a typical rich-burn combustor. The diminution of the temperature peak in lean-burn combustor allowed an optimisation of the NOx emission, but a larger 'hot spot' area is evaluated to produce more temporal temperature variations. The numerical evaluation showed that a typical lean-burn combustor can be as much as 10dB noisier than a typical rich-burn in the low range of frequencies. That instigated the entropy noise optimisation in the lean-burn combustor. In this regard, nine combustor exit temperature profiles were modelled based on varying temperature peak and temperature gradient. The developed LES numerical procedure was used. The results showed that an increase in the temperature gradient making it more pronounced leads to a decrease in the sound pressure level. In addition, the noise level showed an increasing sensitivity on the temperature gradient at which the former was evaluated. At the temperature gradient close to that of a typical rich-burn combustor temperature profile, the sound pressure level for three modelled lean-burn combustors are similar in all the frequencies, whereas at the temperature gradient of the lean-burn combustor, the sound pressure levels are evaluated to have the noise difference of about 10dB.

9.2 Recommendations for Future Work

To the author's best knowledge the presented study is the first successful major numerical and experimental investigation of entropy noise performed in a turbine facility. The generation of additional noise due to temperature difference between the 'hot spot' and its environment was proven by evaluating the sound pressure level in a nozzle configuration with uniform and non-uniform temperature profile generated upstream. Moreover, when the first nozzle configuration was exchanged with the second, characterised by a steadier flow acceleration, the general noise level in the low frequencies was reduced by approximately 5-10dB for the non-uniform temperature profile, and no noise difference was observed for the uniform temperature profile.

However, there are still some issues that require attention. The performed experimental investigation of entropy noise in a full turbine stage configuration showed no additional noise being generated with increase of the mean-averaged temperature of the flow. In addition, the observed noise difference between the uniform and non-uniform temperature profiles in the turbine stage was confined to the frequency range from 500-1000Hz. This does not correspond well neither with the experimental investigation in two nozzle geometries, nor with the general entropy noise theory. The quantification of entropy noise can be made possible by performing a set of experiments with different temperature differences between the 'hot spot' and the 'cold spot'. The temperature difference ratio necessary to make entropy noise influential can be derived by the result of this experimental investigation. Another nozzle geometry can be considered to further furnish the proof of entropy noise generated being determined by an abrupt fluctuation of shear stresses.

Numerical simulation of the cases investigated may provide a good background for explaining entropy noise generation in a turbine stage. The developed numerical method of static pressure signal acquisition can be used to evaluate entropy noise within the turbine stage. This will require an extensive numerical investigation of the rotor blades performing a steady rotation and thus affecting the flow conditions and entropy noise generation. The validation of the numerical method can be perfomed using the experimentally acquired data of the flow conditions over the turbine stage and the aerodynamics of the stator and rotor blades.

The evaluation of Large Eddy Simulation as a turbulence model for the entropy noise numerical investigation can be carried out by comparing the computation costs incurred by the developed numerical technique with that based on the URANS turbulence model. LES is generally regarded as one of the most computationally expensive turbulence model, and although it usually gives good numerical prediction of the combustor flow, including the flow behaviour determined by the temperature inhomogeneities, it can be imperative to perform similar numerical evaluation for the URANS model. The sound pressure level against frequencies for both turbulence models should be compared with the available experimental data and based on that a conclusion regarding efficiency of the URANS and LES turbulence models in entropy noise generation can be drawn.

Entropy noise reduction in a lean-burn combustor can be continued by evaluating the level of temperature fluctuations against frequencies for nine modelled lean-burn combustors. This will allow a reduction of noise in the chosen frequency range, and by varying the optimization criteria an optimised, quiet lean-burn combustor exit temperature profile can be generated.

Estimation of the boundary layer noise and therefore, explanation of the appearance of additional tones when the uniform temperature profile is operated using the precise LES prediction could be performed. This can further validate the developed numerical technique of entropy noise valuation.

Appendix A

Experimental Data Processing

The appendix presents the numerical code written in MATLAB software in order to process the experimental data acquired in the OTRF. The data from pressure transducers was obtained in a form of dynamic pressure fluctuations signal, the part of which corresponding to the rig run had to be processed in order to evaluate the sound pressure level over the frequencies. The code is supplemented with comments explicitly explaining the step-by-step sound pressure level evaluation.

MATLAB Data Processing Code

```
function [ SPLdB, f ] = ProcessOTRF( sig )
% Function for processing OTRF entropy noise test data
% INPUT:
% Input is 'high-speed' data from the OTRF noise tests
% The data is arranged so that each row contains a sequence of samples of
% instantaneous pressure for a given measurement channel
%
% The signal is assumed to have been sampled at 100kHz and must contain
at
% least 0.1 seconds of data (10,000 samples).
%
% Input data must be prepared by trimming pre- and post-run
% data, so that only valid, on-condition, data remains.
%
% OUTPUT:
% SPLdB is an array of Sound Pressure Levels in dB re 2 x 10^-5 arranged
% in rows for each measurement channel.
% f is a vector of frequencies corresponding to each column in SPL (dB)
%
% ALGORITHM:
% All channels are processed regardless of content.
%
% The Welch method is applied to reduce the variance of the resulting
% spectragram. In this approach, the signal is broken into several
blocks,
% an FFT is calculated for each block, and the results are averaged.

Fs = 100000; % Sampling frequency
L = length(sig); % Number of samples in signal

N = 10000; % Block length for FFT. By choosing 10,000 with Fs = 100,000Hz
a 10Hz bandwidth is achieved
overlap = 0.5; % A number representing the maximum permissible percentage
overlap of the blocks.
% This is used only to define the number of blocks. The algorithm will
try to spread the blocks evenly over the entire available signal.
% overlap must be in the range 0 < overlap <= 1.

% Find the maximum number of whole blocks of length N which will fit
% into signal of length L with up to 50% overlap
nblocks = fix(L/((1-overlap)*N)-(1/(1-overlap)-1));

% Build an array containing the starting sample numbers for each block
if L < (1+(1-overlap))*N
    blocks = [1, (L-N)]; % Trying to squeeze in at least two blocks
else
    % Find the maximum number of whole blocks of length N which will fit
    % into signal of length L with up to 50% overlap
    nblocks = fix(L/((1-overlap)*N)-(1/(1-overlap)-1));
    for count = 1:1:nblocks
```

```
        blocks(count) = round(1+(count-1)*(L-N-1)/(nblocks-1));
    end
end

% Create a vector containing the frequencies which will be produced by
the FF
f = Fs/N.*(0:N/2);

% Calculate window
%win = hamming(N,'periodic'); % Generate a Hamming window
%wincorr = 1.855; % Amplitude correction for a Hamming window
%wincorr = 1.586; % Energy correction for a Hamming window
%win = win'; % Transpose win (from column to row)

% Use the following two lines only if no window (i.e. square window) is
wanted
win = 1;
wincorr = 1;

for Chan = 1:1:31 % Loop through the channels to be processed

    P = zeros(nblocks,1+N/2); % Set 'Pressures' array to zero

    for blk = 1:1:nblocks % Loop for each FFT block

        sigblock = sig(Chan,blocks(blk):blocks(blk)+N-1);% Select the
signal block
        sigblock = sigblock - mean(sigblock); % Remove any DC offset
        sigblock = sigblock.*win; % Apply the window to the signal block

        y = fft(sigblock,N); % Calculate the (complex) FFT
        P(blk,1:1+N/2) = abs(y(1:1+N/2)); % FFT is symmetric and complex
so select the positive frequencies and calculate magnitude
        P(blk,2:end-1) = P(blk,2:end-1)*2; % Multiply by two because only
half the spectrum has been retained (but not DC or Nyquist components)
        P(blk,:) = P(blk,:)/N; % Apply FFT length correction
    end

    P = P * wincorr; % Apply window correction
    Psum = sum(P,1)/nblocks; % Sum each column in P (blocks) and
calculate average

    SPLdB(Chan,:) = 20*log10(Psum(1,:)/2e-5); % Convert to decibels
end

end
```

Appendix B

OTRF Test Matrix for Nozzle X

Run Order	Test condition	Inlet temperature	EOTDF Injection temp	ΔT approximately	ΔT/T approximately	Mean NGV exit-mid-span Mach number	Run duration Approximately (s)	Number of runs	Total time (s)	Comment	ΔT/300
1	Uniform	444	0	0	0.0	1.10	0.4	6	2	Background	0
2	Uniform	444	0	0	0.0	0.90	0.4	5	2	Background	0
3	Uniform	305	0	0	0.0	0.9	2	4	6	Injection background	0
4	Uniform	305	300	0	0.0	0.9	2	4	6	Injection background	0.02
5	Non-uniform EOTDF	444	300	144	0.3	0.90	0.21	18	4	Effect of M (where M<1)	0.48
6	Non-uniform EOTDF	444	300	144	0.3	1.00	0.21	9	2	Effect of M (where M>1)	0.48
7	Non-uniform EOTDF	444	300	144	0.3	1.10	0.21	9	2	Effect of M (where M>1)	0.48
8	Uniform	444	0	0	0.0	1.00	0.4	6	2	Background	0
9	Uniform	380	0	0	0.0	0.90	0.5	4	2	Background	0
10	Uniform	380	0	0	0.0	1.00	0.5	4	2	Background	0
11	Uniform	380	0	0	0.0	1.10	0.5	4	2	Background	0
12	Non-uniform EOTDF	380	300	80	0.2	0.90	0.5	4	2	Effect of T (at M<1)	0.27

13	Non-uniform EOTDF	380	300	80	0.2	1.00	0.5	4	2	Effect of T (at Design M)	0.27
14	Non-uniform EOTDF	380	300	80	0.2	1.10	0.5	4	2	Effect of T (at M>1)	0.27
15	Uniform	412	0	0	0.0	0.80	0.4	6	2	Background	0
16	Uniform	412	0	0	0.0	0.90	0.4	6	2	Background	0
17	Uniform	412	0	0	0.0	0.95	0.4	6	2	Background	0
18	Uniform	412	0	0	0.0	1.00	0.4	6	2	Background	0
19	Uniform	412	0	0	0.0	1.10	0.4	6	2	Background	0
20	Non-uniform EOTDF	412	300	112	0.3	0.80	0.25	8	2	Effect of T (at M<1)	0.37
21	Non-uniform EOTDF	412	300	112	0.3	0.90	0.25	8	2	Effect of T (at M<1)	0.37
22	Non-uniform EOTDF	412	300	112	0.3	0.95	0.25	8	2	Effect of T (at M<1)	0.37
23	Non-uniform EOTDF	412	300	112	0.3	1.00	0.25	8	2	Effect of T (at Design M)	0.37
24	Non-uniform EOTDF	412	300	112	0.3	1.10	0.25	8	2	Effect of T (at M>1)	0.37

OTRF Test Matrix for Nozzle 1.5x

Run Order	Test condition	Inlet temperature (K)	EOTDF Injection temp	ΔT approximately	ΔT/T approximately	Mean NGV exit- mid-span Mach number	Run duration approx. (s)	Number of runs	Total time (s)	Comment	ΔT/300
1	Uniform	444	0	0	0.0	0.78	0.4	0	0	Background	0
2	Uniform	444	0	0	0.0	0.90	0.4	6	2	Background	0
3	Uniform	444	0	0	0.0	1.00	0.4	6	2	Background	0
4	Uniform	444	0	0	0.0	1.10	0.4	6	2	Background	0
5	Non-uniform EOTDF	444	300	144	0.3	0.78	0.2	4	0.8	Effect of M (where M<1)	0.48
6	Non-uniform EOTDF	444	300	144	0.3	0.90	0.2	18	4	Effect of M (where M<1)	0.48
7	Non-uniform EOTDF	444	300	144	0.3	1.00	0.2	10	2	Effect of M (where M=1)	0.48
8	Non-uniform EOTDF	444	300	144	0.3	1.10	0.2	10	2	Effect of M (where M>1)	0.48
9	Uniform	412	0	0	0.0	0.80	0.4	5	2	Background	0
10	Uniform	412	0	0	0.0	0.90	0.4	5	2	Background	0
11	Non-uniform EOTDF	412	300	112	0.3	0.80	0.25	8	2	Effect of T (at M<1)	0.37
12	Non-uniform EOTDF	412	300	112	0.3	0.90	0.25	8	2	Effect of T (at M<1)	0.37

OTRF Test Matrix for HP Turbine Stage

Run order	Test condition	Inlet temperature (K)	EOTDF Injection temp	ΔT approximately	ΔT/T approximately	Run duration approximately (s)	Number of runs	Total time (s)	Comment	ΔT/300
1	Uniform	300	0	0	0.0	2	3	6	Injection background	0
2	Non-uniform EOTDF	300	300	0	0.0	2	3	6	Injection background	0
3	Uniform	444	0	0	0.0	0.4	5	2	Background	0
4	Uniform	412	0	0	0.0	0.4	5	2	Background	0
5	Uniform	380	0	0	0.0	0.4	5	2	Background	0
6	Non-uniform EOTDF	444	300	144	0.3	0.4	5	2	Effect of M (where M<1)	0.48
7	Non-uniform EOTDF	412	300	144	0.3	0.4	5	2	Effect of M (where M<1)	0.48
8	Non-uniform EOTDF	380	300	144	0.3	0.4	5	2	Effect of M (where M=1)	0.48

References

Auregan Y., Maurel, A., Pagneux V., Pinton, J.-F., 2002, “Sound-Flow interactions. Lecture Notes in Physics”, Springer-Verlag, Berlin, 286

Bake, F., Kings, N., Fischer, A., Rohle, I., 2009, “Experimental investigation of the entropy noise mechanism in aero-engines”, *International Journal of Aeroacoustics*, vol. 8, pp. 125–142

Bake, F., Michel, U., Rohle, I., 2007, “Investigation of entropy noise in aero-engine combustors”, *Transaction of the ASME*, vol. 129, pp. 370-376

Bake, F., Michel, U., Rohle, I., Richter, C., Thiele, F., Liu, M. & Noll., B. 2005, “Indirect combustion noise generation in gas turbines”, *Proceedings of 11th AIAA/CEAS Aeroacoustics Conference*, pp. 2830-2844

Bake, F., Richter, C., Muhlbauer, B., Kings, N., Rohle, I., Thiele, F., Noll, B., 2009, “The Entropy Wave Generator (EWG): a reference case on entropy noise”, *Journal of Sound and Vibration*, pp. 574-598

Batchelor G.K., 1967, “An introduction to Fluid Dynamics”, Cambridge: University press.

Bloy, A. W., 1979, “The pressure waves produced by the convection of temperature disturbances in high subsonic nozzle flows”, *Journal of Fluid Mechanics*, vol. 94, pp. 465-475

Bohn, M. S., 1977, “Response of a subsonic nozzle to acoustic and entropy disturbances”, *Journal of Sound and Vibration*, pp. 283-297

Boutier, A., 1993, “New trends in instrumentation for hypersonic research”, Springer Science& Business Media Dordrecht, 617

Butler, T. L., Sharma, O. P., Joslyn, H. D., Dring, A. P., 1989, “Redistribution of inlet temperature distortion in a axial flow turbine stage”, *AIAA Journal of Propulsion and Power*, vol. 5, pp. 64-71

Candel, S. M., 1972, “Analytical studies of some acoustic problems of jet engines”, Dissertation, PhD, California Institute of Technology

Cannell, P., Ffowcs Williams, J.E., 1973, “Radiation from line vortex filaments exhausting from a two-dimensional semi-infinite duct”, *Journal of Fluid Mechanics*, vol. 58, pp. 65-80

Chana, K.S., Cardwell, D.N., Jones, T.V., 2013, “A review of Oxford Turbine Research Facility”, *ASME Turbo Expo San Antonio GT2013-95687*

Chu, B. T., Kovasznay, L. S. G., 1958, “Non-linear interactions in a viscous heatconducting compressible gas,” *Journal of Fluid Mechanics*, vol. 3, pp. 494–514

Crighton, D.G., 1972, “Radiation from vortex filament motion near a half plane”, *Journal of Fluid Mechanics*, vol. 51, pp. 357-362

Crighton, D. G., 1975, “Basic principles of aerodynamic noise generation”, *Progress in Aerospace Scieces*, vol. 16, pp. 31-96

Crighton, D. G. et al., 1992, “Modern methods in analytical acoustics: lecture notes”, Springer-Verlag, London, 738

Cumpsty, N. A., Marble, F. E., 1977, “The interaction of entropy fluctuations with turbine blade rows; a mechanism of turbojet engine noise,” *Proceedings of the Royal Society*, London, A., vol. 357, pp. 323–344

Cumpsty, N. A., Marble, F. E., 1977, “Core noise from gas turbine exhausts,” *Journal of Sound vibrations*, vol. 54, pp. 297-309

Cumpsty, N. A., 1979, “Jet engine combustion noise: pressure, entropy and vorticity perturbations produced by unsteady combustion and heat addition,” *Journal of Sound and Vibration*, vol. 66, pp. 527–544

Deardorff, J. W., 1970, “A numerical study of three-dimensional turbulent channel flow at large Reynolds numbers”, *Journal of Fluid Mechanics*, vol. 41, 453-480

Dring, R. P., 1989, “Redistribution of inlet temperature distortion in an axial flow turbine stage”, *AIAA Journal of Propulsion and Power*, vol. 5, pp. 64-71

Dorney, D. J., Gundy-Burlet, K. L., 2011, “Effects of hot streak shape on rotor heating in a high-subsonic single-stage turbine”, *International Journal of Turbo and Jet Engines*, vol. 18, pp. 1-18

Dowling, A. P., Mahmoudi, Y., 2015, “Combustion noise”, *Proceedings of the Combustion Institute*, vol. 35, pp. 65-100

Dowling A. P., Stow S. R., 2003, “Acoustic analysis of gas turbine combustors*”, Journal of Propulsion and Power*, vol. 19, pp. 751-764

Dowling, A.P., Ffowcs Williams, J.E., 1983, “Sound and sources of sound”, Chicester: Ellis Horwood

Duran, I., Moreau, S., 2013, “Solution of the quasi-one-dimensional linearized Euler equations using flow invariants and the Magnus expansion”, *Journal of Fluid Mechanics*, vol. 723, pp. 190-231

Duran, I., Leyko, M., Nicoud, F., Moreau S., Poinsot, T., 2013, “Computing combustion noise by combining large eddy simulations with analytical models for the propagation of waves through turbine blades”, *Comptes Rendus Mechanique*, vol. 341, pp. 131-140

“Entropy noise investigation. Report”, 2012, Rolls-Royce plc.

Ffowcs Williams, J.E., 1963, “The noise from turbulence convected at high speed”, *Philosophical Transactions of the Royal Society of London*, vol. 255, pp. 469-503

Ffowcs Williams, J. E., Howe, M. S., 1975, “The generation of sound by density inhomogeneities in low Mach number nozzle flows,” *Journal of Fluid Mechanics*, vol. 70, pp. 603–622

Ffowcs Williams, J. E., Hawkings, D. L., 1969, “Sound generation by turbulence and surfaces in arbitrary motion”, *Proceedings of the Royal Society*, London, vol. 264, pp. 321-342

Ffowcs Williams, J. E., 1974, “Sound production at the edge of a steady flow”, *Journal of Fluid Mechanics*, vol. 40, pp. 657-670

Garnier, E., Adams, N., 2009, “Large eddy simulation for compressible flows”, Springer: London, 276

Gatski, T. B., Bonnet, J.-P., 2013, “Compressibility, turbulence and high speed flow”, Amsterdam: Elsevier: Academic press, 328

Giauque, A., Huet, M., Clero, F., 2012, “Analytical analysis of indirect combustion noise in subcritical nozzles”, *Transactions of ASME: Journal of Gas Turbines and Power*, 134, 111202

Goh, C. S., Morgans, A. S., 2011, “Phase prediction of the response of choked nozzles to entropy and wave disturbances”, *Journal of Sound and Vibration*, 330, pp. 5184-5198

Goldstein, M. E., 1976, “Aeroacoustics”, New York: McGraw-Hill International Book Co, 293

Goldstein, S., 1960, “Lectures on Fluid Mechanics”, New York: Interscience

Hoch, R., Hawkins, R., 1973, “Recent studies in Concorde noise reduction”, *AGARD Conference Proceedings*, CP-131, Noise mechanisms

Holland, K. R., 2015, “Entropy noise. Deliverable report, Green function technique”, Rolls-Royce plc

Holland, K. R., Nelson, P. A., 2012, “An experimental comparison of the focused beamformer and the inverse method for the characterisation of acoustic sources in ideal and non-ideal acoustic environments”, *Journal of Sound and Vibration*, 331, pp. 4425-4437

Howe, M. S., 1975, “Contribution to the theory of aerodynamic sound, with application to excess jet noise and the theory of the flute”, *Journal of Fluid Mechanics*, vol. 71, pp. 625-673

Howe, M. S., 1998, “Acoustics of fluid-structure interaction”, Cambridge: Cambridge University Press, 560

Howe, M. S., 2003, “Theory of vortex sound”, Cambridge: Cambridge University Press, 216

Howe, M. S., 2010, “Indirect combustion noise”, *Journal of Fluid Mechanics*, vol. 659, pp. 267-288

Howe, M. S., 2015, “Acoustics and aerodynamic sound”, Cambridge: Cambridge University Press, 304

Huet, M., Giauque, A., 2013, “A nonlinear model for indirect combustion noise through a compact nozzle”, *Journal of Fluid Mechanics*, vol. 733, pp. 268-301

ICAO Circular 313, 2007, Outlook for Air Transport to the Year 2025

Ihme, M., Pitsch, H., Bodony, D., 2009, “Radiation of noise in turbulent non-premixed flames”, *Proceedings of the combustion institute*, vol. 32, pp. 1545-1553

Ihme, M., Pitch H., 2012, “On the generation of direct combustion noise in turbulent non-premixed flames", *International Journal*, vol. 11, pp. 25-78

Kaji, S., Okazaki, T., 1970, “Propagation of sound waves through a bade row I. Analysis based on the semi-actuator disk theory”, *Journal of Sound and Vibration*, vol. 11, pp. 339-353

Kato, C., Takano, Y., Iida, A., Ikegawa, M., 1991, “Numerical computation of aerodynamic noise radiated by the large eddy simulation”, *5th Numerical Fluid Dynamics Symposium*, pp. 195-198

Kempton, A.J., 1976, “Heat diffusion as a source of aerodynamic sound”, *Journal of Fluid Mechanics*, vol. 78, pp. 1-31

Kinnear, K. M., Lu, F. K., 1999, “Characterization of thin film heat-flux gauges*”, Journal of Thermophysics and Heat Transfer*, vol. 13, pp. 548-549

Kleissl, J., 2004, “Field experimental study of the Smagorinsky model and application to Large Eddy Simulation”, Dissertation, PhD, Johns Hopkins University

Koupper, C., Gicquel, L., Duchaine, F., Bonneau, G., 2015, “Advanced combustor exit plane temperature diagnostics based on Large Eddy Simulation”, *Flow, Turbulence and Combustion*, vol. 95, pp. 79-96

Kovasznay, L. S. G., 1953, “Turbulence in supersonic flow,” *Aerospace Science and Technology*, Vol. 20, pp. 657-682

Kremer, F., Bogey, C., Bailly, C., 2013, “Influence of resolution and Reynolds number on large-eddy simulations of channel flow using relation filter”, 51st AIAA Aerospace Sciences Meeting including the new horizons forum and aerospace exposition, pp. 67-82

Landau, L. D., Lifshitz, E. M., 1987, “Fluid Mechanics”, Butterworth-Heinemann, 554

Lefebvre, A. H., 1999, “Gas Turbine Combustion”, Taylor&Francis, Philadelphia

Lesieur, M., Metais, O., 1996, “New trends in Large Eddy Simulations of turbulence”, *Annual review of Fluid Mechanics*, vol. 28, pp. 45-82

Leyko, M., Nicoud, F., Poinsot, T., 2009, “Comparison of direct and indirect combustion noise mechanisms in a modern combustor,” *AIAA Journal*, vol. 47, pp. 2709-2716

Leyko, M., Nicoud, F., Moreau, S., Poinsot, T., 2009, “Numerical and analytical investigation of the indirect combustion noise in a nozzle”, *Comptes Rendus Mechanique*, vol. 337, pp. 415-425

Leyko, M., Nicoud, F., Moreau, S., Poinsot, T., 2011, “Numerical and analytical modelling of entropy noise in a supersonic nozzle with a shock”, *Journal of Sound and Vibration*, vol. 330, pp. 3944-3958

Lighthill, M. J., 1952, “On sound generated aerodynamically. I”, *Proceedings of the Royal Society*, London, A., vol. 211, pp. 564–587

Lighthill, M. J., 1953, “On the energy scattered from the interaction of turbulence with sound or shock waves”, *Mathematical Proceedings of the Cambridge Philosophical Society*, vol. 49, pp. 531-551

Lighthill, M. J., 1954, “On sound generated aerodynamically. II”, *Proceedings of the Royal Society*, London. A., vol. 222, pp. 1–32

Lighthill, M. J., 1980, “Introduction to Fourier analysis and generalised functions”, Cambridge: Cambridge University Press, 79

Lighthill, M. J., 2001, “Waves in fluids”, Cambridge: Cambridge University Press, 504

Lu, H. Y., 1977, “An analytical model for entropy noise of subsonic nozzle flow”, *AIAA 4th Aeroacoustic Conference*, pp. 77-1366

Marble, F. E., Candel, S. M., 1977 “Acoustic disturbances from gas non-uniformities convected through a nozzle,” *Journal of Sound and Vibration*, vol. 55, pp. 225-243

Mason, P. J., 1994, “Large Eddy Simulation: a critical review of the technique”, *Quarterly Journal of the Royal Meteorological Society*, vol. 120, pp. 1-26

Meneveau, C., Katz, J., 2000, “Scale-invariance and turbulence models for Large Eddy Simulation”, *Annual Review of Fluid Mechanics*, vol. 32, pp. 1-32

Morfey, C. L., 1973, “Amplification of aerodynamic noise by convected flow inhomogeneities”, *Journal of Sound and Vibration*, vol. 31, 391-397

Muehlbauer, B., Noll, B., Aigner, M., 2008, “Numerical investigation of entropy noise and its acoustic sources in aero-engines”, *Proceedings of the ASME Turbo Expo 2008*, ASME, Berlin, Germany, GT2008-50321

Muir, R. S., 1977, “The application of a semi-actuator disk model to sound transmission calculations in turbomachinery part I: the single blade row”, *Journal of Sound and Vibration*, vol. 54, pp. 393-408

Muir, R. S., 1977, “The application of a semi-actuator disk model to sound transmission calculations in turbomachinery part II: multiple blade rows”, *Journal of Sound and Vibration*, vol. 55, pp. 349-355

Nieuwstadt, F. T. M., Mason P. J., Moeng, C.-H., Schumann, U., 1991, “Large Eddy Simulation of the convective boundary layer: a comparison of four computer forms”, *Turbulent Shear Flows*, vol. 8, pp. 343-367

Pickett, G. F., 1975, “Core engine noise due to temperature fluctuations convecting through turbine blade rows”, *Proceedings of 2nd AIAA Aeroacoustics Conference – AIAA*, 528

Pierce, A. D., 1989, “Acoustics: an Introduction to its Physical Principles and Applications”, American Institute of Physics, 678

Povey, T., Chana, K. S., Jones, T. V., Hurrion, J., 2007, “The effect of Hot-Streak on HP Vane Surface and Endwall Heat Transfer: an experimental and Numerical Study,” *ASME Journal of Turbomachinery*, vol. 129, pp. 32-43

Roach, G. F., 1982, “Green’s functions”, Cambridge: Cambridge University Press, 325

Sagaut, P., Cambon, C., 2008, “Homogeneous Turbulence Dynamics”, Cambridge University Press: Cambridge

Seror, C., Sagaut, P., Bailly, C., Juve, D., 2000, “Subgrid-scale contribution to noise production in decaying isotropic turbulence”, *AIAA Journal*, vol. 38, pp. 1795-1803

Sinai, Y. L., 1980, “The generation of combustion noise by chemical inhomogeneities in steady, low-Mach-number duct flows”, *Journal of Fluid Mechanics*, vol. 99, pp. 383-397

Smagorinsky, J., 1963, “General circulation experiments with the primitive equations. I. The basic experiment”, *Monthly Weather review*, vol. 91, pp. 99

Stow, S. R., Dowling, A. P., Hynes, T. P., 2003, “Reflection of circumferential modes in a choked nozzle,” *Journal of Fluid Mechanics*, vol. 467, pp. 215-239

Strahle, W. C, 1971, “On combustion generated noise”, *Journal of Fluid Mechanics*, vol. 49, pp. 399-414

Strahle, W. C., 1973, “A review of combustion generated noise”, *AIAA Paper*, No. 73-1023, pp. 229-248

Strahle, W. C., Shivashankara, B. N., 1975, “A rational correlation of combustion noise results from open turbulent premixed flames”, *International Symposium on Combustion*, vol. 15, pp. 1379-1385

Strahle, W. C., 1978, “Combustion noise”, *Progress in Energy and Combustion Science*, vol. 4, pp. 157-176

Strahle, W. C., Muthukrishan M., Neale, D. H., 1978, “Separation of hydrodynamic, entropy, and combustion noise in a gas turbine combustion noise component”, *AIAA Journal*, vol. 16, pp. 320-327

Stull, R. B., 1997, “An Introduction to Boundary Layer Meteorology”, Kluwer Academic Publishers, Dordrecht, Netherlands

Tanahashi, M., Tsukinari S., Saiton, T., Miyauchi T., Choi, G. M., Ikame, M., Kishi, T., Harumi, K., Hirooka, K, 2002, “On the sound generation and its controls in turbulent combustion field”, *Proceedings of the 3rd Symposium Smart Control of Turbulence*, pp. 149-160

Tam, C. K. W., 2012, “Computational aeroacoustics: a wave number approach,” Cambridge University Press, New York

“The Jet Engine”, 2005, Rolls-Royce plc

Thomas A., Williams G. T., 1966, “Flame noise: sound emission from spark-ignited bubbles of combustible gas”, *Proceedings of the Royal Society*, London, A294, pp. 449-466

Wu, X., Jacobs, R., Hunt, J., Durbin, P., 1999, “Simulation of boundary layer transition induced by periodically passed wake”, *Journal of Fluid Mechanics*, vol. 398, pp. 109-153